CALCIUM AND MAGNESIUM CONTAINING ANTI-CORROSION FILMS ON MILD STEEL

A thesis submitted to the University of Manchester
for the degree of Doctor of Philosophy
in the Faculty of Engineering and Physical Sciences

2010

Yuanfeng Yang

Corrosion and Protection Centre, School of Materials

Contents

ABSTRACT

Under normal conditions, cathodically protected mild steel in seawater is protected by a precipitated film of calcium carbonate and magnesium hydroxide, the so-called calcareous film. This study has attempted to investigate the dynamics of calcareous deposit formation during cathodic protection and the composition of calcareous deposits formed under different applied current densities, and also the role played by the initial current density in forming a good quality calcareous deposit. In addition, an under protection situation can occur where current demand values are under estimated, or where structures are approaching the end of their design lives. In these conditions, a calcareous film might well occur but complete protection is probably not possible. These situations have also been studied. At low insufficient current densities where steel corrosion is still occurring, a clear correlation exists between the iron containing corrosion product and the overlaying magnesium hydroxide layer. Such effects have also been investigated using pH titration analysis, where the effect of co-precipitation of the iron and magnesium oxides/hydroxides has been shown. At higher current densities a layered precipitate has been shown to occur consisting of an inner magnesium containing layer and an outer calcium containing layer. At obvious overprotection current densities, the mechanical stresses involved in hydrogen evolution are assumed to give rise to film cracking.

To augment and compliment the study on calcareous calcium/magnesium films formed during cathodic protection, a calcium-magnesium containing pigment has also been investigated in aqueous solutions at open circuit as a possible corrosion inhibitor. Another study looked at the same inhibitor in conjunction with a sacrificial zinc anode. Very effective inhibition has been shown with the film containing not only magnesium, calcium and phosphorous but also zinc.

In all the investigations electrochemical methods have been used together with various surface analytical techniques.

Keywords: marine corrosion, cathodic protection, calcareous deposits, corrosion inhibitor, electrochemical methods, surface analytical techniques.

DECLARATION

No portion of the work referred to in this thesis has been submitted in support of an application for another degree or qualification of this or any other university or other institution of learning.

Signature

COPYRIGHTS

ACKNOWLEDGEMENTS

I would like to give my sincerest thanks to my supervisor, Professor David Scantlebury for his support, kindness, guidance, efficient supervision and many invaluable suggestions during the concept of this subject, discussions throughout the three years of my research work, and assistance during the preparation of this Thesis.

I would like to thank Dr Elena Koroleva for her patient assistance and advice during the course of my studies, and especially her invaluable help during the titration study and on the EIS modeling.

I would like to thank The University of Manchester for the award of an EPSRC -Shell - Dorothy Hodgkin Postgraduate Scholarship that has provided me with sponsorship funding and therefore made it possible for me to carry out my Ph.D. over the last three years.

I would like to thank Dr Chris Wilkins for spending long hours assisting me with SEM and EDX analysis, and for his patient encouragement and support.

I would like to thank Dr Hiroyuki Tanabe for his invaluable suggestions during the inhibitive pigment work and for provision of pigment samples.

I would like to thank Judith Shackleton and Gary Harrison for their expert assistance in X-Ray Diffraction and trying to help me find the unidentified peaks.

I give special thanks to the Chinese academic visitors to the Corrosion and Protection Centre; I must specifically mention: Zhiming Gao, Min Du and Qing Qu, who all gave me useful advice on my research work.

Also thanks to my close friends, Yanlong Ma, Fan Zhou, Luo Chen and Fan Yang, you guys won't be forgotten! Thank you all for your special friendship - the last three years would have been very lonely without you. Also my lab mates in D6, especially Ali Adham and Mohamed Orayith, it was good to have you around when I was starting my studies.

Also thanks to the technical and professional support staff in the Centre, especially Sandra Kershaw, Steve Blatch, Alison Pearson, Harry Pickford and Paul Jordan for their help over the last three years.

Last but not least, my Family, especially my Parents and Sister, who all care deeply about me and have constantly encouraged me over the last three years.

PUBLICATIONS

(During my PhD study time)

1. Y. F. Yang, J. D. Scantlebury and E. Koroleva. “Underprotection of mild steel in seawater and the role of calcareous film”. NACE Corrosion Conference, Atlanta, USA, March 2009.

2. J. D. Scantlebury, T. Tsukada, Y. F. Yang and M. Du, “ Long –Term Cathodic Protection Performance Data of Two off-Shore Structures”, NACE Corrosion Conference, Atlanta, USA, March 2009.

3. Y. F. Yang, J. D. Scantlebury, E. Koroleva, O. Ogawa, and H. Tanabe, "A Novel Anti-corrosion Calcium Magnesium Polyphosphate Pigment and Its Performance in Aqueous Solutions on Mild Steel", pp 77–85, ECS Transactions, **24** (1), Fifth International Symposium on Advances in Corrosion Protection by Organic Coatings, 2010.

4. Y. F. Yang, J. D. Scantlebury, E. Koroleva, O. Ogawa, and H. Tanabe, "A Novel Anti-corrosion Calcium Magnesium Polyphosphate Pigment and Its Performance in Aqueous Solutions on Mild Steel when Coupled to Metallic Zinc", pp 163-183, ECS Transactions, **24**(1), Fifth International Symposium on Advances in Corrosion Protection by Organic Coatings, 2010.

5. Y. F. Yang, J. D. Scantlebury and G. M. Dowling. “The Effect of Surface Preparation on the Adhesion of Epoxy Coatings onto Mild Steel”. Trans. Electrochemical Society, 2010. (in print)

6. Y. F. Yang “Surface Analysis of Calcareous Films Produced by Cathodic protection of Mild Steel in Synthetic Seawater”. Poster. NACE Corrosion Conference. San Antonio., USA, March 2010.

Chapter 1. Introduction.

1.1. General background.

The process of corrosion affects both equipment and structures. This on-going state of deterioration in metals adds to the cost of construction and also corrosion protection.

The earliest study on the costs of corrosion to National Economies was the 'Hoar Report', published in 1971 [1], which stated that the corrosion cost to the U.K. was an estimated £1365m per annum or 3-4% of GNP. More recently, in 2006 a new survey on the cost of corrosion in the UK showed that the degradation of infrastructure and loss of product due to corrosive processes amounted to around 2 - 3% of GNP [2]. Most boats, ships and even ocean liners must be dry-docked every 2 to 5 years for major repair and repainting work. This constant process of maintenance and major repair is impossible for massive permanent structures such as oil and gas rigs and large bridges. Similar restrictions regarding the regular correction and restoration of deterioration due to corrosion also applies to submarine pipelines, and more recently; offshore wind farms. All such structures may have a design life of 20 to 50 years with at best a 10 year maintenance period. Efficient and effective protection against corrosion is therefore an absolute necessity if the design life of these facilities is to be realized or exceeded in practice, and also to justify the enormous initial investment costs that these facilities originally demand.

Not only does corrosion have a deleterious influence on metallic structures but it could also impact hugely on the safety of human life and pollution of natural environments. Therefore, the process of corrosion requires continuous and reliable methods of prevention or control. One of the most common corrosive environments is seawater and we will deal with corrosion in marine environments in greater detail later. We will also focus on steel as the most widely used material of construction, and will consider some of the commonly encountered limitations in using this metal.

Seawater is a conductive electrolyte, containing dissolved salts, gases, suspended organic and inorganic matter and live organisms. If these basic original parameters are considered collectively, together with the huge number of additional variables that can naturally occur, and which need to be taken into account, such as wide variations in external

environmental factors like temperature, pressure, hydrodynamic conditions and oxygen concentration, one would be tempted to evaluate corrosion in specific marine environments or ecosystems, rather than to expect to gain a thorough understanding of all possible marine conditions. However, an all-embracing and comprehensively applicable single model would be the ideal.

Steel is still the most common constructional material used in marine conditions. Mild steel, be it for ships, drilling platforms, offshore structure, underwater pipelines or cables, is an attractive material because of its excellent mechanical properties, its weldability and also because it is more abundant and cheaper to produce relative to other materials. However its corrosion resistance is certainly not ideal especially in a corrosive medium such as seawater which contains 3 - 3.5% sodium chloride.

For marine applications, mild steel must be protected against corrosion either by the application of a surface coating, or by using cathodic protection (CP) when under fully immersed conditions, or a combination of both of these methods. Cathodic protection of steel in seawater can give rise to the precipitation of a white chalk-like substance, usually called the calcareous deposit or calcareous film which forms on the protected metal surface, and then subsequently functions to further inhibit the corrosion process. Investigations into this type of coating form a major part of this research work.

1.2. Outline of Thesis.

For the purposes of providing the essential background information to my research work outlined here, Chapter 2 gives an account of the basic theory of corrosion, a discussion of the cathodic protection process and reviews the literature concerning deposition and formation of calcareous deposits and the mechanisms of action of inhibitors in aqueous media. In Chapter 3, an account of the experimental procedures and techniques utilised in this study will be presented.

In Chapter 4, my studies were concerned with the calcareous deposits that formed on mild steel under conditions of under and full protection in artificial sea water at both constant and variable current densities. In real situations, **underprotection** can occur, for example; where current demand values are under estimated, or where structures are approaching the end of their design lives and anodes are severely reduced in size and

hence current output, or in cold deep water situations where the calcareous film is more soluble and reluctant to form. In these situations, a calcareous film might well occur albeit at severely reduced thickness and complete protection is then probably not possible. These conditions were studied in the laboratory using artificial seawater and protection current densities less than would be normally applied in practice. We also focused on the growth, development and modeling of calcium and magnesium deposits that formed on mild steel samples immersed in artificial seawater when subjected to various levels of **full** cathodic protection. From the initial results obtained, we found an optimum level of current density to provide full protection. We extended this work by looking at varying the current densities with time, starting with a high initial current density for a limited time and subsequently reducing the applied current density. Experiments involving weight loss, electrochemical impedance spectroscopy (EIS), and surface analysis techniques using Scanning Electron Microscopy (SEM) and Energy-Dispersive X-Ray Analysis (EDX), together with X-ray diffraction (XRD) and Glow-Discharge Optical-emission Spectroscopy (GDOES) will be described in order to attempt to clarify the situations that exist under these interesting conditions.

In Chapter 5, to augment the studies on calcium and magnesium deposition during CP in seawater, we have investigated a calcium/ magnesium containing anti-corrosion pigment and its effect in aqueous solution on the corrosion of iron. This study has provided an interesting comparison with our previous work on the calcareous films.

Chapter 6 attempts to bring together and evaluate the overall results from all the experimental studies in our previous Chapters by comparing and contrasting the calcium/magnesium films generated by cathodic protection with the calcium/magnesium films generated from using the new corrosion inhibitor; and also discusses possible future work.

1.3. References.

1. Report of the Committee on Corrosion and Protection, HMSO, London, 1971.

2. R. Francis. “A Comparison of the Cost of Corrosion in the USA and UK”. NACE Corrosion 2006, Las Vegas.

3. Recommended Practice: Control of External Corrosion on Underground or Submerged Metallic Piping Systems, SP 0169-2007. NACE, Houston. 2007.

Chapter 2. Literature Review.

2.1. Introduction.

Cathodic protection is perhaps the most powerful technique that is routinely utilised for the prevention of corrosion on underground or submerged metal structures in various environments. By means of an externally applied electric current or coupled with a sacrificial anode, corrosion can be reduced to negligible levels.

The British Standards Institution defines cathodic protection as: "a means of rendering a metal immune from corrosive attack by causing direct current to flow from its electrolytic environment into the metal" [1]. The National Association of Corrosion Engineers defines cathodic protection as: "a technique to control corrosion of a metal surface by making that surface the cathode in an electrochemical cell, by means of an impressed direct current or attachment of sacrificial anodes such as magnesium, aluminum, or zinc" [2].

In the oil and gas industry, one use of cathodic protection is on underground pipelines. The guarantee that no leaks will develop on the soil side of a cathodically protected buried pipeline has made this means of fluid transport economically feasible. Indeed, this method of protection can be a means of directly making significant financial gains, through avoiding the use of overdesign as a safety factor and also indirectly paying less for compensation or insurance because prevention of leaks into the soil avoids pollution of the environment and also possible accidents resulting from fire hazard. A second important aspect of protection is for offshore structures. Structures are frequently designed for a 30/40 year working life with sacrificial anodes providing sufficient current capacity to supply the design current density for the anticipated life of the structure.

In the practical application of cathodic protection to metallic structures, one of the most basic primary concerns is to determine whether the applied current being used is actually adequate for preventing corrosion of the structure in question. Until recently, there was no practical direct method available for evaluating the performance of cathodic protection except weight loss testing, and therefore indirect methods have been defined by measuring the polarized potential of the structure for this purpose. The present day criteria upon which cathodic protection systems are designed are still based on guidelines

defined and originally issued by NACE in 1969 with a very recent update in 2007 [2].

2.2. Electrochemical Aspects of Aqueous Corrosion.

Evans has defined corrosion in his 1946 volume as: "destruction by chemical or electrochemical agencies"; in contrast to erosion, which means destruction by mechanical agencies [3]. Generally, the corrosion of metals in aqueous environments is caused by electrochemical processes.

The electrochemical theory of corrosion is derived from the local model proposed by Evans [3] and the concept of mixed corrosion potential first proposed by Wagner and Traud [4]. They described metallic corrosion as a combination of an anodic oxidation and a cathodic reduction. The anodic dissolution of metal is the same as the oxidation process producing metal ions as in the following equation;

$$M \rightarrow M^{n+} + ne^{-} \quad \ldots\ldots\ldots\ldots\ldots\ldots\ldots\ldots\ldots\ldots\ldots\ldots\ldots\ldots\ldots\ldots\ldots\ldots \quad (2\text{-}1)$$

According to Faraday's law, the rate of oxidization of a metal electrode is directly proportional to the number of coulombs which have passed.

$$Q = \frac{nFm}{M} \quad \ldots\ldots\ldots\ldots\ldots\ldots\ldots\ldots\ldots\ldots\ldots\ldots\ldots\ldots\ldots\ldots\ldots\ldots \quad (2\text{-}2)$$

Where:

Q = charge passed(C).

n = number of electrons for each metal atom.

F = Faraday's number; 96500 $C.mol^{-1}$.

m = the mass of oxidized metal (g).

M = atomic weight of metal (g/mol).

A diagrammatic representation of the processes involved in the corrosion of iron or steel under aqueous conditions is illustrated in Figure 2.1. The region on the metal surface where ferrous ions are released by corrosion is called the anode. Electrons flow in the metal from these anodic sites to regions on the metal surface where reduction reactions take place. These sites are known as cathodes. The energy for this spontaneous corrosion reaction comes from the difference in potential between the anodic and cathodic reactions. The circuit is completed by ion movement in the electrolyte.

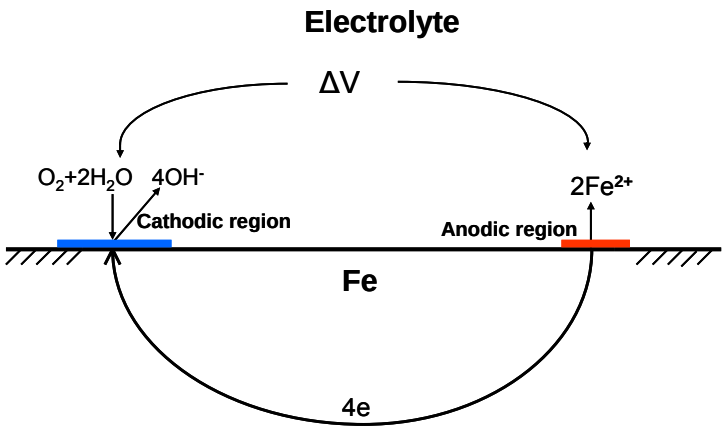

Figure 2.1. Diagram illustrating the mechanism of corrosion in aqueous systems.

In the case of iron or steel the anodic reaction will be:

$$Fe \rightarrow Fe^{2+} + 2e^{-} \quad \ldots\ldots\ldots\ldots\ldots\ldots\ldots\ldots\ldots\ldots\ldots\ldots\ldots\ldots\ldots\ldots\ldots\ldots \quad (2\text{-}3)$$

The cathodic reaction is a reduction process. There are two main reactions that may occur at the cathode during aqueous corrosion. Firstly; a process that consumes dissolved oxygen and generates hydroxyl ions,

$$O_2 + 2\,H_2O + 4e^{-} \rightarrow 4\,OH^{-} \ldots\ldots\ldots\ldots\ldots\ldots\ldots\ldots\ldots\ldots\ldots\ldots\ldots\ldots\ldots\ldots\ldots\ldots\ldots\ldots\ldots\ldots \quad (2\text{-}4)$$

and secondly; a process in which hydrogen gas is generated by the reduction of water when the potential becomes more negative as can be seen from the Pourbaix diagram given in Figure 2.3:

$$2H_2O + 2e^{-} \rightarrow H_2 + 2\,OH^{-} \ldots\ldots\ldots\ldots\ldots\ldots\ldots\ldots\ldots\ldots\ldots\ldots\ldots\ldots\ldots\ldots\ldots\ldots\ldots\ldots\ldots\ldots\ldots\ldots \quad (2\text{-}5)$$

Corrosion products may appear in the form of deposits when the compounds that comprise these anodic and cathodic products react with each other, and this leads to the formation of ferrous hydroxide; given by the reaction:

$$Fe^{2+} + 2\,OH^{-} \rightarrow 2Fe\,(OH)_2 \quad \ldots\ldots\ldots\ldots\ldots\ldots\ldots\ldots\ldots\ldots\ldots\ldots\ldots\ldots\ldots\ldots\ldots\ldots\ldots\ldots\ldots\ldots \quad (2\text{-}6)$$

The ferrous hydroxide may subsequently by oxidized to ferric oxide [Iron (III) oxide], which is the very familiar yellow-brown compound commonly known as rust. This reaction is as follows:

$$4Fe\,(OH)_2 + 2O_2 \rightarrow 2H_2O + 2Fe_2O_3.H_2O \ldots\ldots\ldots\ldots\ldots\ldots\ldots\ldots\ldots\ldots\ldots\ldots\ldots\ldots\ldots\ldots\ldots\ldots\ldots\ldots\ldots\ldots \quad (2\text{-}7)$$

Depending on the conditions, rust can take a variety of physical and chemical forms, with wide variations in colour, degree of hydration and bulk. A shielding effect caused by a thick deposit of rust may influence and alter the corrosion process. For example; reaction (2-7) undergoes modification [5] when the supply of oxygen is limited or restricted. Modified corrosion products are then formed, resulting from the following reactions:

$6Fe(OH)_2 + O_2 \rightarrow 4H_2O + 2Fe_3O_4.H_2O$ *(green hydrated magnetite)* …… (2-8)

$Fe_3O_4.H_2O \rightarrow H_2O + Fe_3O_4$ *(black magnetite)* ..…… (2-9)

The deposition of yellow–brown rust by reaction (2-7) frequently restricts the supply of oxygen to the layer of $Fe(OH)_2$ subsequently formed beneath it. This suggests that rust films might consist of three layers of oxides under different states of oxidation [6, 7].

(i). An inner core of black magnetite.

(ii). A thin layer of its green hydrate.

(iii). An outer coating of ordinary rust.

Dissolution of metal can occur only at the anodic surfaces, but the anodic and cathodic areas may also shift from time to time, so as to give the impression that a uniform rate of corrosion is occurring. However, any product appearing on the cathodic sites will generally restrict the cathodic process, causing it to slow down, and this slowing down of the cathodic reaction is called cathodic polarization. Similarly, anything that directly slows down the anodic reaction is called anodic polarisation.

2.3. Corrosion Thermodynamics.

Thermodynamics provides an understanding of the energy changes involved in the electrochemical reactions of corrosion. It is the energy changes that provide the driving force and control the spontaneous direction of the chemical reactions. Furthermore, thermodynamics provides a basis for expressing relationships between potential and composition of the bulk solution and for calculating surface concentrations of various species at the metal/solution interface. The Nernst equation is of particular importance for computing equilibrium potentials and is used for predicting the domains of corrosion and stability used to develop a potential-pH diagram. However, thermodynamics cannot predict the actual extent or rate of corrosion, so additional information from the kinetics of the reactions involved is required.

2.3.1. Electrode Potentials.

Corrosion occurs because metals have a tendency to return to more oxidized lower energy states. The oxidation reactions liberate energy and the propensity for oxidation varies from metal to metal depending on its electrode potential. The equilibrium electrode potential, E of a metal corresponds to the equilibrium established between its oxidised and reduced species. This means that at the equilibrium potential a metal and its ion will coexist with no tendency for reactions to proceed in predominantly one direction or the other.

A metal in an aqueous environment contains mobile electrons that form a complex interface at the metal/solution interface. This causes a build up of an electrical double layer that will oppose the expulsion of cations into the solution. An increasing electrical force will have the effect of opposing the tendency for chemical ionisation to occur, therefore establishing an electrochemical equilibrium. An example of this is an asymmetrical, polar water molecule, which will be attracted to the conductive surface. It will form an orientated solvent layer, thereby preventing close contact of the ions from the bulk solution. The charged ions will also attract their own polar water molecules, which will further insulate them from the conducting surface. The electric field of the double layer structure inhibits charge transfer, which therefore limits the electrochemical reactions at the surface. Figure 2.2 shows a schematic diagram of the formation of an electrical double layer at the surface of the metal/solution interface [8].

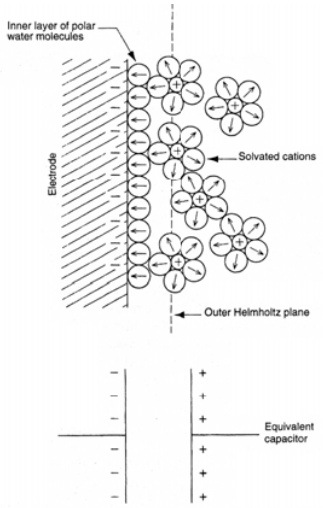

Figure 2.2. Diagrammatic representation of an electrode surface with an equivalent electric capacitor [8].

The electrical double layer produced due to the separation of charge is similar to a charged capacitor. It will have a potential difference between the two layers according to equation (2-10).

$Q = CE$ ……………………………………………………………………….. (2-10)

Where:

Q = electrical charge.
C = capacitance characterising the electrode.
E = potential difference in volts.

The E value in this equation is the electrode potential with respect to a reference electrode [9].

2.3.1.1. Gibbs Free Energy and Cell EMF.

The relationship between the free energy change and the equilibrium potential is required in order to obtain the free energy changes for both the anodic and cathodic reactions, and from which the sum of the free energy changes will give the total free energy change for the overall corrosion process. The Gibbs free energy change, ΔG, is associated with the electrochemical potential, E, at equilibrium, operating under conditions of constant temperature and pressure. ΔG can be related to the reversible electrode potential from the following equation:

$\Delta G = -nFE$ ………………………………………………. ……………………. (2-11)

Where:

ΔG = Free energy change for reaction.
n = Number of electrons involved in the reaction.
F = Faraday Constant (96500 $C.mol^{-1}$).
E = Potential at equilibrium (volts), at constant temperature and pressure.

The free energy change has a sign associated with the direction of the net cell reaction. Only an infinitesimal change in the overall cell potential is required to reverse the reaction direction. The potential, E, is usually constant and is independent of the direction of the reaction. In order to relate the direction sensitive quantity (ΔG) to the direction insensitive observable (E) then the electromotive force (EMF) of the electrochemical cell reaction is required.

The EMF is the maximum potential difference between two electrodes of a galvanic cell. This quantity is related to the tendency for an element, a compound or an ion to gain or lose electrons. EMF refers to a list of standard half-cell electrode potentials. The electrode potentials listed below are those referred to as reduction potentials. The electrode potentials are regarded as the potential of the metallic phase of the electrode with respect to the potential of the electrolyte solution phase of which it is in contact with. Table 2.1 provides a list of standard electromotive force potentials with examples ranging from the "noble" metals such as gold and platinum to much more "active" metals such as potassium and sodium as the possible extremes in the range of electrode potentials observed.

Table 2.1. Standard EMF Potentials [11].

Standard Electromotive Force Potentials (Reduction Potentials)

	Reaction	Standard Potential, e° (volts vs. SHE)
Noble	$Au^{3+} + 3e^- = Au$	+1.498
	$Cl_2 + 2e^- = 2Cl^-$	+1.358
	$O_2 + 4H^+ + 4e^- = 2H_2O$ (pH 0)	+1.229
	$Pt^{2+} + 3e^- = Pt$	+1.118
	$NO_3^- + 4H^+ + 3e^- = NO + 2H_2O$	+0.957
	$O_2 + 2H_2O + 4e^- = 4OH^-$ (pH 7)*a*	+0.82
	$Ag^+ + e^- = Ag$	+0.799
	$Hg_2^{2+} + 2e^- = 2Hg$	+0.799
	$Fe^{3+} + e^- = Fe^{2+}$	+0.771
	$O_2 + 2H_2O + 4e^- = 4OH^-$ (pH 14)	+0.401
	$Cu^{2+} + 2e^- = Cu$	+0.342
	$Sn^{4+} + 2e^- = Sn^{2+}$	+0.15
	$2H^+ + 2e^- = H_2$	0.000
	$Pb^{2+} + 2e^- = Pb$	−0.126
	$Sn^{2+} + 2e^- = Sn$	−0.138
	$Ni^{2+} + 2e^- = Ni$	−0.250
	$Co^{2+} + 2e^- = Co$	−0.277
	$Cd^{2+} + 2e^- = Cd$	−0.403
	$2H_2O + 2e^- = H_2 + 2OH^-$ (pH 7)[a]	−0.413
	$Fe^{2+} + 2e^- = Fe$	−0.447
	$Cr^{3+} + 3e^- = Cr$	−0.744
	$Zn^{2+} + 2e^- = Zn$	−0.762
	$2H_2O + 2e^- = H_2 + 2OH^-$ (pH 14)	−0.828
	$Al^{3+} + 3e^- = Al$	−1.662
	$Mg^{2+} + 2e^- = Mg$	−2.372
	$Na^+ + e^- = Na$	−2.71
Active	$K^+ + e^- = K$	−2.931

[a]Not a standard state but included for reference.

Source: Handbook of Chemistry and Physics, *71st ed., CRC Press, 1991.*

It is impossible to measure the absolute value of any half-cell electrode potential. For this reason only the cell potentials consisting of two half-cell electrode potentials can be measured and one must be selected as a primary reference. The zero, reference point for

the EMF series and other electrochemical potential measurements were arbitrarily selected as the half-cell electrode potential of the hydrogen half-cell at standard state (SHE) [8, 9, 10].

2.3.1.2. Nernst Equation.

The standard state identifies that all reactants and products be at unit activity. There must be some means of calculating half-cell electrode potentials that do not meet these standard state conditions. In 1888, Nernst [12] first derived an equation, which linked the reversible potential of an electrode (measured in volts), designated E, to the standard reversible potential of the electrode couple, designated E_0 that is the thermodynamic value. This equation was able to predict departures from unit activity. The Nernst equation can be written as such:

$$E = E_0 - \frac{RT}{nF}\ln\left(\frac{\prod[\mathrm{Re}\,d]}{\prod[Ox]}\right) \quad \text{..... (2-12)}$$

Where:

E_0 = equilibrium potential for unit activies.

R = universal gas constant (8.314 $Jmol^{-1}K^{-1}$).

T = absolute temperature in degrees Kelvin.

n = charge number of the electrode reaction (number of moles of electrons, involved in the reaction).

F = Faraday constant (96500 $C.mol^{-1}$).

Note: Red denotes the chemical activities of the species on the reduced side of the electrode reaction, whereas Ox denotes the chemical activities of the species on the oxidised side of the electrode reaction.

At 25^{o}C (298.15K) the numerical value of the constants and the conversion of the logarithm of base e (ln) to the logarithm of base 10 (log) are combined to simplify the Nernst equation:

$$E = E_0 - \frac{0.059}{n}\log\left(\frac{\prod[\mathrm{Re}\,d]}{\prod[Ox]}\right) \quad \text{..... (2-13)}$$

2.3.1.3. Effect of pH.

The quantity *2.3RT/F* is equal to 0.059 V at 25^{o} C when all constants are substituted. The activity of water is defined as the unity in aqueous solutions and the definition of pH is pH = -log [H^{+}]. The Nernst equation can be rewritten as:

$$E = E_0 + \frac{2.3RT}{nF}\log \alpha_{H+} = E_0 - 0.059\,pH \quad \ldots\ldots\ldots\ldots\ldots\ldots\ldots\ldots\ldots\ldots\ldots\ldots\ldots\ldots\ldots\ldots\ldots\ldots \text{(2-14)}$$

This implies that the electrode potential for hydrogen evolution changes by 59mV for every pH unit when assuming a pressure of 1 atmosphere [9].

The potential can thus be seen as a measure of oxidising power of the solution. The Nernst equation has correctly predicted that increased oxygen activity causes the half-cell electrode potential for the reaction to become more positive.

2.3.1.4. E-pH Pourbaix Diagram.

Pourbaix [13] devised a compact summary of thermodynamic data in the form of potential-pH diagrams, which relate to the electrochemical and corrosion behaviour of any metal in water. Figure 2.3 shows a typical diagram for iron in water at 25^{o}C. The diagram can be divided into 3 regions; immunity, corrosion, and passivation. However, there are certain limitations on the use of such diagrams. There is very limited information relating to the rates of reaction, and furthermore; the information that is presented is derived from pure metals and environments [13]. It should therefore be noted, that such potential ─ pH diagrams only provide partial information about the reaction rates. The corrosion rates are in the domain of electrode kinetics.

However, a very useful advantage of this type of diagram is that it provides a simple method of predicting a specific condition of potential and pH under which any particular metal either may or may not react with an electrolyte, and it has been shown that use of such diagrams as theoretical model-based predictors of pH and potential values gives good correlations with actual situations [13]. As an example, the situation can be considered when iron is partially covered with its oxide and immersed in a neutral solution at pH 7. If the potential falls to -0.6 V with respect to the standard hydrogen electrode (SHE), it is seen from Figure 2.3 that it is in a condition of immunity. Similarly, if the conditions are the same as those mentioned above, but with a potential which falls to only -0.2 V with respect to saturated calomel electrode (SCE), then the iron will still be

in a condition of corrosion. When the pH is <7 the iron is in a zone of corrosion but when the pH is >7, iron is in a zone of passivation.

Therefore, in order to protect iron against corrosion, protection is based on the fact that the potential becomes reduced to the point where it enters into the domain of immunity, in which region the corrosion of iron is theoretically impossible. For example, when the pH is below 10, Ev = -0.62V (SHE) = -0.89 V (SCE) [13].

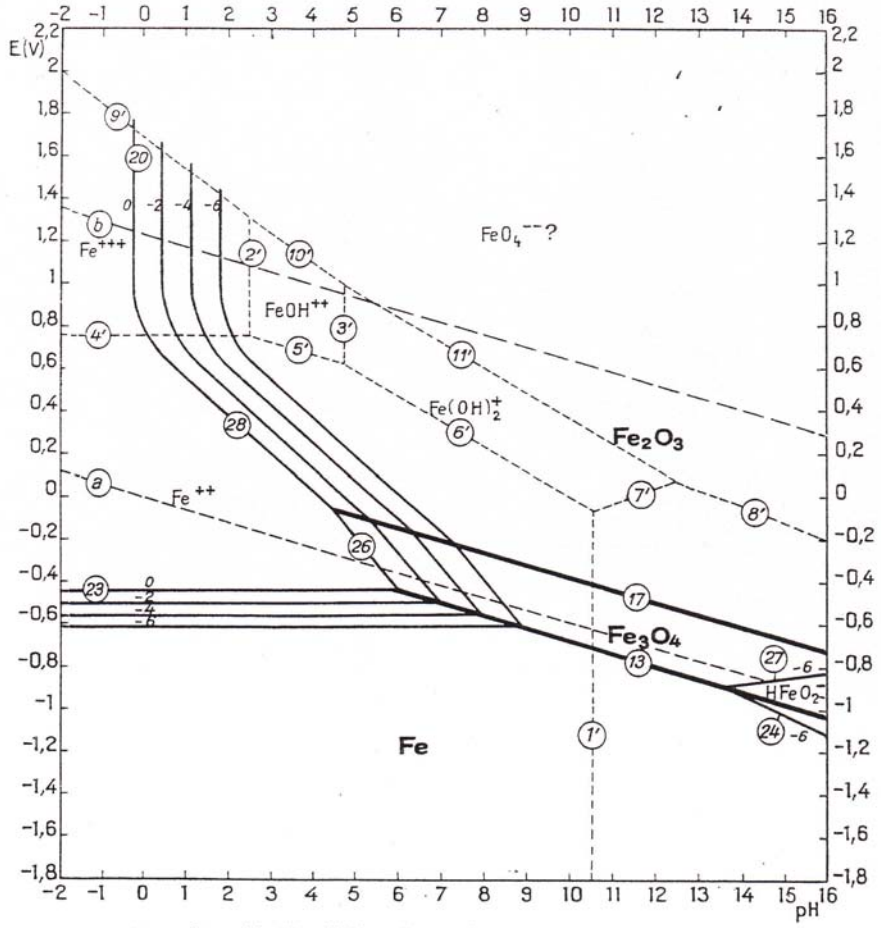

Figure 2.3. E-pH diagram for Fe-H_2O at 25°C. Hydrogen evolution is possible only at potentials below the line b, and only above the line a is oxygen reduction possible [13].

2.4. Electrochemical kinetics of corrosion- Polarization diagrams.

Polarization (η) is defined as the potential change, $E–E_0$, derived from the equilibrium half-cell electrode potential, E_0, due to the net surface reaction rate for the half-cell reaction. Under conditions of cathodic polarization (η_c) electrons are supplied to the surface. Conversely, under conditions of anodic polarization, electrons will be removed from the metal causing a deficiency, therefore resulting in a positive potential change.

There are three types of polarization, these are: activation, concentration, and resistance polarization [14].

2.4.1. Activation Polarization.

2.4.1.1. Introduction.

The Butler-Volmer equation is one of the most fundamental equations in electrode kinetics, and describes the linkages between the current density and the exchange-current densities, the overpotential and the transfer coefficients. It is named after chemists John Alfred Valentine Butler and Max Volmer, and was developed from an article by Volmer in 1930 [15], which was based on an earlier article by Butler [15].

When utilised to characterise the range of electrochemical reactions that occur during corrosion processes, the Butler-Volmer equation describes how the electrical current on an electrode depends on the electrode potential, considering that both a cathodic and an anodic reaction occur on the same electrode [16]:

$$i = i_0 \left\{ \exp\left[\frac{(1-\alpha)\cdot F}{R\cdot T}(E - E_{eq}) \right] - \exp\left[-\frac{\alpha \cdot F}{RT}(E - E_{eq}) \right] \right\} \quad \text{..... (2-15)}$$

Where:

I = electrode current density, A/m^2
i_o = exchange current density, A/m^2
E = electrode potential, V
E_{eq} = equilibrium potential, V
T = absolute temperature, K
F = Faraday constant
R = universal gas constant
A = so-called symmetry factor, dimensionless

For an anodic reaction: $\eta_a = E - E_{eq} > 0$ ..... (2-16)
For a cathodic reaction: $\eta_c = E - E_{eq} < 0$ ..... (2-17)
The terms η_a and η_c are called overpotential.

$$i_a = i_0 \left\{ \exp\left[\frac{(1-\alpha)\cdot F}{R\cdot T}\eta_a \right] - \exp\left[-\frac{\alpha \cdot F}{RT}\eta_a \right] \right\} \quad \text{..... (2-18)}$$

$$i_c = i_0 \left\{ \exp\left[\frac{(1-\alpha)\cdot F}{R\cdot T}\eta_c \right] - \exp\left[-\frac{\alpha\cdot F}{RT}\eta_c \right] \right\} \quad \text{(2-19)}$$

When the overpotential reaches a value > +0.052V [16], in the case of an anodic reaction, the latter can be neglected, and therefore equation 2-18 simplifies to:

$$i_a = i_0 \exp\left[\frac{(1-\alpha)\cdot F}{R\cdot T}\eta_\alpha \right] \quad \text{(2-20)}$$

Similarly, for overpotential more negative than -0.052V [16], for the cathode reaction, the first term can be neglected, so the equation 2-19 simplifies to:

$$i_c = -i_0 \exp\left[-\frac{\alpha\cdot F}{R\cdot T}\eta_c \right] \quad \text{(2-21)}$$

Taking logarithms in equation 2-20,

$$\ln i_a = \ln i_0 + \frac{(1-\alpha)F}{RT}\eta_a \quad \text{(2-22)}$$

and for an anodic reaction:

$$\eta_a = \frac{-RT}{(1-\alpha)F}\ln i_0 + \frac{RT}{(1-\alpha)F}\ln i_a \quad \text{(2-23)}$$

And since $\frac{RT}{F}\ln x = 0.059\log x$, at 25°C, then:

$$\eta_a = \frac{-0.059}{(1-\alpha)}\log i_0 + \frac{0.059}{(1-\alpha)}\log i_a \quad \text{(2-24)}$$

similarly for the cathode reaction:

$$\eta_c = \frac{RT}{\alpha F}\ln i_0 - \frac{RT}{\alpha F}\ln i_c \quad \text{(2-25)}$$

$$\eta_c = \frac{0.059}{\alpha}\log i_0 - \frac{0.059}{\alpha}\log i_c \quad \text{(2-26)}$$

This can then be expressed in following equation:

$$\eta = a + b\log i \quad \text{(2-27)}$$

This is known as Tafel's Law, and it was presented by Tafel in 1905 [16], it states that there exists a linear relationship between the potential and the log of the current density for a given electrochemical reaction.

The terms $\beta_a = \frac{RT}{(1-\alpha)F}$ and $\beta_c = \frac{RT}{\alpha F}$ are defined as Tafel Coefficients, so the equation (2-15) could be expressed as follows:

$$i = i_0 \left\{ \exp\left[\frac{2.303}{\beta_a}(E - E_{eq}) \right] - \exp\left[-\frac{2.303}{\beta_c}(E - E_{eq}) \right] \right\} \quad \text{(2-28)}$$

According to equation 2-23, for anodic polarization:

$$\eta_a = \frac{-RT}{(1-\alpha)F} \ln i_0 + \frac{RT}{(1-\alpha)F} \ln i_a = \beta_\alpha \log \frac{i_\alpha}{i_0} \quad \text{(2-29)}$$

Similarly, in the case of cathodic polarization:

$$\eta_c = \beta_c \log \frac{i_c}{i_0} \quad \text{(2-30)}$$

The overpotential term is frequently used for polarization. The anodic overpotential, η_a, is positive and the β_a will also be positive. For the cathodic polarization, β_c, is negative as η_c is negative as well. β_a and β_c are known as the Tafel constants for the half-cell reaction. The anodic, i_a, and cathodic, i_c, current densities flow in opposite directions. The Tafel relationships described in equations 2-29 and 2-30 are widely used in experiments for activation polarization.

2.4.1.2. Tafel fitting.

Figure 2.4 depicts experimental polarization curves for which the Tafel behaviour has been defined. The slope on a semi-log plot is defined as the Tafel behavior. Figure 2.4 depicts extrapolation of the Tafel behavior to give the corrosion rate, i_{corr} at E_{corr}. This allows corrosion rates to be measured from polarization data. From Figure 2.4, the Tafel slope can be extrapolated to $e_{H^+/H2}$, and the exchange current densities (i_0) obtained from the Tafel curves.

This is the equation of a straight line on a graph of E versus log *i* (or *vice versa*), and this forms the basis of the graphical approach to the description of corrosion kinetics.

To calculate the Tafel Coefficients β_α and β_c, it is a requirement to know the over potential and current at two points on the straight lines that have been fitted to the straight sections on the Evans diagram.

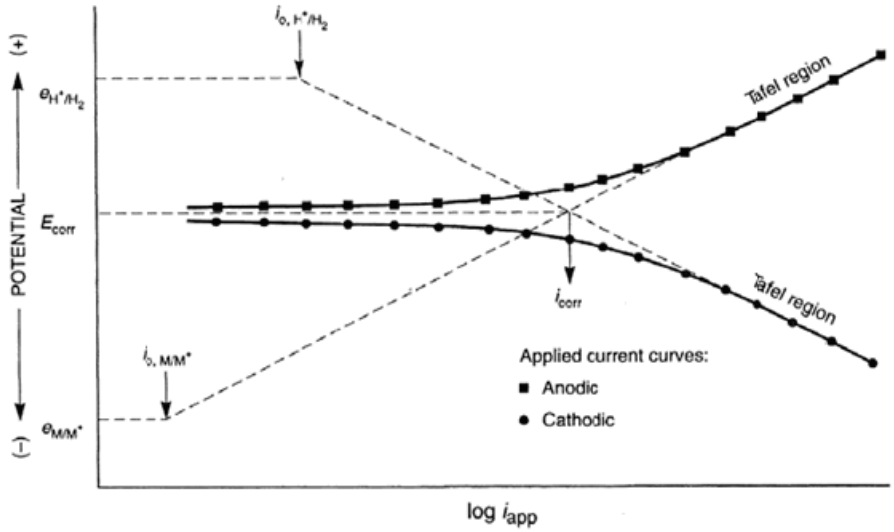

Figure 2.4. Example of an experimental polarisation curve used to determine the Tafel nature [8].

2.4.1.3. Linear polarization resistance (LPR).

Linear polarization resistance is a widely used technique; it is the slope of the E-i relationship at the open circuit potential, and it provides a method of estimating the instantaneous corrosion rate.

Earlier in this Section, we discussed how the Butler Volmer equation can be simplified to give the Tafel equation under conditions where the overpotential is very high or very low, which are both specific instances where the application of the Butler Volmer equation is severely limited. At potentials very close to the corrosion potential another equation can be found which the Butler-Volmer equation approximates to. This is the Stern-Geary equation [16], and in this Section we will derive this equation.

Considering the Butler-Volmer equation, and the fact that as:

$x \to 0$ $\exp(x) \to 1+ x$

Then equation 2-28 becomes:

$$i = 2.303 i_0 \left((1+\frac{\eta}{\beta_a}) - (1+\frac{-\eta}{\beta_c}) \right) = 2.303 i_{corr} \left((1+\frac{\eta}{\beta_a}) - (1+\frac{-\eta}{\beta_c}) \right) \quad \text{..... (2-31)}$$

This equation then becomes:

$$i = 2.303 i_{corr} \eta \left(\frac{\beta_\alpha + \beta_c}{\beta_\alpha \beta_c} \right) \quad \text{..... ..... (2-32)}$$

Which can be rearranged for the potential gradient with respect to the current density:

$$R_P = \frac{\eta}{i} = \frac{\beta_\alpha \beta_c}{2.303 i_{corr}(\beta_\alpha + \beta_c)} \quad \text{..... (2-33)}$$

R_P = polarisation resistance.

If the constant is calculated with values for the Tafel coefficients (β_a, β_c), η normally takes values between 12 and 50 mV and depends on the mechanism of the corrosion [17].

Linear polarisation resistance can be measured in a number of ways [18]:

- The potential can be swept through a narrow range either side of the Open Circuit Potential (OCP), the current recorded and the slope determined.
- The current can be swept through a small range about zero and the potential measured.
- The potential can be stepped between OCP-ΔE/2 and OCP+ΔE/2, where ΔE is a small potential difference (typically 10 to 20 mV). Then R_p can be determined as ΔE/Δ*i*, where Δ*i* is the change in current density.
- An applied current can be stepped between –Δi/2 and + Δi/2 and the corresponding potential step, ΔE, measured. This is the simplest approach for corrosion monitoring, as it automatically makes the measurement centered on the OCP, and the polarisation resistance is directly proportional to ΔE (since R_p=ΔE/Δ*i* and Δ*i* is constant). I performed my linear polarisation resistance testing using this method.

2.4.2. Concentration Polarization.

Concentration polarization refers to an electrochemical reaction in which the velocity of the reaction depends on the rate of approach of ions or molecules to the electrode surface and on the rate of the electrode processes [16].

The concentration profile of an ion in solution, for example H^+, is schematically represented in Figure 2.5. C_B is the H^+ concentration of the uniform bulk solution and δ is the thickness (boundary layer) of the concentration gradient in solution. The half-cell

electrode potential, $e_{H^+/H2}$, of the depleted surface is defined by the Nernst equation as a function of the ion (H^+) concentration or activity.

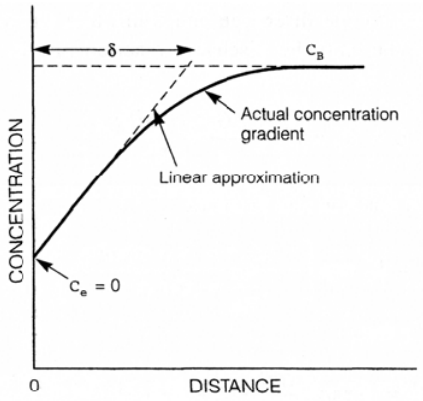

Figure 2.5. Schematic representation showing the concentration of an ion, i.e. H^+, in solution near a surface controlled concentration polarization [8].

In the case of an electrode in which there is no activation polarization, the decrease (potential change) is the concentration polarization, η_{conc}, given as a function of current density in equation 2-34.

$$\eta_{conc} = \frac{2.3RT}{nF}\log\left[1-\frac{i_c}{i_L}\right] \quad \text{.....} \quad (2\text{-}34)$$

The limiting current density i_L can be calculated from equation (2-35).

$$i_L = \frac{D_Z nFC_B}{\delta} \quad \text{.....} \quad (2\text{-}35)$$

Where:

n = number of equivalents exchanged (electrons).

F = Faraday's Constant (96500 $C.mol^{-1}$).

D_z = Diffusion Coefficient of reacting species (i.e. Z is H^+ in this example).

C_B = Concentration of bulk solution species.

δ = Boundary layer thickness (cm).

The limiting current density (i_L) is increased by higher solution concentrations (C_B) which causes the diffusion coefficient of the reacting species (D_z) to increase. A higher temperature also increases D_z and a higher solution agitation will decrease the boundary layer thickness (δ) [see Figure 2.6(b)]. Under conditions where corrosion processes are actively occurring, concentration polarisation is significant primarily for the cathodic reduction reactions. Concentration polarisation for anodic oxidation during corrosion can be ignored, as there is an unlimited supply of metal atoms at the metal/solution interface.

Concentration polarisation can be possible for anodic reactions that have very high corrosion rates or during intentional anodic dissolution by impressed currents [8].

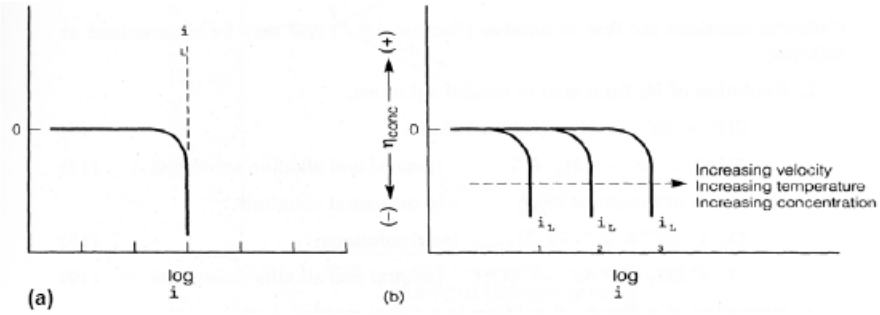

Figure 2.6. Schematic representation of cathodic polarisation [8];
(a) when plotted against the reaction rate and, (b) effect of velocity, temperature and concentration.

2.4.3. Resistance Polarization.

Resistance Polarization causes the potential of both the anode and cathode to differ, due to a potential drop across the solution, and hence the corrosion current is reduced.

Resistance overpotential η_R can be expressed in terms of the resistance of the solution as the following equation:

$$\eta_R = IR_S \qquad \text{(2-36)}$$

where R_s is the solution resistance. For sea water this value is very low about 16 ~ 35 Ω.cm [19] whereas for some paint systems values can be in excess of 10^8 Ω.cm^2 [20].

2.5. Cathodic Protection.

2.5.1. The Theory of Cathodic Protection.

The scientific principles of cathodic protection (CP) were first explained by Sir Humphry Davy in 1824 and 1825 [21, 22, 23]. A fuller discussion of Davy's contribution will be given in Chapter 4. Subsequently in 1938 Hoar [24], and Mears and Brown [25] used Evans diagrams to illustrate cathodic protection, as shown in Figure 2.7. This approach clearly shows how the anodic rates and cathodic rates change as the structure potential moves in a negative direction and how the net current density applied by the CP system is the difference between the local cathode and anode currents.

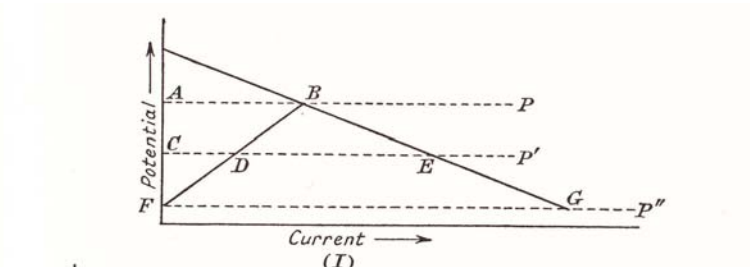

Figure 2.7. Simplified Evans Diagram [26].

2.5.2. The Corrosion of Mild Steel in Seawater on Cathodic Protection.

It will be evident from Figure 2.7, that when a current is applied to the steel surface, the cathodic current increases whilst the anodic current reduces and the pH value then increases resulting from the generation of hydroxyl ions from the oxygen reduction reaction. In the open ocean, pH values are usually within the fairly narrow range from 7.9 to 8.3 [27]. At potentials less negative than -950mv (SCE), the predominant cathodic reaction is diffusion controlled oxygen reduction [28]; and in cases where the potential is more negative than -1100mv (SCE), the alternative and additional cathodic reaction is the activation controlled hydrogen evolution reaction from the reduction of water as indicated in equation 2-5. In either case, the production of hydroxyl ions results in an increase in pH of the electrolyte adjacent to the metal surface. In this way, the increase in pH in seawater will result in the precipitation of insoluble salts; i.e. $CaCO_3$, $Mg(OH)_2$, and these processes can be described by the following series of reactions:

$$OH^- + HCO_3^- \rightarrow CO_3^{2-} + H_2O \quad \text{(2-37)}$$

$$Ca^{2+} + CO_3^{2-} \rightarrow Ca\,CO_3 \quad \text{(2-38)}$$

$$Mg^{2+} + 2OH^- \rightarrow Mg\,(OH)_2 \quad \text{(2-39)}$$

These reactions collectively give rise to the formation of a calcareous film or deposit on the surface of the steel.

As Davy himself showed, the generation of the necessary cathodic protection current and the driving potential may be accomplished in two ways. Attaching the structure to a more reactive metal, a sacrificial anode, is one possibility. The current is produced by dissolution of the reactive metal and the driving potential arises from the differences in the open circuit potentials between the sacrificial anode and the structure to be protected. Alternatively a non consumable anode may be attached to the structure via a DC power supply, an impressed current system. Current is supplied via an oxidation charge transfer reaction at the impressed anode, usually oxidation of the environment. The driving voltage is provided by the DC power supply. Extensive and comprehensive references are available in the literature that discuss fully this aspect of corrosion prevention [1, 2, 6, 8].

2.6. Literature Review of Calcareous Deposits.

Calcareous deposits are white/grey deposits which are known to form on the surfaces of metal structures which are cathodically protected whilst immersed in seawater. The presence of calcareous deposits is regarded as some indication that a measure of cathodic protection is being achieved [29], at least in systems in seawater where it is applied.

Sir Humphry Davy, a Cornishman born in Penzance, presented the very first paper on Cathodic Protection in 1824 [21]. He was investigating galvanic effects between iron (and zinc) and copper in seawater. In his studies on area ratios he happened to notice a white deposit on his copper cathode which on analysis was found to be "carbonated lime, and carbonated and hydrate of magnesia". Again we will be referring to this work in Chapter 4.

Cox [31, 32] carried out extensive studies in this area, leading to both British and American Patents, and in his 1941 British Patent stated: "an invention relating to improved types of inorganic coating formed *in-situ* for protecting metallic surfaces in contact with sea water or other water containing both magnesium and calcium salts, in a concentration range customarily found in sea or seaport water, and to improved procedures for forming and maintaining the desired type of anticorrosive or anti-fouling coating" [32].

Plate 2.1. Portrait of Sir Humphry Davy [30]

Plate 2.2. Statue of Davy with YuanFeng, in Penzance

The properties of calcareous coatings are generally very largely dependent on the chemical composition of the deposited material. Humble [33], states that a current density of 50 mA/ft^2 (538 mA/m^2) is adequate for the complete protection of steel. However, this current density is actually very large and is characteristic of studies on CP of marine structures. The same author also points out that these calcareous film deposits consist principally of calcium carbonate ($CaCO_3$) and magnesium hydroxide [$Mg(OH)_2$], and the ratio between these two compounds in the deposited film is dependent upon the current density, as shown in Figure 2.8. Humble [33] further states that $CaCO_3$ is precipitated first, followed by $SrCO_3$, $MgCO_3$ and finally $Mg(OH)_2$. It would therefore be expected that films formed at normal current densities would be rich in $CaCO_3$. Table 2.1 shows sets of results based on studies by Humble, which gives the range in composition of such coatings that occur with different current densities.

Elebeik [34] stated that the preferential formation of calcium carbonate rather than magnesium carbonate is because of the very much higher solubility of magnesium carbonate.

Thirty to forty years ago, it was common practice to apply a current density that was too low to give immediate protection**.** With North Sea structures for example, current

densities of 130 - 150 mA/m^2 (12 - 14 mA/ft^2) were generally quoted for bare steel [35, 36].

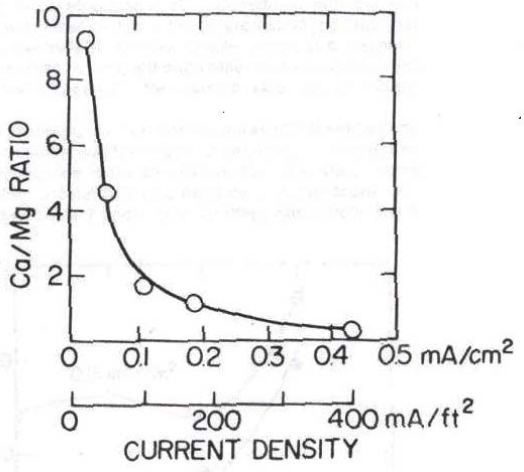

Figure 2.8. Graph illustrating plot of the Ca:Mg ratio of a calcareous deposit as a function of current density [33].

Table 2.1. Analysis of calcareous coatings [33].

Element (%)	Current density (mA/ft^2)			
	50	100	172	400
Na	0.72	0.85	0.78	1.03
Fe	3.78	3.46	2.6	2.12
Si	0.65	1.77	1.3	0.41
Cl	0.44	0.84	0.76	0.55
CO_3	44.62	32.62	29.66	14.7
Ca	28.91	20.88	17.54	6.73
Mg	6.51	13.53	18	29.47
Sr	0.14	0.06	0.04	0.006
OH (calculated)	8.37	18.18	23.35	38.52
Total	94.14	92.19	94.03	93.536

1 mA/ft^2=10.76 mA/m^2

These current densities are an order of magnitude lower than those used by Humble [33] and Cox [32]. However, it should be noted that Humble used magnesium anodes for cathodic protection, which probably explains the very high current densities that had to be employed.

Ulanovskiy [37] reports that a current density of 0.03 mA/cm^2 (300 mA/m^2) shifts the potential of steel from -0.4 V to -0.85 V in 36 hours while a current density of 0.1 mA/cm^2 (1000 mA/m^2) depresses the potential to about -0.8 V and thereafter maintains it constantly at or near this value. Increasing the current density is stated to increase the OH^- content of the calcareous coating, but at a given current density, increasing the

polarisation time reduces the OH^- content of the film; however, the protective properties of the film were reported to be increased with increasing polarisation time. However this work seems to be unaware of the hydrogen evolution reaction and its effect on the degree of protection provided by the calcareous film. We will return to this subject matter later in this Thesis.

During the process of cathodic protection there is an increase in pH at the steel surface. Engell and Forchhammer [38] have calculated that for steel under conditions of complete cathodic protection, the pH value at the metal surface is 10.9 at 20°C; $CaCO_3$ and $Mg(OH)_2$ are precipitated when their respective solubility products in seawater are exceeded. Seawater with a pH of around 8 is regarded as being super saturated with $CaCO_3$ and $Mg(OH)_2$. An increase in pH above 8 would be expected to cause precipitation of these salts and subsequent deposition on the protected metal surface. However, Engell and Forchhammer [38] predict that at 20°C, $Mg(OH)_2$ would be precipitated at pH 9.7 and $CaCO_3$ at pH 7.27, the latter value being lower than the pH of normal seawater. This result apparently indicates that $CaCO_3$ could be readily precipitated in normal seawater without the assistance of cathodic protection. However, assuming a different value for activity coefficients, the calculations gave a pH of 8.7 for precipitation of $CaCO_3$. This appears to be more consistent with the situation that actually occurs in practice.

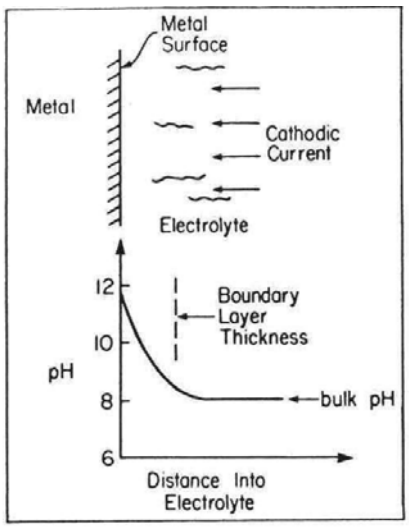

Figure 2.9. Schematic illustration of the pH profile in the electrolyte to a cathodically polarized metal surface [39].

Di Gregorio and Fraser [40] report that X-ray analysis of calcareous deposits have shown their composition to be principally aragonite and calcite (both forms of $CaCO_3$), brucite ($Mg(OH)_2$) and sand (quartz and feldspar). Furthermore, the percentage of brucite increases with increasing current density, whilst the amount of sand decreases, but the amount of $CaCO_3$ appeared to be unchanged. However, this disagrees with the findings of Humble [33] who observed that the amount of $Mg(OH)_2$ increased but the $CaCO_3$ content decreased with increasing current density. Later in this Thesis we will be referring to this work when we discuss our X-Ray analysis data.

Hartt, *et. al*., in Florida [39] have been active in the area of marine corrosion and cathodic protection since 1981. Their major contribution has been the concept of the so-called Slope Parameter and the following Section summarizes this concept. Basically, the slope parameter for a cathodic protection system is the product of the structure surface area and the total resistance in the cathodic protection system. In subsequent work over two decades later, Hartt [41] arrives at this simple linear relationship by manipulating the standard parameters for calculating the current output for a sacrificial anode, as follows:

$$\phi_c = (R_t * A_c) * i_c + \phi_a \qquad \text{...}\ldots\ldots\ldots\ldots\ldots\ldots\ldots\ldots\ldots\ldots \qquad (2\text{-}40)$$

Where:

ϕ_c =The structure protection potential.

R_t = total system resistance.

A_c = structure surface area.

i_c = structure current density.

ϕ_a = operating potential of the anode.

Hartt claims that by using this approach, it is possible to provide correlation between systems that possess widely differing surface areas, for example; laboratory based studies with real offshore structures simply by selecting a suitable choice of resistance in the circuit.

Further experiments designed to investigate and extend this aspect of cathodic protection will be presented in this Thesis in Chapter 4.

Fairhurst [42] uses a schematic diagram shown in Figure 2.10 to describe the time dependant nature of an electrochemical polarization curve for steel in seawater. From the plot shown in Figure 2.10, it can be observed that a high initial current was required to suppress any corrosion of clean bare steel specimens. With time, calcareous deposits then formed and thickened, and subsequently, a much lower current density would then be required to maintain adequate cathodic protection levels.

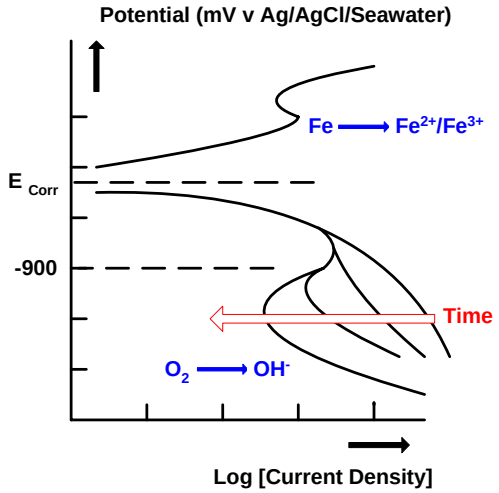

Figure 2.10. Schematic of the Time Dependant Polarization Curve for carbon steel (reproduced from Fairhurst article [42]).

Also in Fairhurst's presentation [43], "Offshore Cathodic Protection, What We Have Learnt?", he compares current density design figures used on a number of progressively deeper water projects in the Gulf of Mexico with those recommended in NACE and DnV standards for shallower waters. It also included actual current density data derived from the first 7 years of cathodic protection monitoring on the Bullwinkle platform.

Table 2.2. Summary of Offshore Structure Cathodic Protection Design Data Versus Water Depth [43].

Source/Field	Year	Depth (m)	Initial CD (mA/m^2)	Mean CD (mA/m^2)	Final CD (mA/m^2)
DnV	-	<30	150(15)	70(6.5)	90(8.4)
DnV	-	>30	130(12)	60(5.6)	80(7.4)
NACE	-	<300	110(10)	55(5)	75(7.7)
MC109	1991	316	123(11.5)	91(8.5)	108(9)
Cognac	1977	320	116(11)	-	-
Bullwinkle	1988	357	194(18)	-	-
*Bullwinkle **	*1988*	*357*	*226(21)*	*32.3(3)*	-
Thunderh.	2003	>462	193(18)	97(9)	129(12)
Pompano	1994	572	127(11.5)	94(8.5)	99(9)
Troika	1997	880	250(23.2)	114(10.5)	135(12.5)
** Data from Bullwinkle's monitoring system*					

The Bullwinkle [43] data is particularly interesting. It shows the original initial design current densities and compares them with those actually measured in practice. The initial design values of 194 mA/m^2 were clearly insufficient to polarize the uncoated bare steel structure and measured values of 226 mA/m^2 were obtained. Although the design steady state values were not quoted, other values quoted in Table 2.2 vary between 55 and 114 mA/m^2 which correlates well with values quoted in our recent publication of around 20 mA/m^2 [44]. It was obvious from our findings that a high initial current density is capable of producing a much more protective calcareous layer [44]. In terms of the structure and morphology of this deposited layer; we shall return to this aspect in the Section 4.4 of Chapter 4.

Recently, presumably due to the availability of relatively inexpensive potentiostats there have been relatively few papers in the literature dealing with the properties of calcareous deposits formed under conditions of constant current density. The majority of publications in this area deal with calcareous deposits formed on steel at constant potentials.

Deslouis, *et. al*., [45] investigated the characteristics of calcium carbonate deposits formed under conditions of cathodic protection at various constant potentials by Electrochemical Impedance Spectroscopy (EIS) and electrohydrodynamical impedance spectroscopy (EHD) without magnesium hydroxide, and details of the equivalent circuits were presented. More recently, the same group of workers [46] also presented data from EIS measurements *in situ* as calcareous deposits were formed at various potentials from - 0.9 to - 1.4 V/SCE, and these calcareous layers were characterized by electrochemical and electrohydrodynamical impedance spectroscopy. See also Section 3.6.7 for further discussion of the work.

Chung, *et. al*., [47] looked at anodic coatings on zinc by means of EIS. Equivalent circuits were proposed by considering the chemical products and physical structures resulting from the corrosion reactions. We will be referring to their equivalent circuit later in this Thesis as a possible model for our calcareous films.

The calcareous deposit that forms on steel surfaces may be compared to a layer of paint. The circuit resistance is known to increase as the layer forms and the current

automatically decreases if the voltage remains the same.

Using Figure 2.11 as a schematic diagram, it is generally believed that calcareous deposits provide protection against corrosion in the following ways:

- They act as a barrier to oxygen.
- Like paints, they are poor electron conductors and cannot support the oxygen reduction reaction on the outer surface.
- Also like paints, they are thought to have a relatively high ionic resistance and to afford some degree of resistance inhibition.
- There might be an increase in the pH of the water film in immediate contact with the metal surface which might provide passivation.

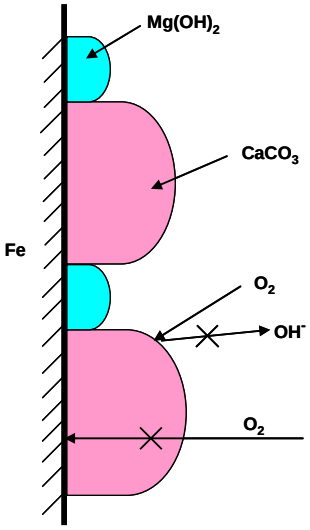

Figure 2.11. Schematic of calcareous film on mild steel surface during cathodic protection in artificial sea water.

The major difference between paints and the calcareous film is that the calcareous film must have the presence of CP albeit not necessarily continuously, in order to maintain itself in a satisfactory condition.

2.7. The Factors Affecting Cathodic Protection in Sea Water.

Many different factors affect cathodic protection, and the major influences are oxygen content, temperature, pH value, velocity of sea water currents, salt content and bacteria. In addition, if the structure is coated, the state of the coating will affect the current required for polarization. Each of these factors will be considered in turn, as follows:

1. **Effect of oxygen:** oxygen is the principal cathodic reactant in seawater. If the activity of oxygen is increased, then the actual corrosion potential (E_{corr}) of the reaction is raised and the corrosion current will be increased [48].

2. **Effect of temperature:** Uhlig [49] has pointed out that when corrosion is controlled by diffusion of oxygen, the corrosion rate at any given oxygen concentration approximately doubles for every 30°C rise in temperature. Also, $CaCO_3$ becomes more insoluble when the temperature increases.

3. **Velocity:** Laque [50] has shown that an increase in the velocity of the seawater surrounding a site of corrosion causes the corrosion products to be removed more rapidly. The amount of oxygen arriving at the cathode surface increases and the rate of corrosion also then increases. Those combined actions will increase the current demand for cathodic protection. Figure 2.12 [51] is based on calculated data and shows that as the velocity of the surrounding water increases from stagnant conditions up to 4 m/s, the rate of corrosion would increase by around 5 times hence increasing the CP demand**.** Similarly there is an increase in corrosion rate with oxygen content. For example in static conditions with the oxygen content of 6 ppm, the CP current demand is 60 mA/m^2 whereas at an oxygen content of 10 ppm moving at 4 m/s requires 350 mA/m^2.

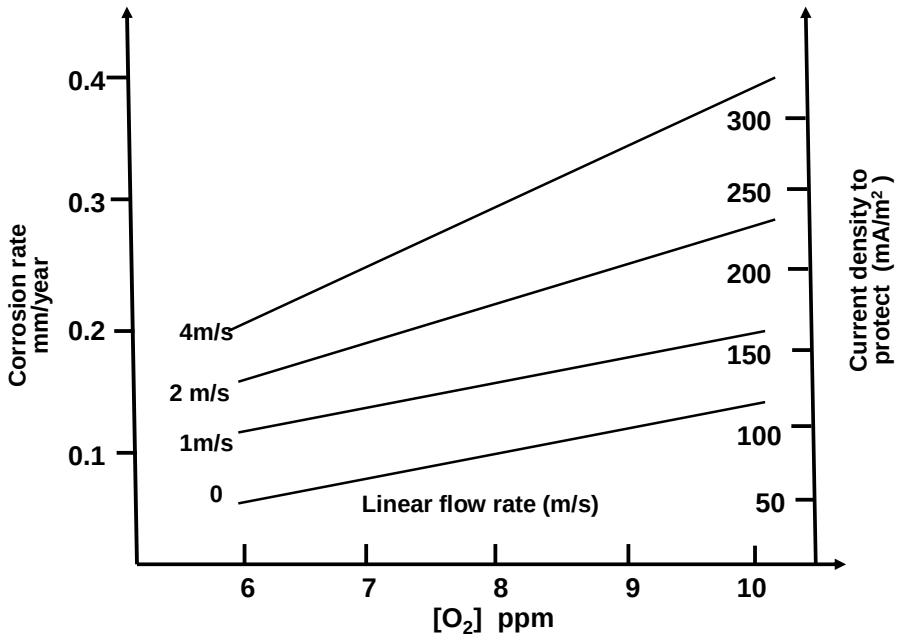

Figure 2.12. Estimated maximum current density required to protect clean steel in North Sea water at 7°C [51] (this data taken from Ashworth [52] and replotted by Scantlebury [51]).

4. **Effect of dissolved salts:** resistivity decreases with an increase in salinity [50]. However; conversely, the oxygen content of the water decreases with increasing concentration of dissolved salts. The rate of corrosion first increases with salt concentration, then decreases. Seawater is approximately equivalent in ionic strength to a 3.5% w/v sodium chloride solution, though it is has a much more complex composition; see Section 2.10.2.

5. **Bacteria:** sulfate-reducing bacteria occur widely in most soils and waters, and their range of distribution is virtually everywhere. Under aerobic conditions when oxygen is present, the bacteria are inactive and they then only become active on their return to an anaerobic environment. Sulfate-reducing bacteria easily reduce inorganic sulfates to sulfides, and are therefore cathodically active [26]. Many publications have indicated that a larger negative potential change in a steel structure in anaerobic soil conditions is necessary to achieve effective cathodic protection. For example, BS code CP1021 suggests that the criterion for steel in an anaerobic environment should be more negative, and at least -0.95 V vs. CSE (-0.874 vs. SCE) [1].

2.8. The Criteria of Cathodic Protection.

2.8.1. Introduction.

After installing cathodic protection it is important to assess whether the system has been successfully protected. Over the years a series of criteria have been put forward, some more successful than others. For many years the most popular and widely accepted set of Standards utilised by the cathodic protection community has been the NACE Recommended Practice RP-01-69 "Control of External Corrosion on Underground or Submerged Metallic Piping Systems". This Code of Practice has been subject to frequent revision, the most recent being 2007 [2]. The latest Code of Practice still contains five criteria for the cathodic protection of steel structures in natural soil and water environments. Each criterion will be stated in turn, together with our personal opinion regarding its validity and applicability.

2.8.2. The Criteria of Cathodic Protection.

1. The -0.85 V criterion:

"A negative (cathodic) voltage of at least 0.85 V as measured between the structure and a

saturated copper-copper sulfate reference electrode (CSE) contacting the electrolyte. Determination of this voltage is to be made with the protective current applied" [53].

We have shown in this Thesis using weight loss methods that this value of potential is insufficient for complete protection of mild steel in artificial sea water.

Page and Sergi [54] have also recently clearly shown by calculation that this value is insufficiently negative. Furthermore, an iR drop exists between the reference electrode and the structure which will generate a measured voltage more negative than the real value. Although recent modifications [2] to RP-01-69 make mention of this fact, there is no real discussion of how this iR drop can be eliminated or compensated for.

2. 300mv change in potential:

"A minimum negative (cathodic) polarization voltage shift of 300 mV, produced by the application of a protective current. The voltage shift is measured between the structure surface and a stable reference electrode contacting the electrolyte. This criterion of voltage shift does not apply to structures in contact with dissimilar metals" [53].

This is a very old criterion, but has no real scientific basis and furthermore, there is no consideration again of the iR drop in the soil.

3. 100mv polarization shift:

"A minimum negative (cathodic) polarization voltage shift of 100 mV measured between the structure surface and a stable reference electrode contacting the electrolyte. This polarization voltage shift is to be determined by interrupting the protective current and measuring the polarization decay. When the current is initially interrupted, an immediate voltage shift will occur. This reading after the immediate shift shall be used as the reading from which to measure polarisation decay" [53].

Readers familiar with the cathodic protection of rebar steel in concrete will immediately recognize the similarity between the above and the 100 mV shift criterion for steel in concrete. However, omitted from the above criterion is any consideration of time scale. Clearly the shift is the amount of depolarization taking place following the switching off of the CP system. Clearly the longer the time which has elapsed, the more the value of

the shift. Thus, some indication of time of depolarization is essential, and this aspect will be mentioned in Chapters 4 and 5.

4. E-logI criterion:

"A structure-to-electrolyte voltage at least as negative as that originally established at the beginning of the Tafel segment of the E-logI curve. This structure-electrolyte voltage shall be measured between the sample surface and a stable reference electrode contacting the electrolyte at the same location where taken to obtain the E-logI curve" [53].

This method is extensively discussed by Evans in his 1960 volume [26]. In spite of Evans' support, this method has not been commonly employed. It was felt that a major feature of this technique involves identifying the Tafel region and any worker actively involved with or familiar with electrochemistry research will be fully aware of the difficulty that this involves for simple specimens under laboratory conditions, let alone a full scale structure in the field.

5. Net protective current criterion:

"A net protective current from the electrolyte into the structure surface as measured by an earth current technique applied to predetermined current discharge (anode) points of the structure" [53].

In common with the opinion of other workers, this author finds that the above statement has either very limited or no real applicability. It is also probable that this criterion will be removed from the forthcoming revision of the above Standard.

2.9. Current Density for Cathodic Protection.

As a general rule, Ashworth and Booker [52] have clearly shown by calculation that in a situation where the open circuit corrosion process is under full cathodic control, which indicates that the cathodic process is under limiting oxygen diffusion conditions, then an accurate determination of the corrosion current is immediately translatable into the specific current density required for cathodic protection. The data from Ashworth [52] has been replotted by Scantlebury [51] and is presented in Figure 2.12 in Section 2.7. There is clear and unambiguous equivalence between the corrosion current measured under

various conditions and the current density required for effective cathodic protection to be achieved.

According to Peabody [55] there are three available methods commonly used to estimate the current density. Each of these methods will be discussed in turn.

1. Temporary ground bed method [55]:

This method involves setting up a temporary ground bed, and then using varying currents, the on and off potentials are determined at various locations around the structure both close to and remote from the ground bed. The optimum current required in order to achieve full protection for the structure can then be obtained.

This method is still in common use, especially where cathodic protection needs to be fitted to an existing structure where design details are either absent or unreliable.

2. E-log I method [56]:

In this method, varying increments of protection current are applied, and the polarization potential (at the point being investigated) is measured for each successive increment. The potentials are then plotted against the logarithm of the applied current. The plot is continued until a definite break in the curve is noted. The corresponding current at this point is then the required current.

As is the case of the Tafel method discussed previously, this technique is rarely used.

3. Mathematical approaches:

Almost 40 years ago, Uhlig [57] derived a set of equations to calculate the required protection current by using Ohms law, and the concept of attenuation along a pipeline. Since then, the widespread use of computers with various powerful mathematical modeling software packages has facilitated many rapid advances in this area. Previous work in this area is contained in Ashworth's book [52] by MA Warne (Application of numerical analysis techniques) with many papers in the on-line corrosion journal [58, 59, 60, 61].

2.10. Marine Corrosion.

2.10.1. Chemical Composition of Seawater.

Water covers 71% of the earth surface, and occurs virtually everywhere. The oceans hold 97% of the worlds surface water, whilst glaciers and polar ice caps account for 2.4% and other land surface water such as rivers, lakes and ponds the remaining 0.6%. Many major industries such as shipping, offshore oil and gas production, power plants and coastal industrial plants are dependant on seawater systems. Unfortunately, the majority of the common metals and alloys (i.e. carbon steel) used to construct the majority of the main primary structures used by all these industries are attacked by seawater or seawater spray. Similar arguments also apply to large permanent structures such as bridges or offshore wind farms. It is therefore obvious that the problems caused by marine corrosion have huge financial cost implications to many industries worldwide.

Seawater is composed of a number of major constituents and traces of almost all naturally occurring substances. Table 2.3 provides details of the average concentration of the 11 most abundant ions and molecules in clean seawater (under conditions of 3.5 % salinity, density of 1.023 $g.cm^3$ at 25^oC). Six elements and their compounds comprise approximately 99% of sea salts, these are: chlorine (Cl^-), sodium (Na^+), sulfur (as SO_4^{2-}), magnesium (Mg^{2+}), calcium (Ca^{2+}), and potassium (K^+).

Table 2.3. Average concentrations of the 11 most abundant ions and molecules in the oceans [62].

	Concentration	
species	$mmol^{-1}.kg^{-1}$	$g.kg^{-1}$
Na^+	468.5	10.77
K^+	10.21	0.399
Mg^{2+}	53.08	1.29
Ca^{2+}	10.28	0.4121
Sr^{2+}	0.09	0.079
Cl^-	545.9	19.354
Br^-	0.842	0.0673
F^-	0.068	0.0013
$HCO3^-$	2.3	0.14
$SO4^{2-}$	28.23	2.712
$B(OH)_3$	0.416	0.0257

Chlorinity, conductivity and salinity are subjected to an arbitrary definition and do not conform simply to the chemical composition. Each of these factors will be discussed and/or defined in turn.

2.10.1.1. Salinity.

Salinity is roughly the number of grams of dissolved matter per kilogram of seawater. This was the original definition, and at one time salinity was determined by evaporating the water and weighing the residual deposit. Salinity is normally derived from chlorinity.

The definition given by Roberge [6] is:

$$S\ (o/oo) = 1.80655\ Cl\ (o/oo) \quad \text{(2-41)}$$

Roberge [6] also states the following: "Generally, salinity of seawater lies between 33 to 37 parts per thousand. A value of 35 parts per thousand, equivalent to 19.4 parts per thousand chlorinity is often taken as the average for 'open-seas' water. Local conditions may affect the value of salinity. For example, the melting of Arctic ice or dilution due to large rivers makes the salinity considerably less. In enclosed seas such as in the Mediterranean, Black Sea and Red Sea rapid evaporation causes the salinity to increase to 40 parts per thousand".

The same author also gives precise explanations and discussions of conductivity and chlorinity, and these are also listed as follows:

2.10.1.2. Conductivity.

"Conductivity of sea water depends strongly on temperature, somewhat less strongly on salinity, and very weakly on pressure. If the temperature is measured, then conductivity can be used to determine the salinity. Salinity as computed through conductivity appears to be more closely related to the actual dissolved constituents than is chlorinity, and more independent of salt composition. Therefore temperature must be measured at the same time as conductivity, to remove the temperature effect and obtain salinity. Accuracy of salinity determined from conductivity: 0.001 to 0.004. Precision: 0.001. The accuracy depends on the accuracy of the seawater standard used to calibrate the conductivity based measurement" [6].

2.10.1.3 Chlorinity.

"Chlorinity refers to the sample of seawater titrated with silver nitrate, to precipitate bromides, iodides and chlorides. To calculate chlorinity the total content of halogen is

taken as being chloride, and chlorinity is defined as the weight in grams of the chloride-ion content per 1000 grams of water" [6].

2.10.1.4. Ions in Seawater.

"A large part of the dissolved components of seawater is present as ion pairs, or in complexes, rather than as simple ions. While the major cations are largely uncomplexed, the anions, other than chloride, are to varying degrees present in the form of complexes. About 13% of the magnesium and 9% of the calcium in ocean waters exist as magnesium sulfate and calcium sulfate respectively.

More than 90% of the carbonate, 50% of the sulfate, and 30% of the bicarbonate exist as complexes. Many minor or trace components occur primarily as complexed ions at the pH and the redox potential of seawater. Boron, silicon, vanadium, germanium, and iron form hydroxide complexes. Gold, mercury, and silver, and probably calcium and lead, form chloride complexes. Magnesium produces complexes with fluorides to a limited extent.

Surface seawater characteristically has pH values higher than 8 owing to the combined effects of air-sea exchange and photosynthesis. The carbonate ion concentration is consequently relatively high in surface waters. In fact, surface waters are almost always supersaturated with respect to the calcium carbonate phases, calcite and aragonite.

The introduction of molecular carbon dioxide into subsurface waters during the decomposition of organic matter decreases the saturation state with respect to carbonates. While most surface waters are strongly supersaturated with respect to the carbonate species, the opposite is true of deeper waters that are often under saturated in carbonates" [6].

2.10.2. Chemical Composition of Artificial seawater.

Artificial seawater (or ASW) is a mixture of dissolved mineral salts (that simulates seawater). From a scientific perspective, artificial seawater has the advantage of reproducibility over natural seawater.

There are several different standards available relating to the precise chemical compositions used as a basis to prepare artificial seawater. Tables 2.4 and 2.5 give details of the average composition of two artificial sea water formulations. For this research project, the 1940 Standard of Lyman and Fleming [63] (s = 3.5%) was selected to prepare artificial seawater, with a pH of around 7.5.

Table 2.4. Chemical composition of artificial seawater based on Lyman and Fleming (s = 3.5%) [63].

Composition	NaCl	$MgCl_2$	$NaSO_4$	$CaCl_2$	K Cl	$NaHCO_3$	KBr	H_3BO_3	$SrCl_2$	NaF
g (per 1000g solution)	23.939	5.079	3.994	1.123	0.667	0.196	0.098	0.027	0.024	0.003

Table 2.5. Chemical composition of artificial seawater based on BS3900-F4:1968 [63].

Composition	NaCl	$MgCl_2$	$MgSO_4$	$CaCl_2$	K Cl	$NaHCO_3$	KBr	water
g (per 1000g solution)	26.5	2.4	3.3	1.1	0.73	0.2	0.28	1000

2.11. Corrosion inhibition of metals in aqueous environments.

2.11.1. Introduction.

In this study, we also looked at a magnesium/calcium containing anti-corrosion pigment as a corrosion inhibitor. It is therefore essential that a basic review of the relevant literature on corrosion inhibition is given.

There are several different forms of corrosion inhibition, and these are normally grouped under the following headings. These are: anodic inhibition, cathodic inhibition and mixed inhibition. These terms relate to whether the inhibitor action reduces the rate of the anodic reaction, the cathodic reaction or the rate of both reactions simultaneously. See Turgoose [64] for a full account of these various modes of inhibition.

As with the terms used to categorise the various modes of corrosion inhibition, and described above, corrosion inhibitors can be classified according to their mode of action: anodic, like sodium phosphate which retards the anodic reaction; cathodic, like calcium bicarbonate which cause interference with the cathodic reaction; or inhibitors that can have both actions. i.e. a dual effect. These dual action inhibitors are usually combinations of inhibitors such as zinc or calcium ions with inhibitive anions like phosphates, borates, carboxylates and molybdates and are sometimes called mixed inhibitors since in principle, the anions can act anodically and the cations can act cathodically.

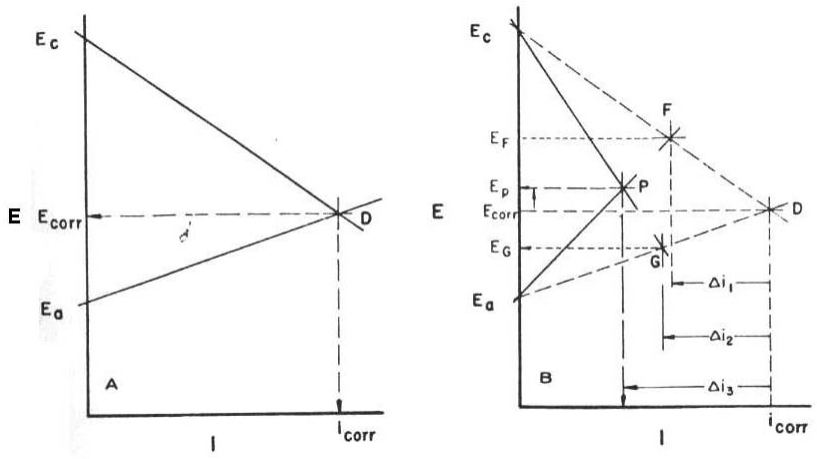

(a) (b)

Figure 2.13. Anodic and cathodic polarization curves. Point D is free corrosion. Point F is added anodic inhibitors, Point G is added cathodic inhibitors, Point P is an added mixture of cathodic and anodic inhibitors. Δi_1, Δi_2, Δi_3 are the reduced corrosion currents, respectively [65]

Figure 2.13 shows the relationship between corrosion (D), protection given by added anodic or cathodic inhibitors (F and G respectively) and inhibition (P). Usually, E_aF is anodic control by using anodic type inhibitors which raise the potential: E_cG is cathodic control by using cathodic type inhibitors which will result in a decrease in the potential. The intersection point P is mixed, and controlled by using mixed inhibition during which the potential is not significantly changed. All of these inhibitors reduce the corrosion current [66].

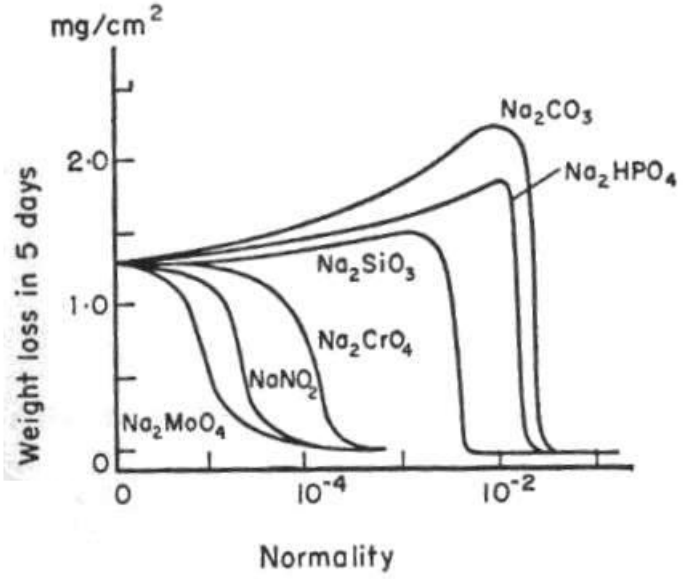

Figure 2.14. Effect of concentration of various inhibitors on the corrosion of iron [66].

Figure 2.14 illustrates a graph reproduced from Pryor and Cohen [66], showing the effect that solutions of different inhibitor concentrations have on the corrosion of iron.

In naturally-occurring fresh water or seawater, there exists several inhibitors, for example, magnesium sulphate and calcium bicarbonate. When water passes through steel pipes or metal structures, these inhibitors hinder the cathodic reaction by depositing magnesium hydroxide or calcium carbonate on the metal surface and hence reduce the process of corrosion [3]. In addition, several of those inhibitors not only have an inhibiting action but also have a significant buffering effect; for example, phosphates can control the pH environment to close to pH 7 [27].

2.11.2. The Classification of Corrosion Inhibition.

2.11.2.1. Anodic inhibition and passivation.

This type of inhibition is characterized by giving an increase in the corrosion potential compared to the uninhibited state [Figure 2.13(b), point F]; passivation may result if the effect is strong enough. In the case of iron and steel, corrosion potentials in the range of 0 to -250mV (SCE) can be observed which are in the same range as passivation potentials. Freely corroding iron would typically have a potential of about -700mV (SCE).

Much of the early work reported in the literature regarding the passivating and anodic inhibiting properties of anions such as chromates, molybdates, nitrites, phosphates, borates, silicates, azelates and benzoates has been reviewed by Thomas [67]**.** In the case of iron and steel, a critical inhibitor concentration for complete protection (C_{inh}) exists which increases with the concentration of aggressive anions (C_{agg}) such as chloride and sulfate according to the logarithmic relation given in equation 2-42:

$$\log C_{inh} = n \log C_{agg} + K \quad \text{(2-42)}$$

Where n and K depend on the nature of the aggressive and inhibitive ions [67-71].

Thus in the absence of aggressive ions, effective inhibitor concentrations for complete inhibition or passivation of iron may only need to be of the order of $5*10^{-4}$M for chromate anions [69], but this figure increases rapidly as C_{agg} increases. On iron, at 10^{-3}M NaCl (~35ppm chloride), the necessary levels of chromate to ensure protection are around 10^{-2}M (~1200ppm).

Minimum figures for inhibition of iron in the absence of aggressive ions are around 10^{-2} M for phosphate and borate [66], about 10^{-3}M for molybdate [72] and benzoate anions [68] and approximately 10^{-4}M to $l0^{-3}$M again for nitrite [70].

The initial concentration for inhibition of steel by lead azelate was found to be in the range of 10^{-5}M to 10^{-4}M at a pH of 4.5 to 5. The efficiency of inhibition was reduced in the pH range of 5 ~ 6 [73]. The corresponding calcium and sodium salts were found to be less efficient at providing effective inhibition, requiring a minimum concentration of about 10^{-3}M and the solution pH appeared to have little effect over the range of 4.5 to 6. All solutions were found to corrosive at a pH of 4.

Besides the influence of aggressive ions, there is a minimum pH at which inhibitors are effective. This generally decreases with increasing inhibitor concentration and aggressive ion concentration. For example, at an anion concentration of 10^{-1}M, the minimum pH for preventing the corrosion of iron or steel is about 1.0 for chromate anions, 5.5 for nitrite anions and 7.0 for phosphate anions. Hydroxide ions also have a passivating influence on iron and steel if present at sufficient concentration and a pH of around 12 is normally needed, i.e. 10^{-2}M in hydroxide ions [67]. Steel in concrete is an example of this situation.

Oxidising inhibitors such as chromate and nitrite do not require oxygen in solution to inhibit whereas non-oxidising inhibitors such as phosphate, molybdates and carboxylates do, this being the basis of one type of inhibitor classification. For non-oxidising inhibitors, the required oxidising power of the solution generally decreases as the inhibitor concentration increases although some oxygen is still needed [67].

It has also been observed that many non-oxidising inhibitors are not effective on addition to a solution containing aggressive ions in which steel has already begun to corrode, and if the potential of the metal has fallen below a certain value dependent on the inhibitor and corrosive conditions [70]. On the other hand, immersion of iron already bearing its air-formed oxide into solutions of inhibitive anions usually results in a thickening of the oxide layer except at relatively low values of solution pH's [67].

In considering the mechanism of action of anodic inhibitors, an increase in the corrosion potential occurs by increasing the polarisability of the anode reaction, but a reduction in

the corrosion current will not occur if the rate of corrosion is under diffusion cathodic control. This often occurs in the case of iron and steel where the corrosion current is controlled by the limiting current density for oxygen reduction [67].

More effective methods of anodic inhibition are associated with maintaining the potential in the passive range such that the existing oxide film remains protective to the underlying metal. The factor determining this is that the potential remains in the protective region between the Flade potential and the breakdown potential if this exists. The current in the passive range should also be as low as possible, indicating a low rate of transportation of metal ions through the film and a low rate of dissolution of metal ions at the oxide-solution interface.

2.11.2.2. Cathodic Inhibition.

This type of inhibition is shown by a decrease in the corrosion potential compared with the uninhibited state (Figure 2.13, point G) and is caused by a reduction in the rate of the cathodic reaction. Unlike anodic inhibition, there is normally no significant sensitivity to the presence of aggressive ions and even small additions of inhibitor can reduce the corrosion rate for a system under cathodic control [67].

There is no critical inhibitor addition below which no inhibition is observed nor is there a minimum addition level below which localized regions of corrosion can occur. For this reason, inhibitors functioning in this way are often classified as safe. The disadvantage compared to anodic inhibition is that corrosion rates are normally only reduced whereas anodic inhibition can lead to passivation and effectively prevent corrosion. [67].

As discussed previously in Section 2.6, in aerated solutions the rate of corrosion of iron and steel is controlled by the rate of oxygen transport to the metal surface. The effects on the cathodic reaction are in this case believed to be due to the formation of relatively thick films of insoluble compounds over cathodic sites which restrict oxygen transport [74]. For this to be effective, the films must of course have low electronic conductivity.

Divalent cations like zinc and magnesium can precipitate as insoluble hydroxides on ferrous metals due to the local concentration of hydroxide ions produced by the cathodic reaction. This topic has already been discussed previously in Section 2.6 dealing with

calcareous films. Soluble calcium salts in waters containing carbon dioxide can also precipitate calcium carbonate at cathodic sites where the relatively high pH allows a sufficiently high carbonate concentration [74]. Where silica or silicates are present in solution, the deposition of calcium silicates at cathodic sites may also contribute to cathodic inhibition [74].

The surface pH on clean metal with oxygen reduction as the cathodic reaction can be calculated [75] in terms of bulk pH and will rise to about 10.0 in unbuffered solutions, provided that the bulk pH does not become too acidic. In general, the possibility of such reactions can be calculated knowing the solution pH, buffering properties, inhibitor concentrations and the solubility products for the insoluble compounds involved.

Once such a film has formed, it appears that the surface pH is not particularly sensitive to the barrier properties of the film and this is presumably due to the fact that both the diffusion of oxygen to the surface and the diffusion of hydroxide ions away from the surface are hindered.

Surface analytical studies have frequently demonstrated the presence of iron in the surface films that form under cathodic conditions [62], and this could imply the formation of insoluble films by reaction of ferrous ions with the inhibitor, but in practice, it is often difficult to decide whether this is an aspect of the observed inhibition or just a consequence of the corrosion of the metal. This feature is also shown elsewhere in this work (Section 5.3.1.2).

Cathodic inhibition is believed to account for the inhibition displayed by polyphosphates on iron and steel when calcium or zinc ions are present in solution, although inhibition of the anode reaction has been reported [74] and pitting and promotion of corrosion under adverse conditions may occur.

Corrosion inhibition is dependent upon appropriate addition levels of polyphosphate, the ratio of calcium or zinc ions to polyphosphate and also on pH [74, 76]. Operating solution pH's are normally within the range 5 to 7, for the reasons cited above and addition levels calculated as P_2O_5 range from 10 to 40 ppm or of the order of 10^{-4}M. It has been suggested that the Molar ratio of P_2O_5 to calcium ions should not be greater than 3:1 [74,

[76]. Corrosion inhibition is found to be better when polyphosphates are employed in conjunction with Ca or Sc ions. Inhibition is also reported to be dependent on flow conditions and time of exposure [14, 77, 78].

Some studies appear to relate the observed inhibition to films formed directly from polyphosphate and the cations present in solution [76], although other studies have considered that phosphate anions rather than polyphosphate are involved in film formation [14, 77, 78] , in which case, formation of calcium and zinc phosphates at cathode sites could occur. Formation of iron phosphates have also been discussed [14]. Small residual quantities of phosphate may be present in the polyphosphate, or may arise as a result of reversion of the polyphosphate to phosphate. In the former case, inhibitor effectiveness could be expected to depend on the residual phosphate concentration [78].

The behaviour of zinc as an inhibitor in solutions containing tripolyphosphate, zinc and calcium ions has been previously investigated by means of impedance, cyclic voltammetry and SEM/EDAX techniques [79]. The inhibition appeared to be cathodic in nature and removal of calcium from the mixture decreased the effectiveness. It was found however, that the formation of the most stable compact films did require the presence of zinc ions in solution.

2.11.2.3. Mixed inhibition.

In the case of mixed inhibition it might be expected that the potential would increase or decrease according to which electrode reaction was most affected by an inhibitor considered to be capable of reducing both electrode reactions (Figure 2.13, point P). However, the potential change does not necessarily reflect whether anodic or cathodic inhibition is predominating because the corrosion rate itself is determined by a rate determining step.

As previously discussed, some inhibitors like chromate can show both anodic and cathodic inhibition where the effects of the latter will predominate at low concentrations. Combinations of inhibitors such as zinc or calcium ions with inhibitive anions like phosphates, borates, carboxylates and molybdates are sometimes called mixed inhibitors since in principle, the anions can act anodically and the cations can act cathodically.

Many combinations of inhibitors do in fact lead to corrosion rates which are often lower than can be explained on the basis of their individual action in a given environment. Thus the addition of polyvalent metal cations to solutions of inhibitive anions often results in a large increase in inhibition. It might be speculated that in some cases mixed inhibitors were simply very efficient anodic inhibitors bringing the critical current density of passivation (i_{crit}) below the available cathodic current density (i_{cath}).

However, in the case of mixtures of zinc with phosphate or molybdate and considering the observed potentials which were too negative to be associated with passivation, the improved effectiveness on ferrous metals was believed to be largely due to cathodic inhibition. In these cases, the efficiency was higher than that of zinc ions alone due to the precipitation of a basic salt, rather than simply zinc hydroxide [64].

In the case of zinc and molybdate, Qian and Turgoose [80] obtained DC polarisation curves and showed that the addition of molybdate to a 0.1M NaCl solution containing zinc ions reduced still further the rate of the cathodic reaction. The solution pH was 6.5. There was some increase in the corrosion potential indicating anodic inhibition but not sufficient to cause passivation. The appearance of a high frequency semi-circle in the AC impedance data suggested the presence of a porous film. SEM/EDAX and XPS indicated the presence of a film composed of zinc and molybdate (VI) ions.

In a comparison of the inhibitive properties of extracts of zinc potassium chromate pigment to those of potassium chromate with respect to mild steel, Mayne and Golden [81] found similar levels of inhibition in the absence of aggressive ions. Higher levels of inhibition for the extract from zinc potassium chromate were found where chloride and sulfate were present at levels sufficient to have prevented passivation.

In the following work reported in this Thesis, we have concentrated mainly on calcium and magnesium cations and an innovative modified Ca/Mg polyphosphate compound (the Japanese pigment D5-B). Although the eventual or ultimate aim is to use this latter compound as an anti-corrosion pigment in paint, the work described here is mainly concerned with the inhibitive properties of this compound dissolved directly into aqueous solution. We have employed a variety of electrochemical and non electrochemical methods using different solutions of this compound, with the aim of identifying the

mechanism of action of inhibition of this product.

2.11.3. Rationale for the study on anticorrosion pigments.

Mayne's original concept of Resistance Inhibition [82, 83, 84] applies to intact, pore free, paint coatings applied to rust free and soluble contaminant free metal substrates. His argument was that although paint coatings were relatively permeable to oxygen and water, provided the coatings functioned as a sufficiently effective barrier to the movement of ions, then the coatings were good anti corrosion coatings as the ionic return path is forced to pass across the intact coating. Values of less than 10^6 $\Omega \cdot cm^2$ were considered as poor quality coatings; greater than 10^8 $\Omega \cdot cm^2$ were found to be excellent [20]. This basic concept, although published some sixty years ago still holds true today.

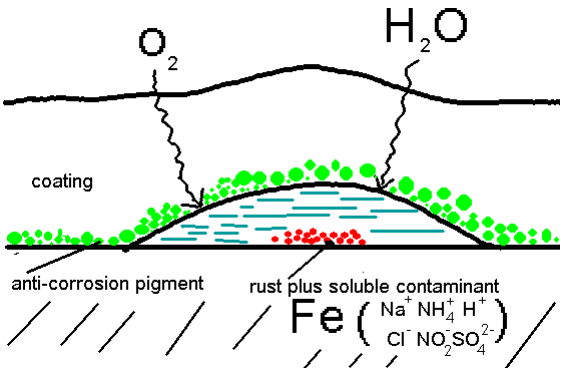

Figure 2.15. Diagram illustrating the structure of the coating with anti-corrosion pigment in rust plus soluble contamination at the interface.

The problem arises when the metal substrate is covered by a contaminated corrosion product before the paint film is applied. Ionic contaminants include cations such as sodium, ammonia and hydrogen ions and anions such as nitrate, chloride and sulfate. In this situation since water can get through the film, underfilm osmotic blistering will occur and corrosion will proceed. Any underfilm corrosion current will have its ionic return path NOT through the coating BUT within the relatively low resistance electrolyte layer within the blister. One way of halting this active corrosion cell is to incorporate anti-corrosion pigment particles within the primer layer of the paint which is adjacent to this active blister. Water transporting across the film picks up soluble corrosion inhibitive material from this pigment and releases it into the blister and stops the corrosion process by inhibiting the electrolyte under the film. See Figure 2.15. However, if the pigment is

too soluble it causes lack of adhesion of the paint; if too insoluble, then not enough of it dissolves to provide effective inhibition.

So, in order to efficiently evaluate the potential of any new anti-corrosion pigment, we need to firstly fully test this material in the absence of a paint film; using electrolytes which might mimic the situation under which this film would be expected to perform under real conditions. Once some understanding of the effectiveness or otherwise of the new pigment is known, tests with real paints can then be undertaken. Therefore, in this study, we looked at the behaviour of the new pigment in a range of selected electrolytes and also carried out a comparison with other commercial pigments using the same electrolytes. This work is described in the later part of this Thesis.

2.12. The Aim of this Research.

The importance of cathodic protection in the context of corrosion in marine environments has already been previously discussed. Whilst there is a general consensus and agreement on the importance of calcareous deposits formed during cathodic protection in sea water, there has not been much detailed information and analysis of such films reported in the literature, and as we have already discussed much of what has been reported is conflicting.

In the early part of this project, my studies were concerned primarily with investigating the relationship between potential and the level of protection. In this work, different current densities (from open circuit, 50, 100, 150, 200, 300 and 400 mA/m^2) were applied to immersed specimens to examine the relationship between current density and potential, and also differences in the calcareous deposit and also corrosion rates were determined by using a weight loss technique (from open circuit to 200 mA/m^2).

The region between the open circuit potential and the protection potential, which denotes a situation where underprotection occurs, is a fascinating one and forms part of this study. Due to the many variable factors that can affect cathodic protection, the polarized potential cannot directly predict the corrosion rates or corrosion situation. However, Ashworth and Booker [52] have suggested that a correlation exists between the dissolution of iron and the potential curve and also between potential and the current density curve for steel in seawater, as shown in Figure 2.16. But this correlation has never been tested or proven.

Since it is obvious that such curves do not accurately represent real data, it was decided to explore this region between open circuit and the protection potential. Therefore, we used weight loss to test the correlation between the dissolution of iron and the potential curve and also between potential and the current density curve for steel in seawater. Longer-term weight loss experiments have also been performed using different current densities. Weight loss measurements were used to work out corrosion rates in under-protection cathodic protection situations with current densities at open circuit (zero), 20, 40, 50, 70,100, 150, and 200 mA/m^2.

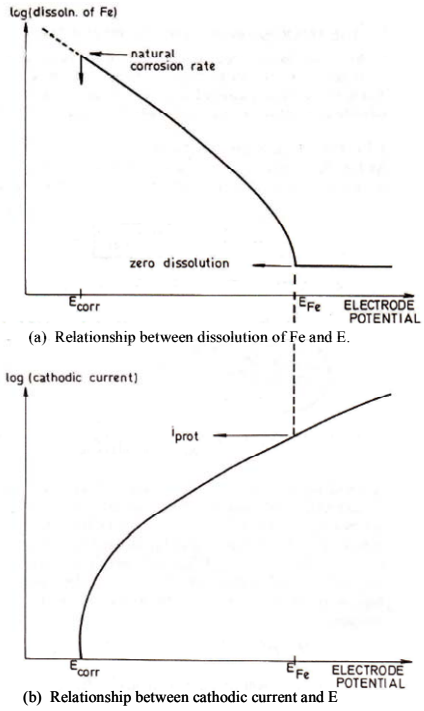

Figure 2.16. Diagrams showing plots of the variation of potential with current density for steel in seawater and the relationship between the dissolution of Fe and the potential curve [52].

Another task of the initial study was to attempt to investigate the dynamics of calcareous deposit formation that occurred under conditions of cathodic protection during the initial stages of immersion in simulated seawater. We aim to show how the composition of calcareous deposits varies with different current densities, and also how the initial current density plays an important role in forming good quality calcareous deposits. The early stages of formation of the calcareous film are important and the structure, composition and electrochemical characteristic of deposits were examined, in order to determine which chemical compound deposits first, and how the layers form. Also, studies were carried out in the initial phase of this project on the growth, development and modeling of calcium and magnesium deposits formed on mild steel immersed in artificial seawater at various levels of cathodic protection. The experiments were performed at short immersion times and using different current densities. The composition of the resulting deposits were analysed and modelled by EIS and also by using a range of analytical instruments/techniques, including: Glow-Discharge Optical-emission Spectroscopy (GDOES), Scanning Electron Microscopy (SEM), Energy Dispersive X-ray Analysis (EDX) and X-Ray Diffraction (XRD).

I also evaluated a novel anti-corrosion pigment (D5-B) containing calcium/magnesium and polyphosphate. The initial results on the performance of this product as a corrosion inhibitor had already been published [85]. These preliminary results indicated that the inhibitor pigment D5-B may be effective as an anti-corrosive inhibitor both in solution or when incorporated into an epoxy paint. We continued and extended this work as the calcium/ magnesium film produced provided an interesting comparison with our previous work on the calcareous films.

The next Chapter will describe in detail the experimental methodologies and analytical instruments and techniques utilised in this research work, then full details of the research studies undertaken in this Project will be presented in Chapters 4 and 5 that follow. Chapters 4 and 5 will present both the Results and the Discussion Sections. In Chapter 6, a general overall discussion of the entire study will be presented, together with suggestions for future research work.

2.13. References.

1. Cathodic protection: Part 1: Code of practice for land and marine application (formerly CP1021). BS 7361: Part 1: 1991, BSI, London. 1991.

2. Recommended Practice. "Control of External Corrosion on Underground or Submerged Metallic Piping Systems". SP 0169-2007, NACE. Houston. 2007.

3. U. R. Evans. "Metallic Corrosion Passivity and Protection". London. Edward Arnold & Co., 2nd Ed., p1. 1946.

4. C. V. Wagner and W. Traud. "On the Interpretation of Corrosion Processes Through the Superposition of Electrochemical Partial Processes and on the Potential Mixed Electrodes" Z. Elektrochem., **44**, pp39l-402. 1938.

5. http://www.concretecorrosion.net/html_en/maitrise/rouille.htm. (9/7/2010)

6. P. R. Roberge. "Handbook of Corrosion Engineering"; McGraw-Hill, New York, 2000.

7. T. Misawa, K. Hashimoto and S. Shimodaira. "Formation of Fe(II)-Fe(III) intermediate green complex on oxidation of ferrous iron in neutral solutions". Corrosion Science. **14**: pp.131-149. 1974.

8. D. A. Jones. "Principles and Prevention of Corrosion". 2nd Edition; Published by Prentice Hall; ISBN: 0-13-359993-0. 1996.

9. J . O'M. Bockris and A. K. N. Reddy. "Modern Electrochemistry 2B: Electrodics in Chemistry, Engineering, Biology, and Environmental Science"; 2nd Edition; Published by Kluwer Academic/Plenum Publishers;ISBN: 0-306-46325-3, 2000.

10. D. J. G. Ives and G. J. Janz. "Reference Electrodes Theory and Practice". Published by Academic Press. Library of Congress Catalog Card Number: 60-16910. 1961.

11. "Handbook of Chemistry and Physics", 71st Edition. CRC Press. New York, 1991.

12. http://www.corrosion-doctors.org/Biographies/Nernst.htm. (9/7/2010)

13. M. Pourbaix and J. A. Franklin (Translated from the French, except Section I,III5 and III6, which were original written in English). "Atlas of Electrochemical Equilibria in Aqueous Solutions". NACE/Cebelcor. Houston, 1966.

14. R. A. Cottis. M.Sc Lecture Notes. Corrosion and Protection Centre. University of Manchester. 2009.

15. http://profiles.incredible-people.com/john-alfred-valentine-butler. (9/7/2010)

16. L. L. Shreir, "Outlines of electrochemistry", in: Corrosion 3rd Edition, Eds L. L. Shreir, R. A. Jarman and G. T. Burstein, Newnes Butterworth, London, Vol., **2**: pp28-36. 1994.

17. N. S. Stevens. M.Sc Lecture Notes. Corrosion and Protection Centre. University of Manchester. 2009.

18. C. Lefrou, R. P. Nogueira, F. Huet and H. Takenouti, "Electrochemistry" in: L. L Shreir. Corrosion, 4th Edition, R. A. Cottis, M. J.Graham, R. Lindsay, S. B. Lyon, J. A. Richardson, J. D. Scantlebury and F. H. Stott (eds); Elsevier, Amsterdam, 2010.

19. F. L. Laque and T. P. May. "Marine corrosion of Metals". The Second International Congress on Metallic Corrosion, NACE, p789. 1961.

20. C. R. Bacon, J. J. Smith, and F. M. Rugg. "Electrolytic Resistance in Evaluating Protective Merit of Coatings on Metals". Ind. Eng. Chem. pp161-167. **140**. 1948.

21. H. Davy. "On the corrosion of copper sheeting by sea water; and on methods of preventing this effect; and on their application to ships of war and other ships". Phil. Trans. Royal Soc., **114**, p151. 1824.

22. H. Davy. "Additional experiments and observations on the application of electrical combinations to the preservation of the copper sheathing of ships", Phil. Trans. Royal Soc. **114**, p242. 1824.

23. H. Davy. "Further researches on the preservation of metals by electrochemical means", Phil. Trans. Royal Soc. **115**, p328. 1825.

24. T. P. Hoar. "A graphical representation of the main parameters associated with cathodic protection" J. Electrodep. Tech. Soc., **14.** p33. 1938.

25 R. B. Mears and R. H. Brown, "Cathodic protection and the use of polarization diagrams", Trans. Electrochem., Soc. **74**. p519. 1938.

26. U. R. Evans. "The Corrosion and Oxidation of Metals". Edward Arnold & Co., London. p275. 1960.

27. D. D. Perrin and B. Dempsey. "Buffer Solutions". J. W. Arrowsmith Ltd. Bristol. p3. 1987.

28. S. Pathmanaban and B. S. Phull, "Calcareous deposits on cathodically protected structures in seawater". Proc. UK National Corrosion Conf., Institute of Corrosion, Leighton Buzzard, UK , p165. 1982.

29. L. M. Applegate. Cathodic Protection. p63, McGraw-Hill Publishers. New York. 1960.

30.http://chemistry.about.com/od/historyofchemistry/ig/Pictures-of-Famous-Chemists/Sir-Humphry-Davy.-0G2.htm. (9/7/2010)

31. G. C. Cox. U. S. Patent. No.2, 200. p469. (1940).

32. G. C. Cox. British. Patent. No.540. p487. (1941).

33. R. A. Humble. "Cathodic Protection of Steel in Sea Water with Magnesium Anodes". Corrosion. 74. pp358-370, 1948.

34. S. Elebeik, A. C. C. Tseung and A. L. Mackay. "The formation of calcareous deposits during the corrosion of mild steel in sea water". Corrosion Science, **26**, No.9. p 669-680. 1986.

35. F. O. Jensen. "Offshore corrosion and its prevention". Paper No.182, Corrosion 76. NACE, Houston. 1976.

36. B. S. Wyatt. "Cathodic Protection of Fixed Offshore Structures" in "Cathodic Protection, Theory and Practice", (eds): V. Ashworth and C. J. L. Booker, Ellis Horwood, Chichester, 1986.

37. I. B. Ulanovskiy. "Corrosion of aluminium in a marine environment" Zashchita Metallov., 8, (2). pp.213-215. 1972.

38. H. J. Engell and P. Forchhammer, "The change of pH under a paint film due to cathodic protection", Corrosion Science. **5**. pp479-488. 1965.

39. W. H. Hartt, C. H. Cluberson and S. W. Smith. "Calcareous deposits on metal surfaces in sea water - a critical Review". Corrosion, **40**, p609, 1984.

40. J. S. Di Gregorio and J. P. Fraser. ASTM STP 558, ASTM publication. pp185-208. 1974.

41. W. H. Hartt. "The Slope Parameter Approach to Galvanic Anode Cathodic Protection Design with Application to Marine Structures". J. Corrosion Science and Engineering. ISSN 1466-8858. **9**, (8). 2004.

42. D. Fairhurst. "Offshore Cathodic Protection. What We Have Learnt?" J. Corrosion Science and Engineering. **4,** (6). WWW.JCSE.org. (9/7/2010)

43. D. Fairhurst. "Offshore Cathodic Protection. What We Have Learnt?" Conference presentation; Cathodic Protection, UMIST, 2002.

44. J. D. Scantlebury, T. Tsukada, Y. F. Yang and M. Du. "Long–Term Cathodic Protection Performance Data of Two Off-Shore Structures". NACE Corrosion Conference. Atlanta. USA, March 2009.

45. C. Deslouis, D. Festy and O. Gil. "Characterization of calcareous deposits in artificial seawater by impedance techniques - I. Deposit of $CaCO_3$ in the absence of $Mg(OH)_2$" . Electrochimica Acta. **43,** (12-13). pp.1891-1901. 1998.

46. Ch. Barchiche, C. Deslouis, D. Festy, O. Gil , Ph. Refait, S. Touzain and B. Tribollet. "Characterization of calcareous deposits in artificial seawater by impedance techniques -

II. Deposit of $CaCO_3$ in the presence of Mg(II)". Electrochimica Acta. **48**. pp1645-1654. 2003.

47. S. C. Chung, J. R. Cheng, S. D. Chiou and H. C. Shih. "EIS behavior of anodized zinc in chloride environments". Corrosion Science. **42**. pp1249-1268. 2000.

48. J. C. Scully. "The Fundamentals of Corrosion". 3rd Ed., Pergamon Press, Oxford. p83. 1990.

49. H. H. Uhlig. "Corrosion and Corrosion Control". 2nd Ed., John Wiley & Sons Inc., New York. p97. 1971.

50. F. Laque. "Marine Corrosion", Wiley, New York, 1975.

51. J. D. Scantlebury. M.Sc Distance Learning Notes. Blackboard Unit 4, Week 5, Section 4.4. Corrosion and Protection Centre. University of Manchester. 2010.

52. V. Ashworth and C. J. L. Booker. "Cathodic Protection Theory and Practice''. Ellis Horwood. Chichester, 1986.

53. http://www.corrpro.co.uk/pdf/TechnicalPapers/12CP%20Review%20of%20 cathodic % 20protection%20criteria.pdf (9/7/2010)

54. C. L. Page and G. Sergi. "Developments in Cathodic protection applied to reinforced concrete". J Materials in Civil Engineering. **12,** (1). pp8-15. 2000.

55. A. W. Peabody. "Control of Pipeline Corrosion". NACE. Houston. p46. 1967.

56. S. P. Ewing and J. F. Bayhi. Corrosion. **4**, (6). p264. 1948.

57. H. H. Uhlig. "Corrosion and Corrosion Control". 2nd Ed., John Wiley & Sons Inc., New York. p396. 1971.

58. V. G. DeGiorgi, E. Hogan, K. E. Lucas and S. A. Wimmer. JCSE Volume 4, Paper 3: Computational Modelling of Shipboard ICCP Systems .(9/7/2010)

59. B. Van den Bossche, M. Purcar, L. Bortels, A. Dorochenko and J. Deconinck JCSE Volume 9, Paper 1: Expert 3D Software Simulations Compared with Experimental Data for the Interference Between a Cathodically Protected Underground Storage Tank (UST) and a Concrete Foundation. (9/7/2010)

60. L. Bortels, B. Van den Bossche, A. Dorochenko and J. Deconinck. JCSE Volume 9, Paper 2: The Use of Dedicated Simulation Software for the Design of the Cathodic Protection of Underground Pipeline Networks. (9/7/2010)

61. E. Santana-Diaz and R. Adey. JCSE Volume 9, Paper 16: Validation of Cathodic Protection Designs using Computer Simulation. (9/7/2010)

62. L. L. Shrier, R. A. Jarman, and G. T. Burstein. "Corrosion 1 & 2", 3rd Edition: Published by Butterworth Heinemann; London, 2000.

63. F. J. Millero, Chemical Oceanography, Taylor and Francis, CRC, Miami, 2006.

64. S. Turgoose. "Mechanisms of corrosion inhibition in neutral environments". in: Chemical Inhibitors for Corrosion Control; (ed). B. G. Clubley. RSC Spc., Pub., No.71. pp72-88. 1990.

65. C. C. Nathan. "Corrosion Inhibitors". NACE. Houston. p11. 1973.

66. M. J. Pryor and M. Cohen. "The Inhibition of the Corrosion of Iron by Some Anodic Inhibitors". J. Electrochem., Soc., **100**. pp203-215. 1953.

67. J. G. N. Thomas. "The mechanism of corrosion prevention by inhibitors". In: Corrosion. 2nd Edition. (Ed). L. L. Shreir. Newnes-Butterworth. London. **1** (18.3). pp34-56. 1976.

68. D. M. Brasher and A. D. Mercer. "Comparative study of factors influencing the action of corrosion inhibitors for mild steel in neutral solutions. 1- Sodium benzoate". Brit., Corros., J. **3** (3). pp120-129. 1968.

69. A. D. Mercer and I. R. Jenkins. "Comparative study of factors influencing the action of corrosion inhibitors for mild steel in neutral solutions. 2- Potassium chromate". Brit., Corros., J. **3** (3). pp130-135. 1968.

70. A. D. Mercer, L. R. Jenkins and J. E. Rhoades-Brown. "Comparative study of factors influencing the action of corrosion inhibitors for mild steel in neutral solutions. 3- Sodium nitrite". Brit., Corros., J. **3** (3), pp136-144. 1968.

71. D. M. Brasher, A. D. Mercer and D. Reichenberg. "Comparative study of factors influencing the action of corrosion inhibitors for mild steel in neutral solutions. 4- Mechanism of action of mixed inhibitors and aggressive anions". Brit., Corros., J. **3** (3). pp144-150. 1968.

72. J. Sinko. "Challenges of chromate corrosion inhibitor pigments; replacement in organic coatings". XXVth International Conference in Organic Coatings (Water-Borne. High Solids, Powder Coatings). Vouliagmeni. July 5-9. pp257-276. 1999.

73. J. E. O. Mayne and E. H. J. Ramshaw. "Inhibition of the corrosion of iron, 2; Efficiency of the sodium, calcium and lead salts of long chain fatty acids". Appl., Chem. **10**. pp419-422. 1960.

74. A. D. Mercer. "Corrosion Inhibition: Principles and Practice". In: Corrosion. 2nd Edition.(Ed). L. L. Shreir. Newnes-Butterworth, London. **2**(18.2)**.** pp9-33. 1976.

75. R. Lindsay. M.Sc Lecture Notes. Corrosion and Protection Centre. University of Manchester. 2009.

76. B. P. Boffardi. Metals Handbook Vol 13. Corrosion 9th Ed. American Society for

Metals. Ohio. 1987.

77. M. Koudelka. J. Sanchez and J. Augustynski. "On the nature of surface-films formed on iron in aggressive and inhibiting polyphosphate solutions" J. Electrochem., Soc. **129**. p1186. 1982.

78. S. M. Seyed Razi. Ph.D Thesis. UMIST. 1989.

79. C. M. Rangel, J. De. Damborenea, A. I. De Sa and M. H. Simplicio. "Zinc and polyphosphates as corrosion inhibitors for zinc in near neutral waters". Brit., Corros., J. **27,** (3). pp207-212. 1992.

80. Y. J. Qian and S. Turgoose. "Inhibition by zincmolybdate mixtures of corrosion of mild steel". Brit., Corr., J. **22**. pp268-271. 1987.

81. J. E. O. Mayne and J. Golden. "Inhibition of the corrosion of mild steel by zinc potassium chromate". Brit., Corr., J. **13.** pp45-49. 1978.

82. J. E. O. Mayne. "Paints for the Protection of Steel - A Review of Research into Their Modes of Action". Brit., Corr., J. **5**. pp151-160. May 1970.

83. J. E. O. Mayne. "The Mechanism of the Inhibition of the Corrosion of Iron and Steel by Means of Paint". Official Digest. pp127-136. Feb. 1952.

84. J. A. Burkill and J. E. O. Mayne. "Zinc phosphate as an anti-corrosion pigment". J. Oil Col., Chem., Ass. **71**, pp273-277. 1988.

85. O. Ogawa, N. Yabumni, T. Tanabe, M. Nagai and H. Tanabe. "Corrosion Resistance of novel developed environmental friendly anticorrosive pigment for paint". Proc EuroCorr (2007).

Chapter 3. Experimental Procedures and Techniques.

3.1. Introduction.

This Chapter will explain the experimental procedures and list the materials used throughout this research project, and also describe the techniques which were applied to analyze the data obtained from the sample testing procedures.

The experimental work described in this Chapter deals firstly with the sample preparation methods, then discusses the fundamental aspects and operating principles of the various electrochemical procedures employed; and also explains the various microscopical and analytical techniques used to evaluate the samples after testing. The detailed structure of the experimental work is outlined below in Figure 3.1.

3.2. Materials.

3.2.1. Working electrode preparation.

Mild steel is the most commonly employed material utilised for the construction of major structures used in aqueous environments. This metal was therefore used throughout this study. The mild steel selected for use as test samples was supplied in panels 50mm*102mm*1mm by Q Panel Ltd (the specific composition of this alloy as provided by the supplier is given in Table 3.1) It was cut into different sizes depending on the particular requirements of the different experimental design situations. The dimensions of the various test specimens used were: $5cm^2$ (2.0cm*2.5cm), $10cm^2$ (2.5cm*4cm) and $16cm^2$ (4cm*4cm). The surfaces of the test specimens were initially prepared by polishing using a series of successively finer grades of silicon carbide abrasive papers. Firstly, 120 grade silicon carbide paper was used for the initial grinding, and then a series of progressively finer abrasive grades were employed down to 4000 grade, which was used to give the final polishing. The specimens were stored in a sealed vessel over silica gel prior to the experiment commencing. Just before the experiments started, the test samples were rapidly degreased in pure alcohol followed by pure acetone, and then finally dried in a stream of cold air.

There were two types of procedures used for final preparation of the working electrodes used for this set of experiments. One type of working electrode that was used for the long

term experiments was prepared by using a piece of copper wire as the electrical contact. The wire was soldered to the top end of the reverse side of each specimen, and the remaining exposed lead was insulated by inserting it into a round 20 cm long portion of plastic tube, which was sealed and insulated from the specimen using 'Rapid Araldite' two-component epoxy resin.

The other type of working electrode used for the short term experiments was polished to a mirror finish by 4000 grade abrasive paper. These samples were then masked by using "Lacquer 45" to give the required area (5 cm^2) of exposed sample, prior to immersion.

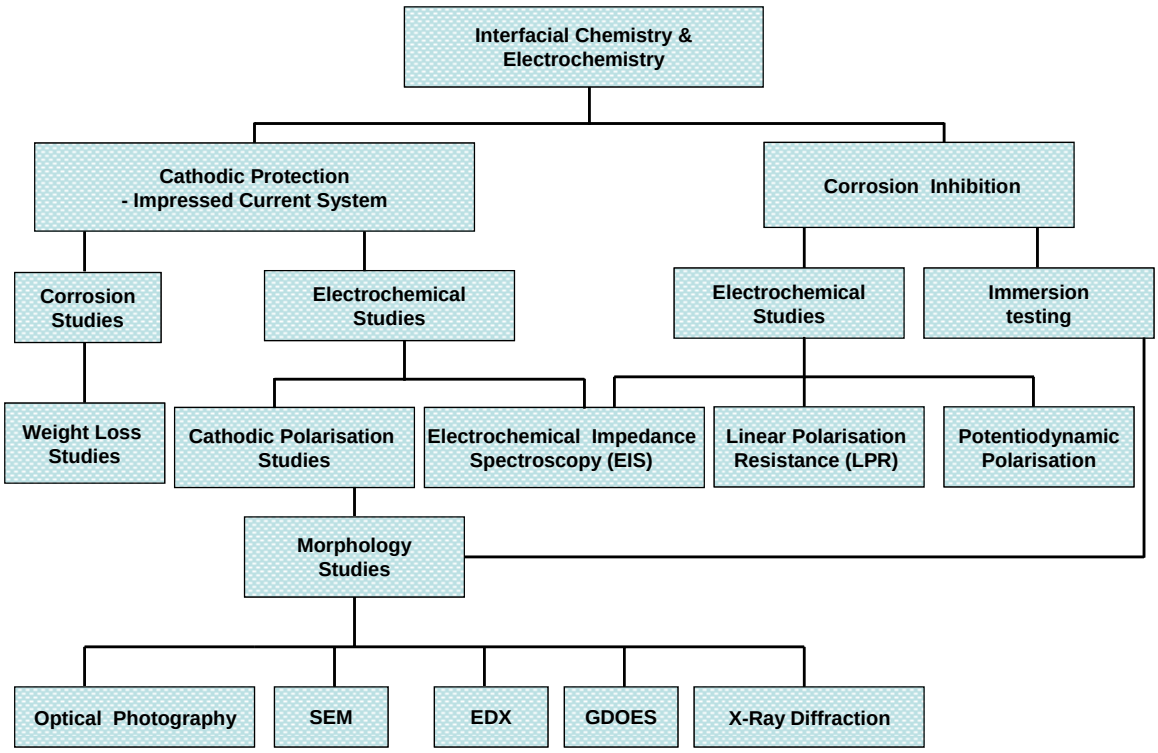

Figure 3.1. Overall Outline of Experimental Work.

Table 3.1. Chemical composition of mild steel.

Element	Fe	C	Mn	P	S
Percent	BAL	0.08-0.13 %	0.3-0.6 %	0.04 %	0.05 %

For these experiments, the electrical connection was made by simply using a piece of copper wire that was temporarily fixed to the sample by using a crocodile clip. Some samples used for GDOES measurements were also given an additional final 'critical'

polishing step by using sub-micron size alumina powder. An Atomic Force Microscope (AFM) was used to confirm that the maximum heights of any remaining peaks were ≤1.0 μm (see Figure 3.26 and Figure 3.27 in Section 3.10).

For inhibitor testing (Chapter 5) samples were prepared by drilling a small hole in the top each mild steel sample and an electrical connection was made using a self tapping screw.

3.2.2. Testing solutions.

In this Thesis, the chemical composition chosen to prepare the artificial seawater electrolyte solution was based on the standard formulation given by Lyman and Fleming (1940; s=3.5%). This formulation is given in full in Table 2.4 in Section 2.10.2. The pH of the testing solution varied between 7.4 and 7.6, but was usually around 7.5.

The procedures utilised to make artificial sea water were as follows:

For each set of experiments, 10 kg of artificial seawater solution was prepared. The sequence of steps utilised was as follows:

1. Initially, 339.39 grams of sodium chloride (10X the weight given in Table 2.4) was weighed out, and added to 2 litres of deionised water in a beaker using a graduated cylinder. A magnetic stirrer and bar was used to ensure that the salt was completely dissolved. This initial saline solution was then poured into a 10 litres high density polyethylene bottle. This solution was the primary stock salt solution. All further solutions prepared were then added in turn to this main stock solution.

2. A similar process was then followed for each of the next three main chemical compounds listed in Table 2.4 (magnesium chloride, sodium sulfate, calcium chloride). A mass of each chemical exactly ten times the amount stated in Table 2.4 was weighed, then added to 1 litre of deionised water in a separate beaker and stirred thoroughly until completely dissolved. Each prepared additional solution was then added to the two litres of original stock sodium chloride solution prepared previously, and stirred until totally mixed.

3. The remaining 6 compounds listed in Table 2.4 were prepared by adding each compound in turn, at 10 times the mass given in Table 2.4, to 1 litre of deionised water in a separate beaker, whilst continuously mixing using a magnetic stirrer and bar. This final solution was then added to the 5 litres of original main stock solution prepared previously, in the 10 kg bottle. Finally, sufficient additional deionised water was then added to give a final solution weight of exactly 10 kg. The final solution was continuously mixed during the entire preparation process, and then used to set up the experiments within several hours.

For the corrosion inhibitor testing experiments, four test solutions were utilized, these were: deionized water, 3.5% NaCl, 0.025M $NaClO_4$ and a simulated acid rain solution which was ten times more concentrated than the normal rain solution. The composition of the acid rain solution [1] was determined by measuring the average concentration of dissolved salts in 8 sites in Manchester over a one year period in 1986. The pH was 4.5. The solution used in these tests was ten times this concentration with a pH of 3.5; the composition of the acid rain solution used in this study is shown in Table 3.2.

Table 3.2. Composition of acid rain solution [1].

Composition	mg/L
Sulphuric acid (1.84 sg)	31.85
Ammonium sulphate	46.20
Sodium sulphate	31.95
Nitric acid (1.42 sg)	15.75
Sodium nitrate	21.25
Sodium chloride	84.85

The pH was adjusted to 3.5 with sodium carbonate or HCl

The procedures utilised to make acid rain were as follows:

1. Initially, 318.5 milligrams of concentrated (sg = 1.84) sulphuric acid (10 X the weight given in Table 3.2) was weighed out, and slowly added to deionised water in a beaker using a graduated cylinder, whilst stirring continuously using a magnetic stirrer and bar. Additional deionised water was then added to give a final volume of exactly 1 litre. This initial solution was then poured into the 10 litres polyethylene bottle. This solution was the primary stock acid rain solution. All further solutions prepared were then added in turn to this main solution.

2. The rest of the salts and acid which are listed in Table 3.2 (ammonium sulfate, sodium sulfate, nitric acid, sodium nitrate and sodium chloride), were then separately weighed out at 10 X the amount given in Table 3.2, then added to and dissolved in deionised water. The volume of each resulting solution was then made up to precisely 1 litre using addition deionised water as required. Each additional 1 litre solution was then added in turn to the original main sulphuric acid stock solution prepared previously, in the 10 litre plastic stock bottle. The solution was continuously thoroughly stirred during the whole preparation and mixing process. Finally, additional deionised water was then added until the final volume of the complete solution was exactly 10 litres.

3. The pH of the prepared complete solution was measured to be around 3.35, and was then critically adjusted with sodium carbonate solution to precisely 3.5. The pH meter used was carefully calibrated prior to use with Standard buffer solutions at pH = 7.0 and pH = 4.0 respectively.

For the corrosion inhibitor testing experiment, the pigments evaluated were supplied by the DAI NIPPON TORYO (DNT) Company as powders, and were the following:
D5-B; calcium polyphosphate, magnesium neutralised (DNT 2008/10/16).
Ca650; aluminium tripolyphosphate, calcium neutralised (DNT 2008/06/30).
KW105; aluminium tripolyphosphate, zinc neutralised (DNT 2008/06/30).
Zinc phosphate; (DNT 2008/06/30).

All four of the above pigments were added at 1.0 Wt. %, in each solution, stirred for 10 minutes than left to settle. The tests were carried out using unfiltered solutions with the pigment residue on the bottom of the beaker.

3.2.3. Auxiliary and reference electrodes.

In this experiment, all potential measurements stated are with respect to a Saturated Calomel Electrode (SCE). The saturated calomel electrode was connected with the test solution by a solid state poly (acrylamide) salt bridge. The salt bridges were manufactured by Labtech. Salt bridges were used to avoid chloride contamination and to reduce any possible iR error in the potential measurements especially in the low conductivity acid rain solutions. Before the experiments, all the SCE reference electrodes

were measured one against another, and only those electrodes whose potentials remained stable within a 5 mV range were used. All those whose potential fluctuations were greater than 5 mV were discarded.

Two types of auxiliary electrode were used, these were a platinum flat anode and a titanium anode coated with iridium-tantalum oxide (Mixed Metal Oxide [MMO]), supplied by BAC Anti-Corrosion.

3.3. Galvanostatic Studies.

3.3.1. Diagram of Experiment.

Galvanostats made by Corrosion Developments (the late Harvey Turner) were used to provide a constant current, and the value of the applied current densities could be adjusted using a built-in variable resistance. In this research, two types of galvanostat were employed for the vast majority of the electrochemical studies. One is suitable for very low current ranges which deliver typically less than 10 μA maximum, whilst the other is applicable for high current uses, which have a maximum output of 50 mA. In the external circuit, a measuring resistor was used (usually 10000 Ω, previously calibrated) to check the current supplied by the galvanostat.

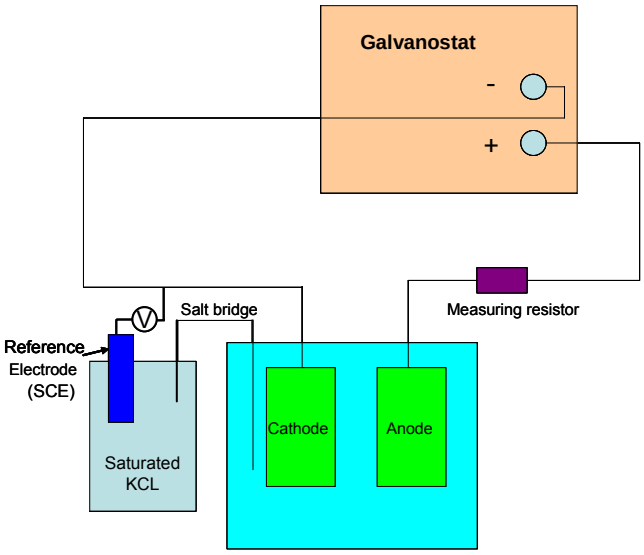

Figure 3.2. Diagram of Experimental set-up used for polarization studies.

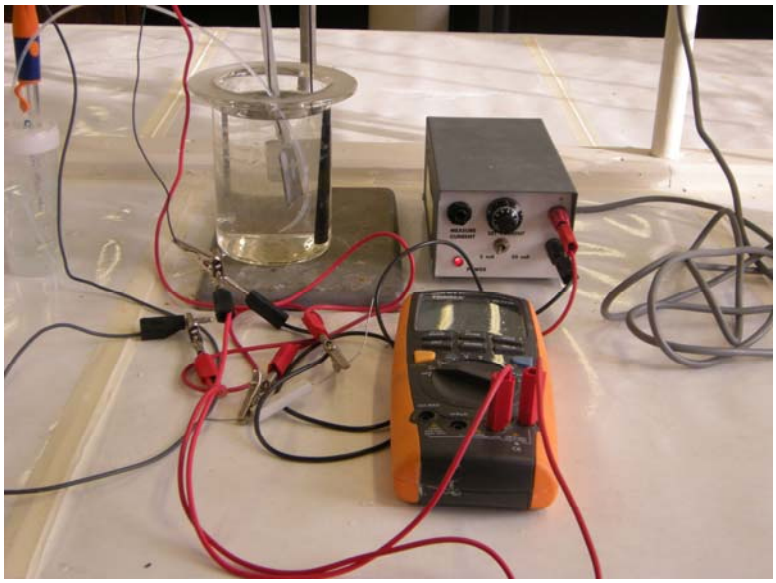

Figure 3.3. Photograph of experimental galvanostatic set-up in laboratory.

The specimens were immersed separately in still artificial sea water with open access to air, and with different polarization current densities. The temperature of the solution was determined by the laboratory temperature which during the period of the experiments reported here varied between 18 to 22 ^{o}C. The specimens were polarised cathodically at constant current densities. Their potentials were measured every six hours for up to seven days (6h, 24h, 48h, 72h, 96h, 120h, 144h and 168h). These specimens were also subjected to impedance analysis daily at the potentials previously measured, not at open circuit. An ACM Gill Impedance Analyser was used and the data was analysed using Zview software. In the data presentation in Chapter 4, the quality of the fit can be seen by comparing the real data with the data from the model.

3.3.2. Data Acquisition System

A Data Acquisition System was utilized for recording the potential every 5 minutes. Only one potential value could be recorded in one circuit. Therefore, in these experiments, a separate power supply was used for each cell. It is capable of recording 6 data (the testing samples connected with C1 to C11 and reference connected with GND channels) sets at the same time and from different circuits.

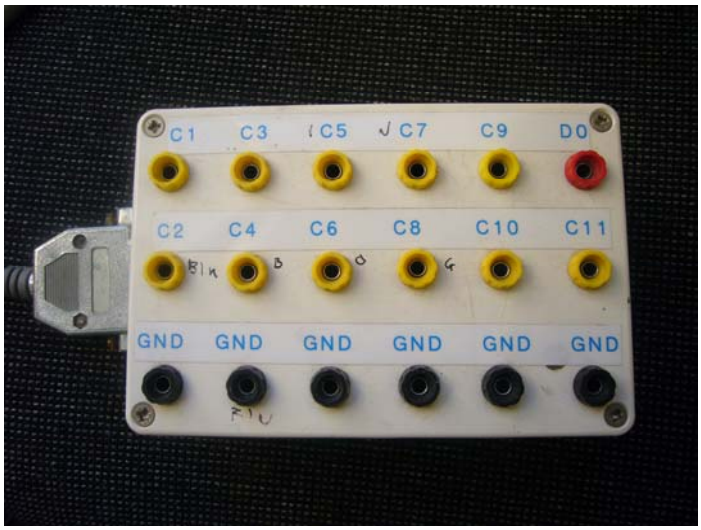

Figure 3.4. Data Acquisition.

3.4. Potential monitoring.

This technique was used to study the potential time behaviour of the steel samples subjected to various cathodic protection situations. The measurement of potential is very simple – a reference electrode is placed in the same solution (or via a Luggin Probe) as the working electrode and a voltmeter with high input impedance is then connected to the two electrodes to measure the voltage difference. As a general rule, the negative terminal of the voltmeter is connected to the reference electrode [2].

3.5. Weight Loss Testing.

Weight loss is probably the most fundamental way to evaluate the effectiveness of any particular corrosion control measure.

In this investigation, we had the choice of using constant current or constant potential cathodic protection (CP). It was decided to use constant current for a variety of reasons: firstly, in a real CP system, the system is designed to supply a constant current to the structure and therefore a constant current is closer to reality. Secondly, if a potentiostat is employed to obtain a constant potential, this arrangement would produce electrochemical chaos at the interface in the event that conditions were to suddenly change. The major previous study that utilized constant current to provide cathodic protection was the early and seminal work by Humble [3], who performed weight loss experiments in June 1946 at Kure Beach with test exposure duration of one year. He describes the techniques that he used as follows: "The cathodes used in these tests were 12 inch by 12 inch by 1/8 inch 'killed' steel plates, which were attached to channeled iron racks using insulated washers. These were immediately coupled to magnesium anodes, three plates being operated at the following current densities: 0.0, 1.0, 2.0, 3.0, 5.0, 7.5 and 10 mA/sq foot (1 mA/ft^2 = 10.76mA m^{-2}). One plate at each current density was removed after three and twelve months exposure. The conditions prevailing at the test site, namely, sea water, which is saturated with respect to oxygen, has a salinity range of from 95 to 104 percent of normal and a temperature range of from 45 to 85^o F. The velocity of the water was zero; its level rising and falling with the tides but with no definite flow ″ [3]. Corrosion product removal was by light sand blasting.

In our study, the data obtained by Humble was replotted and will be presented in Figure 4.5 in Chapter 4. (Section 4.2.2)

I undertook weight loss experiments under laboratory conditions and using artificial seawater. It was decided to mainly explore the particular region between the open circuit and the protection potential which constitutes the so-called 'region of underprotection'.
Mild steel specimens with an exposed area of 10 cm^2 were prepared by polished with silicon carbide paper down to 4000 grade. The anodes were titanium coated with iridium-tantalum oxide (Mixed Metal Oxide [MMO]).

The samples were exposed to the immersion solutions without stirring, and with free access to air. The samples were polarised cathodically at constant current densities. The weight loss specimens were then weighed both before exposure and then again after 30 days testing. The samples were weighed using an electronic balance to within 0.1 mg, and each sample was weighed three times. The balance used was a Mettler (Model AE163). A typical weight loss at open circuit on a 10 cm^2 specimen was around 60 mg.

The main differences between the series of weight loss experiments performed in this Study, and the work undertaken by Humble [3] in 1946 may be summarized as follows:

- His timescale was one year whereas mine was 30 days.
- My experiments were carried out under controlled laboratory conditions, whereas Humble used an unpredictable natural marine environment.
- His medium was real seawater whereas mine was synthetic seawater.
- His current supply used a sacrificial anode system with manual variable resistance to supply the constant current, whereas I used a stabilized constant current power supply.
- He used light sand blasting to remove the films produced on the steel; I used an inhibited acid solution; Clarke's solution; see the following Section.

3.5.1. Cleaning Procedure.

In order to determine the weight loss, it is essential to remove all corrosion products that have formed, but at the same time ensuring that the base metal remains intact. Furthermore, it is imperative that a replicate uncorroded, control specimen is cleaned by the same method as all the test specimens. The specimens were cleaned according to ASTM G1 specification in a Clarks reagent, which was composed of 2.0 % antimony trioxide and 5.0 % stannous chloride per litre of hydrochloric acid (sp. gr., 1.19). The specimens were placed in the Clarks solution for 10 minutes for cleaning at room temperature. Table 4.2 gives real experimental data.

3.5.2. Assessment of Corrosion Damage.

The average corrosion rate is determined by taking into consideration the initial total surface area of the specimen and the mass lost during the test period using the following corrosion rate equation [4]:

$$CR = \frac{Ks}{\rho A} = \frac{MIs}{nF\rho A} = \frac{Mis}{nF\rho} \quad \ldots\ldots\ldots\ldots\ldots\ldots\ldots\ldots\ldots\ldots\ldots\ldots\ldots\ldots\ldots\ldots\ldots\ldots\ldots\ldots\ldots\ldots \quad (3\text{-}1)$$

Where:

CR = corrosion rate (cm/year);

K = rate of corrosion (g/s);

A = area in cm^2;

ρ = density in g/cm^3 (density of carbon steel = 7.86 g/cm^3) (taken from ASTM G1-03 specification);

s = seconds in a year (3.15×10^6);

F = Faraday's constant (C/mole);

I = corrosion current (A);

n = number of electrons for each metal atom.

3.6. Electrochemical Impedance Spectroscopy (EIS).

3.6.1. Introduction.

Electrochemical impedance spectroscopy (EIS) or the AC impedance technique is a particularly useful method used routinely to investigate corrosion mechanisms and the fundamental parameters of electrochemical reactions. EIS techniques have been commonly employed for many years in electrochemical research and corrosion science investigations. Prior to the 1970's, the application of EIS techniques was not so common, but some excellent work was carried out in Cambridge by Hoar and Wood in 1962 on the properties of anodized aluminium [5]. However their equipment was limited to single frequency capacitance bridge methods. In the mid 1970's the advent of the transfer function analyser together with the availability of cheap computational software and hardware has produced an extensive output on electrochemical and corrosion related studies involving AC impedance techniques, which has continued unabated until today.

The popularity of impedance techniques may be explained as follows; firstly; the technique makes use of only very small perturbation signals without disturbing the properties of the electrode that is to be measured. Secondly, it can obtain charge transfer resistance as well as double layer capacitance data in the same measurement. Thirdly, the measurements can be made in solutions with low conductivity whereas, under similar such conditions, D.C techniques are subjected to significant errors due to large ohmic drops. When electrochemical impedance techniques are used, the solution resistance can be easily measured and thus eliminated [6-9]. Fourthly, the equipment is relatively inexpensive and it is very easy to obtain large quantities of data rapidly.

It should always be borne in mind that the system under investigation must fulfill the Kramers Kronig criteria [10]. This is simply stated by the following requirements:

Stability: i.e. the system must not change during the measurement period.
Linearity: i.e. the system must not exhibit any abrupt discontinuities.
Causality: i.e. the response must be due to the applied perturbation.
Finite: i.e. at very high frequencies and at very low frequencies the system must tend to zero.

3.6.2. The basic principles of Electrochemical Impedance Spectroscopy (EIS).

For any electric circuit, which consists of various passive elements (i.e. resistors, capacitors and inductors) the behaviour of the whole circuit to an applied ac voltage, is dependent upon both the behaviour of individual elements, and also on their arrangement in the circuit with respect to each other.

If a dc direct voltage is applied to the elements that comprise the equivalent circuit, the resulting current can be measured using Ohms law.

For the case where a low amplitude sine wave E_{ac}, of a particular frequency, is applied across a passive element, then:

$$E_{ac} = E_0 \sin(\omega t) \quad \text{(3-2)}$$

Where:

E_{ac} = potential at time t;

E_0 = maximum voltage amplitude;

ω = is the angular frequency, $\omega = 2\pi f$;

t = is the time.

Under these conditions, the resulting current response of a sine wave I_{ac} will be given by:

$$I_{ac} = \frac{E_{ac}}{X} \quad \text{(3-3)}$$

Where:

I_{ac} = current at time t;

X = the reactance of the particular passive element in the electrical circuit.

When the applied signal is a sinusoidal voltage wave and the resulting signal is a sinusoidal current wave, then X is called the impedance Z; conversely, when the applied signal is a sinusoidal current wave, the resulting signal is a sinusoidal voltage wave, X which is called the admittance Y.

The value of the reactance of a capacitor or an inductor can be expressed as a complex quantity by the complex operator j, $j = \sqrt{-1}$ [11], and using this notation the reactance of the elements are given by [12]:

For a resistor: $X_R = R$

For a capacitor: $X_C = 1/-j\omega C$

For an inductor: $X_L = j\omega L$ …… (3-4)

For the impedance, $Z(\omega)$, as mentioned above is a complex quantity and can be represented in Cartesian as well as polar co-ordinates. In polar co-ordinates the impedance of the data is represented by:

$$Z(\omega) = |Z(\omega)|e^{\phi(\omega)} \quad \text{……} \quad (3\text{-}5)$$

Where:

$|Z(\omega)|$ = Magnitude of the impedance and ϕ is the phase shift.

In Cartesian co-ordinates the impedance is given by,

$$Z = Z' + jZ'' \quad \text{……} \quad (3\text{-}6)$$

Where:

Z' = the real part of the impedance;

Z'' = the imaginary part.

For the admittance,

$$Y = Y' + jY'' \quad \text{……} \quad (3\text{-}7)$$

$$Z = \frac{1}{Y} = \frac{Y'}{Y'^2 + Y''^2} + j\frac{-Y''}{Y'^2 + Y''^2} \quad \text{……} \quad (3\text{-}8)$$

Since the impedance is a vector, it is possible to represent it in a complex plane plot such as a Nyquist plot which consists of a set of points each representing the magnitude and direction of the impedance vector at a particular frequency [11]. Data obtained by EIS is often expressed graphically in a Bode plot or a Nyquist plot together with the Bode plot. The Nyquist plot can be used to show the variation in impedance with different frequencies and can be considered as an extension of the Argand diagram which uses frequency as a parameter variable. The Bode plot can have *log(f)* or *log(ω)* as the x axis, and the $|Z|$ and ϕ as the y axis. I used a combination of Nyquist and Bode plots to present my data.

$$\tan\theta = \frac{Z''}{Z} \quad \text{……} \quad (3\text{-}9)$$

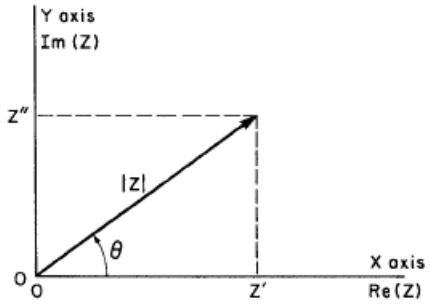

Figure 3.5. Argand plot showing impedance vector Z [13].

3.6.3. The impedance of electrode electrolyte interfaces.

At the electrode electrolyte interface, the simplest reduction reaction is given by:

$Ox + ne^- \rightarrow Red$ …… (3-10)

In the above reaction, the impedance of the electrode electrolyte interface will be due to the combination of: (1) the electrochemical double layer, (2) the constant phase element (CPE), (3) the Ohmic resistance of the system, (4) the Warburg impedance. Each of these components will be discussed further.

(1) The electrochemical double layer C_{dl}.

The electrochemical double layer behaves like a parallel plate capacitor due to the separation of the charge between each side of the interface, the capacitance exhibited by C_{dl} is dependent on the relative conductivity of the media, the ionic concentration, and the thickness of the double layer. It is not a perfect capacitor, i.e. the relationship between the charge across the interface and applied potential is not linear. However, by using only small voltages that have small perturbations ($E_{ac} \leq 20$mV), the relationship approximates to a linear one.

(2) The Constant Phase Element CPE.

This Section was obtained from the excellent internet articles from Bob Rogers who originally worked for Gamry [14].

"The Constant Phase Element (CPE) is an non-intuitive circuit element that was discovered (or invented) while looking at the response of actual real-world systems. In some systems, the Nyquist plot was expected to be a semicircle with the center on the X -

axis. However, the observed plot was indeed the arc of a circle, but with the center some distance below the x-axis."

"These depressed semicircles have been explained variously by a number of phenomena depending on the nature of the system being investigated. However the common thread among these explanations is that some property of the system is not homogeneous or that there is some distribution (dispersion) of the value of some physical property of the system. The CPE is usually represented by two parameters, Q° and n".

"It is tempting to simply associate the value of Q° for a CPE with the capacitance value, C, for an equivalent capacitor. The value range of n is between 0 and 1. When n = 0, Q° = R. When n = 1, Q = C."

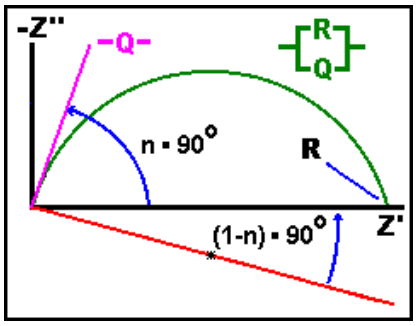

Figure 3.6. Nyquist Plot of a solitary CPE [14].

"In Figure 3.6, a Nyquist Plot is shown with a solitary CPE (symbolized by Q), it is just a straight line which makes an angle of (n*90°) with the x-axis as shown in pink. The plot for a resistor (symbolized by R) in parallel with a CPE is shown in green. In this case the center of the semicircle is depressed by an angle of (1-n)*90°" [14].

"Mathematically, the impedance of a CPE is given by:

$$Z = \frac{1}{Q^0}(j\omega)^{-n} = \frac{1}{Q^0\omega^0}e^{-\frac{\pi}{2}ni} \quad \text{..... (3-11)}$$

Where:

Q° = has the numerical value of the admittance ($1/|Z|$) at ω=1 rad/s. The units of Q° are F/cm^2;

n = constant, 0<n<1."

There are two parameters are used to describe the CPE in Zview software: these are CPE_{-T} and CPE_{-P} (CPE_{-T} = Q° and CPE_{-P} = n). We will consider them later in Chapter 5.

(3) Ohmic resistance R_{Ω}.

The Ohmic resistance of the system consists of a combination of the electrolyte resistance, the resistance of the connection leads and the charge transfer resistance of the electrode. In general the last two resistances are negligible compared to the solution resistance; therefore the Ohmic resistance and the solution resistance may be taken as the same.

The electrode reaction could be represented as impedance due to charge transfer and mass transport, and the impedance due to the mass transport is represented by the Warburg impedance, the charge transfer resistance can be considered as a simple resistance.

(4) Warburg impedance.

(i) Introduction to the Warburg impedance.

This Section has been largely transferred from the website of Rogers and Gamry [14] with minor modifications.

"The Warburg impedance represents the impedance exhibited by the mass transport (diffusion) of electroactive species, to and from the from the electrode surface. At high frequencies the Warburg impedance is small since diffusing reactants don't have to move very far. At low frequencies the reactants have to diffuse further, thereby increasing the Warburg impedance.

The equation for the "infinite" Warburg impedance is:

$$Z_W = \sigma\omega^{-\frac{1}{2}}(1-j) \quad \ldots\ldots\ldots\ldots\ldots\ldots\ldots\ldots\ldots\ldots\ldots\ldots\ldots\ldots\ldots\ldots\ldots\ldots \quad (3\text{-}12)$$

Where σ is the Warburg coefficient and is defined as:

$$\sigma = \frac{RT}{n^2F^2A\sqrt{2}}\left(\frac{1}{C_O^*\sqrt{D_O}} + \frac{1}{C_R^*\sqrt{D_R}}\right) \ldots\ldots\ldots\ldots\ldots\ldots\ldots\ldots\ldots\ldots\ldots\ldots\ldots\ldots \quad (3\text{-}13)$$

Where:

ω = radial frequency;

D_O = diffusion coefficient of the oxidant;

D_R = diffusion coefficient of the reductant;

A = surface area of the electrode;

n = number of electrons transferred;

C* = bulk concentration of the diffusing species (moles/cm^3);

$j = \sqrt{-1}$.

This relationship assumes that the induced concentration wave diminishes at an infinite distance from the surface. However frequently this is not the case and the concentration wave vanishes at a finite distance from the surface, normally within the Nernst Diffusion Layer. If the diffusion layer is bounded, the impedance at lower frequencies no longer obeys the equation above. By re-defining the boundary conditions so that the concentration wave is zero at the distance δ from the surface (where δ is the Nernst diffusion layer distance), the Warburg impedance is given by the following equation (3-14):

$$Z_O = \sigma\omega^{-\frac{1}{2}}(1-j)\tanh(\delta(\frac{j\omega}{D})^{1/2}) \quad \text{(3-14)}$$

Where:

δ = Nernst diffusion layer thickness;

D = the average value of the diffusion coefficients of the diffusing species" [14].

(ii) Warburg Impedance as applied to this Thesis.

In the data obtained in our work on the calcareous films the general shape indicated a lack of a 45° slope at low frequencies and thus the appropriate Warburg analysis was according to the Finite Warburg Method, not the Infinite.

The experimental data were analysed by the EIS data fitting computer programs (Zview software). For Warburg short W_S case, there were three parameters which were given to describe the Finite Warburg $W_{S\text{-}R}$, $W_{S\text{-}T}$ and $W_{S\text{-}P}$ (Actually $W_{S\text{-}P}$ is normally 0.5).

The relationship between the impedance and the parameters can be expressed as:

$$Z = \frac{W_{S-R}}{\sqrt{\omega}}(1-j)\tanh[W_{S-T}\sqrt{j\omega}] \quad \text{(3-15)}$$

Where:

$W_{S\text{-}R}$ is equal to the Warburg coefficient;

$W_{S-T} = \delta / D^{1/2}$, δ is the Nernst diffusion layer thickness, and D is the average value of the diffusion coefficients of the diffusing species;

ω = angular frequency of the ac signal.

We will be examining the parameters $W_{S\text{-}R}$ and $W_{S\text{-}T}$ and their variation with current density and time in Chapter 4, later in this Thesis.

(5). Equivalent circuit.

For a simple electrochemical process, an equivalent circuit refers to the simplest form of a circuit that retains all of the electrical characteristics of the original electrochemical system. In its most common form, an equivalent circuit is made up of linear elements; the system may be represented by a simple electrical circuit including resistors, capacitors, or inductors. However, more complex equivalent circuits are sometimes used that approximate the nonlinear behavior of the original system as well.

3.6.4. The mathematical approach.

Considering a corroding metal, an equivalent circuit that represents such a system can be illustrated by Figure 3.7 (a metal-solution interface).

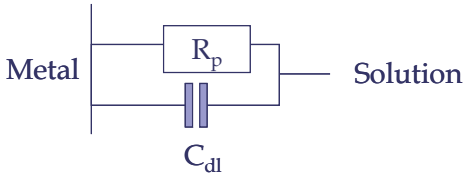

Figure 3.7 An equivalent circuit for corroding metal [4].

The simplest circuit is a resistor, corresponding to the polarization resistance R_p, connected in parallel with a capacitor, corresponding to the double layer capacitance C_{dl} [15].

The current that may flow through the resistance can be given as follows:

$$I(t) = \frac{V(t)}{R_P} \quad \text{(3-16)}$$

This current is known as the Faradic current and it is related to the oxidation and reduction processes of the species involved. The current that flows through the capacitor depends not on the applied voltage, but on the rate of voltage change and can be given as follows [15]:

$$I(t) = C_{dl}\frac{dV(t)}{dt} \quad \text{(3-17)}$$

The total current that passes through the circuit is equal to the sum of current that passes through the resistor and the current that passes through the capacitor and can be given by the sum of equations 3-16 and 3-17) as follows [15]:

$$I(t) = \frac{V(t)}{R_P} + C_{dl}\frac{dV(t)}{dt} \quad \text{(3-18)}$$

Where:

$I(t)$ = the total current.

As mentioned earlier, the current passing through the capacitor depends on the rate of voltage change, and if this change is minor, the second part of equation 3-18 can be ignored, thus the resulting current can be given by the first term [15]:

$$I(t) \approx \frac{V(t)}{R_P} \quad \text{(3-19)}$$

The signal applied by any EIS machine is normally very small. The reason for this signal being minor is to prevent disturbance to the system being studied, and this is one of the important advantages of EIS.

As we mentioned above, the small perturbating voltages ($E_{ac} \leq$20mV) are indeed small. In addition, the signal is a sinusoidal signal, and consequently the applied voltage can be given by equation 3-20 [15]:

$$V(t) = V_0 \sin(\omega t) \quad \ldots\ldots\ldots\ldots\ldots\ldots\ldots\ldots\ldots\ldots\ldots\ldots\ldots\ldots\ldots\ldots\ldots\ldots\ldots\ldots\ldots\ldots \quad (3\text{-}20)$$

Where:

$V(t)$ = the applied voltage;

V_0 = the maximum amplitude of the voltage;

ω = the angular frequency.

The sinusoidal voltage signal can then be plotted as shown in Figure 3.8.

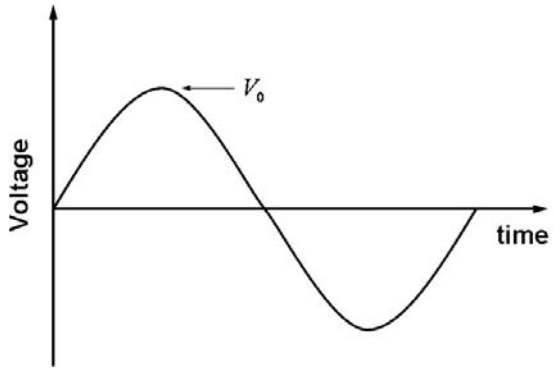

Figure 3.8. Sinusoidal voltage signal [15].

The rate of the voltage change in equation (3-20) can be expressed as follows:

$$\frac{dV(t)}{dt} = V_0 \omega \cos(\omega t) \quad \ldots\ldots\ldots\ldots\ldots\ldots\ldots\ldots\ldots\ldots\ldots\ldots\ldots\ldots\ldots\ldots\ldots\ldots\ldots\ldots\ldots\ldots \quad (3\text{-}21)$$

Consequently when the voltage is being applied to both the resistor and the capacitor in the circuit, the resulting current can be expressed as follows:

$$I(t) = \frac{V_0}{R_P} \sin(\omega t) + V_0 \omega C_{dl} \cos(\omega t) \ldots\ldots\ldots\ldots\ldots\ldots\ldots\ldots\ldots\ldots\ldots\ldots\ldots\ldots\ldots\ldots\ldots\ldots\ldots\ldots\ldots\ldots \quad (3\text{-}22)$$

The two components of the current can be plotted against time, as in Figure 3.9. The first part is called “in phase” with an applied voltage (zero current occurs at the same time as zero voltage, and the peak current occurs at the same time as the peak voltage). The second part is called “out of phase”, and in this case (zero current occurs at the same time as the peak voltage, and the peak current occurs at the same time as the zero voltage), the magnitude of both terms (components) is proportional to the applied voltage V_0 [15].

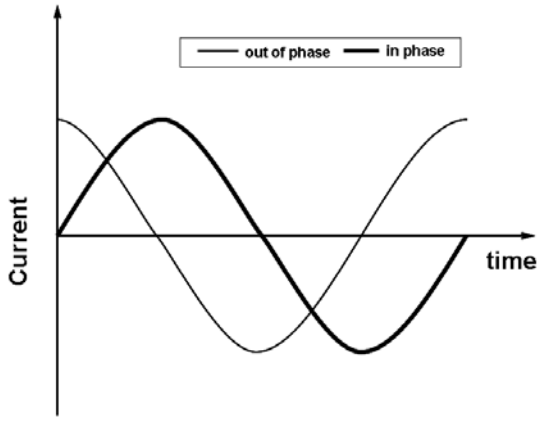

Figure 3.9. The two components of current response of the circuit in Figure 3.8 [15].

The same two components can be plotted in a different way by dividing the "in phase" and "out of phase" components of the current by the applied voltage V_0 (see Figure 3.10).

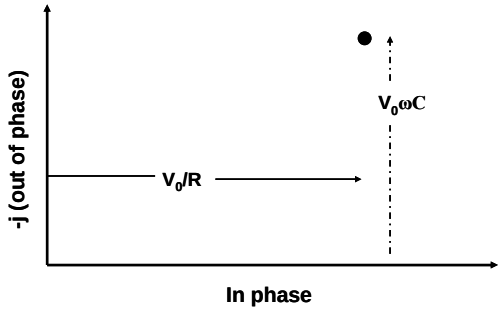

Figure 3.10. In- phase and out-of- phase current components plotted as one frequency [15].

We can represent this by saying that the in-phase current is proportion to $1/R_P$, and the out-of-phase current is proportion to jwC_{dl}, where the j operator indicates a 90^o phase shift between the input voltage and resulting current. If the same current components were plotted for a wide range of frequencies the resulting plot would be similar to the Nyquist plot apart from the labeling on the x and y axes [15] (Figure 3.11).

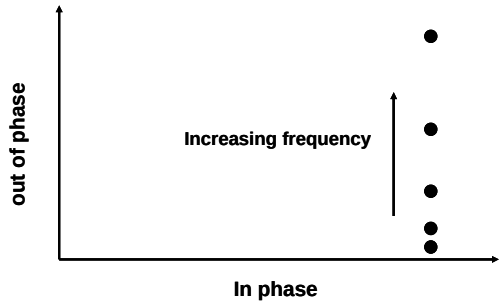

Figure 3.11. In phase and out of phase current components plotted at different frequencies [15].

When any measurements are carried out, the total current is actually measured rather than measuring the two components of the current, and it is valuable to have one expression for the current as follows [15]:

$$I(t) = I_0[\sin(\omega t)\cos\phi + \cos(\omega t)\sin\phi] \quad \text{(3-23)}$$

or: $I(t) = I_0 \sin(\omega t + \phi)$ (3-24)

Equation 3-24 above describes another sine wave but shifted in phase along the time axis compared with the voltage by an angle ϕ in equation 3-23.

$$I_0 \cos\phi = \frac{V_o}{R_P} \quad \text{(3-25)}$$

$$I_0 \sin\phi = V_0 \omega C_{dl} \quad \text{(3-26)}$$

From equations 3-25 and 3-26, we can then obtain the following equation:

$$\frac{I_0}{V_0} = \sqrt{\frac{1}{R_p^2} + \omega^2 C_{dl}^2} \quad \text{(3-27)}$$

$$\tan\phi = \omega R_P C_{dl} \quad \text{(3-28)}$$

I_0/V_0 is known as the admittance modulus which usually written as $|Y|$ and ϕ is the phase angle.

By using the symbol Y for the admittance, a similar equation to 3-18 can be written as follows:

$$Y(\omega) = \frac{1}{R_P} + j\omega C_{dl} \quad \text{(3-29)}$$

or: $Y(\omega) = Y' + jY''$ (3-30)

Where Y' represents the real component and Y'' represents the imaginary component. In this case, the admittance depends on frequency, which is why it is described as $Y(\omega)$. Y' is proportional to the in-phase current component and Y'' is proportional to the out of phase current component and both of them depend on the frequency. In reality the

conventional impedance measurements are generated by applying a voltage, and then measuring the current response which is given by equation 3-24. However, impedance data is normally presented as a modulus Z and phase angle (Bode plot) or the real and imaginary parts (Nyquist plot) [15].

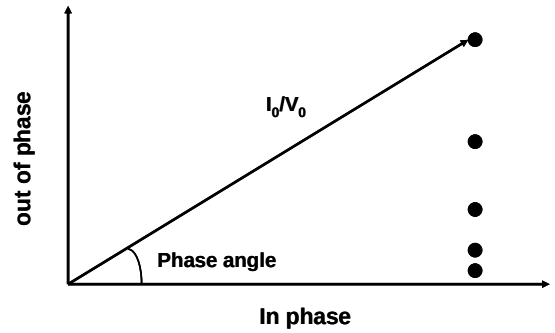

Figure 3.12. Modulus and phase angle at different frequencies [15].

The graph given in Figure 3.12 shows the relationship between the admittance modulus ($|Y|$) and the phase angle at different frequencies.

3.6.5. Impedance of a simple circuit.

In standard impedance measurements, the solution resistance R_s should be considered in the equivalent circuit, therefore, when the solution resistance is considered, the equivalent circuit can then be represented by Figure 3.13.

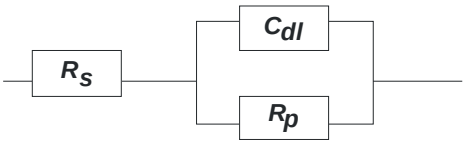

Figure 3.13. The Randles equivalent circuit for a corroding interface [4].

In many cases, the Bode plot, (log Z versus log ω and log ω versus θ), as illustrated in Figure 3.14, is used to analyze the impedance data. In Bode plots, resistive and capacitive regions are clearly distinguished together with information provided by the frequency dependence of the phase angle, which is a very sensitive indicator of small changes in such spectra [16].

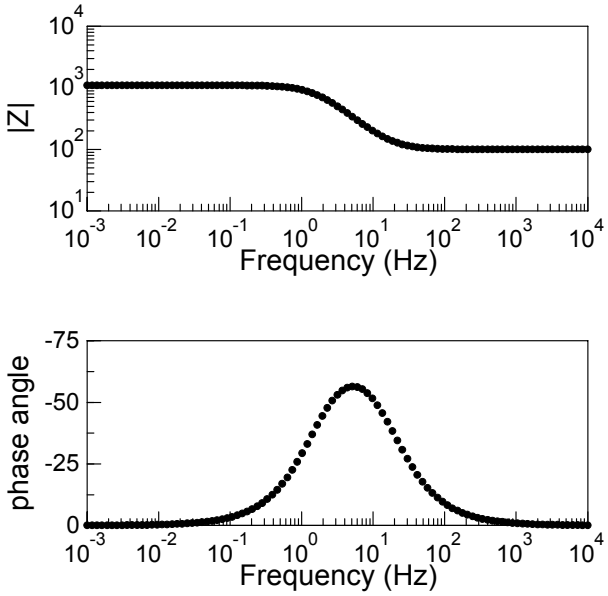

Figure 3.14. Example of a Bode Plot for the equivalent circuit given in Figure 3.13,with component values of R_s = 100 Ω, R_p = 1000 Ω, C_{dl} = 0.0001 F. Note that |Z| tends to R_s at high frequency and to $R_s + R_p$ at low frequency [17].

On the Bode plot, a resistor produces a horizontal line on the amplitude plot with amplitude equal to the resistance and a constant phase of zero on the phase plot. A capacitor produces an amplitude that falls with a slope of -1 as the frequency increases (the amplitude of the impedance is $1/(2\pi fC)$, where f is the frequency and C the capacitance), and a constant phase of -90°; because we are normally dealing with resistors and capacitors, it is common to invert the phase axis (i.e. plot – phase), so that a useful means of representing this variation with frequency is the Nyquist plot, as capacitive circuit elements give data above zero [2].

A Nyquist Plot is shown in Figure 3.15. This diagram consists of a set of points, each representing magnitude and direction of the impedance vector at a particular frequency.

The Nyquist Plot normally plots the imaginary part of the impedance against the real part. The Nyquist plot invariably inverts the imaginary axis (i.e. it plots the imaginary component of impedance with increasingly negative values on the y-axis), so that capacitive circuit elements plot above the x-axis. One weakness of the Nyquist plot compared to the Bode plot is that it does not implicitly include the frequency of each measurement point, so at least some points should have their frequency indicated [2].

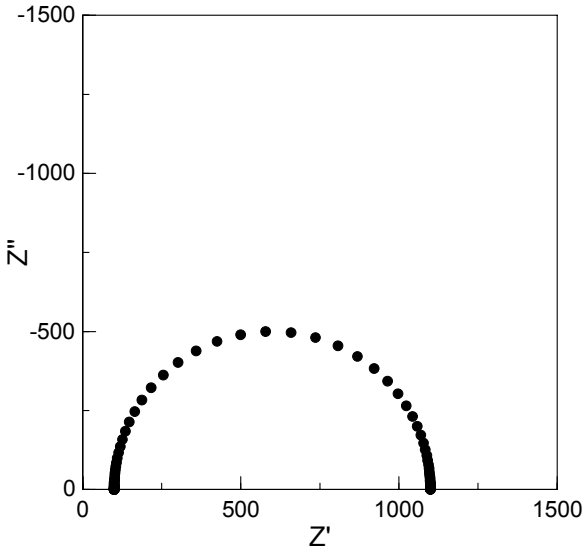

Figure 3.15. Example of a Nyquist Plot [17].

According to the equation 3-29, considering the solution resistance R_S, the total impedance can be expressed by [4]:

$$Z = R_s + \frac{R_P}{1 + j\omega CR_P} \quad \text{(3-31)}$$

$$Z = R_s + \frac{R_P}{1 + j\omega CR_P}\left(\frac{1 - j\omega CR_P}{1 - j\omega CR_P}\right) \quad \text{(3-32)}$$

$$Z = R_s + \frac{R_P}{1 + \omega^2 C^2 R_P^2} - \frac{j\omega CR_p^2}{1 + \omega^2 C^2 R_P^2} \quad \text{(3-33)}$$

3.6.6. Disadvantages of the EIS technique.

We have already explained some advantages of the EIS technique in Section 3.6.1. It is useful to mention here some disadvantages. There are a few limitations associated with the use of Electrochemical Impedance Spectroscopy (EIS). Firstly, in some instances, an appropriate model cannot be found to fit the impedance data and in other cases even when the equivalent circuit has known component values, it may not be resolved.

Sometimes, fitting problems may arise because of distorted semi-circles [18]. Therefore, in such cases, the interpretation of the impedance data is usually difficult and care must be taken when doing so.

Finally, the measurements obtained using Electrochemical Impedance Spectroscopy (EIS) are sequential; e.g. each frequency point is considered in turn, which means that to obtain frequency spectra from, say 10 KHz to 10 mHz, it takes some time depending on how powerful the impedance machine is. This can be a long time for rapidly corroding systems whose rate of reaction is changing quickly. Also, at low frequencies, the system may be subject to noise 'pick-up' which can lead to frequency scatter on the impedance plot. Despite these drawbacks, Electrochemical Impedance Spectroscopy (EIS) has proven to be a valuable technique and can provide important information about the nature of corrosion processes in many systems [19].

3.6.7. EIS for calcareous films.

The use of electrochemical impedance spectroscopy for corrosion rate estimation and also corrosion behavior research studies is well established. The large number of papers available in this area is a good indicator of the many studies that have been undertaken in the field of determination of coatings [20], inhibitors, rebar steel embedded in concrete, properties, evaluation of dissolution and the passivation phenomena**,** measurement of corrosion rate at the corrosion potential and data analysis. The regular series of Conferences entitled: "Electrochemical methods in Corrosion Research", with its accompanying published volumes of Proceedings is probably a good starting point to obtain reference information on all these research areas [21]. A Google search on this title reveals 151000 links to this subject.

There are very few papers available in the literature that deal with the performance of mild steel under conditions of cathodic protection and evaluated using EIS techniques. Thompson, *et. al*., recognized that EIS was a useful monitoring tool for detecting corrosion on cathodically protected carbon steel structures in soil and concrete [22, 23].

The most recent and extensive studies in this area are from France. Deslouis [24], [25] and his collaborators published two fundamental papers in this area. Their first published article was entitled: "Characterization of calcareous deposits in artificial seawater by impedance techniques-I. deposit of $CaCO_3$ without $Mg(OH)_2$''[24], and they described calcium carbonate deposits grown under conditions of cathodic protection and characterized by both EIS and electrohydrodynamical impedance spectroscopy (EHD) impedance. They stated "in particular, from the EHD impedance data, it was possible to

estimate the average value of crystal size in the first phase to about 30-50 μm and covered fraction from the high frequency capacitance". Subsequently, the same group of authors continued and extended this work [25] with the paper entitled: "Characterization of calcareous deposits in artificial seawater by impedance techniques-3. Deposit of $CaCO_3$ in the presence $Mg(OH)_2$". This later article focused on "calcareous deposits grown under cathodic protection which were characterized at various constant potentials from -0.9 to -1.4 V/SCE", the calcareous layers were characterized by electrochemical and electrohydrodynamical impedance spectroscopies.

From the impedance studies, Deslouis [24], was able to conclude that "the continuous calcium carbonate film covers the metal and is characterized by a faradaic impedance Z_f at the pores' bottom in parallel with the double layer capacitance C_{df} relative to the same area. These two elements are in series to a resistance R_f due to finite conductivity of electrolyte solution in thin pores and whole arrangement is placed in parallel to capacitance C_f reflecting the dielectric nature of the $CaCO_3$ layer".

They assumed that the metal becomes covered by calcium carbonate 'islands' with inner porous defects and macroscopic exposed areas, see Figure 3.16.

As a conclusion to their initial work, the same authors [24] proposed an electrical equivalent circuit, which is based on the parallel combination of the characteristic impedance of the $CaCO_3$ sites and the parallel association Z/C_d over the uncovered areas. In Figure 3.16 the elements have the same physical-chemical meanings but for very different area values. One major criticism of the two major studies discussed above, is that they seem to have used extremely high current densities (sometimes as much as 5000 mA/m^2), and have ignored the obvious presence of the hydrogen evolution reaction.

In our study, we had access to two impedance setups. In our study on calcareous films we used the growth of calcium/magnesium containing films as anti-corrosion barriers on iron. We have investigated two deposition processes; one is a pH driven precipitation reaction set up by the cathodic reduction process using CP in seawater. Furthermore, from the characteristics of cathodic protection, we wanted to try to find the relationships between various different current densities and cathodic polarization in artificial sea water by electrochemical impedance spectroscopy (EIS) signals.

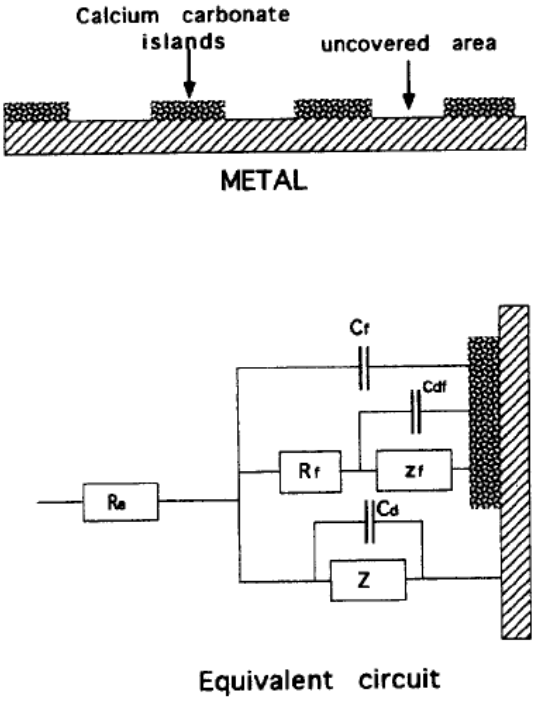

Figure 3.16. Schematic of partly covered interface with calcium carbonate crystals and related electrical equivalent circuit [24].

The second deposition process that we investigated was with anti-corrosion pigments. We used a conventional open circuit investigation with an anticorrosion pigment D5-B containing calcium, magnesium and polyphosphate.

Both the testing frequencies at the start were 10000 Hz, whilst the final test frequencies were 0.1 Hz., and impedance devices were calibrated weekly with a dummy cell modeling a simple Randles circuit which consisted of just three basic components; namely two resistors and a capacitor (R_1 = 100 Ω, R_2 = 1000Ω, C_1 = 1μF).

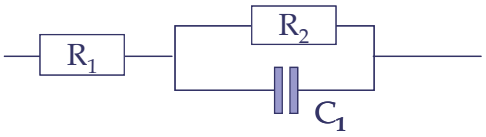

Figure 3.17. Real circuit of dummy cell [4].

3.7. Potentiodynamic polarization study.

Potentiodynamic polarization is a well known technique in corrosion studies. It requires a potentiostat, a linear sweep generator (to produce the potential sweep) and a recording device of some kind to record the current and potential. Typical values of sweep rate are in the order of 1 mVs^{-1}, which was used in this work.

We used a Solartron 1286 Electrochemical Interface, which controlled by a desk top computer running dedicated Corrview 3.0 software. Corrosion rate data was generated with this system from Linear Polarisation Resistance and also from Tafel extrapolation and will be discussed in Chapter 5.

3.8. Scanning Electron Microscopy (SEM) and Energy-Dispersive X-Ray Analysis (EDX).

3.8.1. Introduction.

The technique of Scanning Electron Microscopy (SEM) was employed extensively throughout this study to examine and obtain images of both the surface morphology and internal structure of corrosion deposits and films on samples of mild steel. The associated analytical facility of Energy Dispersive X-Ray (EDX) analysis was used to identify and quantify the elemental composition of the deposited surface films on the sample surfaces, formed as a result of immersion in different electrolytes. EDX was also used to determine the distribution of selected elements over the surface of the sample. It should be noted, that these different techniques are essentially part of one instrument: the EDX facility (basically an X-Ray detector and associated software) is incorporated intimately as part of the SEM itself, and cannot function without the operation of the SEM, since the generation of the analytical X-ray signal is dependant on the interaction between the incident electron beam and the sample in the SEM. Note also that the acronyms EDAX and EDS (Energy Dispersive Spectrometer) are often used interchangeably in place of EDX by different instrument manufacturers but are essentially the same technique. Therefore, collectively, these techniques (SEM and EDX) were considered one of the major procedures that were used to conduct this research. A brief description and discussion of the operating principles and capabilities respectively of these essential techniques is given in the following Sections. Both Goldstein, *et. al*., [26] and Echlin [27]

have recently given a comprehensive account of the theory, operating principles and capabilities of SEM and EDX.

3.8.2. Basic Principles of Scanning Electron Microscopy (SEM).

A microscope is an instrument that allows images to be obtained of a sample at magnifications greater than 30 times life-size (the term 'macro' is applied to instruments that image at magnifications from 5 X to 30 X). Since the recent development of new innovative instruments such as the Atomic Force Microscope (AFM) and the acoustic microscope, the older definitions of a microscope as being based on instruments that utilize optical systems (either light-rays or electron beams) for imaging at magnification above 30X are no longer applicable. The technique of AFM was used briefly in this Study, and will be discussed further in Section 3.10. There are three main types of Electron Microscope, these are: the Scanning Electron Microscope (SEM), the Transmission Electron Microscope (TEM) and instruments that have a dual function capability: – the Scanning-Transmission Electron Microscope (STEM). Only the SEM will be discussed here. Essentially, in a Scanning Electron Microscope, a beam of electrons is generated by an electron gun in a high vacuum column, at an accelerating voltage of between 1.0 to 30 kV, but usually within the range 5.0 kV to 20 kV, then collimated into a coherent beam, using a system of electromagnetic coils or lenses; then passed down through the main electron gun column into the specimen chamber, where it is focused into a fine spot, then scanned rapidly over the surface of the sample. Two processes then occur simultaneously: secondary electrons are emitted from the sample as a result of ionization processes, and in addition, some electrons from the primary beam (generated by the electron gun), are reflected or 'bounced back' from the sample as a result of interactions with the nuclei of the elements of the sample. These latter electrons are termed 'backscattered electrons' or the BSE signal. Both types of electrons are then collected separately by a specific type of electron detector, and the resulting signals are then processed, amplified and displayed to give an image which can then either be viewed and/or stored digitally. Secondary electron detectors are normally a combined scintillator and photo-multiplier system, known as an Everhart-Thornley detector which is mounted to one side of the specimen stage; whilst most modern BSE detectors are a compact semiconductor design and mounted directly onto the final electron objective of the microscope (i.e. immediately above the sample).

Generally, secondary electron (SE) images are used to give high resolution images of the sample surfaces as three-dimensional surface topography, with good depth of field; whilst BSE images can provide useful analytical information about the sample, since the electrons from the primary beam that are backscattered have interacted with the atoms of the sample. BSE images at 8 kV give good 'orientation contrast', whilst BSE images at 20 kjV give atomic number contrast, since the intensity of the BSE signal is strongly related to the atomic number (Z) of the specimen, the BSE images can provide information about the elemental composition in the sample surface, or the near-surface region (~ 1.0 to 2.0 μm). Figure 3.18 illustrates schematically the main SEM instrument that was used throughout this study.

There are several types of SEM instrument available, which vary either in terms of the type of electron gun used to produce the primary beam of electrons, or in either/both the type of vacuum system and electron detector used to collect the emitted/reflected electrons. There are three types of electron gun in common use – two of these are 'thermionic'; i.e. where electrons are generated as a result of emission through heat – most typically by a heated (to ~ 2000 – 2700 K) thin (~ 100 μm diameter) tungsten wire or filament formed into a 'hairpin' shape, which emits electrons and these are attracted and channeled by a charged anode, then passed through an electron optics system of electromagnetic coils to give a coherent beam of electrons. The second type of thermionic electron gun is a lanthanum hexaboride (LaB_6) type, which also operates on a 'thermal' principle to emit electrons, but is much more efficient than a basic heated filament. The third and most efficient type of electron producing source is a Field Emission Gun (FEG) type, which consists of a very sharp tungsten tip situated adjacent to a high electric field (a highly charged anode) and electrons then 'tunnel' out of the tip. Such a system is not 'thermal' (although most currently available FEG guns also heat the tungsten tip to improve efficiency) and is extremely efficient since the energy distribution of a FEG system is much narrower than the two 'thermal' filament types. Although the filaments in thermal electron guns are cheap to replace (~ £25.00 each), they have low brightness, a limited lifetime (~ 150 hours) and large energy spread. In contrast, a FEG tip will last for about 2 years of constant operation, but costs around three thousand pounds. Most of the SEM investigations in this study were undertaken using a FEI (Phillips) XL-30 FEG SEM (Figure 3.19).

One disadvantage of most SEM instruments, is that the electron gun (especially a FEG – tip) must always operate in an extremely high vacuum, and any specimen being examined must be electrically conductive in order to allow electrons from the primary beam to flow to earth, and hence avoid the build up of regions of 'charge' on the surface of the sample, which results in severe degradation of the image. This phenomenon is discussed later (see Section 3.8.4) in terms of sample preparation requirements prior to SEM study.

About 15 years ago, a new type of SEM instrument known as an Environmental SEM or ESEM became readily available, that allowed non-conductive samples to be directly imaged in an SEM, without the need to first coat them with a thin film of sputtered or evaporated metal (usually gold or platinum) or carbon. Apart from the fact that sputtered metal coatings are approximately 7.0 to 25 nm thick, they severely restrict the use of EDX analysis. The ESEM was originally developed with the main aim of being able to examine non-conductive biological samples whilst still hydrated, and without the risk of producing imaging artifacts caused by critical point drying or other sample preparation techniques. A full account of the development of ESEM instruments has been given by Danilatos [28].

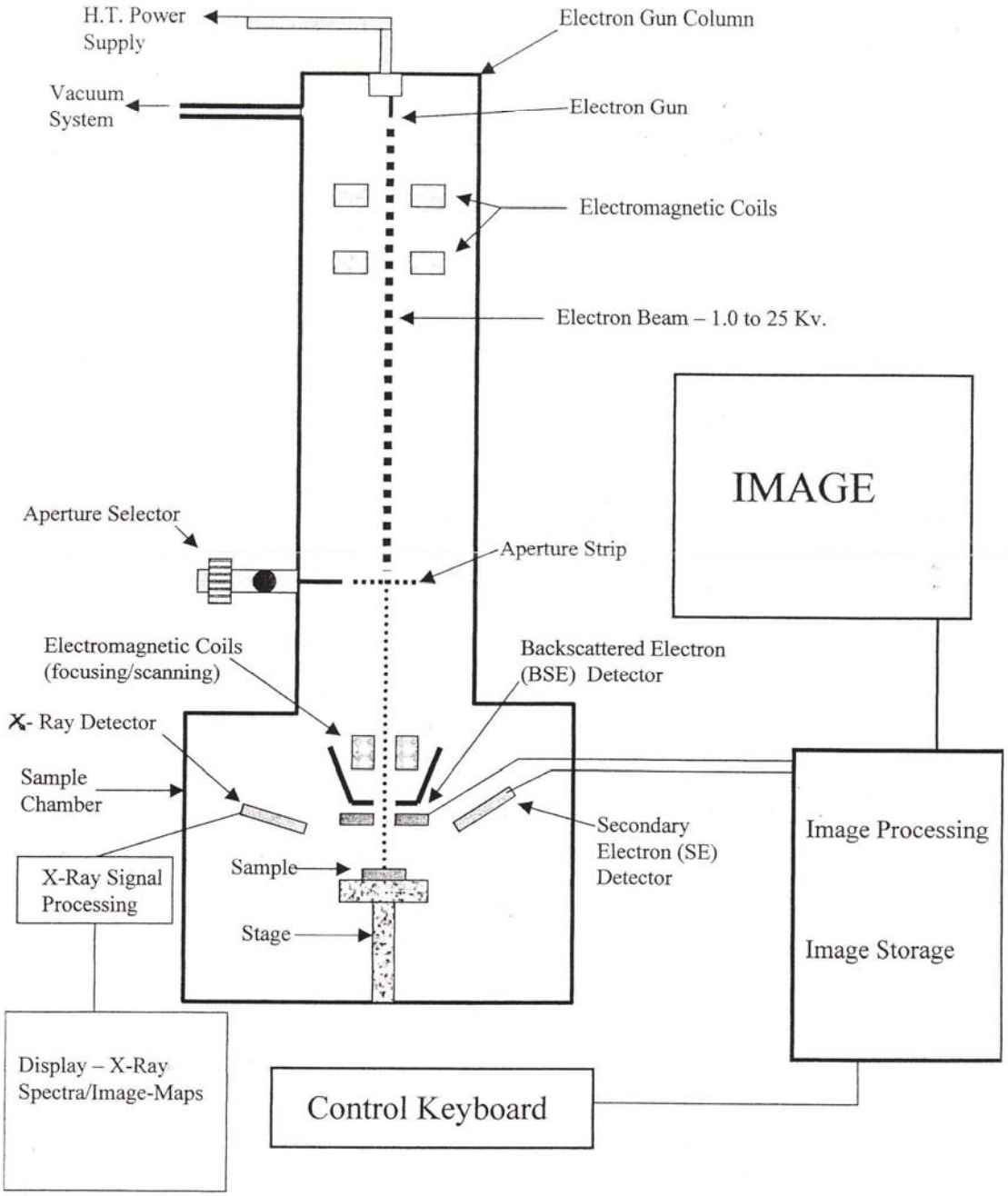

Figure 3.18. Schematic of FEI XL 30 FEGSEM.

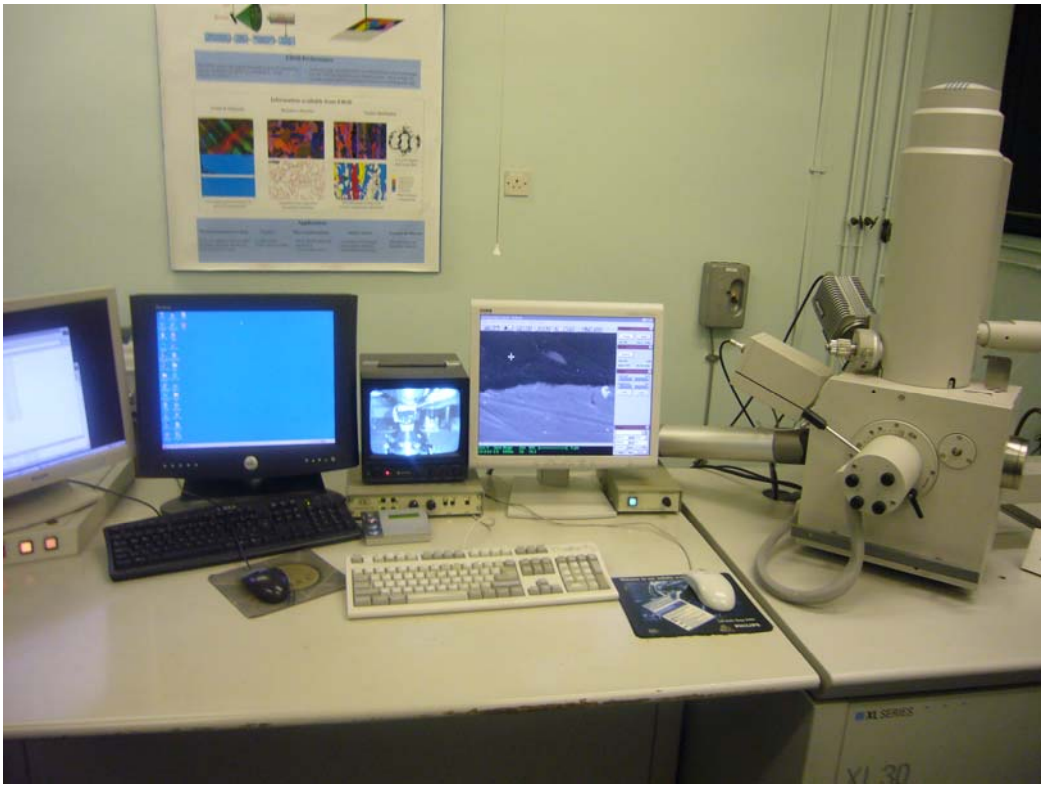

Figure 3.19. Photograph of FEI XL 30 FEGSEM.

Both an ESEM, and the more recently available variant of the ESEM known as a Variable Pressure SEM or VPSEM are able to eliminate the high vacuum requirements of the SEM by separating the vacuum environment in the specimen chamber from the high vacuum environment in the main column and electron gun region. In a typical ESEM (or VPSEM), two Pressure Limiting Apertures (PLAs) separate the specimen chamber from the electron gun column. All the regions are separately pumped, and this gives a graduated vacuum from 10 Torr in the specimen chamber, to 10^{-8} Torr in the column and 10^{-10} Torr in the electron gun emission chamber. By using an electrically cooled (Peltier) stage, water can be maintained in the liquid state within the specimen chamber. The presence of gas in the specimen chamber produces two important effects, these are induced intrinsic signal amplification, and charge neutralisation. Secondary electrons emitted by the sample accelerate within the detector field as imposed by the detector. They then collide with gas molecules. These collisions result in ionization of the gas, creating positive ions and also additional secondary electrons called environmental secondary electrons. The continuous repetition of this process results in a proportional cascade amplification of the original secondary electron signals that are strong enough to be detected. The positive ions are attracted to the sample surface as negative charge

accumulates from the beam on the (in the case of a non-conductor) insulated specimen surface. This is how the positive ions effectively suppress charging artifacts. The elimination of charging allows the imaging of non-conductive samples in their natural uncoated state, with a free choice of accelerating voltages. A very recent comprehensive discussion of the operating principles and capabilities of the ESEM has been given by Stokes [29].

Most new dedicated ESEM instruments image using a new type of secondary electron detector, known as a Gaseous secondary electron detector or GSED, whose main function is to collect secondary electrons for imaging, but eliminate the 'noise' forming electrons. Note that VPSEM instruments are a simpler variant of an ESEM, and sometimes use a modified BSE detector for low vacuum imaging. VPSEM instruments have the advantage of being 'dual purpose', and easily able to switch between low vacuum or high vacuum operation, but still with the capability of imaging uncoated non-conductors. A Zeiss EVO-55 VPSEM was used for some detailed preliminary studies in the initial stages (First Year) of this Project. Goldstein, *et. al*., [26] have given a detailed description of the available types of SEM instruments and their capabilities.

Depending on the type of instrument, SEM instruments are capable of providing images of sample surfaces at magnifications up to (realistically) around 250,000 X, and with an achievable resolution of around 1.0 nm. However, this would be under ideal operating conditions, using a high vacuum FEG instrument, and with an optimum sample type. It should be noted, that the term 'magnification' has little meaning, since it is possible to generate images with 'false' magnification, whereby the image of the sample is made larger, but with no additional increase in the amount of information contained therein. The term 'resolution' is now used to describe the main operating capability of any microscope, and is defined as the minimum distance between two separate features on the specimen, that any instrument is capable of defining/imaging, such that the image that is obtained shows the two features as being separate. The particular FEG-SEM (FEI XL30) mainly used in the latter part of this Study has a resolution of around 1.8 nm.

Two main SEM instruments were used then this research project, these were a Zeiss Evo 55 VPSEM, and a FEI (Phillips) XL-30 FEGSEM. As stated above, the Zeiss Evo 55 was used during the early part (the first year) of this Project, but the FEI XL 30 FEG-SEM

and associated RONTEC EDX system (see next Section) was utilised as the primary analytical facility for the remainder of the work reported here.

3.8.3. Energy Dispersive X-Ray Analysis (EDX).

One of the consequences of the bombardment of any material with a high energy electron beam is the production of X-rays, whose wavelength depends on the nature and characteristics of the elements that are present in the specimen. In basic terms, the X-rays arise when an inner shell electron of an atom within the sample surface region is sufficiently excited by the primary electron beam of the SEM, to leave the atom entirely or go into a higher un-occupied energy level. The space created by the excited electron is filled by another electron which drops from a higher energy level and emits an X-ray photon of energy equal to the energy lost by the electron falling between the two atomic shells. These X-rays are collected by a detector and separated on the basis of their energy. This is the principle of Energy Dispersive X-Ray Analysis (EDX) which is most often associated with Scanning Electron Microscopy. Note that some X-ray based analytical instruments are capable of separating X-rays on the basis of wavelength, and are hence known as Wavelength-Dispersive X-Ray Analysis or WDX systems. The EDX technique can be considered as the most versatile system for the analytical micro characterisation of materials. It has been applied in this Ph.D study both to give quantitative analyses of the elemental composition of deposited corrosion films, and also to obtain elemental maps of the distribution of selected elements within sections of such deposits, mainly iron, calcium, magnesium and oxygen.

All EDX systems can function in various different operating modes, depending on the type of analysis that is required. The first type of operating mode, is known as ‘spectrometer’ mode, whereby the instruments functions as a basic spectrometer, and provides a full spectra and quantitative data regarding ALL the elements that are present either over the whole area of the sample being scanned (and imaged) by the SEM electron beam, or within a pre-defined small area or spot. Note that the accelerating voltage of the SEM electron beam must be sufficiently high enough to be able to detect the elements that it is desired to detect. Usually, the accelerating voltage must be at least twice as high as the particular energy of the individual electron shell (i.e. K, L, *etc*) of the atom of the specific element being analysed. For example the ‘K’ shell peak for the element iron (Fe) is 6.4 keV, which would require a minimum accelerating voltage of

13.0 kV for effective detection. Note that for some heavier elements, it is impractical to use the 'K' energy shell peak for analysis, since the accelerating voltage required would be far too high, and therefore the EDX system performs the analysis using a peak from a lower energy shell (L or M). As an example, the KA (= Kα) peak for gold (Au) is 68.8 keV, which would require an accelerating voltage of around 140 kV for effective detection!, and therefore the 'L' shell peak at 9.7 keV (which requires an SEM accelerating voltage of 20 kV for effective detection) is used. However, it should also be noted, that since EDX analysis usually requires fairly high accelerating voltages to be employed, this creates a minimum 'interaction volume' at the sample surface; i.e. the specific region where beam/atom interactions occur that generate X-rays, as a result of beam penetration. This is usually a minimum of around 2 – 3 μm^3. Care must therefore be taken when using the 'spot' analysis facility at high magnifications:- even at a magnification of 25,000 X, the spot analysis area is actually about 25% of the area of the sample being examined.

The other main EDX operating mode is known as 'imaging mode' and involves two further operating functions:- these are 'mapping' mode and 'line scan' mode. In Mapping Mode, the EDX system shows the distribution of several selected elements as a series of coloured dot maps, either singly, or overlaid on the corresponding SE image. In line scan mode, a secondary electron image is first obtained, then a line is drawn on the image, and several elements are selected as required. The EDAX system then gives a graph with coloured plots corresponding to each selected element, of relative percentages of all the elements along the selected line. Once the analysis is completed, it is then possible to read off the precise relative percentages of all the elements along the line with an accuracy of 2 - 3 μm.

A full account of X-ray analysis in the SEM using EDAX has been given by Lyman, *et. al*., [30] and Goldstein, *et. al*., [26].

As discussed previously, a Zeiss EVO 55 VPSEM and a FEI XL 30 FEGSEM were used in this Project, both of which were fitted with integrated EDX analysis systems.

3.8.4. Sample preparation for SEM and EDX.

As mentioned previously (Section 3.8.2), when a sample is being examined in a high vacuum SEM, the surface of the sample receives electrons from the primary beam and looses electrons by either secondary emission or backscatter. Therefore, the specimen may have either a net loss or gain of electrons and will charge up positively or negatively. Any such charging effects are undesirable, and may cause image brightness, beam distortion and loss of resolution. Charging effects can be minimized or eliminated either by the use of an electrically conducting specimen that is able to maintain a constant zero potential by means of electron flow through the specimen stub and stage to earth, or by coating the sample with a conducting film such as carbon or gold which will prevent the build up of charge. A thorough account of sample preparation techniques for SEM has recently been given by Echlin [27].

Throughout this study, there were two main types of samples that were examined and analysed using SEM and EDX techniques: either the surface deposits on the flat face of a mild steel sample were examined in order to investigate the surface morphology and composition of the corrosion or film deposit, or alternatively; the sample was first sectioned in order to investigate the internal structure of the deposit, and also to determine any variation in the elemental composition of the coating through the Z-direction.

After the sample had been immersed in a test solution for a period of time, it was taken out, quickly immersed in deionised water for 5 seconds to remove the soluble seawater salts from the sample surface, and then rapidly rinsed in pure acetone for 5 seconds, before thoroughly drying in cold air for at least 5 minutes. If the surface of a flat sample was to be examined, then the flat samples were mounted onto a standard 20 mm diameter aluminum SEM pin stub either by using a double-sided adhesive carbon ‘tab’, or double sided adhesive copper tape. As stated previously, for imaging in the conventional (high vacuum) SEM, specimens must be electrically conductive, at least at the surface.

In the case of samples that were to be examined as cross-sections, the sample was then carefully and slowly cut in half using a dry hand saw and the two portions were placed into the middle of a polythene mould with a support. An epoxy resin mixture was then poured into the mould, to a sufficient depth to completely cover the sample. The samples

were then placed into an oven at 60^{o}C for 48 hours, to polymerise the resin. After polymerization and cooling, the surfaces of the cured resin blocks with the cross-sectioned samples were then polished using a series of successively finer grades of silicon carbide abrasive paper, ranging from 120 to 4000 grade. Firstly, 120 grade silicon carbide papers were used for the initial grinding, and then a series of progressively finer abrasive grades was employed down to 4000 grade for the final polishing. Care was taken to avoid any contamination by water or organic solvents at this stage.

Some samples were sputter coated with gold, if it was only desired to examine the surfaces and obtain good quality images of surface morphology. However, carbon coating was used for all samples that were analysed using EDX, since the gold coating would have given a significant 'false' peak, and would also completely prevent a true elemental map being obtained.

An SEM examination and subsequent analysis using EDX was performed for all samples at the end of the immersion experiments. Either whole samples (to examine surfaces) or resin-embedded sample cross-sections were mounted onto aluminium SEM specimen stubs using either adhesive carbon tabs or double-sided adhesive copper mounting tape, then samples were carbon coated using an Edwards Carbon coater. Samples were usually coated once, then turned 180 degrees and coated again to avoid shadowing and charging effects. However; it was noted, that some samples such as those with calcareous film deposits containing a thick layer of aragonite, required carbon coating three times (turning the sample through 120º after each coating) in order to minimize charging effects. A coating thickness reference chart was used to estimate that samples were coated with carbon to a thickness of approximately 5.0 to 8.0 nm. All SEM/EDX results presented in the following Chapters were obtained from prepared samples examined using a FEI XL 30 FEGSEM, with attached RONTEC EDX system running Quantax Esprit 1.8 analytical software.

In the Results Sections of the experimental Chapters that follow, the SEM photomicrographs of the samples are presented as secondary electron (SE) images, recorded digitally (as TIFF files), which give optimum image quality to show surface topography with good depth of field (in contrast to backscattered electron [BSE] images). The results of the EDX analysis are given either as results from the EDX system

operating in Spectra Mode (SM) or Imaging Mode (IM). Data from the Spectra Mode results are shown as a series of spectrum peaks, that identify all the elements within a sample, and these results are usually shown with the corresponding quantification data, usually as an Excel Table, which gives the relative percentages of all the elements present at the sample surface, expressed either as Wt% or At No%,

The analyses performed using the Imaging Mode of the EDX facility were carried out using the system operating in either Electron Mapping Mode or Line Scan Mode. The Electron Mapping Mode indicates the occurrence and distribution of selected elements over the sample surface; either singly, or in combination, and/or overlaid over the corresponding secondary electron image. The Line Scan Mode shows the quantitative variation in the relative percentages of several selected elements over a pre-determined line on the sample surface, and is a very sensitive quantitative technique.

EDX analysis was primarily used to determine the presence, relative percentages and distribution of the elements carbon, sodium, calcium, magnesium, chlorine, sulfur, oxygen, iron and phosphorus within the surface region of the deposited films, and also to test for the presence of zinc where appropriate.

To ensure that all results obtained could be directly comparable, the same SEM instrument operating parameters (accelerating voltage [20KV], spot size, working distance [WD] *etc*), were maintained for all imaging and EDX studies, for all samples. Note that due to occasional problems with the SEM to EDX system communication software, the real WD was sometimes not displayed in the EDX images.

In addition, to further maintain consistency in the SEM and EDX results, and to allow precise comparisons to be made between SEM micrographs obtained for different samples, secondary images were usually recorded for the same selected range of instrument magnifications, for each sample, throughout the study. These magnifications were mainly: 500 X, 1000 X, 2000 X and 5000X. These magnifications correspond to the scale bars given on the SEM images of 50.0 μm, 20.0 μm, 10.0 μm and 5.0 μm respectively. Note that for ease of explanation, the magnifications referred to throughout the following text and Figure legends refer to the instrument magnification setting only, and do not give the actual real magnifications of the images as presented in this Report.

As with the previously discussed SEM/EDX examination of sample surfaces, the sample sections were then examined and analysed using a FEI XL 30 FEGSEM, equipped with a RONTEC EDX system (see Section 3.8.3**.** for full description).

SEM Images of all samples together with EDAX analyses of corrosion deposits and films were recorded, and are presented in Chapters 4 and 5.

3.9. X-Ray Diffraction.

The technique of X-ray diffraction or XRD is now the most commonly employed analytical technique for the identification of crystalline substances. This technique has many major advantages over other methods of analysis such as EDX, which can only indicate which elements are present in a sample, since XRD is capable of precise identification of chemical compounds, and in addition, can provide other information such as the type of crystal structure present. For example, the compound calcium carbonate ($CaCO_3$), which is a major component of calcareous films, can exist in many forms, and with many crystal structures which all have quite different physical properties. The technique of XRD can give a huge amount of other information about a sample, besides just elemental composition, including determining the stress in crystalline materials for failure prediction, grain orientation (texture) data which can determine physical properties, crystallite size and lattice strain, and crystal structure determination.
The principles of X-ray diffraction are based on the theory of X-ray crystallography, which were first proposed by Max von Laue in 1912, and published in 1913 [31], as a result of experiments aimed at studying the interaction of X-rays with single crystals. Von Laue was awarded the Nobel prize for physics in 1914 as a result of this work. Note that this was only 17 years after the initial discovery of X-rays by Wilhelm Röntgen in 1895. Based on these early experiments, in 1919, Hull [32] presented a paper entitled "A New Method of Chemical Analysis", in which he described the fundamental concepts of modern X-ray diffraction, and was able to state: "….*every crystalline substance gives a pattern; the same substance always gives the same pattern; and in a mixture of substances each produces its pattern independently of the others*". The X-ray diffraction pattern of any individual substance is therefore like a precise fingerprint of that substance, and also, these precise fingerprints can be readily identified even in complex mixtures of compounds. XRD techniques are therefore ideally suited to the identification and

characterisation of 'unknown' powders. Furthermore, with suitable instruments, since the usual sample preparation technique for powder samples involves packing the sample into a holder to provide a flat surface, the technique is also directly applicable to the precise analysis of thin films and corrosion deposits. Note that about 95% of all solid matter is crystalline, so XRD techniques are almost universally applicable. The technique of powder/polycrystalline diffraction is now the most widely used analytical method for the identification of unknown powder samples, and such methods have been in common use for many decades. A comprehensive review of the history of the development of XRD techniques and associated instrumentation has been provided by Warren [33].

The operating principles of a modern XRD machine are still based on the fundamental experiments reported by von Laue [31] in 1913, and the first practical X-Ray diffraction apparatus was described by Davey [34] in 1921. When X-rays interact with any solid material, the resultant scattered beams can 'add together' in a few directions, and thereby reinforce each other to yield diffraction. Diffraction therefore occurs when the scattered waves are moving 'in phase' with each other. This phenomenon is termed 'constructive interference', and therefore the degree of regularity of the material is responsible for the diffraction of the beams, and the diffraction pattern generated by any substance is therefore absolutely characteristic of; and specific to that compound. The fact that the material must possess a regular periodic structure as a fundamental prerequisite in causing constructive interference, means that X-ray diffraction only occurs with, and can only be applied to, crystalline substances. A full discussion of the theory of X-ray diffraction is beyond the scope of this Section introduction, but a brief summary of the essential operating principles and theory will be given. There are several recent comprehensive reviews available in the literatures which give a full account of the theory and operating principles of X-ray diffraction techniques [33, 35]. In addition, several extensive reviews are available that discuss fully the specific applications of XRD techniques in the area of materials science, and also to the identification of deposit layers and powders [36, 37].

As stated above, XRD techniques are only applicable to crystalline materials. A crystal can be defined as comprised of a regular repeated array of identical lattice points which can be atoms, ions or molecules. The lattice is effectively infinite. The smallest unit of the crystal structure, which reflects the overall shape of the crystal, is called the unit cell.

There are only seven basic shapes of unit cell, and these form the seven essential crystal systems, which are: cubic, tetragonal, orthorhombic, hexagonal, monoclinic, rhombohedral (trigonal) and triclinic. Note that only these seven basic shapes can exist, since there are only seven ways in which atoms etc, can be packed together to form a space filling lattice. However, sometimes, extra lattice points occur, for example when there may be an atom in the centre of a face or in the centre of the unit cell. When these extra lattice points are combined with the seven crystal systems, this results in 14 possible Bravais lattices. All crystalline materials fall into one of these groups, although they can be of different sizes and can have different aspect ratios within the constraints of symmetry. The full symmetry of a crystal lattice is described by the space cell, which relates the symmetry of the unit cell to those around it. There are 230 space groups.

Since crystals consist of lots of unit cells packed together to form a regular array, it will be evident that there will be planes of atoms, called lattice planes that exist at the basic structural level. The spacing of these lattice planes are called *d*-planes, and these spacings are measured in Ångstroms (10^{-10} m). The process of X-ray diffraction actually measures these *d*-spacings, and from this information it is possible to determine the size and shape of the crystal, and in turn; the crystal structure is determined by the composition of the material. This information therefore allows a precise identification of the material, usually by comparing any diffraction pattern that is obtained for a particular substance with a library or data-base of known patterns. This aspect will be discussed later in this Section.

A coherent beam of monochromatic X-rays of known wavelength is required for XRD analysis. Striking a pure anode of a particular metal with high-energy electrons in a sealed vacuum tube generates X-rays that may be used for X-ray diffraction. The wavelengths of the X-rays produced are dependant on the anode material of the X-ray tube. Most X-ray tubes used for X-ray diffraction of inorganic materials use a copper anode, although a cobalt anode is used mainly for ferrous samples. The X-ray spectrum produced by any tube consists of two parts; these are the continuous radiation, which is unwanted, and the characteristic lines. It is the strongest characteristic line, the Kα, which is used for X-ray diffraction, and all other unwanted lines and radiation are usually removed using filters, or a device known as a monochromator. The Kα line for X-rays generated from a copper anode is 1.54Å.

X-Rays are normally characterised by their wavelength or their energy which can be connected by the following relation:

$$E = hc/f \quad \ldots\ldots\ldots\ldots\ldots\ldots\ldots\ldots\ldots\ldots\ldots\ldots\ldots\ldots\ldots\ldots\ldots\ldots\ldots\ldots\ldots\ldots \quad (3\text{-}34)$$

Where:
E = the energy;
H = the Planck's constant (6.62559* 10^{-27}erg sec);
c = the velocity of light (3 * 10^{10} cm/sec);
λ = the wavelength.

Following the above discussion and for ease of explanation; X-rays can be considered as a beam of particles called photons, and each photon has its particular energy which can be calculated according to the following relation:

$$E = h \times f \quad \ldots\ldots\ldots\ldots\ldots\ldots\ldots\ldots\ldots\ldots\ldots\ldots\ldots\ldots\ldots\ldots\ldots\ldots\ldots\ldots\ldots\ldots \quad (3\text{-}35)$$

Where: f = the frequency of the wave.

A main components of a typical X-ray diffraction instrument, commonly called a Diffractometer, are shown in Figure 3.20. The essential parts of a diffractometer consist of only five main parts, these are:
(1) the X-ray tube used to generate the X-ray beam;
(2) the 'primary optics' between the X-ray tube and the sample, which consists of a tube mainly containing a series of slits that regulates the area of the sample being irradiated;
(3) the sample holder;
(4) the 'secondary optics' between the sample and the detector, which consists primarily of a set of receiving slits that control resolution, together with a curved crystal monochromator, whose function has already been discussed;
(5) the detector.

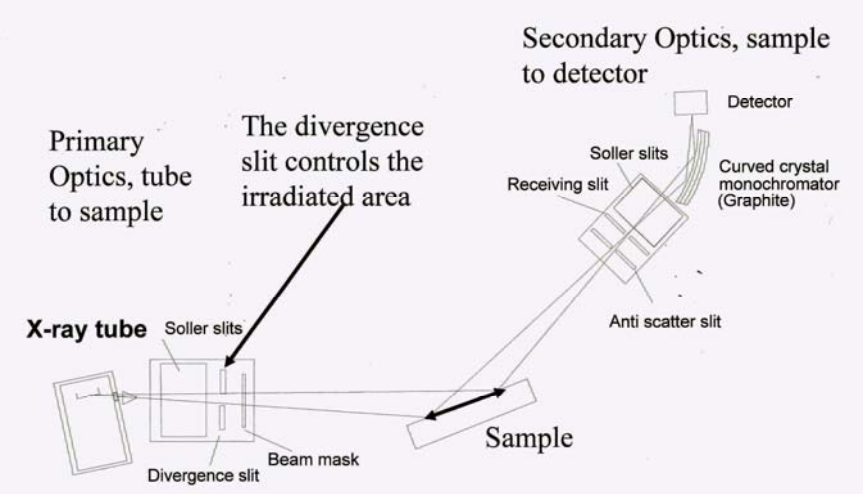

Figure 3.20 Diffractometer [34].

During operation, the sample is irradiated by the X-ray beam, and the detector is then moved through a specific angle: 2θ, known as the Bragg angle, whilst continuously collecting the X-ray diffraction pattern.

The Bragg angle is given by Bragg's Law, which describes the angle at which a beam of X-rays of a particular wavelength diffracts from a crystalline surface. Bragg's Law is as follows:

$$\lambda = 2d \sin\theta \quad \text{(3-36)}$$

Where:
θ = Bragg angle;
λ = is the incident wavelength;
d = is the spacing between different planes, as atoms in any crystal materials are arranged in a specific way to form various planes and the spacing between such planes can be used to calculate the wavelength.

This relationship is illustrated diagrammatically in Figure 3.21.

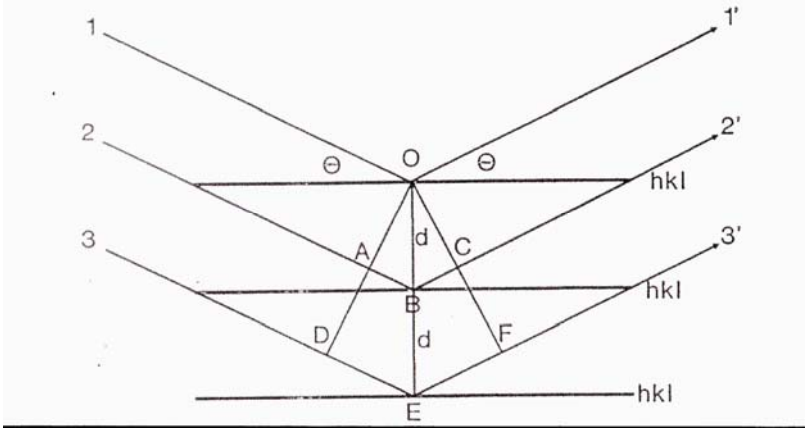

Figure 3.21. Diagram illustrating Bragg's Law [34].

Based on Bragg's law (Equation 3-36), we can measure the Bragg angle (2θ). This is the position of the Bragg reflection, or peak. Then, since we know the wavelength (λ), of the X-rays, we can then calculate the *d*-spacing (the distance between different planes in the crystal) from Bragg's Law (Equation 3-36). The *d*-spacing is characteristic of the compound under investigation and the calculated values of the *d*-spacing can be matched against a data bank that is stored digitally in the hard-drive of the XRD machine (currently approximately 120,000 compounds – this will be discussed later). The diffraction results are in the form of a unique series of reflections, which form the diffraction pattern. Consequently, the exact composition of any compounds can be identified.

A typical X-ray diffraction pattern is in the form of a graph, with a series of peaks (the actual diffraction pattern), with the horizontal axis being 2θ, or twice the Bragg angle; and the vertical axis is the intensity, or the X-ray count measured by the detector, which is a function of the crystal structure and the orientation of the crystallites. Note that in reality, although the diffraction pattern is given as a 2-dimentional graph, the radiation diffracted by any sample is in the form of cones, known as Debye Cones.

Note that only one of the XRD machines in the Materials Science Centre is suitable for performing X-ray diffraction on thin layers, which was obviously applicable to our samples. This machine is referred to as the 'big XRD', and is a Phillips XPERT Pro-MRD X-Ray Diffraction System. Also, it should be noted that a special technique must be used to analyse a thin layer. The angle of incidence of the incoming X-radiation must

be fixed at a low angle, typically around 3º, sometimes referred to as ω, so that it skims through the top layer and does not penetrate into the substrate. Also, different X-ray optics must be used, the sample must also be flat, and quite large (ideally > 5.0 mm across). Once obtained and stored, diffraction patterns are compared with known patterns held in a database known as the Powder Diffraction Data Base (PDF), this currently holds over 120,000 entries, gathered over the last 50 years!.

Figure 3.22. Philips 'Big XRD' = Phillips XPERT Pro-MRD X-Ray Diffraction System.

3.10. Atomic Force Microscopy (AFM).

3.10.1. Introduction.

The Atomic Force Microscope (AFM) belongs to a class of instruments known collectively as Scanning Probe Microscopes or SPM. Scanning Probe Microscopy has been defined as "Microscopy using scanning mechanical tips utilising a variety of physical near-field interactions, with an emphasis on the study of materials at a scale or resolution better than achievable by other techniques" [38]. The main variants of SPM such as Scanning Tunneling Microscopy (STM) and AFM are dependant on the mode of interaction of the scanning tip with the surface being scanned. In STM, the interaction is electrical, whilst in AFM the interaction is force.

The invention and early development of the scanning probe microscope and its variants can really be directly attributed to only one researcher and his co-workers: Binnig and Rohrer [39] invented the Scanning Tunneling Microscope (STM) in 1982, and this then led to the development of the Atomic Force Microscope (AFM) by Binnig, *et. al*., in 1986 [40]. Binnig and Rohrer were awarded the Noble prize for physics in 1986.

A STM is capable of imaging atoms or sets of atoms, and current instruments are also capable of performing precise manipulations of atoms and molecules.

After the invention of the STM, the next major development in the area of SPM, was the invention of the Atomic Force Microscope (AFM) by Binnig *et al*., in 1986 [40]. However, the concept of a functional instrument was really developed by Meyer and Amer [41]. The AFM operates on the very simple principle of 'stylus profilometry', in which a stylus or sharp probe is 'dragged' over the surface of a sample, then the height deflection at each point is measured and used to build up a 'line profile' of the surface. By scanning over the whole sample surface in a series of lines, a three-dimensional map of the surface topography of the specimen can be generated, although with fairly low resolution. In a way, Meyer and Amer [41] were ahead of their time in several ways, since they combined the basic concept of the AFM produced by Binnig, *et. al*., [39], which simply used a microscale version of a stylus profilometer, but then Meyer and Amer [41] added a laser beam as the sensing device to accurately record the deflection in height at each point in the scan. In this way, a 3-D map of the surface topography of the specimen is generated,

with sub-atomic resolution. This operating principle is now in common use in all AFM instruments which have been produced since the first commercial AFM (the Nanoscope II, made by Digital Instruments – now Veeco Instruments Inc [42]) became available in 1991/2. The AFM has a huge advantage over the STM in that the interaction between the scanning tip or probe is force, and not electrical, and the AFM is therefore capable of imaging the surfaces of non-conductors with sub-nanometre resolution. Note that AFM images are in the form of 3-dimensionl maps of surface topography comprised of digital sets of X, Y and Z data points, and are fully quantitative.

The basic elements of an AFM as devised conceptually by Meyer and Amer [41] are shown in Figure 3.23.

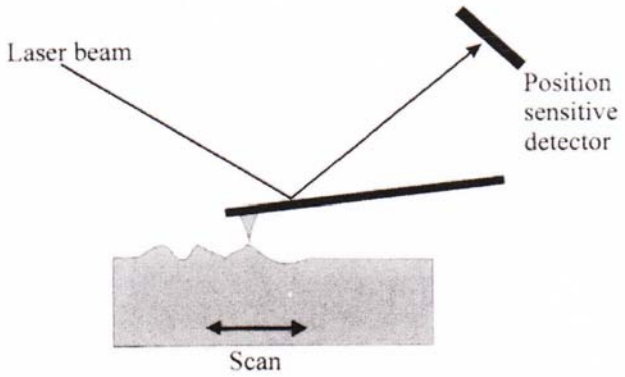

Figure 3.23. Essential component of an AFM [41].

A sharp tip made of silicon nitride mounted on a spring 'beam' or cantilever is scanned over the surface of the sample, and the vertical deflections are measured by a laser beam reflected off the back surface of the tip and onto a position sensitive detector (thereby determining the Z-or height variations at each point in the scan). This design is essentially the same as the first commercial instrument, called the Nanoscope II produced around 1991, by the Digital Instruments Company, based in California, U.S.A.

The results obtained from early studies using the Nanoscope II showed immediately that this technique had huge potential for ultrastructural investigations of surface morphology of virtually any material, and in almost any gaseous atmosphere or liquid, with virtually no sample preparation required. One of the main disadvantages of the Nanoscope II, was the difficulty in identifying the position of the area being scanned on the specimen

surface, and this led to the development of the Nanoscope III, which was the instrument used in this study.

The Nanoscope III AFM also has the capability of functioning in various sophisticated operating modes such as 'Tapping Mode' *etc*, and addition of other facilities such as 'Phase Extender Module' *etc*. This new operating modes enable the AFM to image beyond beyond simple topographical mapping to detect (and image as contrast changes) variations in composition, adhesion, friction, viscoelasticity, micromechanical variations and other properties. The Nanoscope III, in common with all modern AFM instruments, is capable of imaging sample areas (X – Y plan direction) up to 125 X 125 μm, and around 6.0 μm in the Z (height) direction, with sub-nanometre resolution. Figure 3.24 illustrates diagrammatically the main components of a Nanoscope III AFM facility [42].

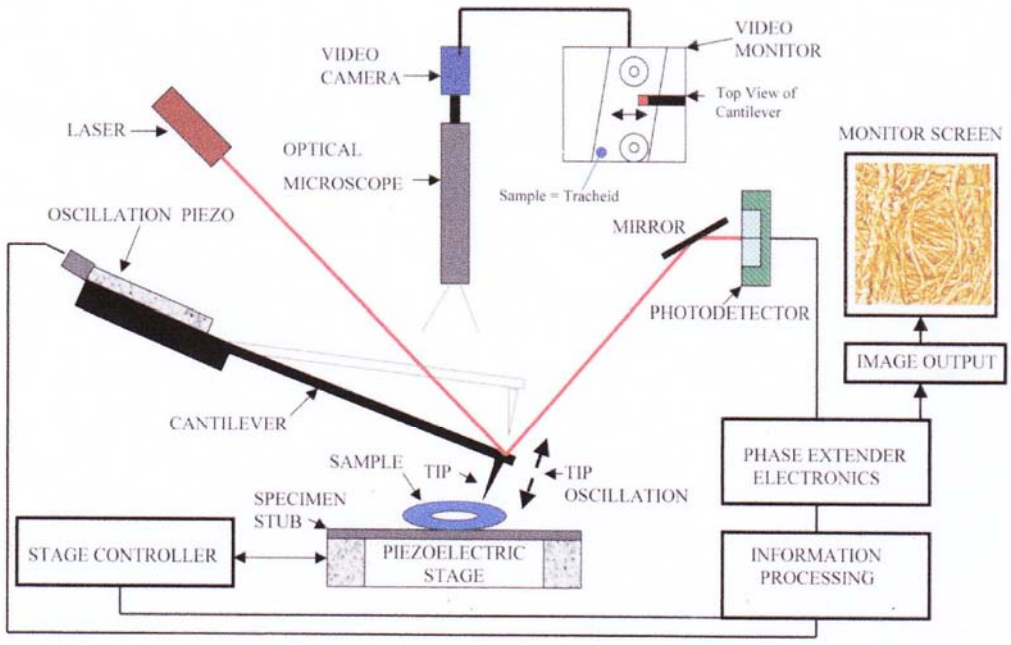

Figure 3.24. Schematic of Digital Instruments Nanoscope III AFM [42].

More recent developments of AFM imaging have been the capability to measure relative stiffness of surface features, frictional forces, temperature differences, magnetic force gradients and distributions and variation in capacitance [42]. Specialized 'fluid cells' are also available to allow AFM imaging in any liquid, or to scan and image specimens whilst chemical reactions are in progress.

3.10.2. AFM examination of polished samples.

A Nanoscope III AFM with 'J' scanner was used in this Study to obtain AFM images of mild steel test specimens prior to experiments, in order to investigate the roughness (in the Z-direction) of the sample surfaces after preparation of the sample surfaces by grinding using a series of progressively finer abrasive grades of silicon carbide abrasive papers, followed by final polishing using alumina powder. These micrographs are presented in Figures 3.25 and 3.26, and illustrate the effectiveness of the sample preparation procedures employed in this Project.

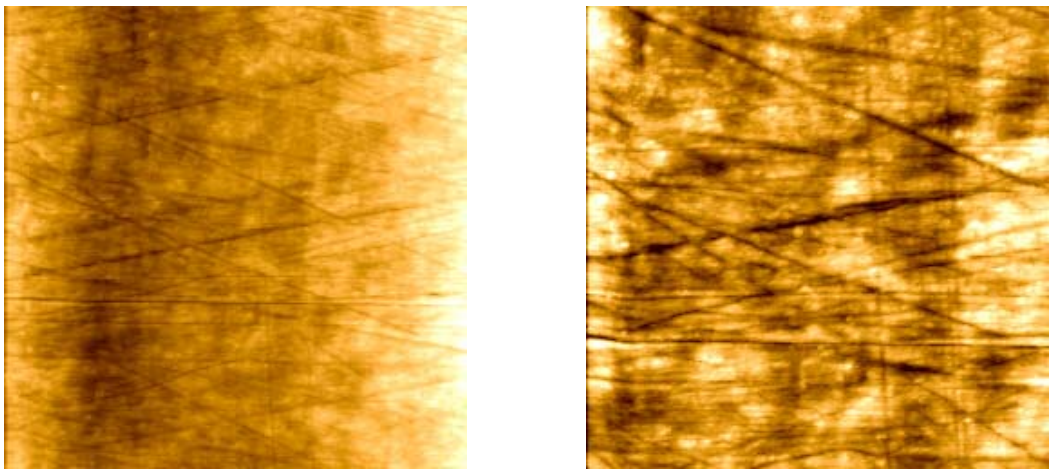

(a) (b)

Figure 3.25. AFM images of sample surfaces polished without alumina: (a) 20µm (b) 10µm scan area.

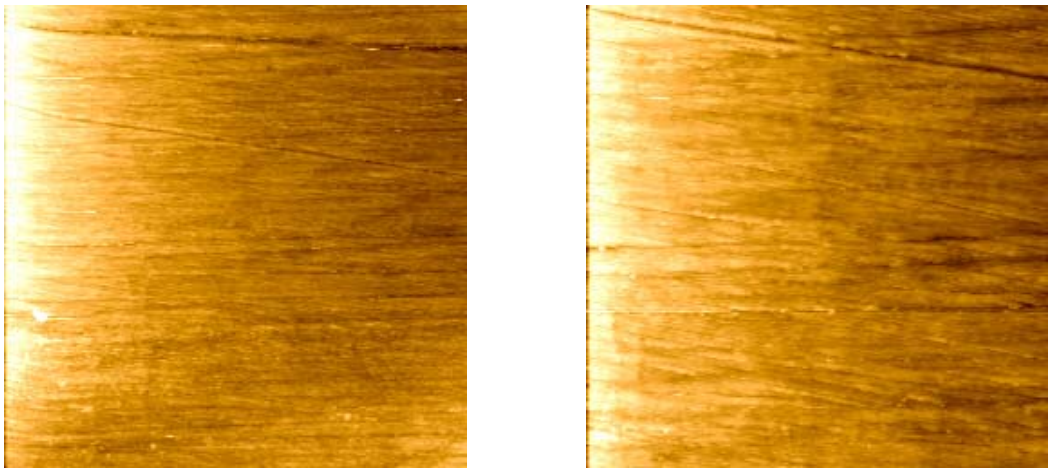

(a) (b)

Figure 3.26. AFM images of sample surfaces polished with alumina: (a) 20µm (b) 10µm scan area.

3.11 Glow-Discharge Optical-emission Spectroscopy (GDOES).

The technique of Glow-Discharge Optical Emission Spectroscopy (GDOES) is an extremely useful method for the surface analysis of thin films. It is one of the few techniques that are capable of providing a depth profile analysis of the quantitative composition of a deposit layer on a metal substrate.

The analytical technique of SEM in conjunction with EDX has already been used in this Study (Section 3.8) to analyse the composition of a corrosion deposit layer in cross-sections, but this method, although very effective; involves a time consuming procedure requiring several successive processes of resin embedding, cutting and surface polishing, before mounting the samples for examination in the SEM/EDX facility.

Although other techniques of analysing thin films by means of determining composition during depth profiling are available, these techniques; such as Auger Electron Spectroscopy (AES) and X-Ray Photoelectron Spectroscopy (XPS) combined with ion-sputtering, are only applicable to analysing thin film deposits of less than 1.0 μm in thickness.

The technique of GDOES has been developed as a method of optical emission spectrometry, combined with glow discharge. It is highly suited to the quantitative compositional analysis of depth profiles of deposited surface layers on metals. Suzuki, *et. al*., [43] and references cited therein, have fully described this technique, and discussed the application of the method for the quantitative analysis of oxide films on steel. The main advantages of GDOES over other techniques, include a high sputtering rate of typically 10 – 100 nm s^{-1}; analysis of the mean concentration within diameters of several millimetres, and simultaneous analysis of a number of elements. In addition, the sensitivity of GDOES is relatively high when compared to other surface analysis methods such as Auger Electron Spectroscopy (AES) [43]. A typical GDOES apparatus usually consists of several integrated instruments, including a Grimm glow lamp and a multi-channel spectrometer, which provides in-depth quantitative composition analysis of the surface film being analysed, by means of argon ion sputtering. The analysis signal being collected and evaluated by the spectrometer is therefore a function of the sputtering time, assuming the sputtering conditions (and hence rate) are both constant and known.

Suzuki, *et. al*., [43] were able to demonstrate that GDOES is suitable for performing both quantitative compositional analysis and determining the depth of thin film deposits on steel from 10 nm to 100 μm in thickness.

According to Wikipedia [44] "The simplest type of glow discharge is a direct-current glow discharge. In its simplest form, it consists of two electrodes in a cell held at low pressure (0.1–10 torr). The cell is typically filled with argon, but other gases can also be used. An electric potential of several hundred volts is applied between the two electrodes. A small fraction of the population of atoms within the cell is initially ionized through random processes (thermal collisions between atoms or with alpha particles, for example). The ions (which are positively charged) are driven towards the cathode by the electric potential, and the electrons are driven towards the anode by the same potential. The initial population of ions and electrons collides with other atoms, ionizing them. As long as the potential is maintained, a population of ions and electrons remains. Some of the kinetic energy of the ions is transferred to the cathode. This happens partially through the ions striking the cathode directly. The primary mechanism, however, is less direct. Ions strike the more numerous neutral gas atoms, transferring a portion of their energy to them. These neutral atoms then strike the cathode. Whichever species (ions or atoms) strike the cathode; collisions within the cathode redistribute this energy until a portion of the cathode is ejected, typically in the form of free atoms. This process is known as sputtering. Once free of the cathode, atoms move into the bulk of the glow discharge through drift and due to the energy they gained from sputtering. The atoms can then be collisionally excited. These collisions may be with ions, electrons, or other atoms that have been previously excited by collisions with ions, electrons, or atoms. Once excited, atoms will lose their energy fairly quickly. Of the various ways that this energy can be lost, the most important is radiatively, meaning that a photon is released to carry the energy away. In Optical Atomic Spectroscopy, the wavelength of this photon can be used to determine the identity of the atom (that is, which chemical element it is) and the number of photons is directly proportional to the concentration of that element in the sample. Some collisions (those of high enough energy) will cause ionization. In Atomic Mass Spectrometry, these ions are detected. Their mass identifies the type of atoms and their quantity reveals the amount of that element in the sample."

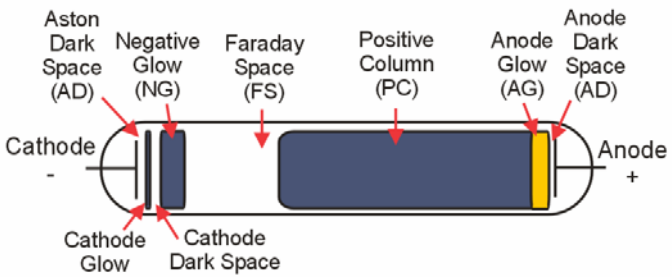

Figure 3.27 The working principle of GDOES [44]

Figure 3.27 An electric glow discharge tube featuring its most important characteristics: (a) An anode and cathode at each end (b) Aston dark space (c) Cathode glow (d) Cathode dark space (also called Crookes dark space, or Hittorf dark space) (e) Negative glow (f) Faraday space (g) Positive column (h) Anode glow (i) Anode dark space.

In the same article under Uses in Analytical Chemistry, they state:

"Glow discharges can be used to analyze the elemental, and sometimes molecular, composition of solids, liquids, and gases, but elemental analysis of solids is by far the most common. In this arrangement, the sample is used as the cathode. As mentioned earlier, gas ions and atoms striking the sample surface and knock atoms off of it (a process known as sputtering). The sputtered atoms, now in the gas phase, can be detected by atomic absorption, but this is a comparatively rare strategy. Instead, atomic emission and mass spectrometry are usually used. Collisions between the gas-phase sample atoms and the plasma gas pass energy to the sample atoms. This energy can excite the atoms, after which they can lose their energy through atomic emission. By observing the wavelength of the emitted light, the atom's identity can be determined. By observing the intensity of the emission, the concentration of atoms of that type can be determined. Energy gained through collisions can also ionize the sample atoms. The ions can then be detected by mass spectrometry. In this case, it is the mass of the ions that identifies the element and the number of ions that reflects the concentration.

Both bulk and depth analysis of solids may be performed with glow discharge. Bulk analysis assumes that the sample is fairly homogeneous and averages the emission or mass spectrometric signal over time. Depth analysis relies on the fact that the depth increases as time goes by. Tracking the signal in time, therefore, is the same as tracking the elemental composition in depth. Depth analysis requires greater control over

operational parameters. For example, conditions (current, potential, pressure) need to be adjusted so that the crater produced by sputtering is flat bottomed (that is, so that the depth analyzed over the crater area is uniform). In bulk measurement, a rough or rounded crater bottom would not adversely impact analysis. Under the best conditions, depth resolution in the single nanometer range has been achieved (in fact, within-molecule resolution has been demonstrated)" [44].

In our investigation, we used a GD PROFILER 2 GDOES machine (Manufactured by Horiba Jobin yvon) operating at 700Pa to 35W. Depth analysis was performed using a Quanfum XP.

3.12. References.

1. J. D. Scantlebury, S. B. Lyon, J .B. Johnson and G. E. Thompson. "Realism in cyclic cabinet corrosion tests - The use of artificial acid rain solution and objective materials assessment". Proc., ASTM Symposium: "Cyclic cabinet corrosion testing". pp1-14. Fort Worth. Texas. November 1993.

2. R. A. Cottis. "Electrochemical methods for the study of corrosion". In: Corrosion, 4th Edition. (ed). L. L. Shreir. Elsevier, London, 2010.

3. R. A. Humble. "Cathodic Protection of Steel in Sea Water with Magnesium Anodes". Corrosion. 74. pp358-370, 1948.

4. R. A. Cottis. M.Sc Lecture Notes. Corrosion and Protection Centre. University of Manchester. 2009.

5. T. P. Hoar and G. C. Wood. "The sealing of porous anodic oxide films on aluminium". Electrochimica Acta. **7**. pp333-353. 1962.

6. W. J. Lorenz and F. Mansfeld. "Techniques for characterization of electrodes and electrochemical processes" in Proceedings 5th International Congress on Metallic Corrosion. **3.** p2081.1981.

7. C. Gabrielli. "Identification of Electrochemical Processes by Frequency Response Analysis". Technical Report No.004/83. Solartron. Pl. August.1984.

8. D. C. Silverman and J. E. Carrio. Corrosion. **44**, (5). p280. 1987.

9. I. Costa. The effect of minor addition elements on the corrosion resistance of coated and uncoated mild steel, PhD Thesis. UMIST. p51.1991.

10. http://en.wikipedia.org/wiki/Kramers%E2%80%93Kronig_relation. 9/07/2010

11. W. Lederman. Complex Numbers. Routledge and Kegan. London, U.K. 1962.

12. K. Hladky, L. M. Callow and J. L. Dawson. "Corrosion rate from impedance measurements, an introduction". Brit., Corrosion J. **15,** (1): pp 20-25. 1980.

13. E. Barsoukov and J. R. Macdonald, (eds). Impedance Spectroscopy, theory, experiment and application, 2nd ed. John Wiley & Sons Publication. 2005.

14. http://www.consultrsr.com/resources/eis/cpe1.htm. 9/07/2010

15. R. A. Cottis and S. Turgoose. "Elecrochemical Impedance and Noise". In: Corrosion Testing Made Easy, (ed). B. C. Syrett. NACE Publication: Houston. Texas. USA. 1999.

16. F. Mansfeld.. "Use of electrochemical impedance spectroscopy for the study of corrosion protection by polymer coatings" Corrosion**. 44, (**8). p558. August 1988.

17. R. A. Cottis. "Corrosion Monitoring – What's the Point". In: Corrosion Monitoring in Nuclear Systems, (ed). S. Ritter. European Federation of Corrosion, 2008.

18. G. W. Walter. "A review of impedance plot methods used for corrosion performance analysis of painted metals". Corrosion Science. **26,** (9): pp. 681-703. 1986.

19. J. M. Mclntyre and H. Q. Pham. "Electrochemical Impedance spectroscopy, a tool for organic coating optimization". Progress in Organic Coatings. pp 201-207. 1996.

20. B. J. Hepburn, K. R Gowers and J. D. Scantlebury, The interpretation of low frequency AC impedance data for organic coatings on mild steel". Brit. Corr. J. **21**, (2). p105. 1986.

21. C. P. Woodcock, D. J. Mills and H.T. Singh. "Use of electrochemical noise method to investigate the anti-corrosion properties of a set of compliant coatings". Prog. Organic Coatings, **52**(4), 257-262, 2005.

22. N. G. Thompson. Corrosion. **44**, (8). p581. 1988.

23. N. G. Thompson, G. T. Ruck, K. J. Walcott, and G. H. Koch, "The detection of the presence or absence of corrosion of cathodically protected structures". The Annual Report on the Proceedings of the 1986 International Gas Research Conference, Toronto, p108. 1986.

24. C. Deslouis, D. Festy, and O. Gil. "Characterization of calcareous deposits in artificial seawater by impedance techniques-I. Deposit of $CaCO_3$ in the absence of $Mg(OH)_2$" . Electrochimica Acta. **43**, (12-13). pp1891-1901. 1998.

25. Ch. Barchiche, C. Deslouis, D. Festy, O. Gil , Ph. Refait , S. Touzain and B. Tribollet. "Characterization of calcareous deposits in artificial seawater by impedance techniques - II. Deposit of $CaCO_3$ in the presence of Mg(II)". Electrochimica Acta. **48**, pp1645- 1654. 2003.

26. J. Goldstein, D. E. Newbury, D. C. Joy, C. E. Lyman, P. Echlin, E. Lifshin, L. C. Sawyer, and J. R. Michael. 'Scanning Electron Microscopy and X-Ray Microanalysis. Springer. 2002.

27. P. Echlin. 'Handbook of Sample Preparation for Scanning Electron Microscopy and X-Ray Microanalysis'. Springer. 2009.

28. G. D. Danilatos. "Foundations of Environmental Scanning Electron Microscopy". In: P.W. Hawkes (Ed.). Advances in electronics and electron physics. Academic Press Inc., 71. p2. 1990.

29. D. J. Stokes. "Principles and Practice of Variable Pressure/Environmental Scanning Electron Microscopy" (VP-ESEM). John Wiley and Son Ltd. p221. 2008.

30. E. Lyman, D. E. Newbury, J. I. Goldstein, D. B. Williams, A. D. Romig, Jnr., J. T. Armstrong, P. Echlin, C. E. Fiori, D. C. Joy, E. Lifshin and K-R. Peters. "Scanning Electron Microscopy, X-Ray Microanalysis, and Analytical Electron Microscopy – A Laboratory Workbook". Plenum Press. 1990.

31. M. von Laue. "Röntgenstrahlinteferenzen". Physikalische Zeitschrift. 14 (22/23). p1075. 1913.

32. A. W. Hull. "A New Method of Chemical Analysis". J. Am. Chem. Soc. 41. p1168. 1919.

33. B. E. Warren. "X-Ray Diffraction" (2nd Edition). Dover Publication. U.S.A. pp381. 1990.

34. W. P. Davey. "A New X-Ray Diffraction Apparatus". J. Op. Soc. Am. 5. pp. 479-492. 1921.

35. F. H. Chung and D. K. Smith. "Industrial Applications of X-Ray Diffraction". Marcel Dekker Pub. pp 1006. 1999.

36. V. K. Pecharsky and P. Y. Zavalij. "Fundamentals of Powder Diffraction and Structural Characterisation of Materials". Springer Verlag. pp. 713. 2005.

37. C. Suryanarayana and M. G. Norton. "X-Ray Diffraction: A Practical Approach". Plenham Press. New York. pp273. 1998.

38. Anon. U.K. Science and Engineering Council (SERC). Report of First Initiative on Development of Scanning Probe Microscopy Techniques. Publ., SERC. Pp103. 1993.

39. G. Binning and H. Rohrer. "Scanning Tunneling Microscopy". IBM Journal of Research and Development. **30**. p4. 1982.

40. G. Binnig, C. F. Quate and Ch. Gerber. "Atomic Force Microscope". Phys. Rev. Lett., **56** (9). pp 930 – 933. 1986.

41. M. Meyer and N. M. Amer. "Optical-beam-deflection atomic-force-microscopy: the NaCl (001) surface". App. Phys. Lett., **56** (21). pp2100-2101. 1990.

42. Veeco Instruments Inc. http://www.veeco.com/ 29/07/2010.

43. S. Suzuki, K. Suzuki and K. Mizumo. "Quantitative GDOES Analysis of Oxide Films on Steel". Surface and Interface Analysis. 22 (1-12). pp134-138. 1994.

44. http://en.wikipedia.org/wiki/Glow_discharge. 29/07/2010.

Chapter 4. Cathodic Protection of Mild Steel in Artificial Seawater and the Role of the Calcareous Film.

4.1. Introduction.

4.1.1. General Background.

As we have already mentioned in Chapter 2 the scientific principles of cathodic protection were first explained by Davy in his three classic papers published in 1824 and 1825 [1], [2], [3]. A copy of the crucial paragraph in his first paper is given below.

in an elementary work on chemistry, published in 1812. Upon this view, which has been adopted by M. BERZELIUS and some other philosophers, I have shown that chemical attractions may be exalted, modified, or destroyed, by changes in the electrical states of bodies; that substances will only combine when they are in different electrical states; and that, by bringing a body naturally positive artificially into a negative state, its usual powers of combination are altogether destroyed; and it was by an application of this principle that, in 1807, I separated the bases of the alkalies from the oxygene with which they are combined, and preserved them for

MDCCCXXIV. X

He also observed and made an intelligent guess at the nature of the calcareous films which form during cathodic protection.

I had anticipated the deposition of alkaline substances in certain cases upon the negatively electrical copper. This has actually happened. Some sheets of copper, that have

244 *Sir* HUMPHRY DAVY'S *additional experiments*

been exposed nearly four months to the action of sea water, defended by from $\frac{1}{35}$ to $\frac{1}{80}$ of their surface of zinc and iron, have become coated with a white matter, which, on analysis, has proved to be principally carbonated lime, and carbonate and hydrate of magnesia. The same thing has occurred with two harbour boats, one of which was defended by a band of zinc, the other by a band of iron, equal to about $\frac{1}{35}$ of the surface of the copper.

The next real breakthrough in the understanding of cathodic protection was in 1938 with the simultaneous and independent publications by Hoar [4], and Mears and Brown [5]. Their arguments were based on the Evans Diagram which had recently been proposed and indeed Hoar was working in Evans' laboratory at the time.

In 1960, U.R. Evans himself explained the general principle of cathodic protection referring to both the Hoar and the Mears and Brown publications [6]. Evans made the following statement:

*"**General Principles**: Consider a piece of metal immersed in a corrosive liquid of sufficient conductivity to allow the intersection point B to be used as an indication of the corrosion-velocity (Figure 4.1). Now apply a current from an external anode. Clearly the sum of current from the external anode and the "corrosion-current" due to local anodes still operating on the surface must exactly balance the cathodic current. Thus if the external current is represented by the length DE, the corrosion-current will be CD, and the potential will be represented by C. If we depress the potential to F, the corrosion-current becomes zero, and the specimen is completely protected. Thus to attain cathodic protection, the **potential of the whole must be brought down to the open-circuit potential of most active anodic point**; this principle, expressed in two different ways, was published in the same year by T. P. Hoar, and by R. B. Mears and R. H. Brown, who arrived at it independently.*

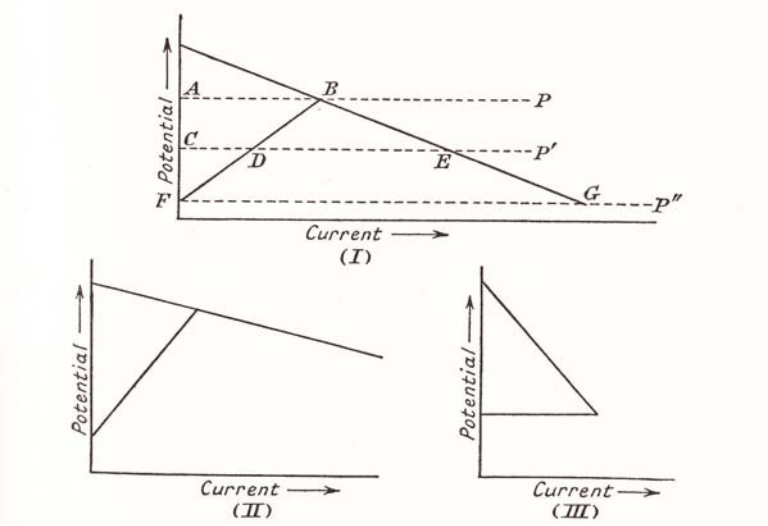

Figure 4.1. Graphical representation of cathodic protection (schematic) [6].

Hoar has pointed out that the amount of current needed to bring down the potential to the required level depends on the conditions, and particularly on the oxygen-supply; if the rate of oxygen-replenishment at the cathodic area is high, the current needed for protection becomes considerable. The argument just developed involves several assumptions, namely that the specific conductivity in the corroding liquid is so high that the potential is defined by the intersection of two polarization curves, and that the protecting current is applied in such a way that all parts of the specimen have equal chances of benefitting from it"

According to Figure 4.1, this approach clearly expressed by Evans shows how the anodic rates and cathodic rates change as the structure potential moves in a negative direction and how the net current density applied by the CP system is the difference between the local cathode and anode currents (Figures 4.1(II) and (III)).

In this Chapter we will be looking at the situations that occur during conditions of underprotection, full protection and overprotection. The state of underprotection exists between the open circuit potential, point A in Figure 4.1(I) and point F in the same figure. and the protection potential. Within this zone, which is termed the region of underprotection, the full protection potential has not been fully attained, and insufficient current is being supplied to achieve effective protection. Some corrosion of the partially protected steel will therefore take place. Conversely, a region of overprotection exists where the potential lies significantly beyond the protection potential. In this state, the current that is being applied is more than sufficient to attain full protection, and the surface might be covered with a protective calcareous film.

4.1.2. Rationale for Carrying Out the Cathodic Protection Experimental Programme.

There are several reasons for undertaking this study and this is an appropriate place to explain and justify them.

4.1.2.1. Nature of the corrosion process.

There is a school of thought based mainly in the US and centered on Uhlig's book [7]. It regards the aqueous corrosion process as consisting of local and clearly defined anodic and cathodic areas, and it is illustrated schematically in Figure 4.2.

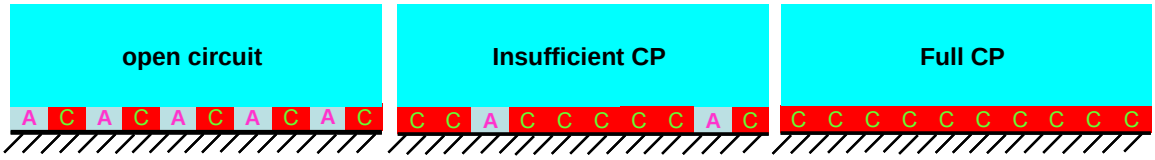

Figure 4.2. Schematic of Uhlig's model of different levels of cathodic protection [7].

According to Uhlig's model, during cathodic protection, anodic areas are one-by-one converted into cathodic areas. At the protection potential, all the anodic areas have disappeared. However, at an underprotected potential, some anodic areas exist and are still locally corroding at the same rate. This would lead to a corrosion model where obviously protected cathodic areas exist and there would be anodic areas corroding at the same rate as at open circuit. So during underprotection one would expect well defined uncorroded and corroded areas on the same panel, giving rise to a form of pitting corrosion. The visual appearance of an under protected specimen should show these pits clearly if the above mechanism holds true.

4.1.2.2. Nature of the film produced.

The film produced on partially protected steel in seawater has never been investigated and furthermore it is unclear whether such a film is uniform across the steel. Indeed one might expect the film to differ depending on whether it was growing on a prior anodic or cathodic site. We will return to this idea later. Also, if the applied current density is very high, and the potential is far beyond the protection potential, this might also affect the film. Other aspects of the film growth include time and current density, both of which will also be studied.

4.1.2.3. Polarisation behaviour.

In his introductory section of the text on cathodic protection which he also co-edited, Ashworth [8] generated two schematic curves. In Chapter 2, Figure 2.16 is copied from his book and is also reproduced later as Figure 4.9(a) in Section 4.2.3. He plots potential versus the logarithm of the corrosion rate and potential versus the logarithm of the current density. It is probable that Ashworth assumed the logarithmic nature of current density because he expected Tafel behaviour. He then made the following assumption with the oft repeated but never proven statement that "the first increment of potential fall is more effective in preventing dissolution than the next increment" [8]. To our knowledge this statement has never been verified experimentally which we will attempt to do.

4.1.2.4. The accurate protection potential for mild steel in seawater.

We have already seen in Chapter 2 that most texts on corrosion science and corrosion engineering assume the protection potential for mild steel in a variety of neutral environments (save those involving sulphate reducing bacteria) to be -850 mV (Cu/Sat $CuSO_4$), or -774 mV (SCE). The original publication [9] where this value was proposed states that this value "is probably in the neighbourhood of -850 V". A more recent publication by Gummow [10], considers in great detail these protection criteria. The protection potential of -850 mV CSE, is -532 NHE which on the Pourbaix diagram corresponds to the E^0 for the Fe/Fe^{++} system with a ferrous ion concentration of 10^{-2} gram ions/L (Figure 2.3). Clearly, in seawater the ferrous ion concentration is much lower and therefore the thermodynamic protection potential is theoretically significantly lower. Occasionally in some more scholarly texts [11], the lack of thermodynamic justification for this figure is stated but nowhere to our knowledge has an experimentally justified value of the protection potential been produced.

4.1.2.5. Overprotection and film detachment.

At high current densities, there is always the risk of film detachment due to hydrogen evolution. We will be looking at this process in greater detail in this Chapter.

4.1.2.6. Current density changes.

There is some indication from the literature [12], [13], [14], that a high initial current density followed by a reduction in current is more successful than a relatively low constant current density. We will carry out some initial experiments in this area to assess this claim.

4.1.3. The nature of our investigation.

It was decided to tackle the issues raised above and attempt to clarify the situation. Our main set of experiments was a series of constant current density polarization studies accompanied by weight loss measurements. In our investigation we had the choice of constant current density or constant potential cathodic protection. It was decided to use constant current density for a variety of reasons. Firstly in a real cathodic protection system, the cathodic protection system is designed to supply a constant current density to the structure and therefore a constant current system would be closer to reality. Secondly the use of a potentiostat to obtain a constant potential would produce electrochemical mayhem at the interface if conditions were to suddenly change. As well as constant current density polarization studies, we also used a combination of photography, electrochemical impedance spectroscopy (EIS), SEM/EDX, GDOES, XRD analysis and pH titrations to further investigate this situation. The precise experimental conditions have already been described in Chapter 3, Sections 3.5, 3.6, 3.8, 3.9 and 3.11.

4.2. Weight loss experiments.

The major previous study using constant current cathodic protection was the early and seminal work by Humble [15]. His weight loss data was obtained using sandblasted steel plates which were exposed for one year at Kure Beach NC. He also used a light sand blast to remove the calcareous films subsequently produced. His data are replotted in Figure 2.17 (Chapter 2).

4.2.1. Potential Measurements.

We carried out a thirty day constant current exposure in the laboratory in artificial seawater. The experiments were performed in the region of underprotection at current densities between open circuit and the full protection situation. Three specimens were exposed for each value of current density and each measurement was plotted separately to indicate the variability in the experiment. At the same time, the potentials were measured daily.

Table 4.1. Details of sample test conditions listing final potentials and applied current densities.

Current Density (mA/m^2)	Final Potential after 30 days testing (mV).		
	Sample 1	Sample 2	Sample 3
Open circuit	-640	-638	-645
10	-700	-697	-705
20	-735	-737	-730
40	-750	-745	-748
50	-751	-750	-756
70	-783	-780	-781
100	-836	-835	-840
150	-895	-900	-902
200	-950	-947	-960

Potentials were measured daily during the 30 day period at the different current densities. It shows a very rapid potential change in the negative direction upon initial immersion and approaches steady state at around 30 days. These plots are given in Figures 4.3 (a)-(i) below. The final potentials were taken at 30 days (Table 4.1) and used to generate a set of potential versus corrosion rate and potential versus current density graphs.

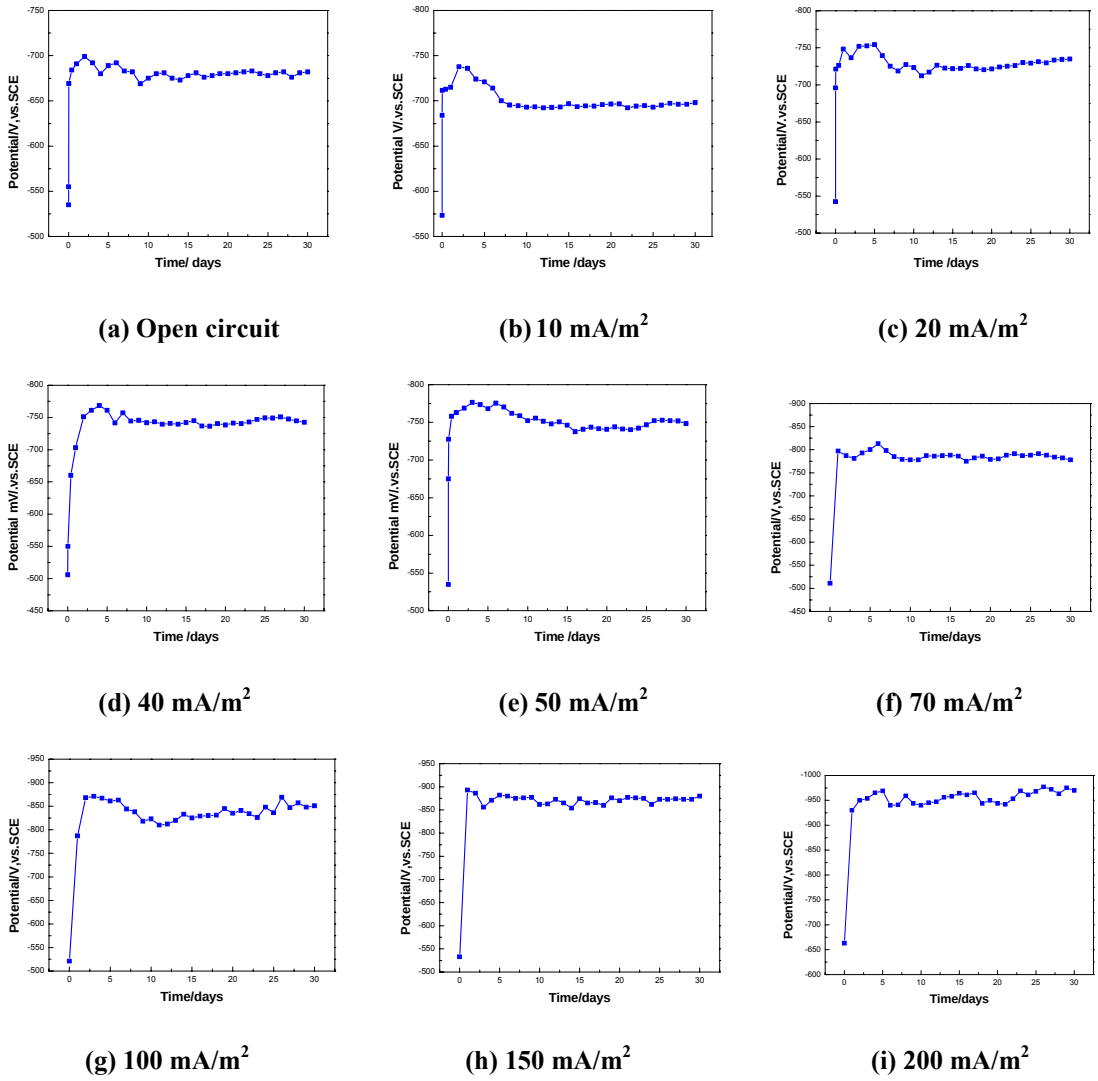

Figure 4.3. Set of graphs showing plots of daily potential/time measurements over a 30-day test period with different applied current densities in artificial seawater.

4.2.2. Weight loss graphs.

Table 4.2 provides the complete weight loss data from our studies. Weight loss has been converted into penetration rate in mm/y to be able to compare our data (Figure 4.4) with that of Humble. Subsequently, as well as our own data, we have included Humble's data (given in Figure 4.5), on the same graph. These comparative plots are shown in the graph given in Figure 4.6.

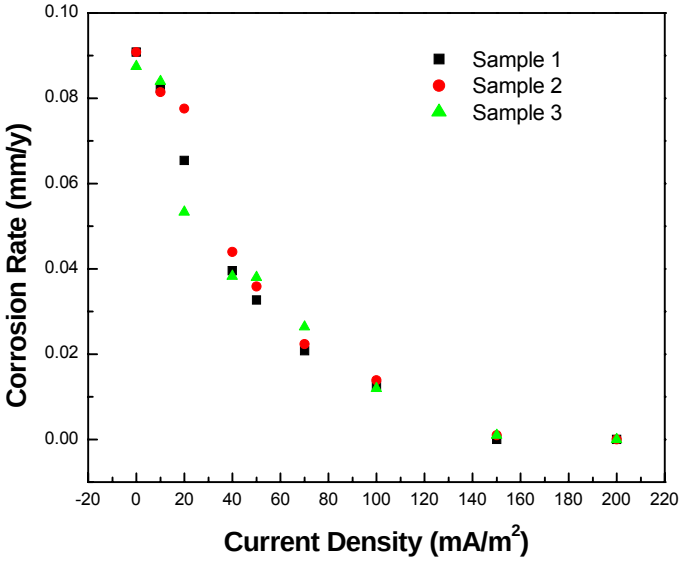

Figure 4.4. Graph showing plots of the relationship between corrosion rate and applied current densities.

Table 4.2. Weight loss data and applied current densities.

Current Density (mA/m^2)	Weight Loss (mg)		
	Sample 1	**Sample 2**	**Sample 3**
Open circuit	56.8	56.8	56.2
10	52.8	52.3	53.9
20	42,1	49.8	34.2
40	25.4	28.2	24.6
50	21.1	23.1	24.4
70	13.4	14.4	16.9
100	8.1	8.9	7.7
150	0	0.7	0.7
200	0	0	0

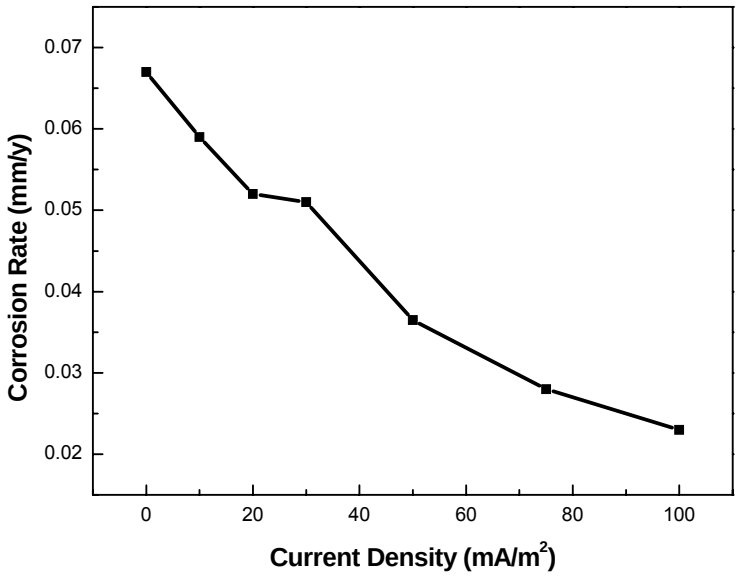

Figure 4.5. Replotted from Humble [15].

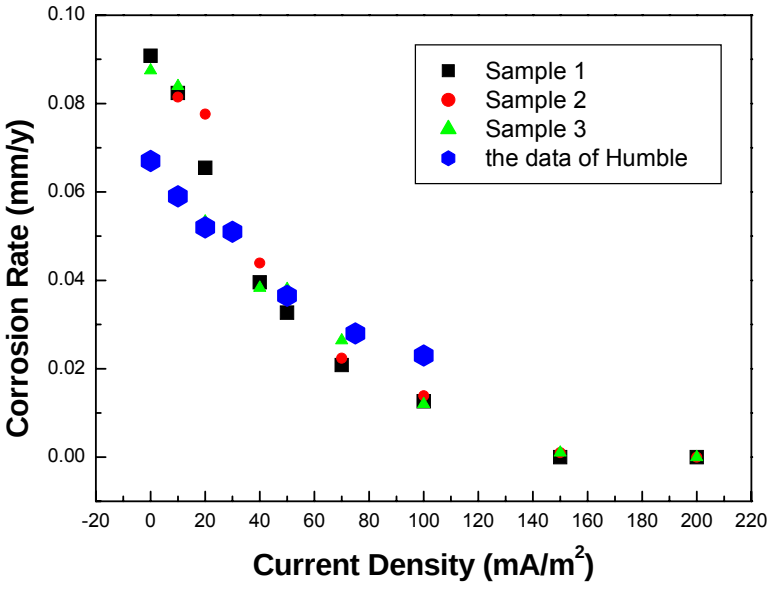

Figure 4.6. Comparison of our data with the data of Humble.

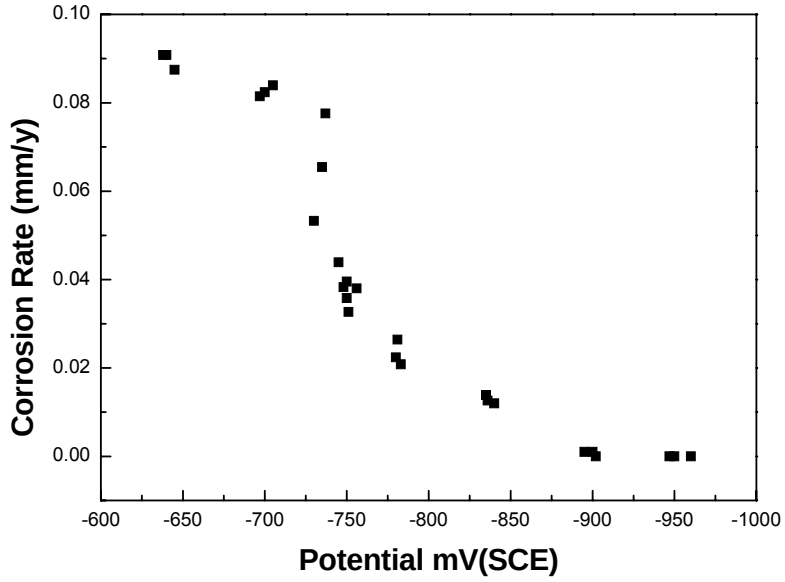

Figure 4.7. Graph showing plots of the relationship between corrosion rate (mm/y) and the final potential.

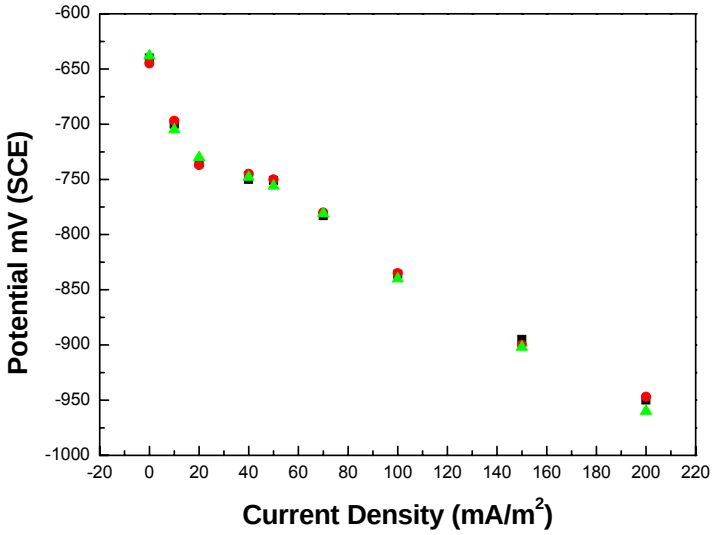

Figure 4.8. Graph showing plots of the relationship between applied current density and sample final potential for all samples at the different applied current densities.

From the data presented in Figure 4.4, the open circuit corrosion rate of 0.09 mm/y agrees surprisingly well with the data obtained by Humble [15] from experiments undertaken at Kure Beach which gives a figure of 105 g/ft^2 (0.067 mm/y) after one year exposure. Prior to the work by Humble, an earlier (1940) study at open circuit by Hudson [16]

involved securing 60 steel panels to the floating Gosport Ferry pier in Portsmouth Harbour for a period of 442 days exposure. The average annual corrosion rate determined was found to be 0.13 mm/y. The difference in corrosion rate obtained by Hudson compared with the later work (1948) by Humble (around 90% greater) may well reflect the enclosed situation in Portsmouth Harbour where the level of pollution would have been much higher than in our experiments or in Humble's work at Kure Beach.

4.2.3. Results and discussion.

Again, the data contained in Figures 4.4 and 4.6 is comfortingly reassuring and indicates what has always been generally assumed, namely the more negative the potential, the higher the current density and the lower the corrosion rate. However some unexpected behaviour may be observed. Contrary to Ashworth's [8] schematic, given in Figure 4.9 (a), the real graph of potential versus current density given in Figure 4.9 (b) can hardly be described as semi logarithmic. The most reasonable curve is probably linear at least until a value approximating to the protection current density is attained where the weight loss falls to zero. The implication of this response is that it seems to be described not by the Tafel equation but by an Ohmic type process, that is; not by an electrochemical activation process but by some resistive process. One might speculate as to the origin of this resistance; it is tempting to suggest the resistance of the calcareous film might be a prime candidate.

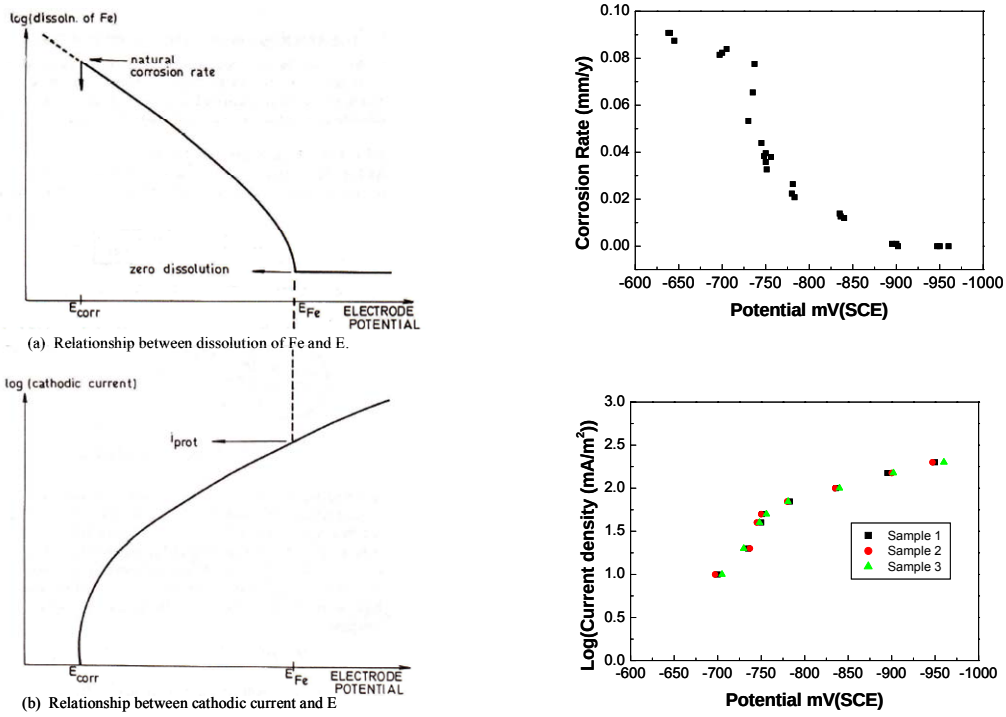

(a) **(b)**

Figure 4.9. Schematic diagrams showing plots of the variation of potential with current density for steel in seawater and the connection between the dissolution of the potential curve: (a) data from Ashworth [8], (b) my experimental data.

4.2.4. Protection Potential.

One interesting point that may be noted from Figure 4.7, is that the potential of -783 mV (SCE) which is very close to the accepted protection potential of -774 mV (SCE) still gives a finite and measureable corrosion rate of 0.023 mm/y which is still quite a significant metal loss, amounting to about 25% of the loss observed at the open circuit value. To achieve full protection a further 113 mV of potential shift is necessary to bring the potential down to -895 mV (SCE) where corrosion has virtually ceased. This data is thought to be highly significant in practice where the -774 mV (SCE) [equivalent to -850mV (CSE)] is widely used.

4.3. Investigation of the nature of the surface film.

This study examines the appearance and composition and lateral (Z–direction) compositional variation of the surface films formed by applying different levels of cathodic protection.

To understand the presence and composition of any surface films formed, the surface morphology was investigated using optical (digital) photography, glow-discharge optical-emission spectroscopy (GDOES), Scanning Electron Microscopy (SEM) in conjunction with Energy Dispersive X-Ray Analysis (EDX) and X-Ray Diffraction after the experiment. The electrochemical impedance spectroscopy (EIS) measurements were performed *in situ* as deposits were forming on electrodes polarized at current densities between 0 (open circuit) and 400 mA/m^2 using the polarized potential achieved at that particular time.

4.3.1. Measurement of Potential.

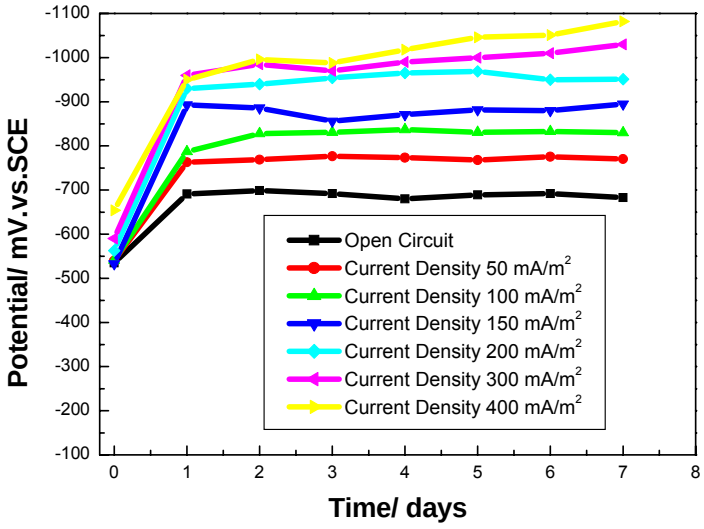

Figure 4.10. Graph showing plots of potential – time curves at various current densities over a period of one week.

Figure 4.10 shows the potential vs. time plots obtained for mild steel samples at different current densities between open circuit and 400 mA/m^2 obtained after one week immersion in artificial seawater. The higher applied current densities cause the potential of the sample generally to become more negative. The visual appearances of the deposits are significantly different. We will consider this further in Section 4.3.2.

4.3.2. Optical images.

Plate 4.1 shows images of the surfaces of the full set of 5 mild steel samples, from open circuit conditions, together with applied current densities of 50 mA/m^2 to 200 mA/m^2 after 6 hours of immersion. The images were produced by scanning the surface of each sample using an Epson DX4850 flat-bed scanner and not with an optical (film) or digital camera. The excellent image quality obtained and inherent lack of reflections is a feature of these images. Samples were scanned at a resolution of 300 dpi. There is an obvious water-line with the immersed region at the top of the photograph.

From Plate 4.1, it was evident that even after 6 hours immersion, significant deposits have already appeared on the surfaces of the samples. The results shown in Plate 4.1(a - d) show that the specimens immersed in artificial sea water did not appear to suffer localised corrosion in the under-protection situation (open circuit to 150 mA/m^2) and the yellow-brown deposits visible were assumed to be $Fe_2O_3 \cdot H_2O$. X-Ray analysis will confirm this later. Plate 4.1(e) shows the sample surface after 6 hours immersion under conditions of complete cathodic protection, which was covered by white/grey deposits, which we shall show later to consist mainly of a magnesium containing calcareous film. This will be proven by GDOES, EDX and XRD studies later in this Chapter, see Sections 4.3.3, 4.3.4 and 4.3.6.

Similar sets of experiments were also carried out for immersion periods of 1 day, 3 days and one week, in order to show the effects of increasing immersion time. A full discussion of the results of the SEM/EDX investigation of the samples immersed for 1 day and 3 days is provided in Section 4.3.4.

(1) 6 hours immersion.

(a) Open circuit for 6 hours

(b) 50 mA/m^2 for 6 hours

(c) 100 mA/m^2 for 6 hours

(d) 150 mA/m^2 for 6 hours

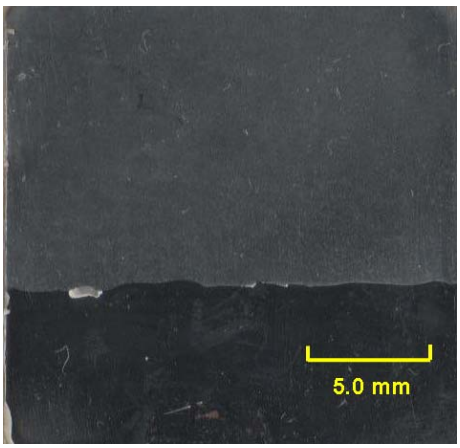

(e) 200 mA/m^2 for 6 hours

Plate 4.1. Images from digital scanner, of surfaces of the five mild steel samples after immersion in artificial seawater for 6 hours at various levels of current density.

(2) One week immersion

(a) Open circuit for 1 week

(b) 50 mA/m^2 for 1 week

(c) 100 mA/m^2 for 1 week

(d) 150 mA/m^2 for 1 week

Plate 4.2. Images from digital scanner, of the surfaces of the seven samples after immersion for one week in artificial seawater at various levels of current density.

(e) 200 mA/m^2 for 1 week

(f) 300 mA/m^2 for 1 week

(g) 400 mA/m^2 for 1 week

Plate 4.2. (continued) Images from digital scanner, of the surfaces of the seven samples after immersion for one week in artificial seawater at various levels of current density.

Plate 4.2 shows scanned images of the surfaces of the full set of 7 mild steel samples, after being immersed in artificial seawater for one week, and subjected to various applied current densities, ranging from open circuit to 400 mA/m^2. It was evident that there were significant deposits present on the surfaces of the samples after exposure for 7 days to artificial seawater. Plates 4.2(a) to (c) show that the surfaces of the samples were covered by a visible yellow-brown deposit which is assumed to be $Fe_2O_3 \cdot H_2O$. These conditions where the current density is 100 mA/m^2 or less are assumed to be the underprotection situation. Plates 4.2(d) and (e) [150 mA/m^2 and 200 mA/m^2 respectively] show the appearance of the specimen surfaces under conditions of almost completely cathodic protection and mainly covered by white/grey deposits; which are the calcareous films. Plate 4.2(f) [300 mA/m^2] shows the sample surface was almost totally covered by a white/ grey deposit. Similarly, Plate 4.2(g) shows a scanned image of the surface of the sample that was subjected to an overprotection current density of 400 mA/m^2, and it is evident that the sample surface is totally covered by a white deposit (a calcareous film).

Points of interest to note are that the 150 mA/m^2 and 200 mA/m^2 panels show much less rust on the surface, than the samples at the lower current densities. In addition, there appears to be no visible rust in the samples at 300 mA/m^2 and 400 mA/m^2, which are almost covered by grey/white deposits. Also, at open circuit the rust seems more coarse, and then gets more compact at the higher current densities and that there appears, at least from visual examination, to be no tendency for the anodic and cathodic areas to be delineated.

4.3.3. Results from GDOES study.

GDOES was chosen as a method to investigate the formation of calcareous films, because this technique can detect compositional changes with depth and time for very thin films. Therefore, for our study, it was especially useful for looking at changes in composition of the deposited film during the very early stages (6 hours) of film growth at various current densities.

The graphs shown in Figures 4.11 and 4.12 are typical GDOES data plots of metal surfaces covered by deposits. Figures 4.11 and 4.12 are given as examples of GDOES data plots obtained for the deposits formed over 6 hours of immersion, in both the underprotected (50 mA/m^2) and cathodic protection (200 mA/m^2) situations respectively. Proceeding from left to right across the graph indicates loss of the film with time due to sputtering, and indicates how the composition of the film varies with time. The first vertical dotted pink line at the left hand side (earlier time) of the X-axis (Time) represents the film surface, whilst the second pink line (later time) represents the film-steel interface.

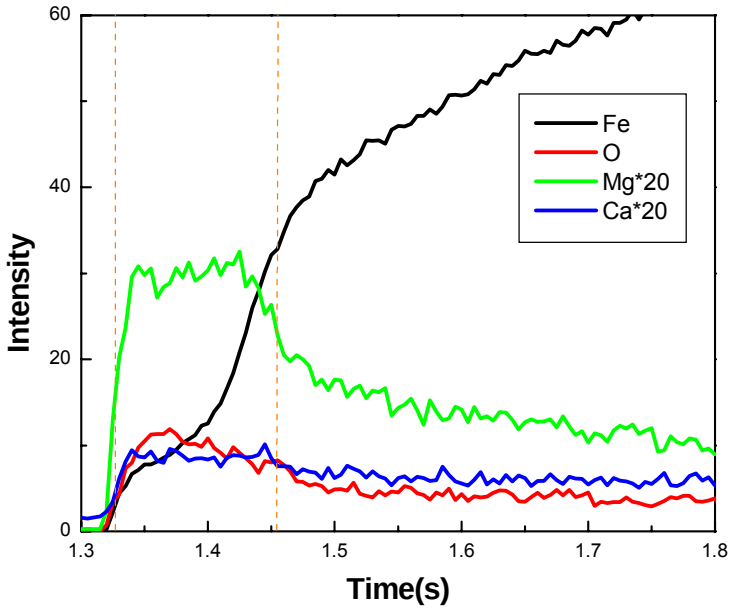

Figure 4.11. GDOES plot of deposit obtained using an applied current density of 50 mA/m^2 for 6 hours

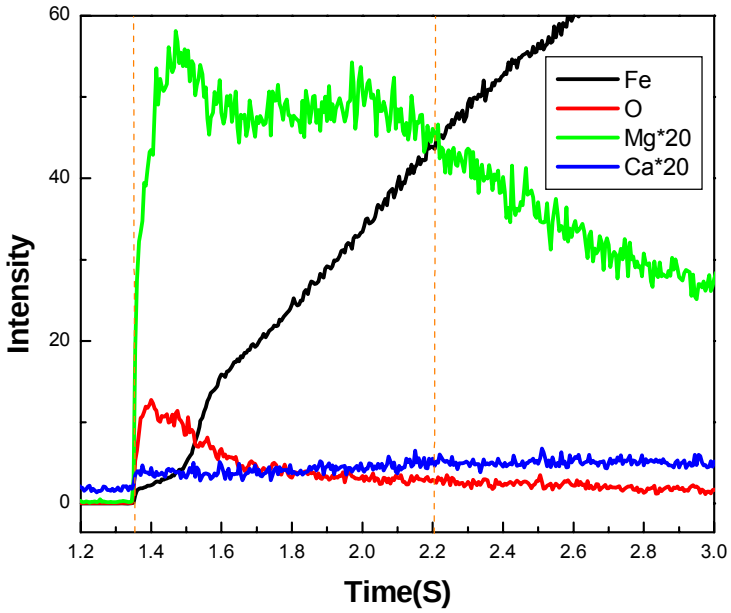

Figure 4.12. GDOES plot of deposit obtained using an applied current density of 200 mA/m^2 for 6 hours.

It should be noted, that in Figures 4.11 and 4.12, the traces for magnesium and calcium are expanded by a factor of 20 times compared with oxygen and iron.

For the 2 examples of deposit (50 mA/m^2 and 200 mA/m^2 for 6 hours) investigated during this study using the GDOES technique, the change in composition of the 4 selected elements investigated (Fe, O, Mg and Ca) within the film at various depths from the surface are shown in Figures 4.11 and 4.12. In Figures 4.11 and 4.12, the film thickness is represented by 0.15s and 0.85s respectively. It does seem to show that there is a significant amount of magnesium in the deposit together with some calcium, and also that the magnesium content has increased at the higher current density of 200 mA/m^2.

It should be noted, that access to the GDOES facility was fairly restricted, especially towards the later stage of the Project, and only a limited number of samples could be investigated using this analytical technique. It was not feasible to use this technique to complement/corroborate results from later experiments where we analysed the deposits formed over 3 days immersion.

4.3.4. SEM/EDX.

The formation, growth and morphology of calcareous deposits, formed under the various conditions (different immersion periods and applied current densities) described earlier, were investigated using Scanning Electron Microscopy (SEM) and Energy Dispersive X-Ray Analysis (EDX)**.**

The samples were examined and analysed using a FEI XL 30 FEGSEM, equipped with an integrated RONTEC EDX system (see Section 3.8 for full description). SEM imaging was performed in both secondary electron (SE) and backscattered electron (BSE) operating modes. Results are presented in the following Sections as sets of secondary electron (SE) images from digital photomicrographs, together with selected EDX full spectrum analyses, and also selected EDX element distribution maps and line scans (both obtained using EDX 'imaging mode') to show the occurrence and distribution of the elements Fe, Ca, Mg and O.

4.3.4.1. Short term immersion.

In order to investigate the composition of a calcareous deposit formed during only a short period of immersion (a few hours), under conditions of cathodic protection, a mild steel sample was prepared and immersed for 6 hours in artificial seawater at an applied current density of 200 mA/m^2. In addition, a subsequent experiment was carried out using a group of 5 samples immersed for 1 day in artificial seawater, at current densities ranging from open circuit to 300 mA/m^2. These five values of current densities were chosen because open circuit and 100 mA/m^2 are typical of under protection, 150 mA/m^2 is just fully protected, 200 mA/m^2 is well protected, and 300 mA/m^2 is possibly over protected.

(1) 6 hours immersion.

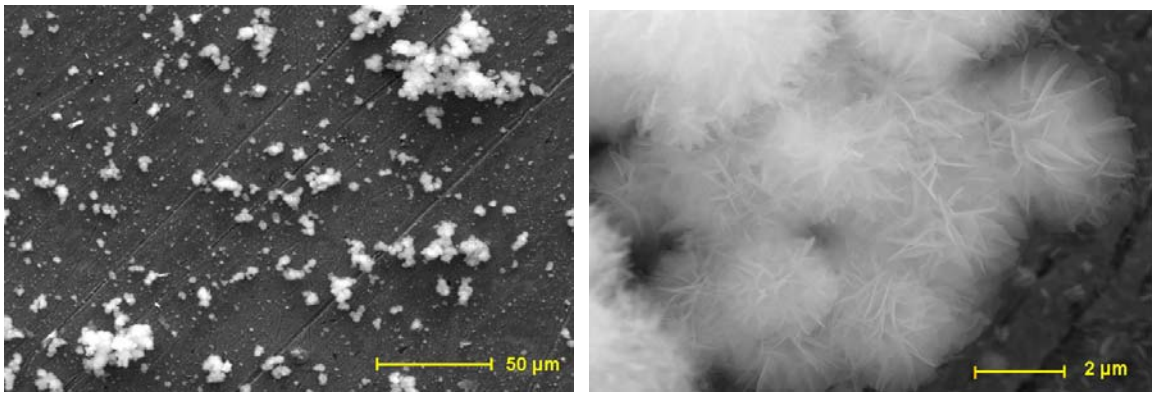

(a) Secondary Electron image taken at 500X **(b) Secondary Electron image taken at 10000X**

Plate 4.3. SEM images of deposit formed on mild steel sample immersed in artificial seawater for 6 hours, using an applied current density of 200 mA/m^2.

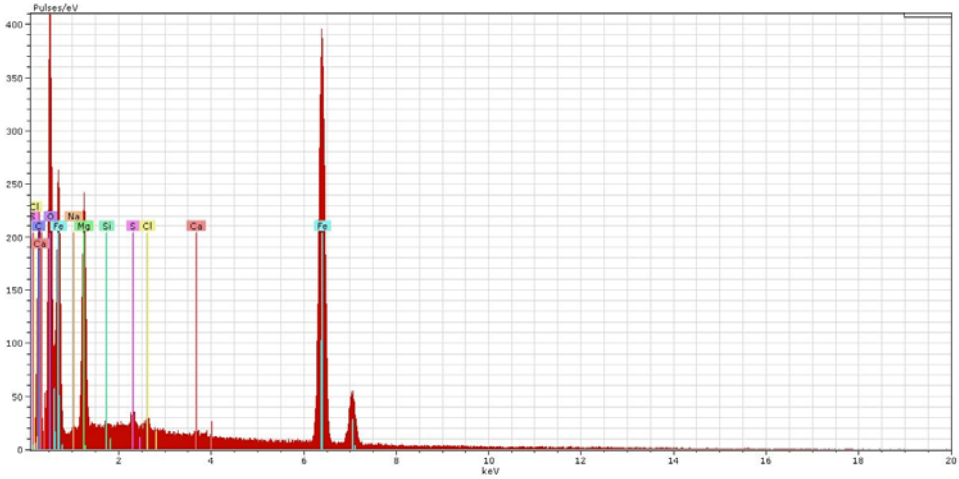

Figure 4.13. EDX spectra of surface deposit obtained after immersion for 6 hours in artificial seawater using an applied current density of 200 mA/m^2.

Plate 4.3 shows SEM images of the deposits formed on a mild steel sample during 6 hours immersion in still artificial sea water with an applied current density of 200 mA/m^2. It is obvious that some deposits have formed on the sample surface which has the appearance at low magnification (X 500) of sparsely distributed aggregates with a granular morphology (Plate 4.3(a)), and an image taken at a higher magnification to show the fine structure of the deposit in more detail is given in Plate 4.3(b). Also, according to the corresponding results of the EDX analysis of this deposit given in Figure 4.13, a significant amount of magnesium was detected, but no indication of the presence of calcium. So we could therefore assume it was mainly a magnesium containing compound that is deposited during periods of short time immersion in seawater under conditions of cathodic protection.

(2) 1 day immersion.

Plate 4.4 shows a set of secondary electron SEM images that illustrate the morphology of the various deposits formed on mild steel during a 1 day immersion period in still artificial sea water with a range of current densities varying from 0 to 300 mA/m^2. The relative percentages of various elements obtained using EDX quantification at these different applied current densities are presented in Table 4.3.

The set of SEM images presented in Plate 4.4 shows the secondary electron SEM micrographs of surface deposits formed on the sample surfaces after immersion in seawater for 1 day at applied current densities ranging from 0 (open circuit) to 300 mA/m^2 respectively. From the SEM image obtained for the open circuit situation, and shown in Plate 4.4(a), and the corresponding EDX result given in Table 4.3, it was observed that there is mainly deposition of rust, and the percentage of magnesium was 0.81%, whilst the percentage of calcium was 0.2% which can probably be ignored because this value is lower than the normal detection limits of the EDX system (0.3%). At the other (higher) applied current densities, both magnesium and calcium were found. Also, from Table 4.3, it can be seen that the percentages of magnesium and calcium both increase concurrently with increasing applied current density.

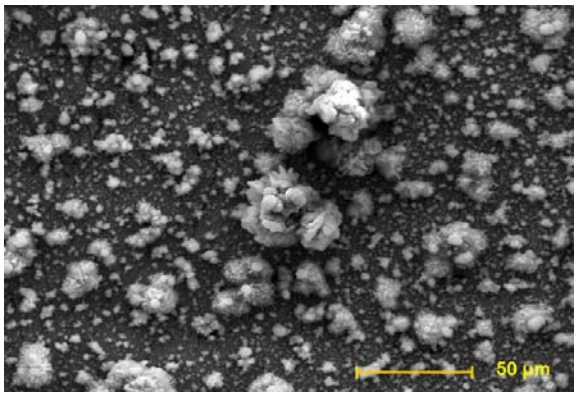

(a) Open circuit

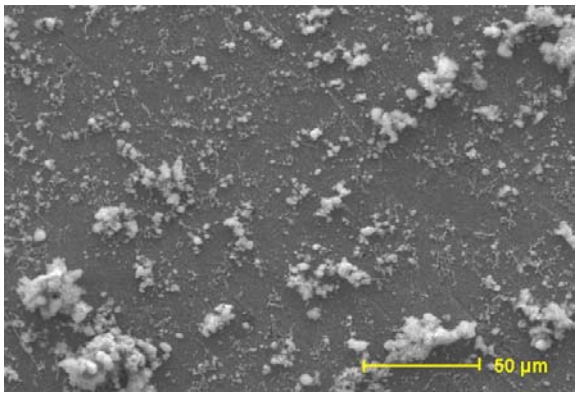

(b) 100 mA/m^2

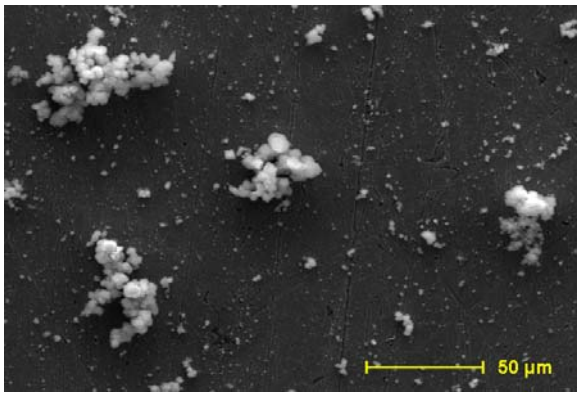

(c) 150 mA/m^2

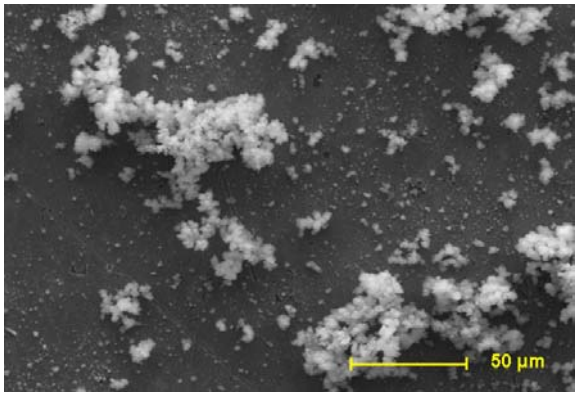

(d) 200 mA/m^2

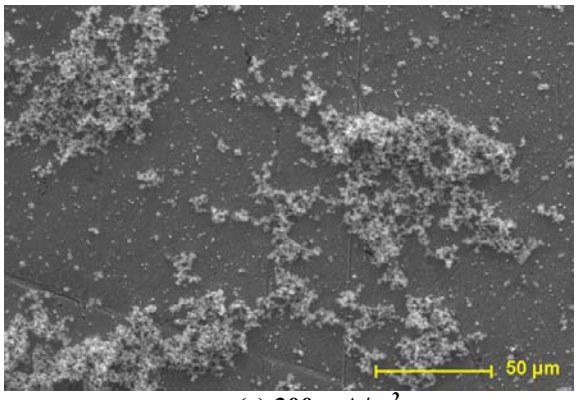

(e) 300 mA/m^2

Plate 4.4. SEM images of surface deposits formed on mild steel samples after immersion for 1 day in artificial seawater at different current densities ranging from 0 to 300 mA/m^2 (Secondary electron images taken at 500 X).

Table 4.3. The relative percentages of various elements in surface film deposits formed on steel samples after 1 day immersion in artificial seawater obtained using EDX quantification at different applied current densities.

Applied Current Density (mA/m^2)	Percentage of Element (%)								
	Carbon	Oxygen	Sodium	Magnesium	Silicon	Sulfur	Chlorine	Calcium	Iron
open circuit	8.1	15.47	2.19	0.81	0.05	0.28	2.94	0.2	9.95
100	9	11.7	8.46	2.31	0.13	0.16	3.17	0.38	64.58
150	14.2	20.3	0.71	3	0.41	0.40	0.39	0.4	59.88
200	16.2	20	0.9	5.25	0.44	0.53	1.01	0.54	55.1
300	19.6	19.9	2.12	6.1	0.36	0.28	0.97	0.57	50.1

4.3.4.2. Intermediate term immersion (3 days immersion).

The SEM micrographs shown in Plate 4.5 illustrate the morphologies of the deposits formed after immersion in still artificial sea water for 3 days at the different applied current densities. From Table 4.4, which gives the relative percentages of the various elements obtained using EDX quantification, it can be observed that in the open circuit situation, the amount of calcium in the deposit is 0.13%, which is below the detection limits (~0.3%) of the instrument, but magnesium was definitely detected (1.53%). Also, these observations indicate that the composition of the deposits change significantly with immersion time. If the results obtained for the EDX element quantifications for 1 day and 3 days immersion are compared, it is clearly evident that the percentages of Mg obtained after 3 days at all current densities is greater than those seen after 1 day immersion, and in addition, in the case of applied current densities of 200 mA/m^2 and 300 mA/m^2, there is a massive increase in the percentage of Ca observed after 3 days compared to the 1 day immersion period (0.54/0.57% to 2.52/3.04% respectively).

It was also interesting to note, that; after 3 days immersion, although the percentage of Mg found after 3 days immersion was significantly higher than the percentage determined after 1 day immersion, in the fully protected and overprotected situation (200 mA/m^2 and 300 mA/m^2 respectively) the percentages of Mg observed were less than those observed at the underprotected current densities of 100 mA/m^2 and 150 mA/m^2.

In view of these findings, it was felt necessary to undertake a further set of immersion experiments over a longer period. A one week experiment was therefore carried out at a range of different applied current densities.

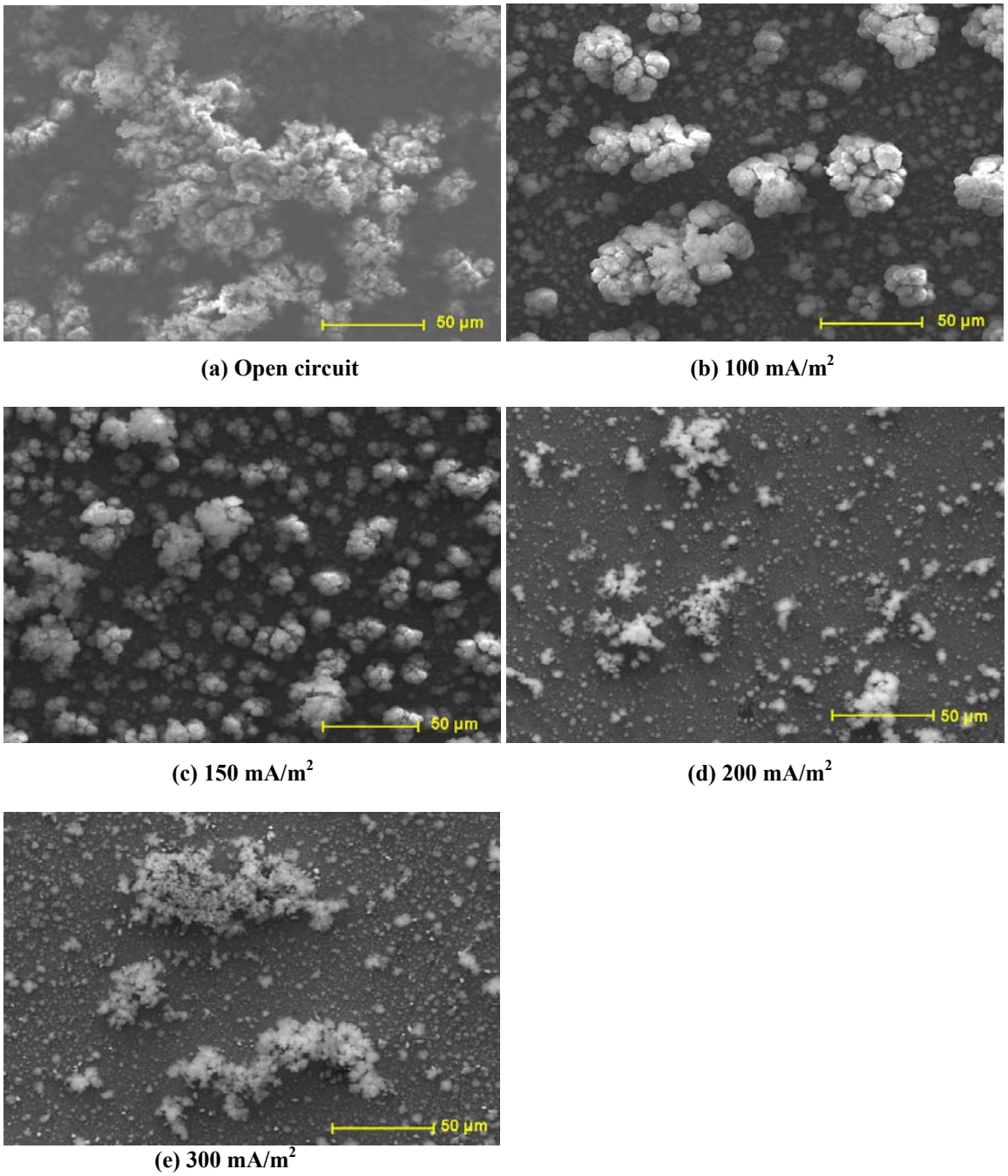

(a) Open circuit **(b) 100 mA/m^2**

(c) 150 mA/m^2 **(d) 200 mA/m^2**

(e) 300 mA/m^2

Plate 4.5. SEM micrographs of surface deposits obtained after 3 days immersion in artificial seawater using different applied current densities (secondary electron images taken at 500X).

Table 4.4. The relative percentages of various elements obtained using EDX quantification in surface film deposits formed on steel samples after 3 days immersion in artificial seawater at different applied current densities.

Applied Current Density (mA/m^2)	Percentage of Element								
	Carbon	**Oxygen**	**Sodium**	**Magnesium**	**Silicon**	**Sulfur**	**Chlorine**	**Calcium**	**Iron**
open circuit	5.1	45.52	1.49	1.53	0.05	0.26	0.31	0.13	45.58
100	10.46	38.88	0.63	11.07	0.09	0.27	0.26	0.32	38
150	10.6	37.18	0.92	14.11	0.07	0.29	0.62	0.36	35.8
200	13.5	24.47	0.1	9.83	0.05	0.07	0.12	2.52	49.2
300	16.9	24	0.21	9.64	0.07	0.11	0.17	3.04	45.85

4.3.4.3. One week experiment.

In this part of the study, polished mild steel samples were immersed for a week in artificial seawater at various applied current densities. The range of current densities chosen were: open circuit, 50 mA/m^2, 100 mA/m^2, 150 mA/m^2, 200 mA/m^2, 300 mA/m^2 and 400 mA/m^2. The scanned optical images of the sample surfaces after 7 days immersion have already been given in Plate 4.2. To investigate the underprotection situation, the results of the SEM imaging studies and associated EDX element distribution mappings will be presented and discussed for samples at applied current densities between 0 to 200 mA/m^2.

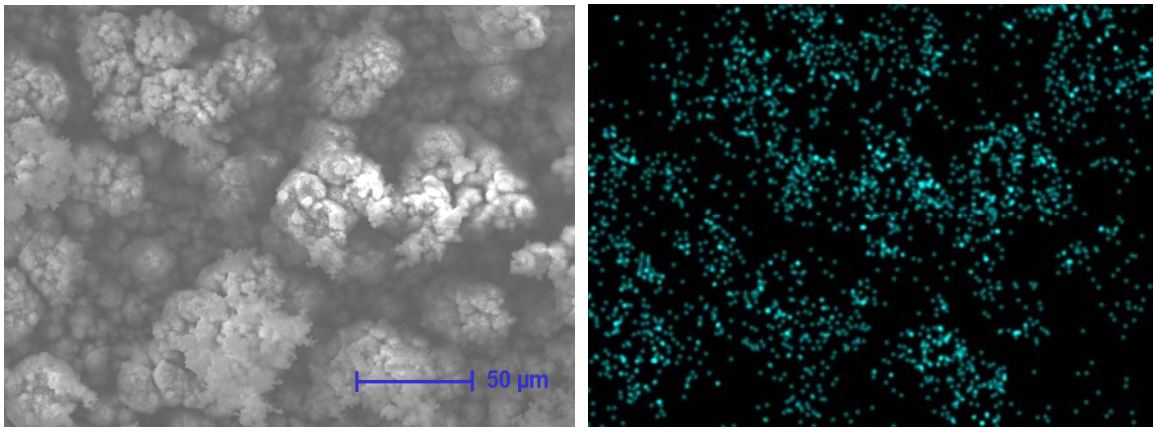

(a) Secondary image taken at 500x **(b) EDX element map of distribution of Mg**

(c) EDX element map of distribution of O **(d) EDX element map of distribution of Fe**

Plate 4.6. Secondary Electron SEM image and corresponding EDX element distribution maps for Mg, O and Fe of deposit obtained at open circuit for one week: a. SE image; b - d. EDX maps for Mg, O and Fe respectively.

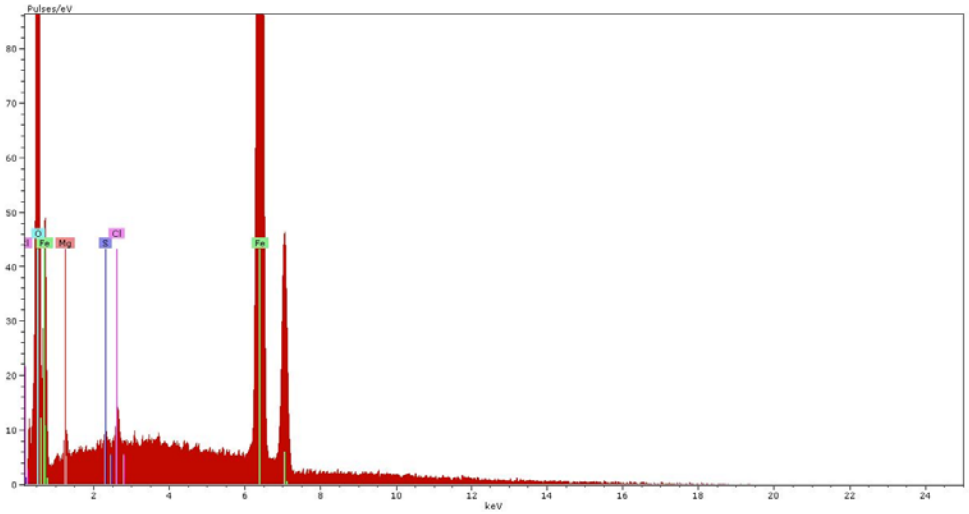

Figure 4.14. EDX spectra of surface of deposit obtained at open circuit for one week.

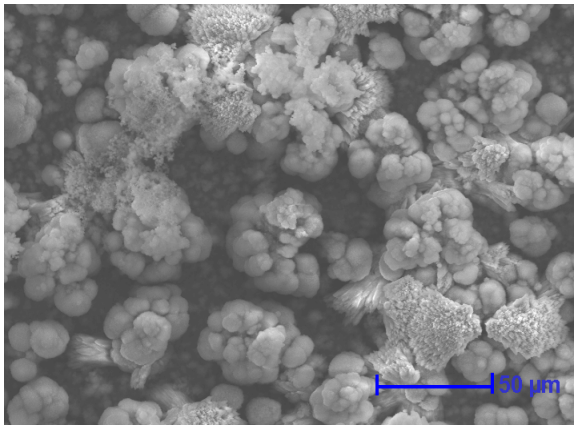

(a) Secondary image taken at 500x

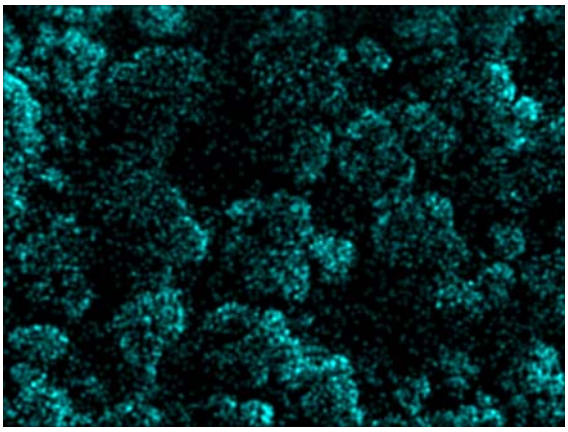

(b). Single EDX element map of distribution of Mg

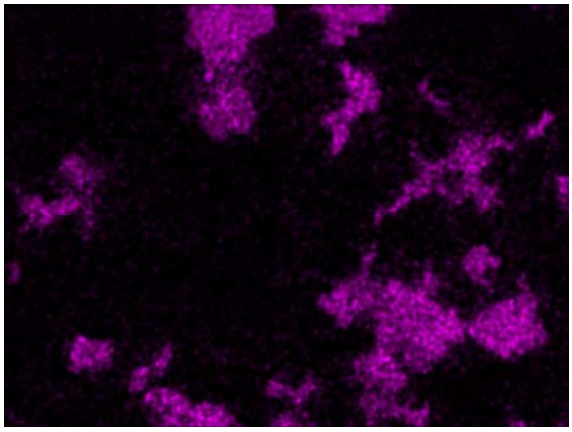

(c). Single EDX element map of distribution of Ca

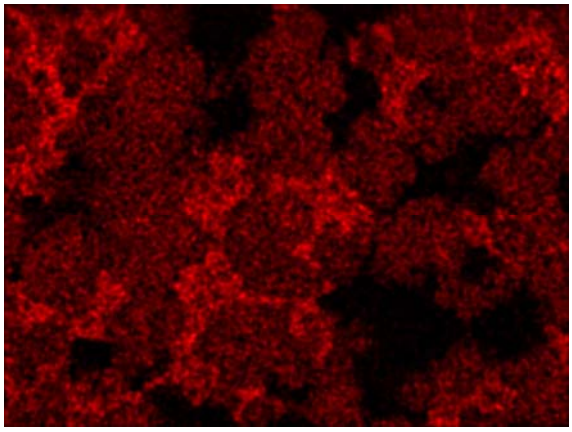

(d). Single EDX element map of distribution of Fe

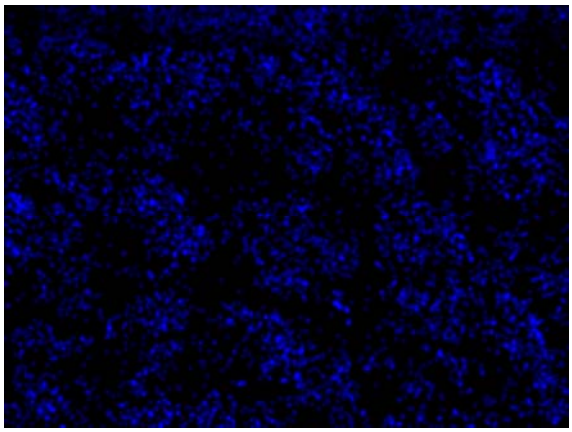

(e). Single EDX element map of distribution of O

Plate 4.7. Secondary Electron SEM image and corresponding EDX element distribution maps of deposit obtained using an applied current density of 50 mA/m^2 for 7 days: a. SE image, b – e. EDX maps for Mg, Ca, Fe and O respectively.

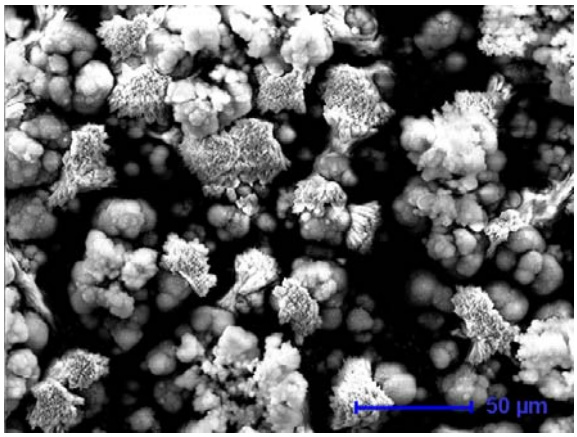

(a) Secondary image taken at 500x

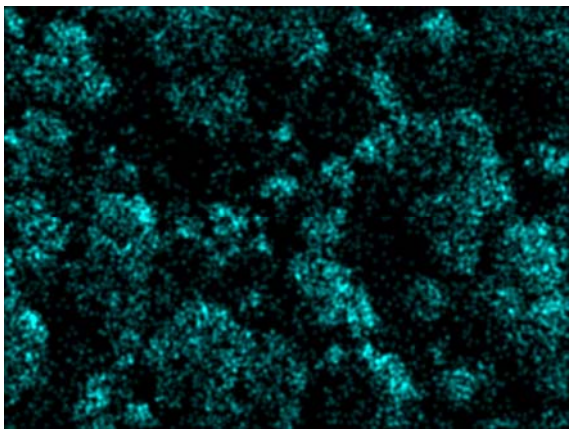

(b). Single EDX element map of distribution of Mg

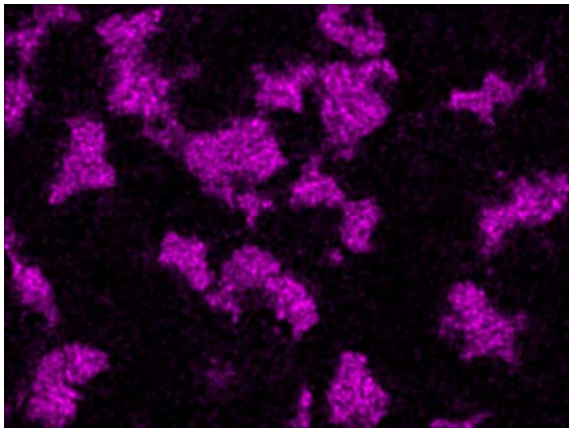

(c). Single EDX element map of distribution of Ca

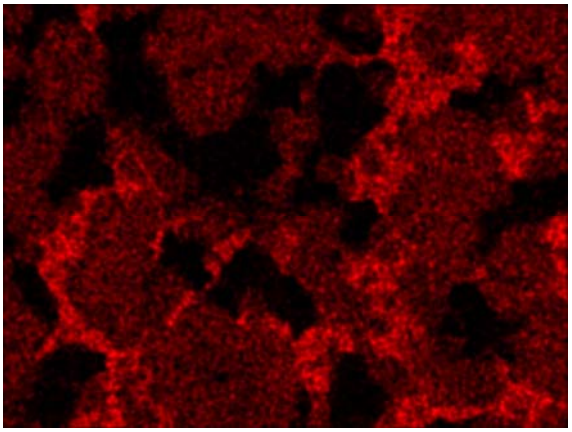

(d). Single EDX element map of distribution of Fe

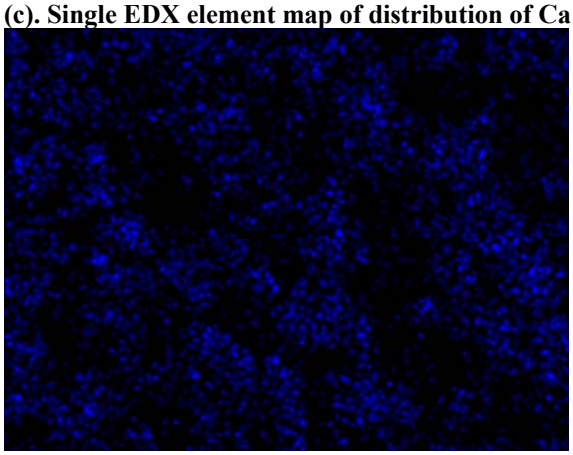

(e). Single EDX element map of distribution of O

Plate 4.8. Secondary Electron SEM image and corresponding EDX element distribution maps of deposit obtained using an applied current density of 100 mA/m^2 for 7 days: a. SE image; b – e. EDX maps for Mg, Ca, Fe and O respectively.

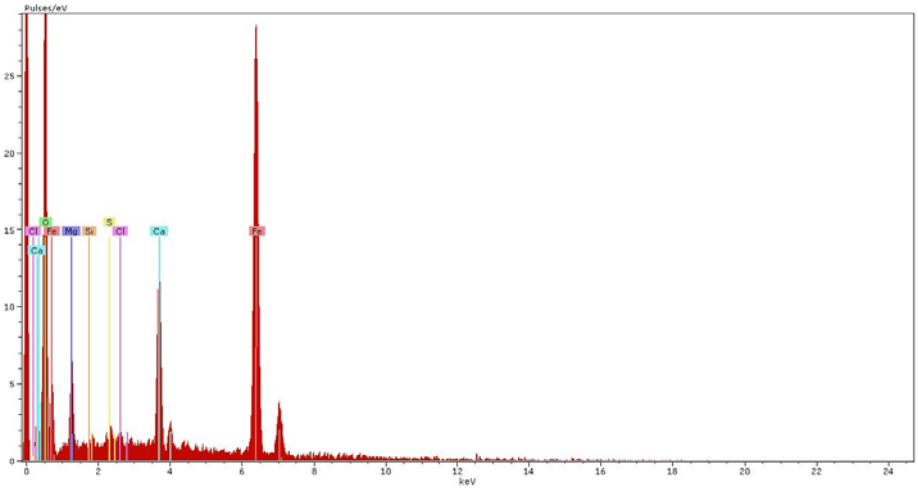

Figure 4.15. EDX spectra of surface of deposit obtained using an applied current density of 50 mA/m^2 for 7 days.

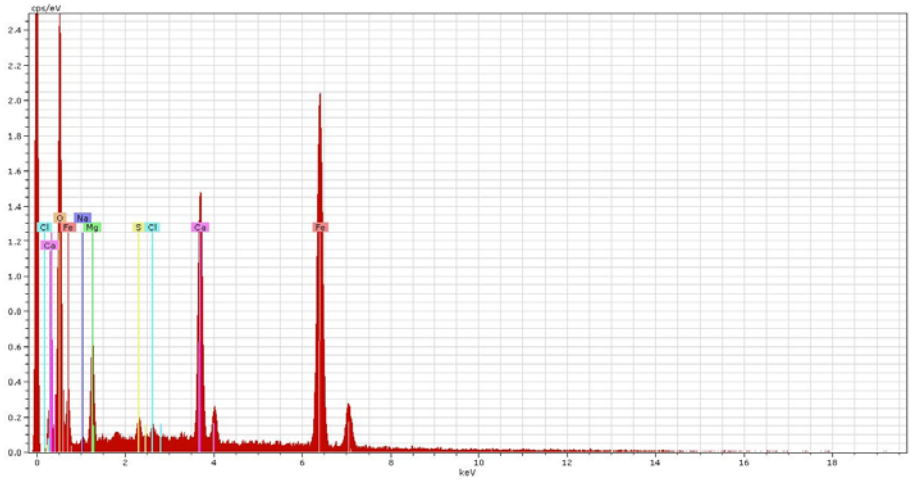

Figure 4.16. EDX spectra of surface of deposit obtained using an applied current density of 100 mA/m^2 for 7 days.

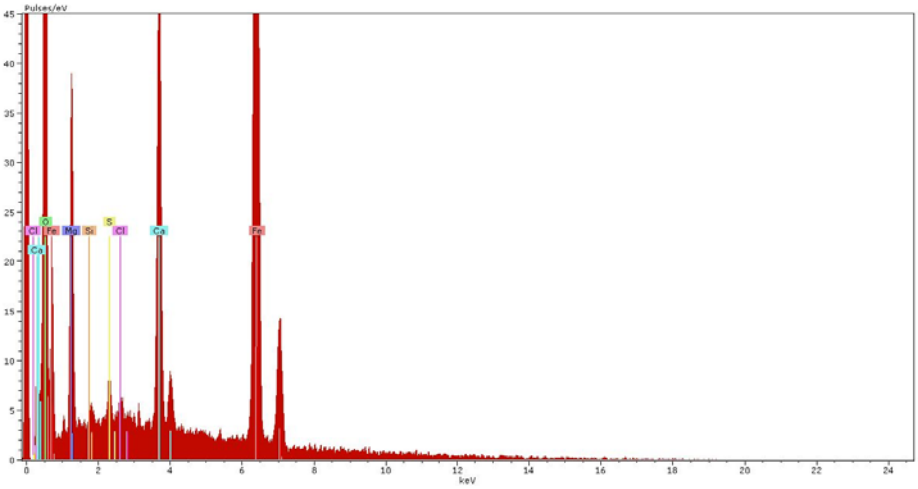

Figure 4.17. EDX spectra of surface of deposit obtained using an applied current density of 150 mA/m^2 for 7 days.

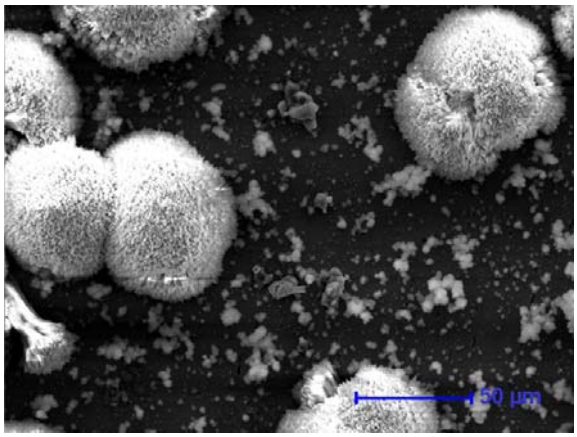

(a) Secondary image taken at 500x

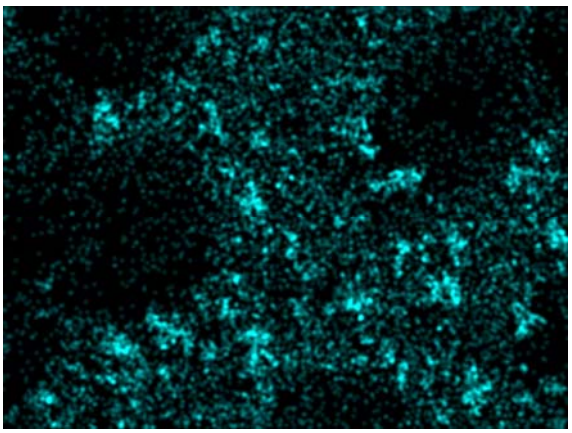

(b). Single EDX element map of distribution of Mg

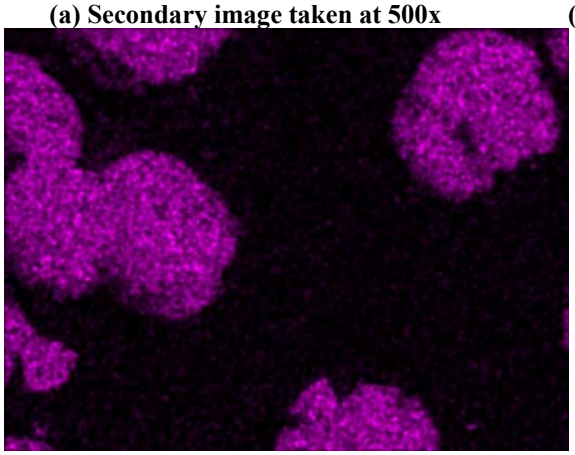

(c). Single EDX element map of distribution of Ca

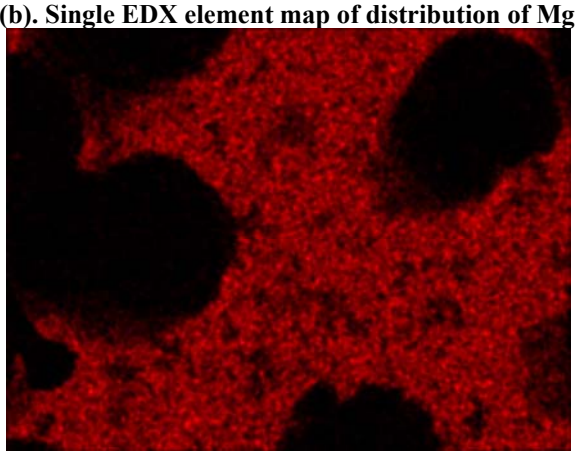

(d). Single EDX element map of distribution of Fe

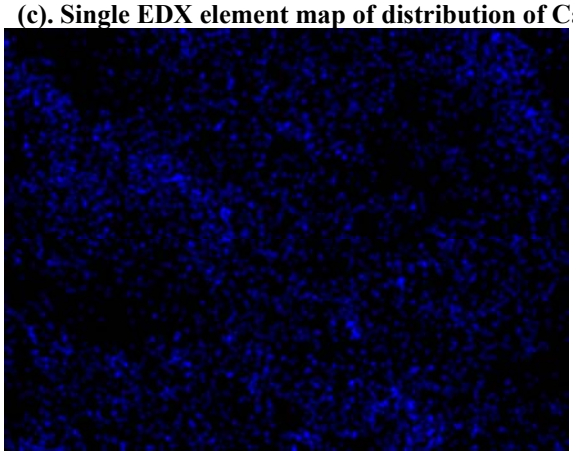

(e). Single EDX element map of distribution of O

Plate 4.9. Secondary Electron SEM image and corresponding EDX element distribution maps of deposit obtained using an applied current density of 150 mA/m^2 for 7 days: a. SE image; b – e. EDX maps for Mg, Ca, Fe and O respectively.

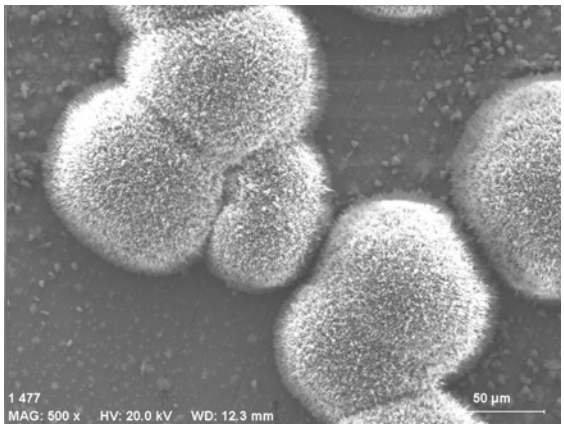

(a) Secondary image taken at 500x

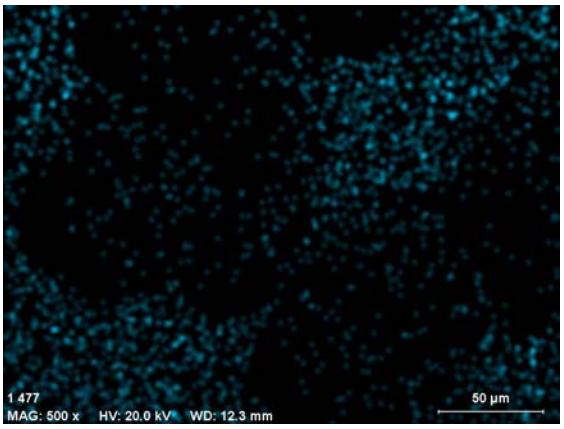

(b). Single EDX element map of distribution of Mg

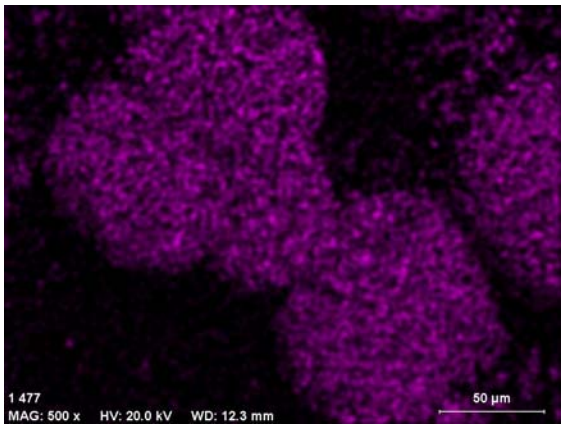

(c). Single EDX element map of distribution of Ca

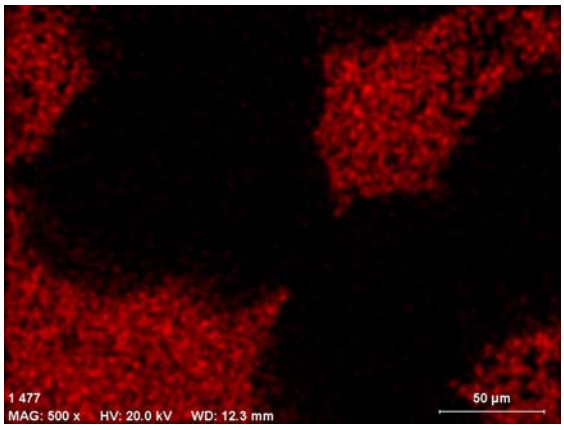

(d). Single EDX element map of distribution of Fe

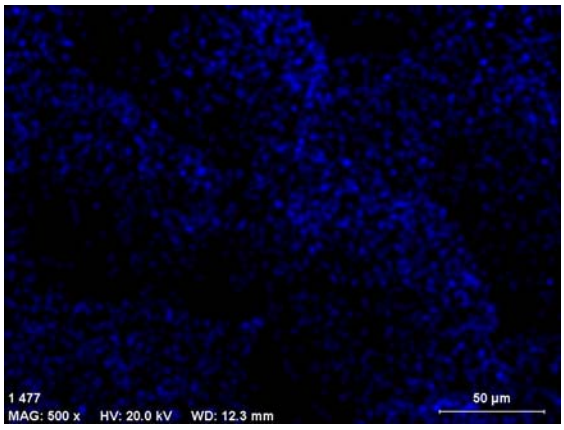

(e). Single EDX element map of distribution of O

Plate 4.10. Secondary Electron SEM image and corresponding EDX element distribution maps of deposit obtained using an applied current density of 200 mA/m^2 for 7 days: a. SE image; b – e. EDX maps for Mg, Ca, Fe and O respectively.

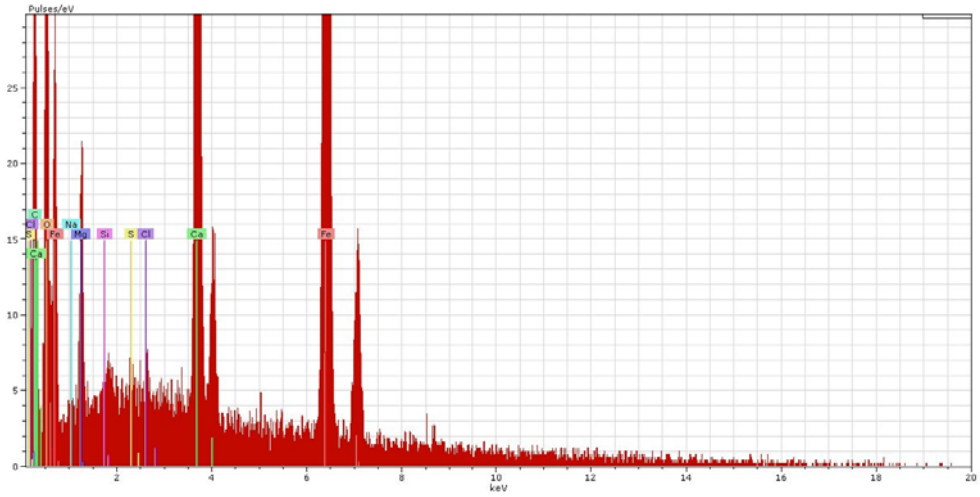

Figure 4.18. EDX spectra of surface of deposit obtained using an applied current density of 200 mA/m^2 for 7 days.

Table 4.5. The relative percentages of various elements obtained using EDX quantification, of surface film deposits on steel samples at different applied current densities after 7 days immersion in artificial seawater.

Applied Current Density (mA/m^2)	Percentage of Element								
	Carbon	Oxygen	Sodium	Magnesium	Silicon	Sulfur	Chlorine	Calcium	Iron
open circuit	4.82	64	1	0.87	-	0.25	0.39	-	28.68
50	8.08	63.55	1.41	4.08	0.3	0.7	1.99	1.67	18.22
100	20.18	53.04	1.25	2.12	-	0.4	0.12	5.95	16.92
150	17.48	52.35	1.35	3.96	0.25	0.4	1.8	7.74	14.67
200	20.42	37.33	2.01	6.21	0.87	0.42	0.49	17.8	14.4

Plates 4.6 - 4.10 show the SEM micrographs and corresponding EDX maps of Mg, Ca, Fe and O of the calcareous film deposits formed on the surfaces of the mild steel samples, after immersion in artificial seawater for 7 days at the different applied current densities ranging from open circuit to 200 mA/m^2. For each sample, the SEM images and associated EDX maps were recorded at the same magnification to give the same equivalent analysis area in each case. Figures 4.14 to 4.18 give the associated full EDX spectra of all elements detected from the same region of the surface of the deposits, and the quantitative relative percentages of these elements are given in Table 4.5.

Plate 4.6 gives a secondary electron SEM image and corresponding EDX element maps of the surface of the deposit formed under open circuit conditions, and shows mainly rust nodules on the surface and magnesium deposits overlaying the rust, but calcium was not detected, being below the detection limits of the EDX system (around 0.3%), this is a similar result to that observed after 1 day and 3 days immersion, and discussed previously.

The SEM images and EDX maps of the deposit formed at 50 mA/m^2, and illustrated in Plate 4.7, show even more magnesium and calcium on the surface than the previous (open circuit) sample. The deposits shown in Plate 4.9 and Plate 4.10 which were formed at 150 mA/m^2 and 200 mA/m^2 respectively show an obvious and large calcium containing precipitate. This early precipitation of magnesium is certainly contrary to the usual account which cites solubility product arguments [13], [15] to support early calcium precipitation. It may be however, that the nucleation of magnesium compounds onto/into the rust layer is a result of co-precipitation of those hydroxides [17]. This aspect of co-precipitation will be returned to later in this Chapter and discussed further in the titration Section (Section 4.3.5). From Table 4.5, the percentage of calcium in the deposit increased as the applied current densities were increased.

The images shown in Plates 4.11 and 4.12 illustrate the microstructure of calcareous films formed under conditions of over protection. Samples were immersed for a period of one week in artificial seawater, and higher current densities of 300 mA/m^2 and 400 mA/m^2 were applied.

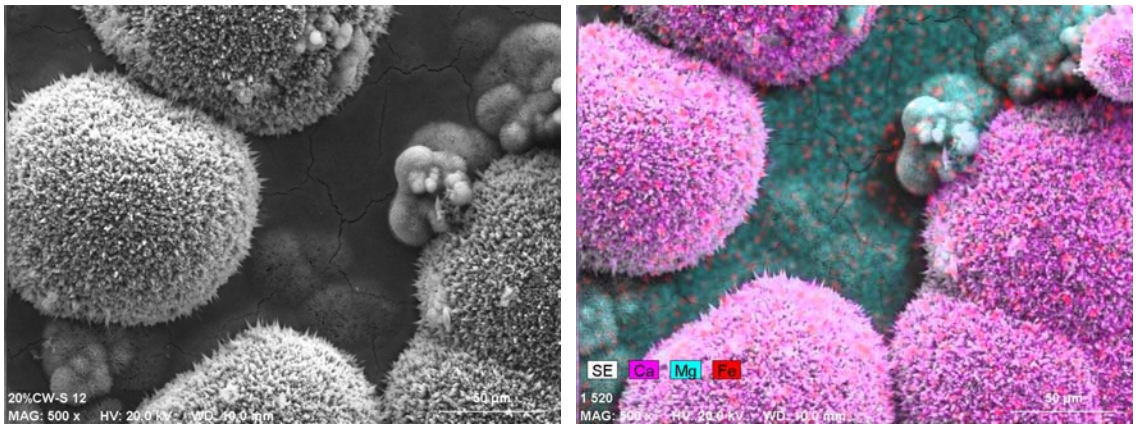

(a) Secondary image taken at 500x **(b) Combined SE image and EDX maps at 500x**

Plate 4.11. Secondary Electron SEM image and combined SEM/EDX element map image of deposit obtained after 7 days immersion in artificial seawater using an applied current density of 300 mA/m^2: a. SE image; b. SE image with corresponding overlaid EDX element distribution maps for Ca, Mg and Fe.

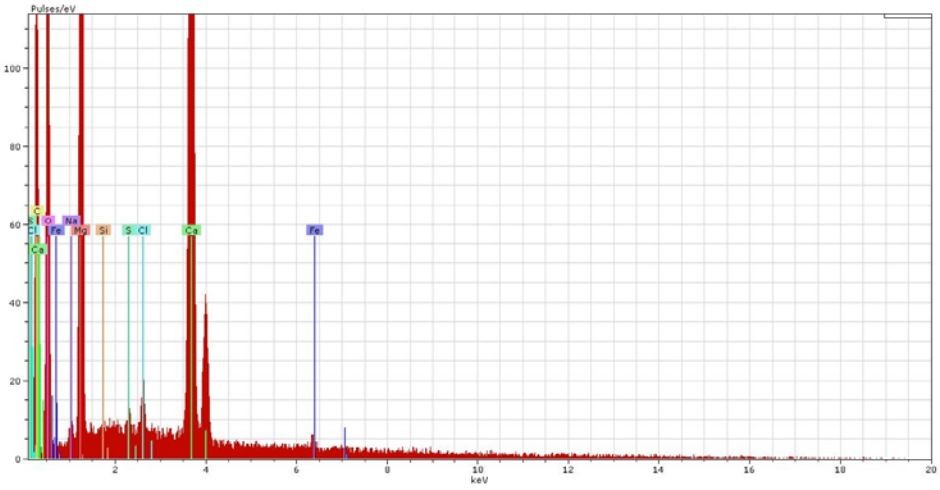

Figure 4.19. EDX spectra of surface deposit obtained after immersion in artificial seawater for 7 days using an applied current density of 300 mA/m^2.

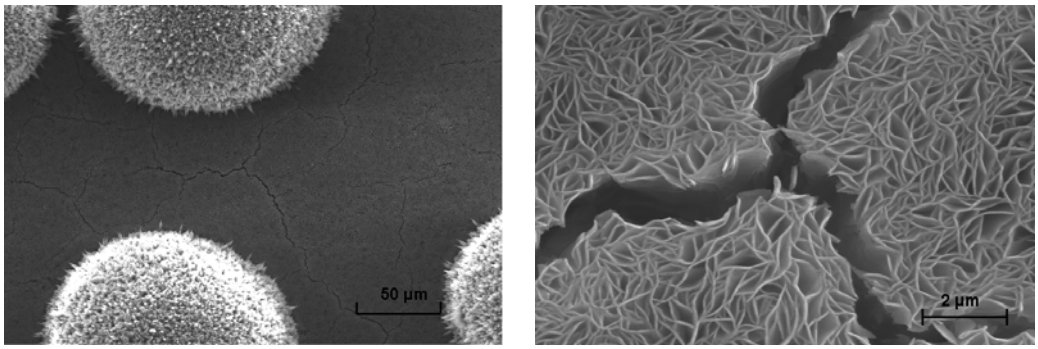

(a) Secondary image taken at 500x **(b) Secondary image taken at 10000x**

Plate 4.12. SEM images at various magnifications of deposit formed after 7 days immersion in artificial seawater using an applied current density of 400mA/m^2.

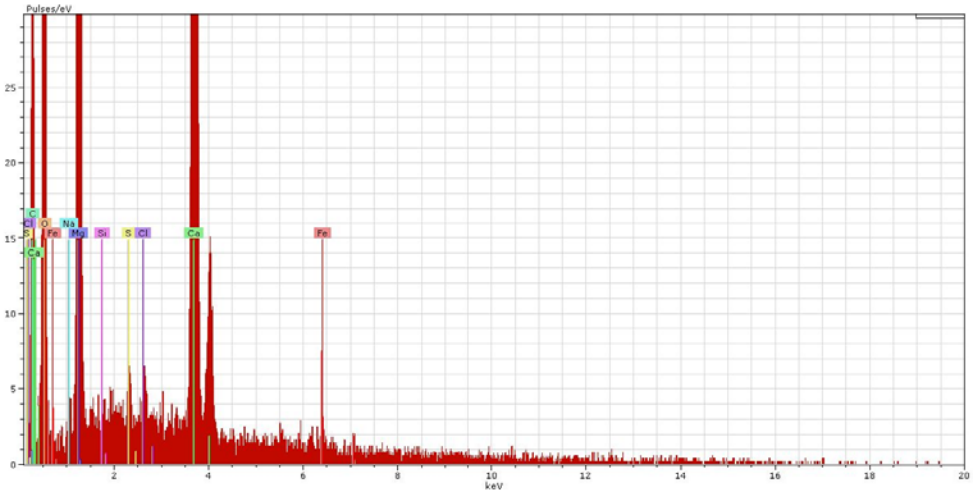

Figure 4.20. EDX spectra of surface deposit obtained after 7 days immersion in artificial seawater using an applied current density of 400 mA/m^2.

Table 4.6. The relative percentages of various elements obtained using EDX quantification, of surface film deposits on steel samples after 7 days immersion in artificial seawater at applied current densities of 300 mA/m^2 and 400 mA/m^2.

Applied Current Density (mA/m^2)	Percentage of Element								
	Carbon	Oxygen	Sodium	Magnesium	Silicon	Sulfur	Chlorine	Calcium	Iron
300	16	49.33	0.29	17.64	0.14	0.19	0.52	15.12	0.34
400	18	48.09	0.35	17.3	0.24	0.27	0.43	14.9	0.37

From the secondary electron SEM images and corresponding EDX element distribution maps shown in Plate 4.11 and the associated EDX spectra given in Figure 4.19, it was evident that there are significant deposits of calcium distributed over much of the sample surface, while the results presented in Table 4.6 show that the percentages of iron in these two cases is extremely low (0.34% and 0.37%) which are both only just over the detection limits of the instrument. The calcium containing regions have the typical distinctive microstructure and characteristic surface morphology of aragonite deposits, which have also been noted by other workers [13]. Similar calcium containing deposits were also found to cover most of the surface of the sample immersed for 7 days in artificial seawater at an applied current density of 400 mA/m^2, which would also provide conditions of overprotection, as illustrated in Plate 4.12 and confirmed by the EDX spectra given in Figure 4.20.

In addition, another reason why it is probably reasonable to assume that the samples at the applied current densities of 300 mA/m^2 and 400 mA/m^2 are almost certainly over-protected is because there were some cracks on the surfaces of the samples, which are clearly evident in the high magnification image given in Plate 4.12(b), (note that the potential of the sample at applied current density of 400 mA/m^2 was around -1050 mV in Figure 4.10), so the cracking and detachment of the sample surface that is evident in Plate 4.12(b) was possibly caused by hydrogen evolution.

4.3.4.4. SEM and EDX examination of sample/deposit cross-sections.

From the results discussed previously in Section 4.3.4.1 and 4.3.4.2, which describes the short term immersion experiments of 6 hours, 1 day and 3 days duration, the surface topography and composition of the deposits were determined using basic SEM imaging and EDX analyses. However, to improve our understanding of the build up of the deposition process, some analyses of cross-sections were also carried out. It was anticipated that this procedure would provide useful information regarding the structure and elemental composition of the films during the formation process, and also show the distribution of the various Ca and Mg rich mineral deposits through the Z-direction of the film. Due to the fact that the thinner films formed during short periods of immersion (6 hours and 24 hours) were extremely fragile, this technique was only suitable for thicker films formed over several days of immersion, and only four current densities were investigated. These were 100 mA/m^2, 150mA/m^2, 200 mA/m^2 and 300 mA/m^2 and again were for a seven day period of immersion. The experimental procedures used have already been described in Chapter 3. As with the previous experiments, four values of current densities were chosen because 100 mA/m^2 is typical of under protection, 150 mA/m^2 is just fully protected, 200 mA/m^2 is well protected, and 300 mA/m^2 is possibly over protected.

(1) Applied current density 100 mA/m^2.

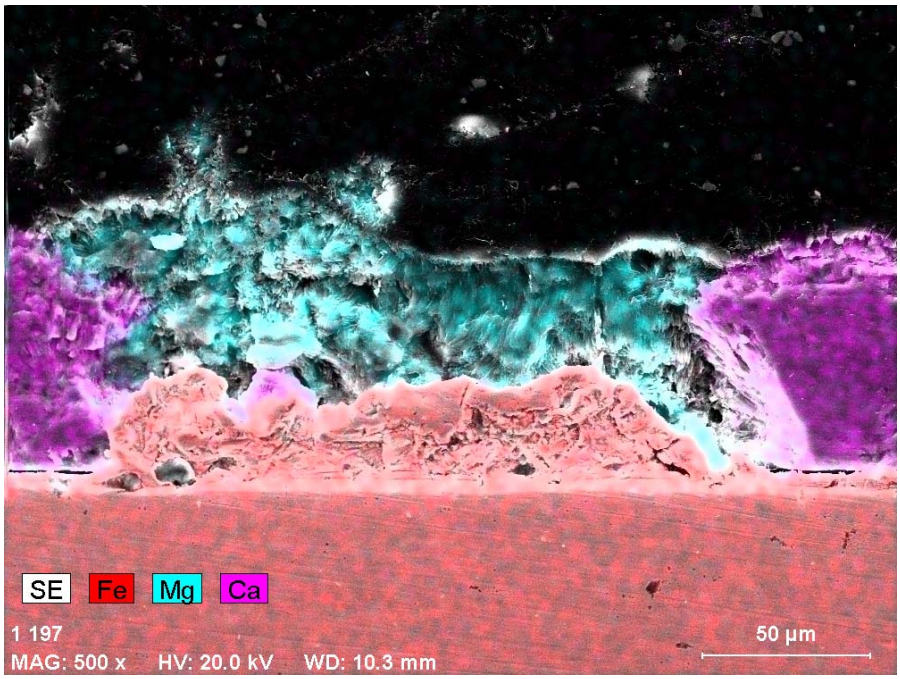

Plate 4.13(a). SEM micrograph and overlaid corresponding EDX element distribution maps for Fe, Mg and Ca; of cross-section of calcareous deposit formed after 7 days immersion in seawater.

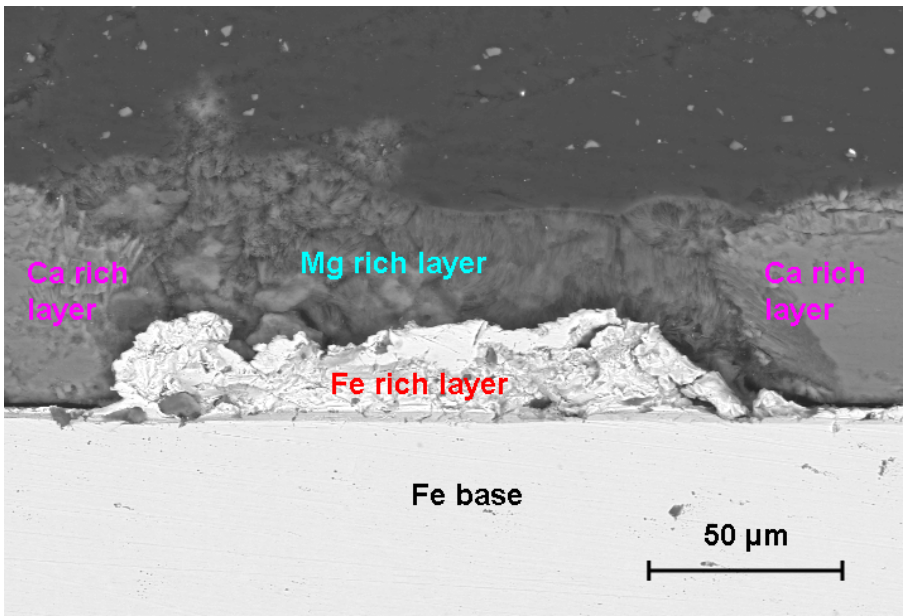

Plate 4.13(b). SEM micrograph showing cross-section of deposit formed after 7 days immersion in artificial seawater.

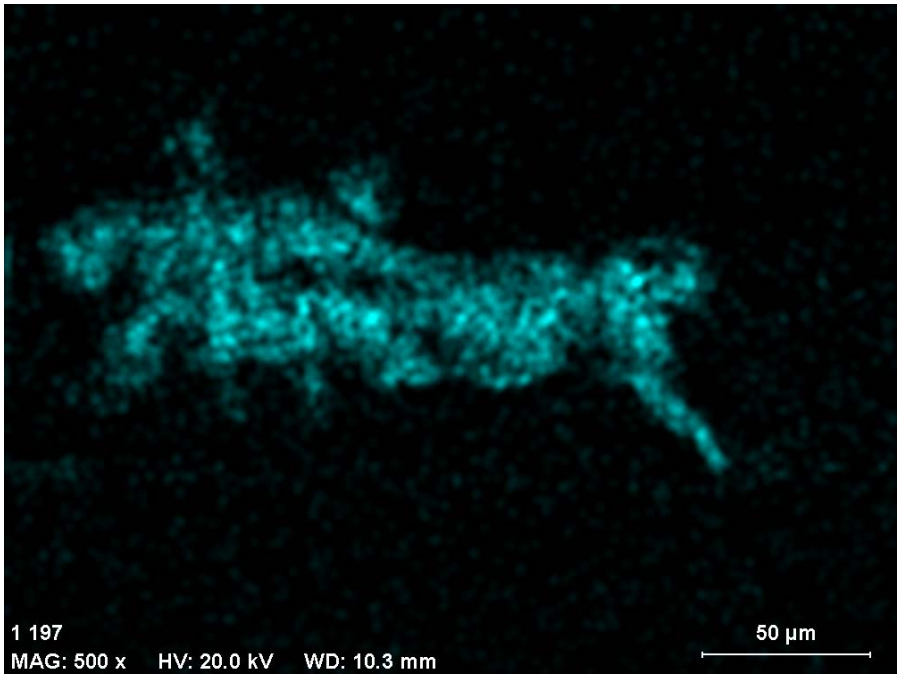

Plate 4.13(c). Single EDX element map, showing occurrence and distribution of Mg, over surface of sample cross-section illustrated previously in Plate 4.13(a, b).

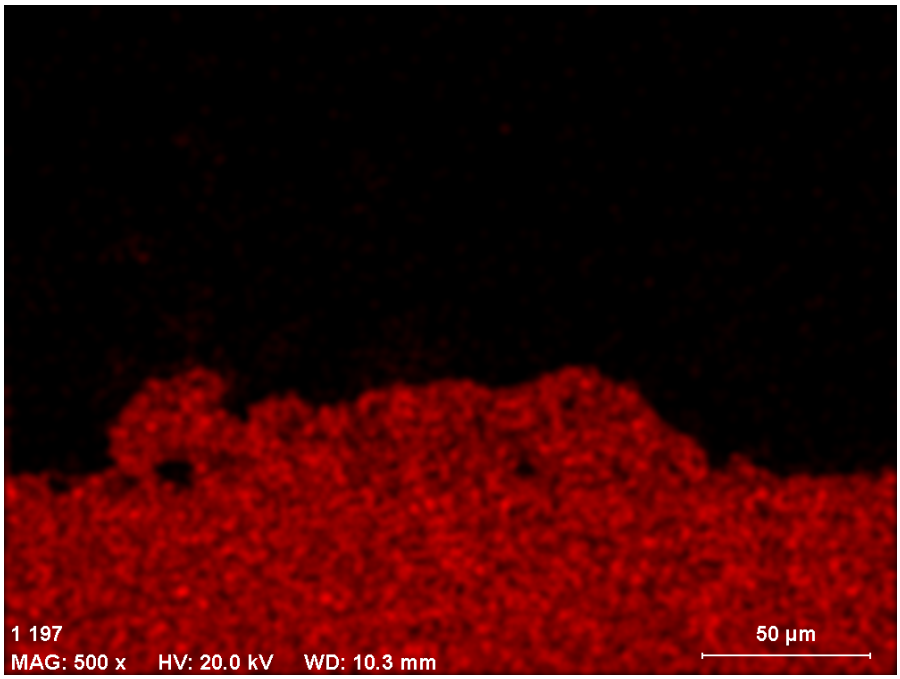

Plate 4.13(d). Single EDX element map, showing occurrence and distribution of Fe, over surface of sample cross-section illustrated previously in Plate 4.13(a, b).

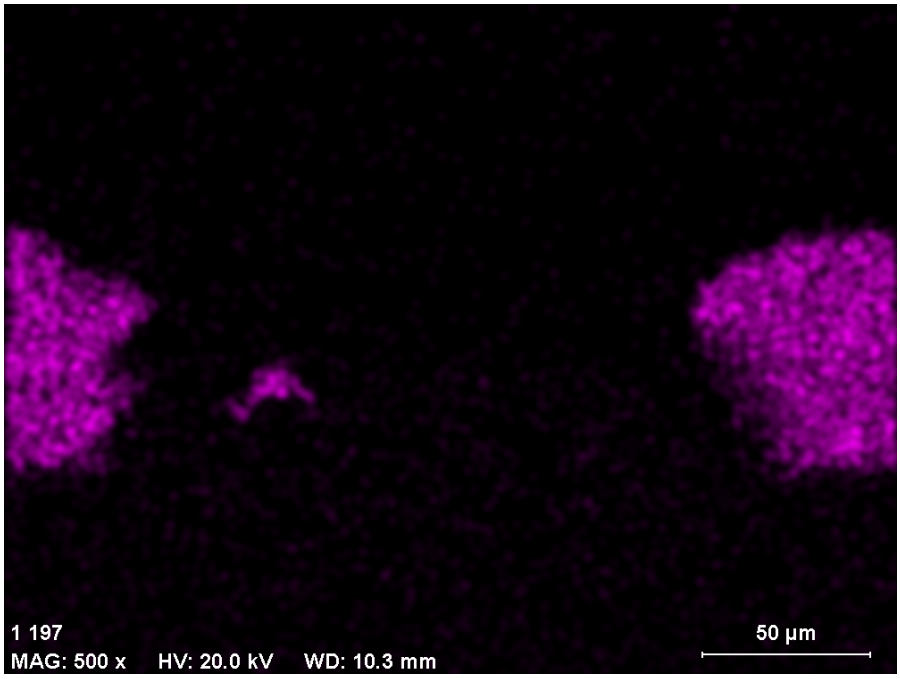

Plate 4.13(e). Single EDX element map, showing occurrence and distribution of Ca, over surface of sample cross-section illustrated previously in Plate 4.13(a, b).

Plate 4.13. SEM and EDX analysis of cross-section of deposit formed at applied current density of 100 mA/m^2 during 7 days immersion in artificial seawater.

(2) Applied current density 150 mA/m^2.

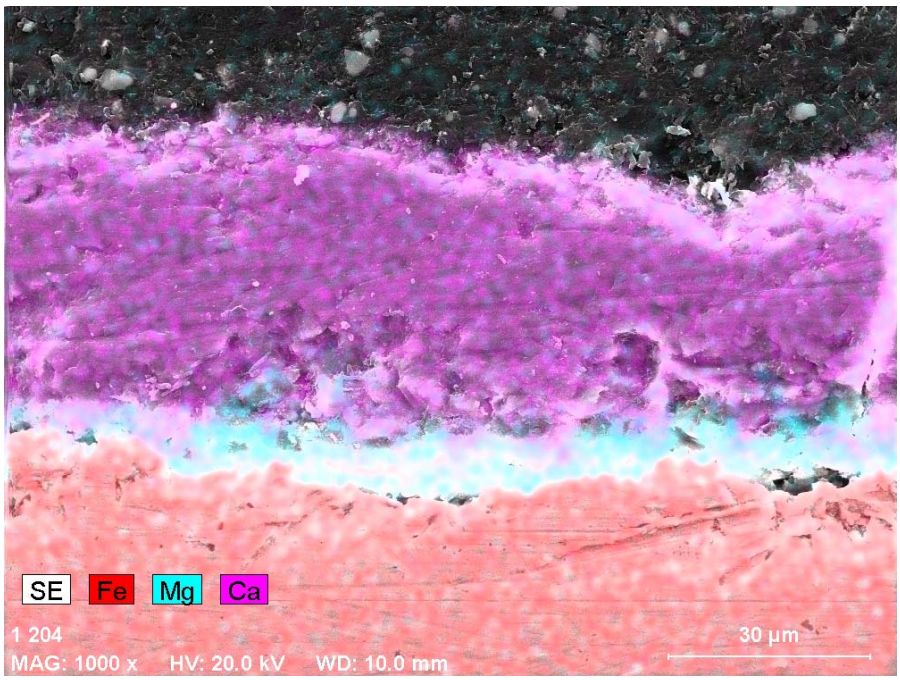

Plate 4.14(a). SEM micrograph and corresponding EDX element distribution maps for Mg and Ca, of cross-section of calcareous deposit formed after 7 days immersion in seawater.

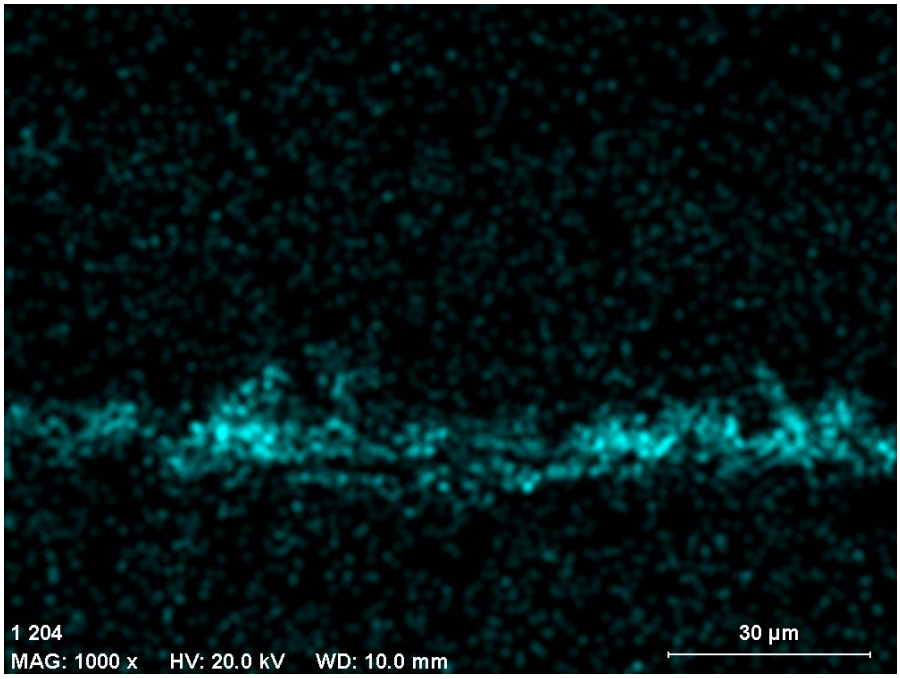

Plate 4.14(b). Single EDX element map, showing occurrence and distribution of Mg, over surface of sample cross-section illustrated previously in Plate 4.14(a).

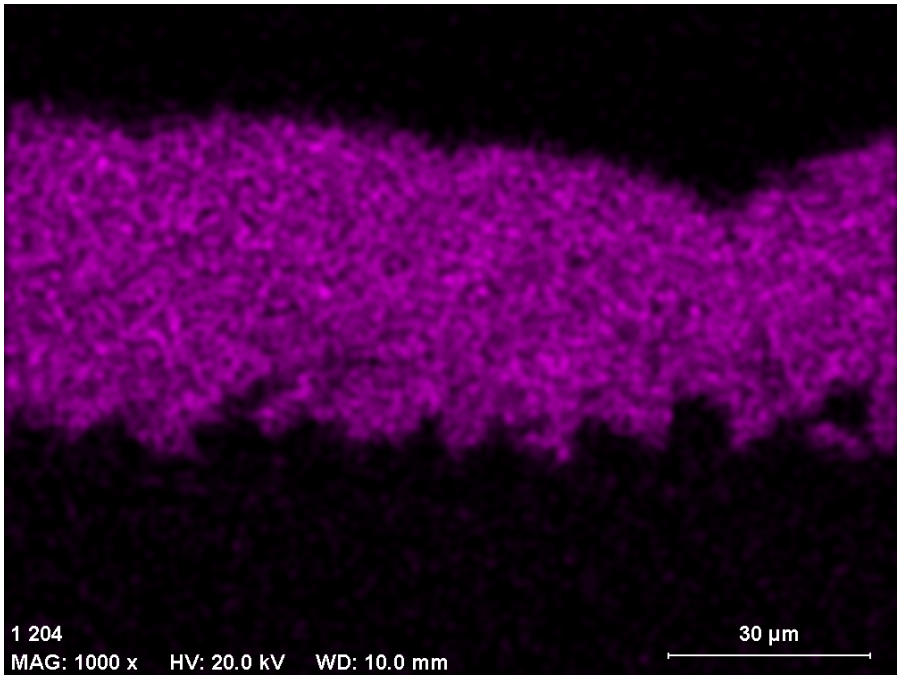

Plate 4.14(c). Single EDX element map, showing occurrence and distribution of Ca, over surface of sample cross-section illustrated previously in Plate 4.14(a).

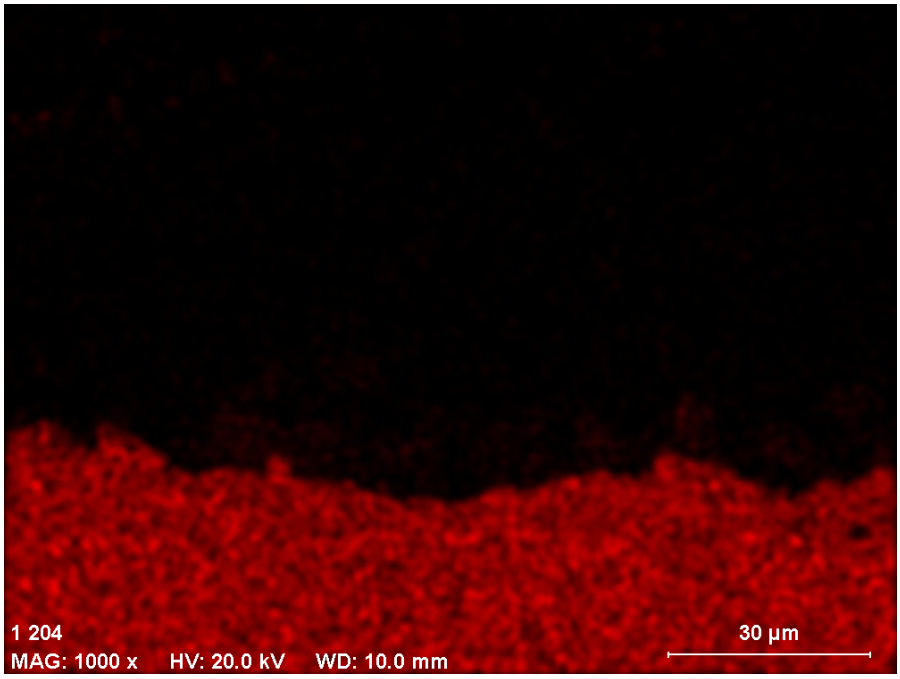

Plate 4.14(d). Single EDX element map, showing occurrence and distribution of Fe, over surface of sample cross-section illustrated previously in Plate 4.14(a).

Plate 4.14. SEM images and associated EDX mapping results for cross-section of deposit obtained using an applied current density of 150 mA/m^2 for 7 days immersion.

(3) Applied current density 200 mA/m^2.

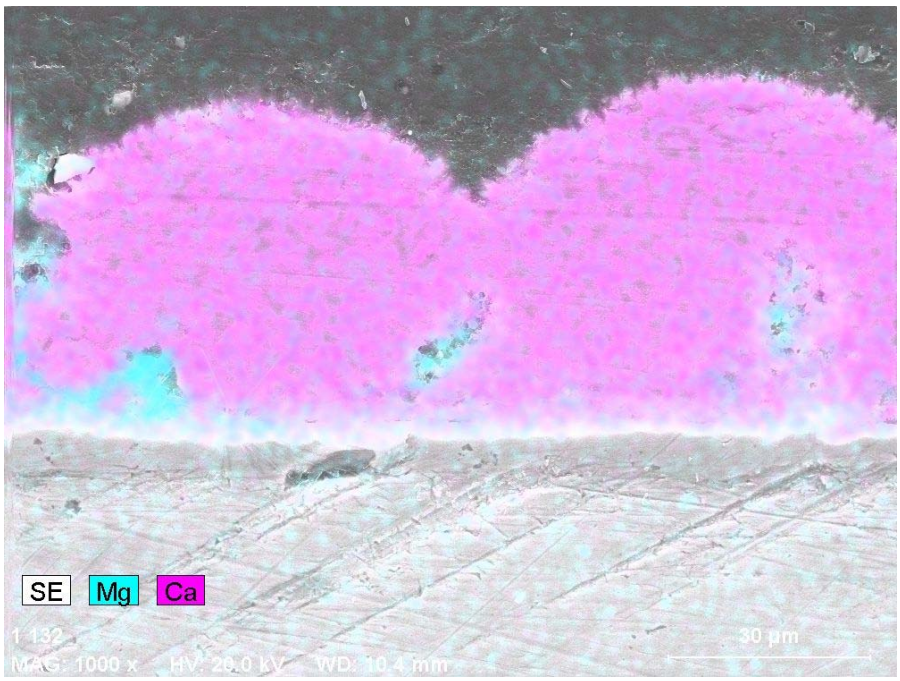

Plate 4.15(a). SEM micrograph and corresponding EDX element distribution maps for Mg and Ca, of cross-section of calcareous deposit formed after 7 days immersion in seawater.

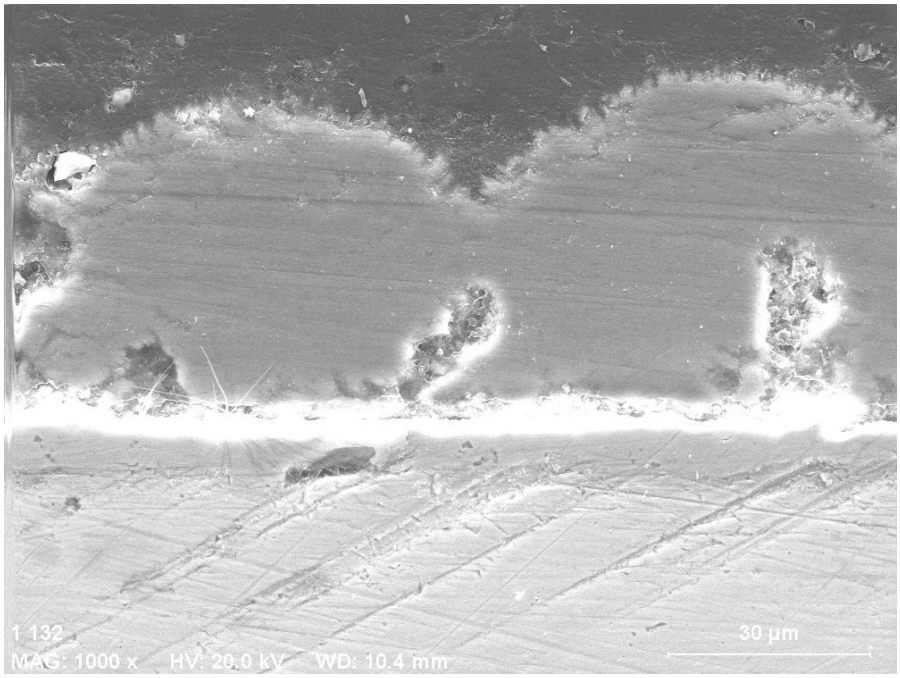

Plate 4.15(b). SEM micrograph showing cross-section of deposit formed after 7 days immersion in artificial seawater.

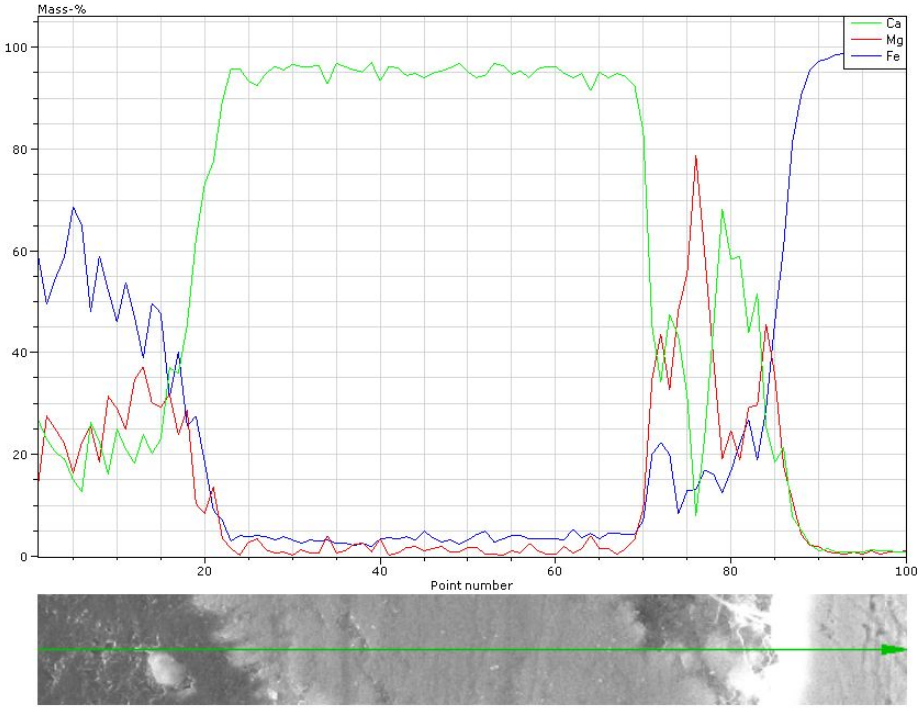

Plate 4.15(c). EDX quantitative line-scan (top graphic) showing variation in relative percentages of Ca, Mg and Fe over selected (green) line on sample cross-section (lower micrograph).

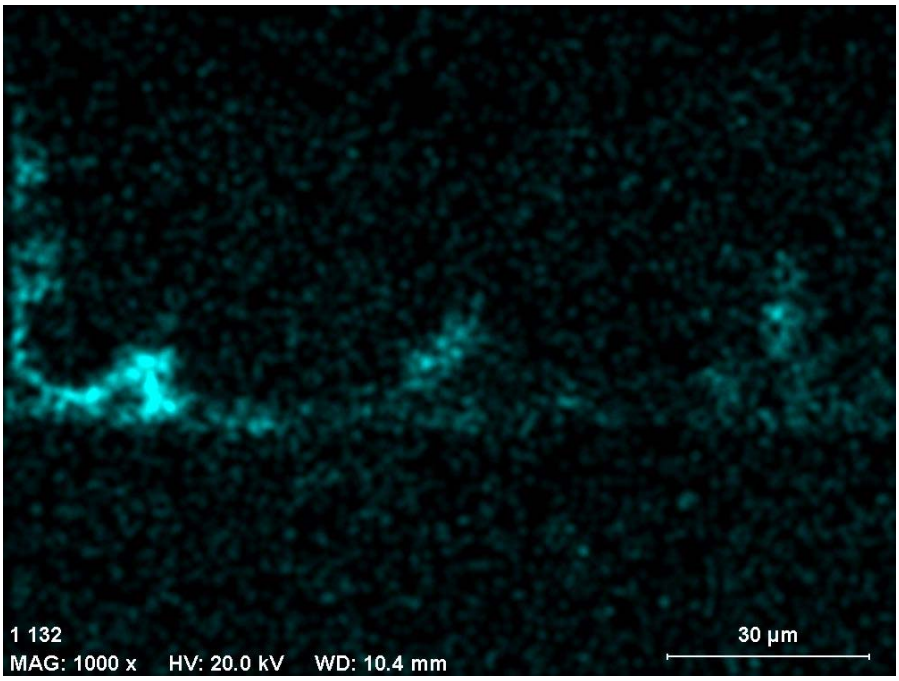

Plate 4.15(d). Single EDX element map, showing occurrence and distribution of Mg, over surface of sample cross-section illustrated previously in Plate 4.15(a, b).

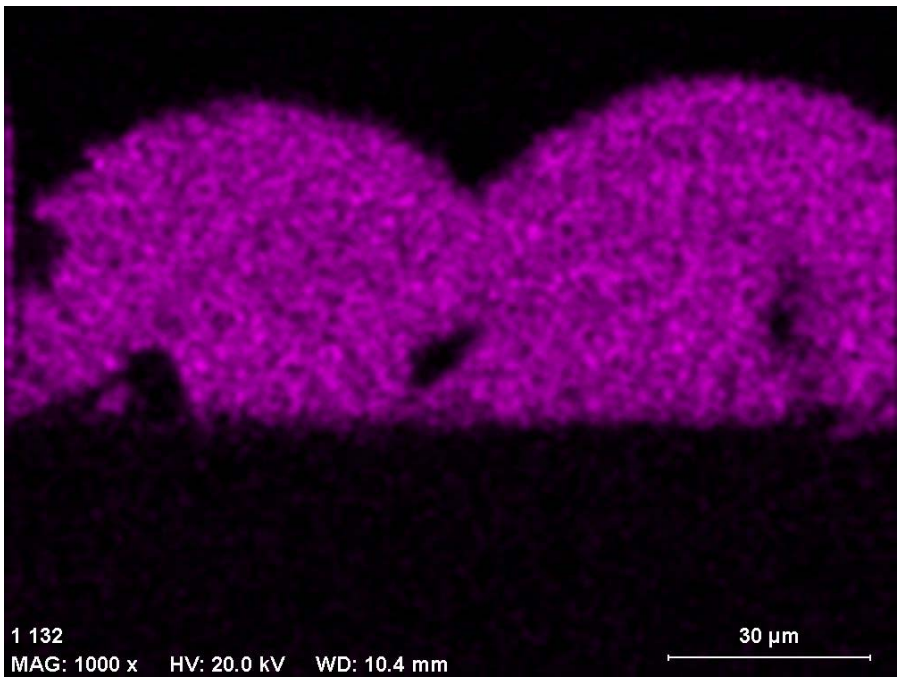

Plate 4.15(e). Single EDX element map, showing occurrence and distribution of Ca, over surface of sample cross-section illustrated previously in Plate 4.15(a, b).

Plate 4.15. SEM images and associated EDX mapping results for cross-section of deposit obtained using an applied current density of 200 mA/m^2 for 7 days.

(4) Applied current density 300 mA/m^2.

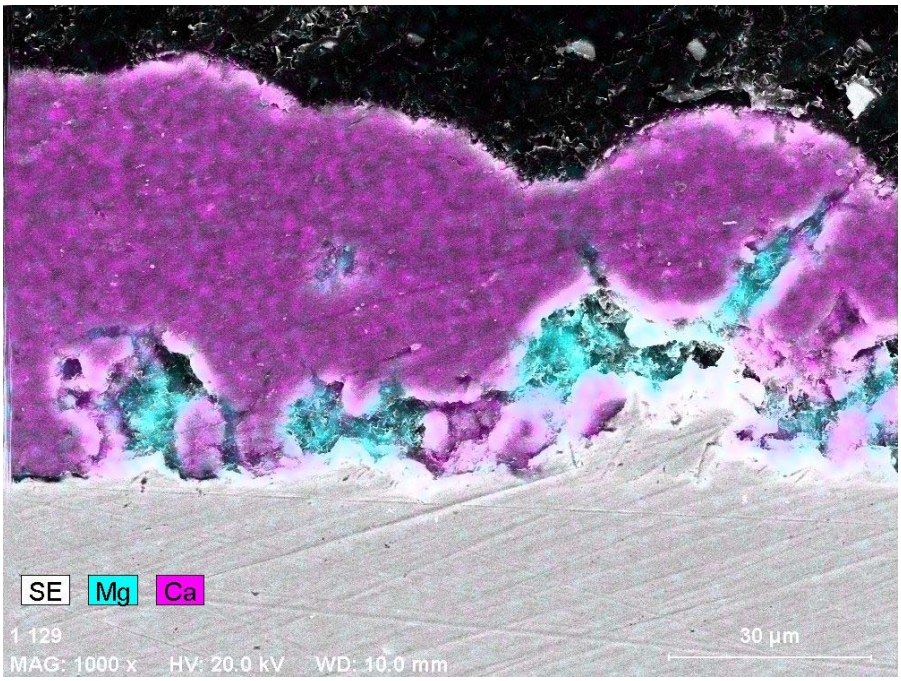

Plate 4.16(a). SEM micrograph and overlaid corresponding EDX element distribution maps for Mg and Ca, of cross-section of calcareous deposit formed after 7 days immersion in seawater.

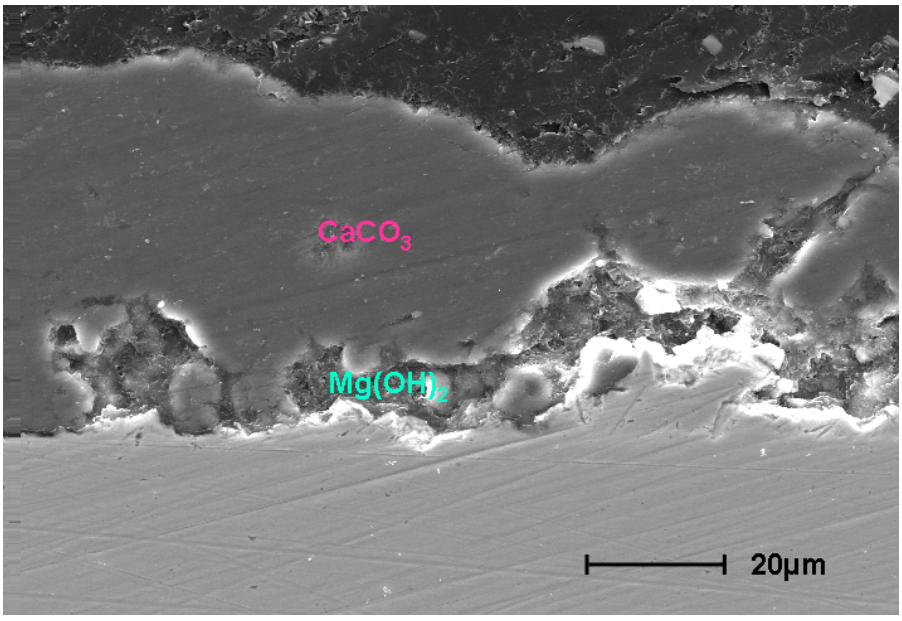

Plate 4.16(b). SEM micrograph showing cross-section of deposit formed after 7 days immersion in artificial seawater.

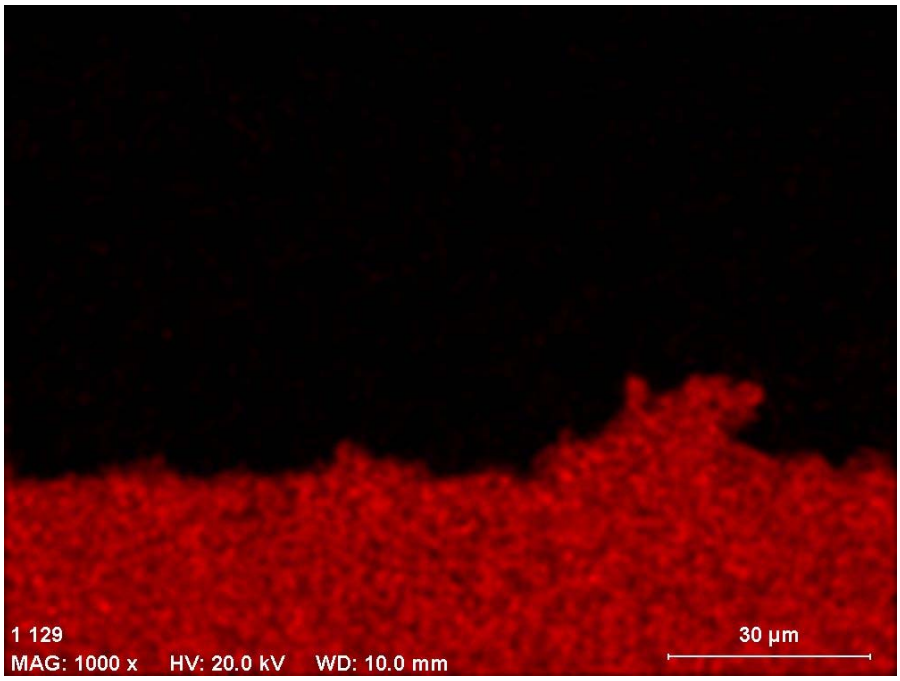

Plate 4.16(c). Single EDX element map, showing occurrence and distribution of Fe, over surface of sample cross-section illustrated previously in Plate 4.16(a, b).

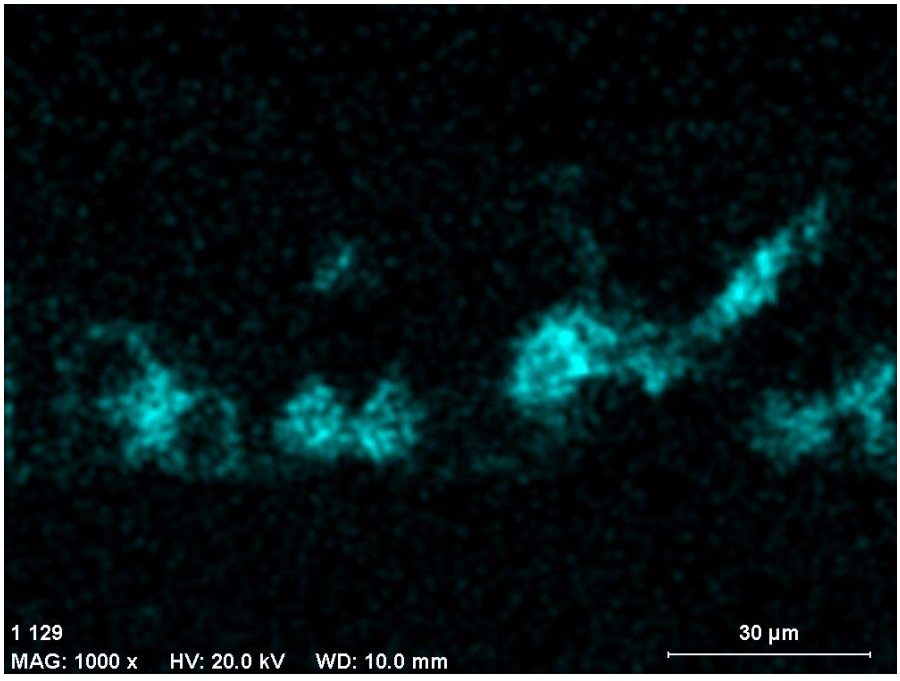

Plate 4.16(d). Single EDX element map, showing occurrence and distribution of Mg, over surface of sample cross-section illustrated previously in Plate 4.16(a, b).

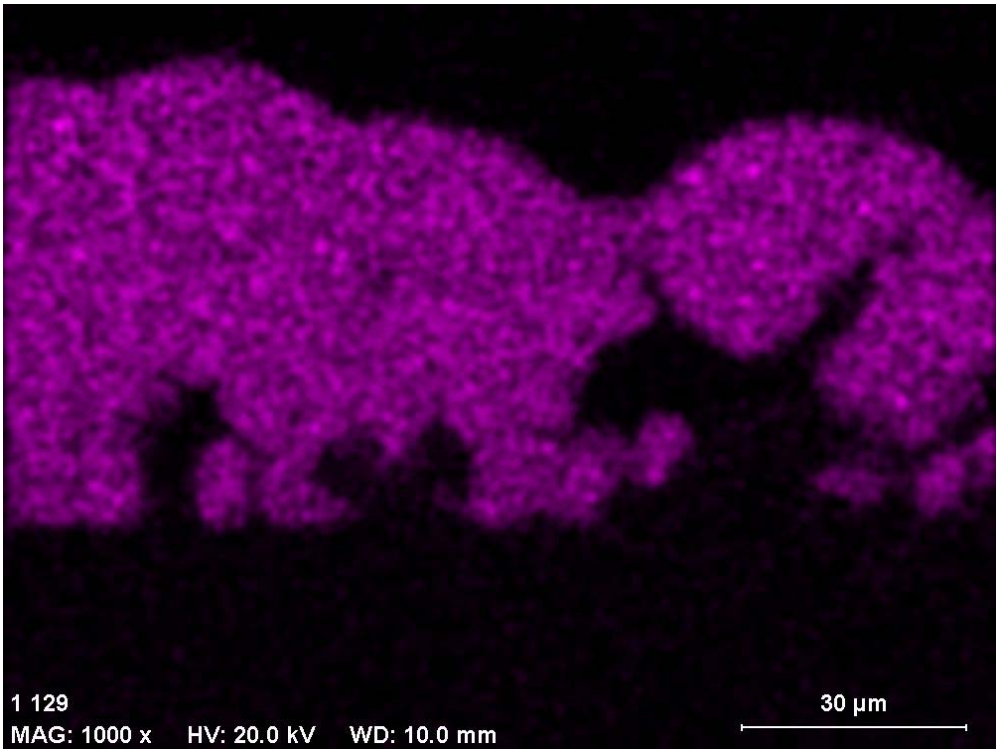

Plate 4.16(e). Single EDX element map, showing occurrence and distribution of Mg, over surface of sample cross-section illustrated previously in Plate 4.16(a, b).

Plate 4.16. SEM images and EDX mapping results for cross-section of deposit obtained using an applied current density of 300mA/m^2 for 7 days.

The results of the SEM investigation and EDX analyses for all samples studied are presented in the preceding Plates 4.13 to 4.16. The selection of SEM micrographs shown, together with the corresponding elemental maps and line scans show the occurrence and distribution of Mg, Ca and Fe within the sectioned deposits at the end of the 7 day immersion period.

Furthermore, from Plates 4.13 to 4.16, it is evident from the integrity of these layers, that it appears that at the lower current density of 100 mA/m^2 (Plate 4.13) [potentials of around -840 mV] the layers formed are well defined, intact and adherent both to the steel substrate and to each other.

Plates 4.13(a) and (b) give information regarding the under-protected (100 mA/m^2) situation, Plates 4.13(a) and (b) show a clear example of the way the magnesium containing deposit is interrelated with the underlying growing iron oxide. The magnesium is always found above this iron deposit and the reasons why this is the case may well

involve the phenomenon of co-precipitation and hence this provides the justification for our further study using acid - base titration (Section 4.3.5).

Plates 4.14 and 4.15 show the elemental distributions for Mg, Ca and Fe over the cross-section of the deposit obtained with applied current densities of 150 mA/m^2 and 200 mA/m^2 respectively. The thinner bottom layer is probably $Mg(OH)_2$ and the thicker top layer is $CaCO_3$ (aragonite, see XRD Section 4.3.5). In addition, Plate 4.15(c) shows quantitative line scans of a region of the cross-section of the deposit where the ratio of Ca, Mg and Fe varies across the Z-direction of the deposit. There is a low Ca/Mg ratio adjacent to the sample surface, whilst a higher Ca/Mg ratio was observed furthest from the metal surface. These observations indicate that the Mg containing compound deposits first and the Ca- rich compound deposits later. At the current densities of 200 mA/m^2 and 300 mA/m^2 (Plates 4.15 and 4.16), some cracks appear and it is perhaps reasonable to suggest that this phenomenon is due to hydrogen evolution from the steel. In this condition, the cathodic reaction of water reduction occurs ($2H_2O + 4e^- \rightarrow 2OH^- + H_2$). This is also in accordance with the SEM photomicrographs presented in Plates 4.11 and 4.12, which clearly show regions at higher magnification, where the underlying regions of the films have cracked and become detached at the higher current densities, as discussed in Section 4.3.4.3.

Overall, the SEM and EDX results obtained of the samples at full cathodic protection levels revealed that the deposits were composed of two layers with a clear boundary. In Plates 4.14 to 4.16, the inner layer is Mg-rich, whilst the outer layer was Ca-rich. From the later XRD results the outer layer was subsequently shown to be aragonite ($CaCO_3$), whilst the inner layer was originally thought to be to be brucite ($Mg(OH)_2$) but the subsequent analysis by X-Ray Diffraction did not provide absolute confirmation of this assumption [See Section 4.3.6 for account of the XRD study].

4.3.5 Titration experiment.

The titration experiments were used to establish the pH of possible precipitation from seawater. It is well known that the pH of any precipitation process can be predicted from calculations based on knowledge of the solubility-product constant and the concentration of cations and anions of the particular compound in solution.

For example, the pH of calcium carbonate precipitation can be calculated from following equations. The $CaCO_3$ has the solubility-product constant of $K = [Ca^{2+}]*[CO_3^{2-}]=3.8*10^{-9}$ [17] at 20°C and as we have seen earlier in Chapter 2 the typical concentration of Ca^{2+} in seawater is 1.123g/1000g solution namely $[Ca^{2+}] = 0.01M$. With this knowledge, the concentration of CO_3^{2-} when $CaCO_3$ precipitates will be:

$$[CO_3^{2-}] = \frac{K_{CaCO3}}{[Ca^{2+}]} = 3.8*10^{-7} M \quad \ldots\ldots\ldots\ldots\ldots\ldots\ldots\ldots\ldots\ldots\ldots\ldots\ldots\ldots\ldots\ldots \quad (4\text{-}1)$$

The process of $CaCO_3$ precipitation that occurs when CO_3^{2-} formed during the reaction of $NaHCO_3$ present in the seawater with an alkaline solution is according to the reaction 4-2,

$$NaHCO_3 + OH^- = H_2O + 2Na^+ + CO_3^{2-} \quad \ldots\ldots\ldots\ldots\ldots\ldots\ldots\ldots\ldots\ldots\ldots\ldots\ldots\ldots\ldots\ldots \quad (4\text{-}2)$$

Where the concentration of OH^- is equal to the concentration of CO_3^{2-} during reaction 4-2. Taking into consideration equation 4-1, the concentration of OH^- will be:

$$[OH^-] = [CO_3^{2-}] = 3.8*10^{-7} M \quad \ldots\ldots\ldots\ldots\ldots\ldots\ldots\ldots\ldots\ldots\ldots\ldots\ldots\ldots\ldots\ldots \quad (4\text{-}3)$$

The concentration of H^+ during precipitation of $CaCO_3$ from seawater will be:

$$[H^+] = \frac{10^{-14}}{[OH^-]} = \frac{10^{-14}}{3.8*10^{-7}} = 2.63*10^{-8} M \quad \ldots\ldots\ldots\ldots\ldots\ldots\ldots\ldots\ldots\ldots\ldots\ldots\ldots\ldots \quad (4\text{-}4)$$

So the pH for precipitation of $CaCO_3$ is $pH = -log\ [H^+] = 7.58$.

Similarly in order to precipitate $Mg(OH)_2$ with the solubility-product constant

$K = 6*10^{-10}$ [17] and the concentration of $[Mg]^{2+} = 0.053M$, which is a typical concentration of $[Mg]^{2+}$ in seawater (5.07g/1000g solution), a significantly higher pH is required if we compare this with the pH necessary for $CaCO_3$ precipitation to occur.

The magnesium hydroxide precipitates according to the reaction:

$Mg^{2+} + 2OH^- = Mg(OH)_2$, where $K = [Mg^{2+}]*[OH^-]^2$.

The concentration of OH^- when $Mg(OH)_2$ precipitates can be calculated from K and will be:

$$[OH^-] = \sqrt{\frac{K_{Mg(OH)2}}{[Mg^{2+}]}} = \sqrt{\frac{6*10^{-10}}{5.3*10^{-2}}} = \sqrt{1.13*10^{-8}} = 1.06*10^{-4} M \quad \text{..... (4-5)}$$

The pH of $Mg(OH)_2$ precipitation will be:

$$[H^+] = \frac{10^{-14}}{[OH^-]} = \frac{10^{-14}}{1.06*10^{-4}} \approx 10^{-10} \text{ M} \quad \text{..... (4-6)}$$

So the pH for precipitation of $Mg(OH)_2$ is around 10.

There is general agreement in the literature that calcium carbonate precipitates at a less alkali pH compared with the pH of magnesium hydroxide precipitation [13]. This was clearly shown by the calculations and equations given above, and we have confirmed that a pH of 7.58 is required for precipitation of $CaCO_3$, whilst a pH of 10 is required for precipitation of $Mg(OH)_2$ from seawater. When the steel is under cathodic protection in seawater, the pH near the steel surface slowly becomes more alkaline due to undergoing a cathodic reaction of oxygen reduction and the deposition of calcium carbonate is expected to occur first. The rationale for our titration experiments arises from our studies on the deposited films formed during cathodic protection at the conditions when steel was underprotected. In every case it was demonstrated that the compound that is initially precipitated next to the iron-containing corrosion products is possibly brucite ($Mg(OH)_2$), and not calcium-rich aragonite (calcium carbonate, $CaCO_3$). The study of the SEM micrographs and X-ray analysis data given in Plate 4.11 (Section 4.3.4.4) indicate that there is an association between the iron corrosion product and the overlaying magnesium rich compound, which is possibly $Mg(OH)_2$ (brucite). The presence of brucite in the vicinity of iron hydroxides might be explained by the co-precipitation of brucite during formation of corrosion products when steel corrodes. The possibility of co-precipitation is based on the work by Packter and Derby [18] who established and examined the mechanisms of co-precipitation of magnesium and iron hydroxides from aqueous solution using potentiometric titration.

The $Fe(OH)_3$ precipitates at a significantly lower pH compared to that of $CaCO_3$ and this pH can be calculated from the solubility-product constant K = $6.3*10^{-38}$ [17] of iron hydroxide and the reaction of hydroxide formation $Fe^{3+} + 3OH^- = Fe(OH)_3$. For the

reaction of hydroxide formation $K = [Fe^{3+}]*[OH^-]^3 = 6.3*10^{-38}$ and assuming that the concentration of $[Fe^{3+}] = 0.01M$ (the concentration of Fe^{3+} has been chosen similar to the concentration of Ca^{2+} in seawater), the concentration OH^- and H^+ during iron hydroxide precipitation will be:

$$[OH^-] = \sqrt[3]{\frac{6.3*10^{-38}}{10^{-2}}} = \sqrt[3]{6.3*10^{-36}} = 1.8*10^{-12}\,\text{M} \quad \text{(4-7)}$$

$$[H^+] = \frac{10^{-14}}{[OH^-]} = \frac{10^{-14}}{1.8*10^{-12}} = 5.4*10^{-3}\,\text{M} \quad \text{(4-8)}$$

The pH for precipitation of $Fe(OH)_3$: pH = -log $[H^+]$ = 2.26.

For the underprotected steel situation where iron (III) hydroxides will be formed due to corrosion of steel, the $Mg(OH)_2$ might be precipitated together with iron (III) hydroxides at a pH = 2.26, and hence well before precipitation of $CaCO_3$. It is therefore necessary to prove that $Mg(OH)_2$ will precipitate with iron (III) hydroxides at pH = 2.26, instead of its expected precipitation at pH = 10, and so the titration experiment should verify this fact and was conducted in this study.

In our situation, the experiment chosen had the accurately prepared alkali solution in the burette which is then slowly added in carefully controlled drop-by-drop increments into a beaker containing the solutions under examination, also at exactly known Molar concentrations. The course of the reaction was followed by continuous measurements of pH. Stocks of the Analar-grade laboratory reagents magnesium chloride ($MgCl_2$) and iron (III) chloride ($FeCl_3$), together with a standard sodium hydroxide solution of 1M concentration were supplied by the Fisher Company. The required concentration of sodium hydroxide solution (0.01M) was prepared by diluting the stock 1M sodium hydroxide solution with deionised water. The magnesium chloride solution (0.05M) was prepared directly from the Analar-grade reagents, such that the Mg concentration in the testing solution was the same as the concentration of magnesium chloride in seawater. The 0.01M concentration iron (III) chloride solution was similarly prepared.

The individual solutions of 0.05M $MgCl_2$ and 0.01M $FeCl_3$ together with the mixture of 0.05M $MgCl_2$ and 0.01M $FeCl_3$ were titrated by 0.01M NaOH. For all the titration experiments performed, the volume of the solutions under examination was 20.0 ml, and

contained in a 200 ml beaker, and was continuously stirred using a magnetic stirrer and bar, at 30 r.p.m. The sodium hydroxide solution was carefully added in single drops, whilst the solution temperature was maintained at 20^{o}C. For all titration experiments, the course of both the single precipitation and the co-precipitation reactions were constantly monitored using a pH meter (HI2210 pH Meter). Before the testing commenced, the pH meter was calibrated by using two standard buffer solutions, firstly at pH 7, then followed by pH 4.

In preliminary runs, the sodium hydroxide solution was added in small increments to well past the equivalent volume for a complete reaction to occur.

A total of three sets of titration experiments were performed, these were:

(a) Single titrations for both 0.01M $FeCl_3$ and 0.05M $MgCl_2$.

(b) A co-precipitation for 0.01M $FeCl_3$ and 0.05M $MgCl_2$ combined.

(c) A co-precipitation for 0.01M $FeCl_3$ combined with seawater.

Typical pH vs V_{OH} plots for the separate titration of 0.01M iron (III) chloride ($FeCl_3$) and 0.05M magnesium chloride ($MgCl_2$) solutions with 0.01M sodium hydroxide solution are presented in Figure 4.21. The initial pH of the 0.05M $MgCl_2$ solution was 6.2, which is close to the pH of neutral solution (the red $MgCl_2$ line). The first drop of 0.01M NaOH increased the pH to 9 and after addition of 15 ml of NaOH the pH was increased to 9.8 and remained relatively constant during addition of a further 45 ml of NaOH solution. The final pH of the solution when titration was stopped was 10.

During titration the total of 60 ml of 0.01M NaOH solution that was used was found to be insufficient to complete the reaction:

$MgCl_2 + 2NaOH \rightarrow Mg(OH)_2 + 2NaCl$…… (4-9)

200 ml is required of 0.01M NaOH to react with 20 ml of 0.05 M $MgCl_2$ with an OH/Mg ratio of 2. Therefore the titration curve represents the initial formation of $Mg(OH)^{+}$ with the first 15 ml of NaOH solution when the pH had risen to 9.8 and the commencement of precipitation of $Mg(OH)_2$ then occurred during pH variation between 9.8 and 10 with the addition of a further 45 ml of NaOH solution. At this stage the solution became milky.

The precipitation of $Mg(OH)_2$ has not been completed; however, the pH of precipitation, 10 is confirmed to be similar to the calculated pH.

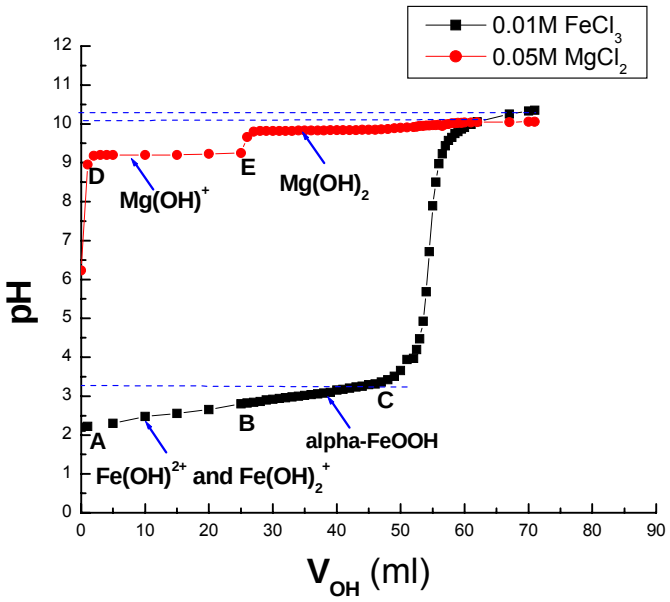

Figure 4.21. Diagram showing individual pH titration curves of both iron (III) chloride ($FeCl_3$) and magnesium chloride ($MgCl_2$) with 0.01M sodium hydroxide (NaOH) solution.

Analysis of the titration of the 0.01M $FeCl_3$ solution with the 0.01M NaOH solution indicated that during titration within the region indicated by Points A and B (the black $FeCl_3$ line in Figure 4.21), the pH increased from 2.15 to 2.8, and the solution colour changed from orange to slight red, indicating the successful formation of the $Fe(OH)^{2+}$ cation, and then $Fe(OH)_2^+$, and finally a colloidal dispersion of iron (III) hydroxide. Precipitation of an orange deposit, which was microcrystalline α-FeOOH [18] commenced around Point B (pH = 2.8) at OH/Fe = 30/20 = 1.5, and then proceeded to complete precipitation of microcrystalline α-FeOOH at OH/Fe = 60/20 = 3, which was at Point C (pH = 3.10). Addition of further excess of sodium hydroxide solution resulted in a rapid rise in pH to 10.4. The stages of α-FeOOH formation are presented in the reactions:

$FeCl_3 + NaOH \rightarrow Fe(OH)^{2+} + Na^+ + 3Cl^-$ …….. (4 -10)

$Fe(OH)^{2+} + NaOH \rightarrow Fe(OH)_2^+ + Na^+$ …….... (4 -11)

$Fe(OH)_2^+ + NaOH \rightarrow$ α-FeOOH $+ Na^+ + H_2O$ …… (4 -12)

The pH vs V_{OH} plot for the co-precipitation from a mixed solution of 0.01M iron (III) chloride ($FeCl_3$) and 0.05M magnesium chloride ($MgCl_2$) [the concentration of

magnesium chloride was the same as that in artificial seawater], by addition of 0.01M sodium hydroxide solution, is presented in Figure 4.22.

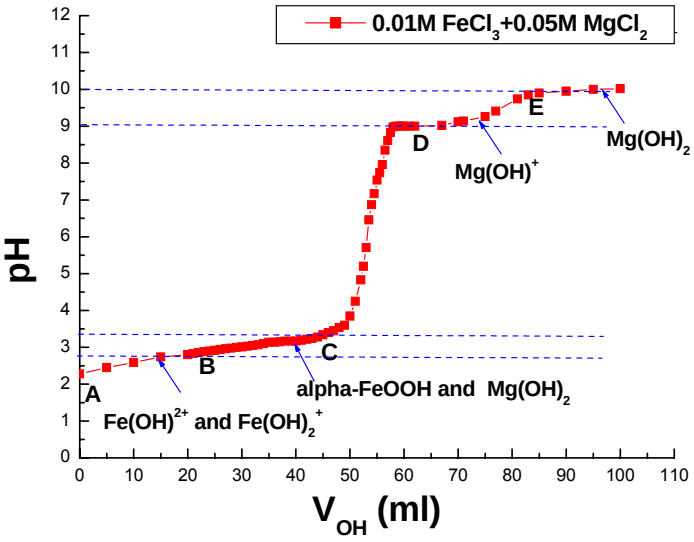

Figure 4.22. Diagram showing pH titration plots of iron (III) chloride ($FeCl_3$) and magnesium chloride ($MgCl_2$) with 0.01M sodium hydroxide (NaOH) solution.

The pH value of the solution mixture was initially 2.2 (at Point A on the red plot line). Then addition of the sodium hydroxide to the solution mixture, the precipitation of α-FeOOH commenced at Point B (pH around 2.9). Formation of microcrystalline α-FeOOH encourages co-precipitation of $Mg(OH)_2$ and promotes the interaction between the α-FeOOH and $Mg(OH)_2$ resulting in formation of magnesium iron (III) hydroxides [18]. The co-precipitation increases the final pH of the BC region to 3.4, The sharp pH rise after point C (pH around 3.7) indicates completion of the α-FeOOH formation (the reactions are described in Equations 4-10, 4-11 and 4-12). 60 ml of 0.01M NaOH solution is required to form α-FeOOH from 20 ml of 0.01M $FeCl_3$ solution. On addition of further sodium hydroxide, the formation of $Mg(OH)^+$ began at Point D (pH about 9.2). The expected precipitation of $Mg(OH)_2$ commenced at Point E (approximate pH 9.8) and continued at pH = 10 to the end of titration.

A similar experiment was carried out on the mixed artificial seawater that consisted of 0.41M NaCl, 0.05M $MgCl_2$, 0.03M Na_2SO_4, 0.002M $NaHCO_3$, 0.01M $CaCl_2$, 0.009M KCl and in the presence of 0.01M iron (III) chloride ($FeCl_3$) solution. The pH vs V_{OH} plot for the course of the titration of 0.01M iron (III) chloride ($FeCl_3$) and artificial seawater with 0.01M NaOH solution is presented in Figure 4.23. The results shown in Figure 4.23

(the line segment B′C′) is very similar to the results obtained in Figure 4.22 (also shown as the similar line segment B-C). This indicates that a similar reaction has occurred leading to the formation of an intimately mixed co-precipitate between α-FeOOH and $Mg(OH)_2$. The difference between the titration of $MgCl_2$ and artificial seawater in the presence of $FeCl_3$ is the appearance of the small shoulder around a pH of 7.6 on the seawater titration curve that is probably associated with formation of $CaCO_3$. In order to form calcium carbonate from 0.009M $NaHCO_3$ solution, 4 ml of 0.01M NaOH solution is required.

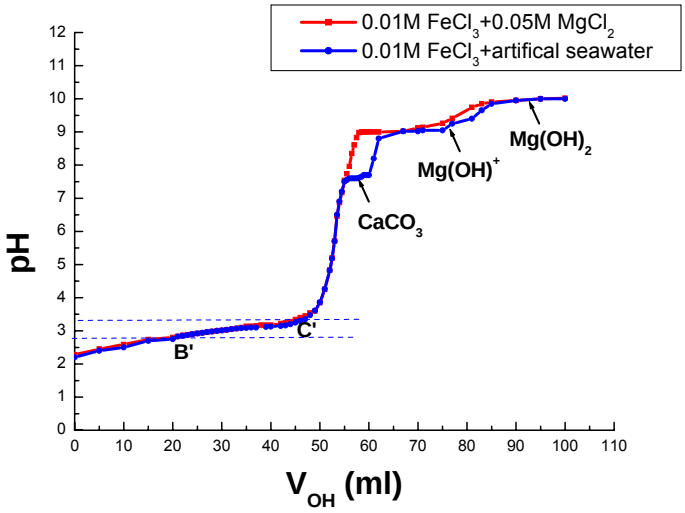

Figure 4.23. Diagram showing pH titration plot of iron (III) chloride ($FeCl_3$) and artificial seawater with 0.01M sodium hydroxide (NaOH) solution.

We have therefore shown that the formation of mixed compounds of magnesium and iron hydroxides is highly possible during cathodic protection of mild steel with underprotected conditions in seawater by a process of co-precipitation of magnesium hydroxide from seawater with iron hydroxides formed during corrosion of the steel.

4.3.6. XRD.

The fundamental operating principle of this powerful analytical technique is based on Braggs law. The XRD investigation was conducted to investigate the presence of other chemical compounds on the metal surface. The full explanation of how this technique works and how data can be generated is well researched, but complex, and the basic concepts and introduction have already been summarized and discussed earlier in this

Thesis in Chapter 3, Section 3.9. All the XRD testing reported in this study was carried out using a Philips XPERT instrument manufactured by Philips Analytical.

The mild steel testing samples used were produced using our standard method described previously in Chapter 3, Section 3.2.1, and immersed for one week in artificial seawater at different levels of galvanostatic polarization with applied current densities ranging between 0 (open circuit condition) and 400 mA/m^2. After polarization, samples were rinsed in deionised water for 5 seconds, then washed in ethanol and dried. Glancing angle X-Ray Diffraction was carried out by analysis of spectra obtained against a High Score plus ICDD PDF4 database with a beam size of 10 mm^2 and a test area of 10 mm^2. The data displays are given after the relevant X-Ray counts/θ plots, and are colour coded. The relevant reference databases are quoted and the likely crystal structures are provided.

(1) Open circuit.

Figure 4.24. XRD pattern for sample surface after immersion in artificial seawater for 7 days (Applied current density was 0 (open circuit)).

Table 4.7. The Compound Name and Chemical Formula using XRD quantification, of calcareous films on steel samples after immersion in artificial seawater for 7 days (Applied current density was 0 (open circuit)).

Visible	Ref. Code	Score	Compound Name	Scale Factor	Chemical Formula
*	00-006-0696	45	bainite, ferrite, ledkunite	0.105	Fe
*	00-044-1415	22	Lepidocrocite, syn	0.061	FeO(OH)
*	00-056-1302	2	Iron Oxide	0.219	Fe_2O_3

Figure 4.24 and Table 4.7 show the XRD analysis results for the sample at open circuit, after immersion for one week in artificial seawater. As expected, the deposit is mainly γFeO(OH) and iron oxide. One might expect some magnesium containing compounds in view of the results from our previous work. It is possible that the values are below the detection limits of the XRD system, or perhaps the magnesium compounds are screened by the iron corrosion products.

(2) 50 mA/m^2 for a week.

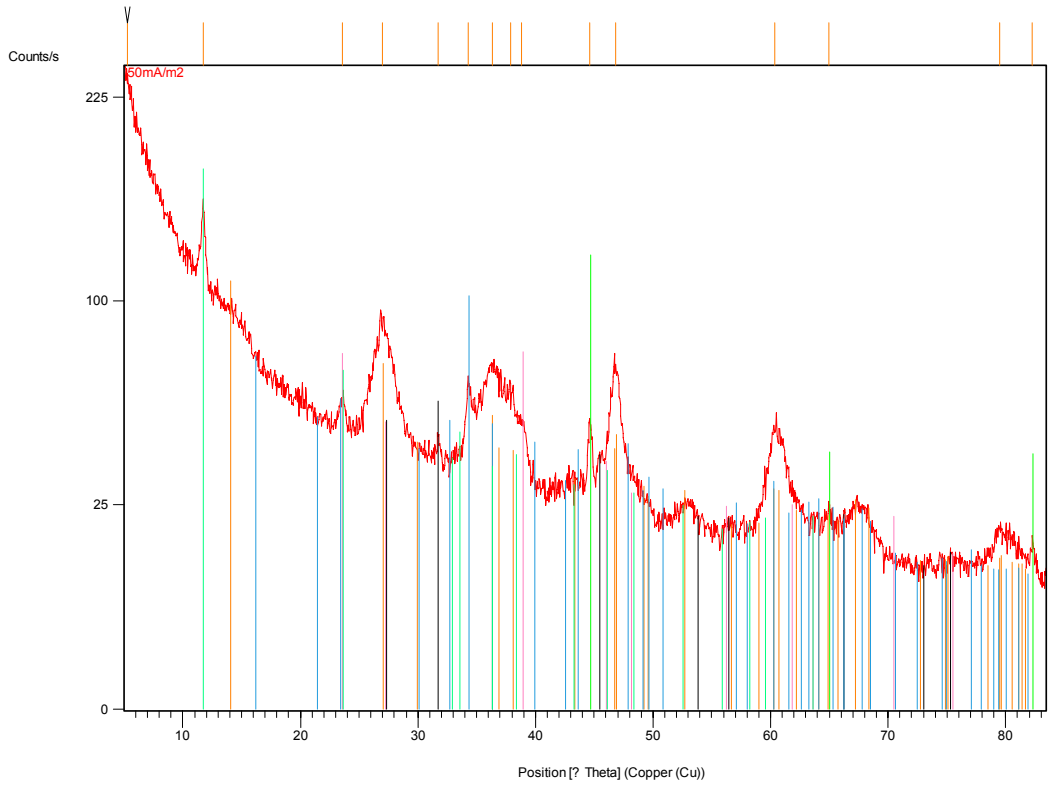

Figure 4.25. XRD pattern for sample surface after immersion in artificial seawater for 7 days (Applied current density of 50 mA/m^2).

Table 4.8. The Compound Name and Chemical Formula using XRD quantification, of calcareous films on steel samples after immersion in artificial seawater for 7 days (Applied current densities of 50 mA/m^2).

Visible	Ref. Code	Score	Compound Name	Scale Factor	Chemical Formula
*	00-006-0696	50	bainite, ferrite, ledkunite	0.219	Fe
*	01-088-0236	40	Sodium Sulfide	0.245	$Na_{1.976}$ S
*	00-044-1415	46	Lepidocrocite, syn	0.716	FeO(OH)
*	00-005-0628	18	Halite, syn	0.163	NaCl
*	04-010-1206	30	eitelite, syn	0.477	$Na_2 Mg (CO_3)_2$
*	00-046-0098	57	Green Rust	0.626	$Fe_6(OH)_{12} (CO_3)$

Figure 4.25 and Table 4.8 show the results of the XRD analysis for the sample at current density of 50 mA/m^2 after immersion for one week in artificial seawater. There is some quantity of a phase of a substance known as eitelite, which is a compound of sodium, magnesium and carbonate (CO_3). Also, there is also some ferrite and rust. This result is in accordance with both previous SEM/EDX results and GDOES data. In the underprotection situation, the magnesium has been precipitated with iron which we showed previously in Section 4.3.5 using titration.

(3) 100 mA/m^2 for one week.

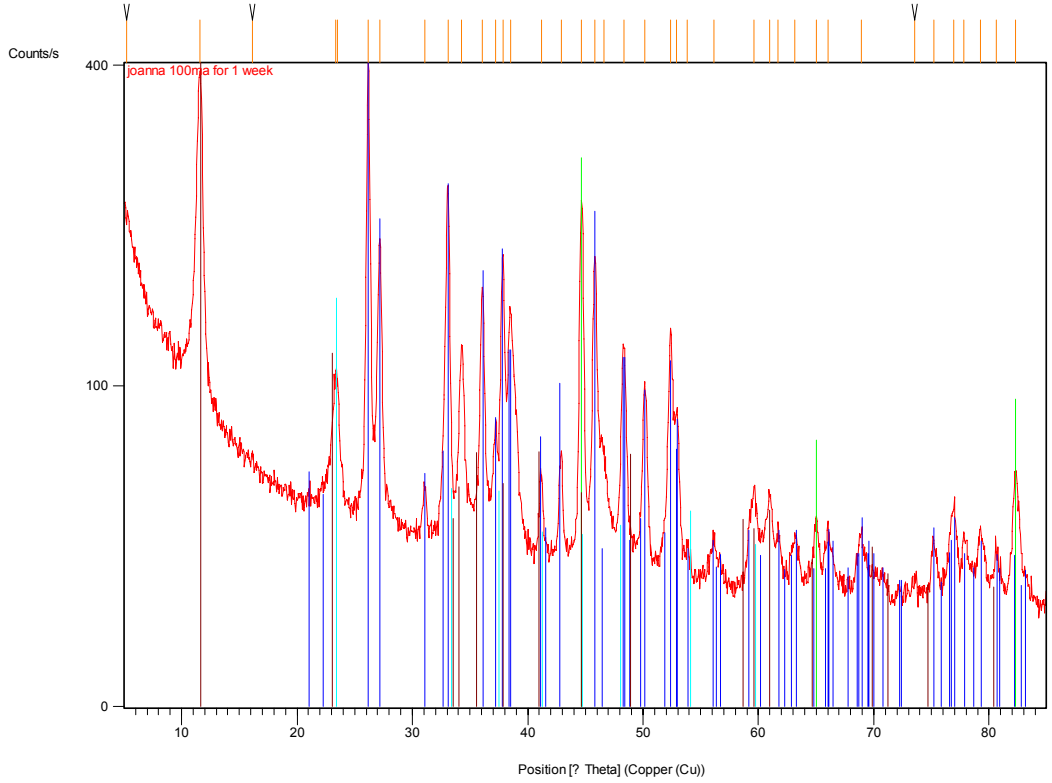

Figure 4.26. XRD pattern for sample surface after immersion in artificial seawater for 7 days (Applied current density of 100 mA/m^2).

Table 4.9. The Compound Name and Chemical Formula using XRD quantification, of calcareous films on steel samples after immersion in artificial seawater for 7 days (Applied current densities of 100 mA/m^2).

Visible	Ref. Code	Score	Compound Name	Scale Factor	Chemical Formula
*	00-041-1475	86	Aragonite	0.923	$CaCO_3$
*	00-006-0696	53	bainite, ferrite, ledkunite	0.566	Fe
*	00-046-1436	46	Bernalite	0.257	$Fe_3(OH)_3$
*	00-024-1091	48	Sjogrenite	0.840	$Mg_6Fe_2CO_3(OH)_{16}\cdot 4H_2O$

Figure 4.26 and Table 4.9 show the results of the XRD analysis for the sample at current density of 100 mA/m^2 after immersion for one week in artificial seawater. The deposit layer is mostly comprised of $CaCO_3$ as aragonite, with the usual ferrite. The iron compounds are an unusual monovalent hydroxide known as bernalie, together with a complex iron and magnesium hydroxide/carbonate compound known as sjogrenite. In this underprotected situation, this curious compound may well be the result of the coprecipitation of Fe and Mg which we also showed in the previous Section using titration.

(4) 150 mA/m^2 for a week.

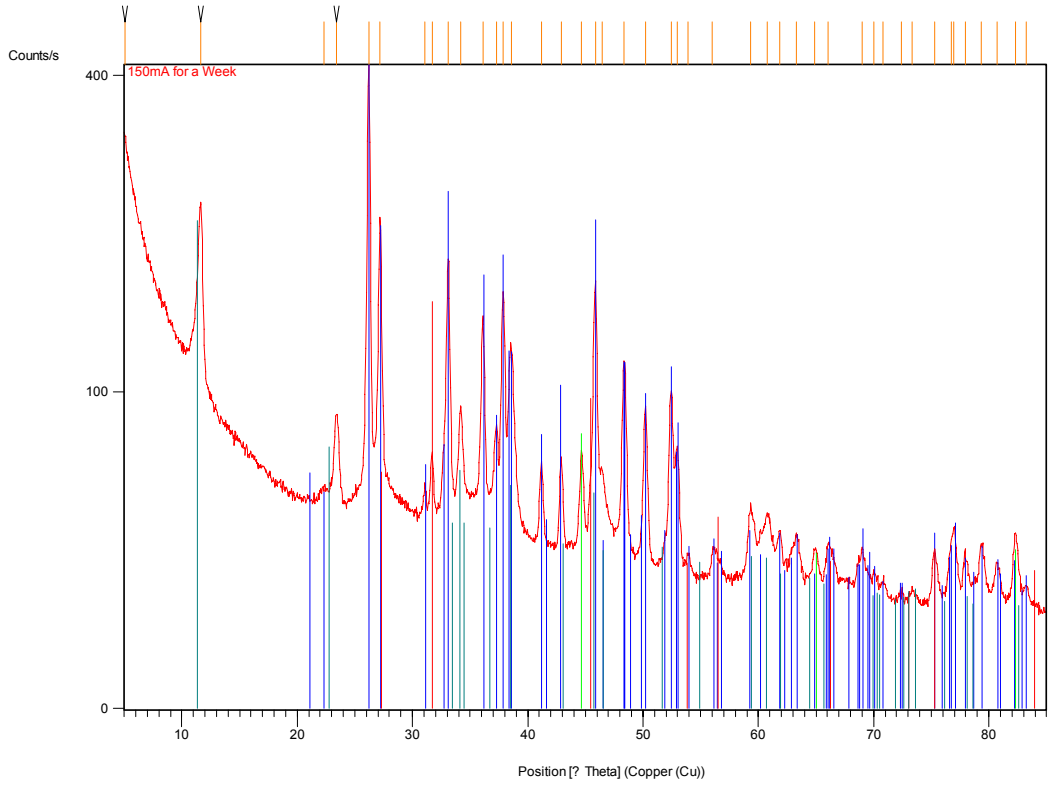

Figure 4.27. XRD pattern for sample surface after immersion in artificial seawater for 7 days (Applied current density of 150 mA/m^2).

Table 4.10. The Compound Name and Chemical Formula using XRD quantification, of calcareous films on steel samples after immersion in artificial seawater for 7 days (Applied current density of 150 mA/m^2).

Visible	Ref. Code	Score	Compound Name	Scale Factor	Chemical Formula
*	00-041-1475	86	Aragonite	0.877	$CaCO_3$
*	00-006-0696	49	bainite, ferrite, ledkunite	0.113	Fe
*	00-005-0628	44	Halite, syn	0.112	NaCl
*	01-070-2150	43	Pyroaurite	0.283	$(Fe_2Mg_6(OH)_{16}CO_3(H_2O)_{4.5})_{0.375}$

Figure 4.27 and Table 4.10 show the results of the XRD analysis for the sample at current density of 150 mA/m^2 after immersion for one week in artificial seawater. The layer is mostly composed of $CaCO_3$ as Aragonite. However, there is also a substantial amount of a complex iron and magnesium hydroxide/carbonate phase similar to Pyroaruite. This pattern is a poor fit at low angle, there are some displaced reflections. However, overall it is a reasonable fit particularly as all of the matched reflections are quite broad, and they have similar shapes. The layer is quite thick as the ferrite substrate is only just visible; it is of similar thickness to the deposit formed on the sample at an applied current density of 400 mA/m^2. $Mg(OH)_2$ alone as Brucite was not present, but Pyroaurite was detected and like the previous sample it is probably caused by the coprecipitation of Fe and Mg.

(5) 200 mA/m^2 for a week.

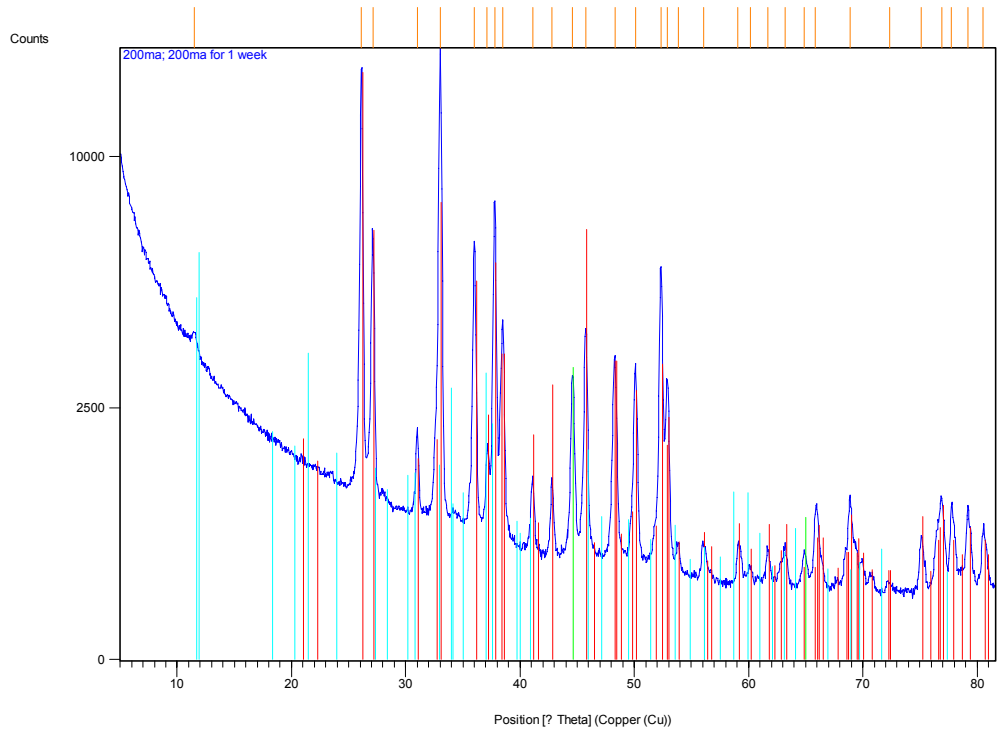

Figure 4.28. XRD pattern for sample surface after immersion in artificial seawater for 7 days (Applied current density of 200 mA/m^2).

Table 4.11. The Compound Name and Chemical Formula using XRD quantification, of calcareous films on steel samples after immersion in artificial seawater for 7 days (Applied current density of 200 mA/m^2).

Visible	Ref. Code	Score	Compound Name	Scale Factor	Chemical Formula
*	00-041-1475	71	Aragonite	0.811	$CaCO_3$
*	00-006-0696	40	ferrite, substrate	0.189	Fe
*	00-007-0420	20	Magnesium Chloride Hydroxide Hydrate	0.189	$Mg_3(OH)_5Cl{\cdot}4H_2O$

Figure 4.28 and Table 4.11 show the results of the XRD analysis for the sample at current density of 200 mA/m^2 after immersion for one week in artificial seawater. The layer is almost all composed of calcium carbonate occurring as aragonite. The XRD pattern from the iron substrate is also visible. There is a small reflection at about 11.6 degrees two theta which may arise from a compound known as Akaganeite (Fe based) or from a complex compound consisting of magnesium chloride hydroxide hydrate.

(6) 300 mA/m^2 for a week.

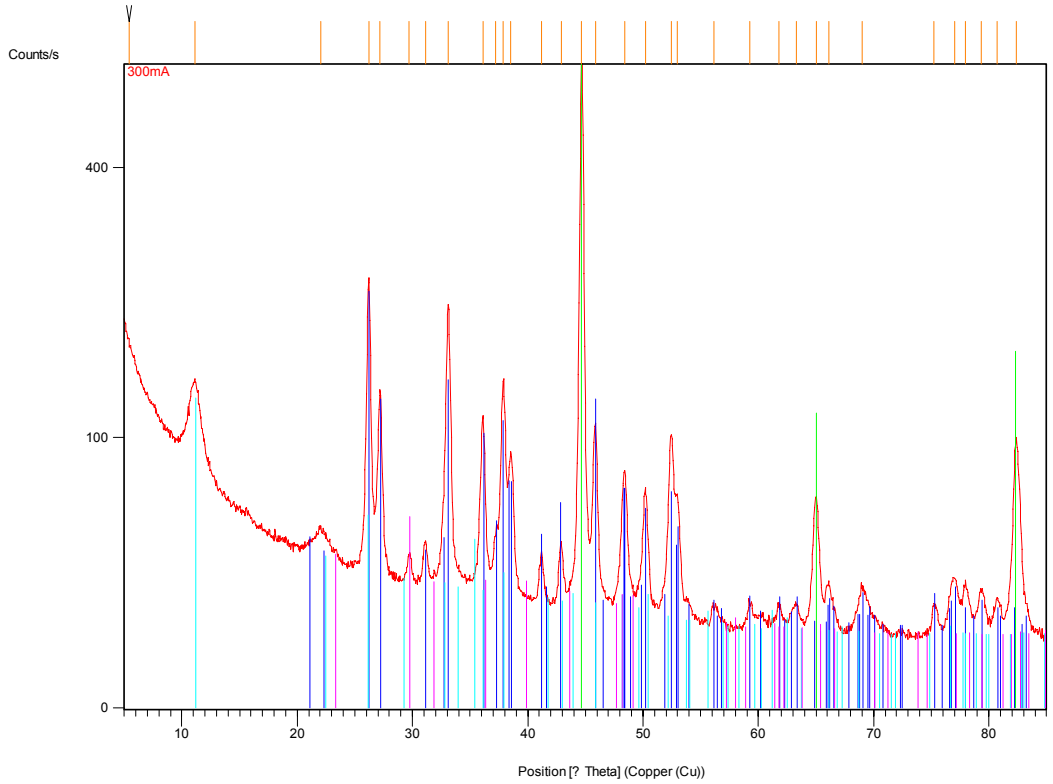

Figure 4.29. XRD pattern for sample surface after immersion in artificial seawater for 7 days (Applied current density of 300 mA/m^2).

Table 4.12. The Compound Name and Chemical Formula using XRD quantification, of calcareous films on steel samples after immersion in artificial seawater for 7 days (Applied current density of 300 mA/m^2).

Visible	Ref. Code	Score	Compound Name	Scale Factor	Chemical Formula
*	00-041-1475	88	Aragonite	0.438	$CaCO_3$
*	00-006-0696	54	bainite, ferrite, ledkunite	0.938	Fe
*	04-007-2834	56	iron(III) oxide chloride	0.280	FeClO
*	01-086-2336	40	Calcite, magnesian	0.037	$(Mg_{0.129} Ca_{0.871})(CO_3)$

Figure 4.29 and Table 4.12 show the results of the XRD analysis for the sample at current density of 300 mA/m^2 after immersion for one week in artificial seawater. The layer mainly consists of aragonite and magnesian (the latter compound is a combined magnesium and calcium carbonate). The presence of this compound, if true is very interesting. Originally, it has always been thought that the calcium and magnesium are precipitated as different and separate compounds. This dolomite-like carbonate suggests that there may well be co-precipitation at this particular current density and interfacial pH, but in this instance between the calcium and the magnesium. The necessary confirmatory titration experiments that would be necessary to confirm this are clearly part of future work.

(7) 400 mA/m^2 for a week.

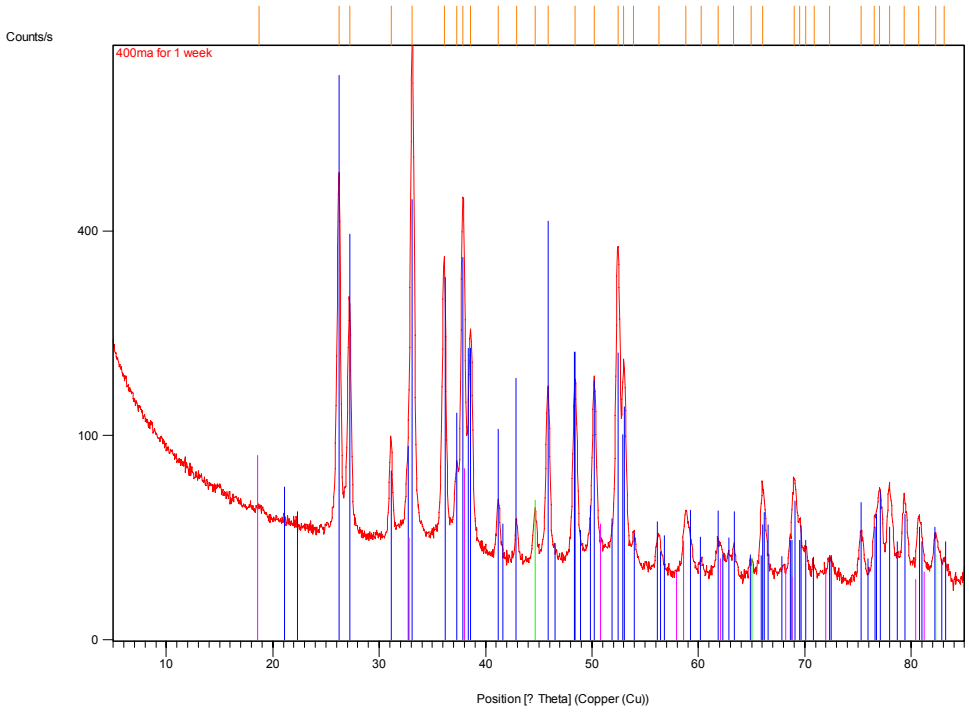

Figure 4.30. XRD pattern for sample surface after immersion in artificial seawater for 12 days (Applied current density of 400 mA/m^2).

Table 4.13. The Compound Name and Chemical Formula using XRD quantification, of calcareous films on steel samples after immersion in artificial seawater for 7 days (Applied current density of 400 mA/m^2).

Visible	Ref. Code	Score	Compound Name	Scale Factor	Chemical Formula
*	00-041-1475	88	Aragonite	0.809	$CaCO_3$
*	00-006-0696	46	bainite, ferrite, ledkunite	0.034	Fe
*	04-011-5938	28	Brucite, syn	0.265	$Mg(OH)_2$

Figure 4.30 and Table 4.13 show the results of the XRD analysis for the sample at current density of 400 mA/m^2 after immersion for one week in artificial seawater. The layer is mostly $CaCO_3$ occurring as aragonite. There may be a very small amount of $Mg(OH)_2$ as Brucite, only one very small, broad reflection is visible. The $Mg(OH)_2$ and Fe was probably detected because hydrogen evolution caused film detachment causing the under layer of $Mg(OH)_2$ and the Fe in the exposed base metal to be detected. In this situation there is no evidence of a mixed calcium/magnesium carbonate, presumably because the interfacial pH is more alkali.

4.3.7. General Discussion based on SEM/EDX and XRD results.

At this stage some general observations may be made. The open circuit EDX maps shown in Plate 4.6 show an obvious deposit on the surface which clearly contains magnesium and iron, the magnesium map corresponds to the surface deposits and the iron appears to be uniformly dispersed. There was no obvious calcium deposit found either by EDX (Figure 4.14) or from the X-Ray Diffraction (XRD) analysis (Figure 4.24). These findings are contrary to data obtained by Hudson [16], who found white calcium deposits in certain areas. However Hudson suggested that his calcium rich regions were associated with cathodic calcium rich areas over mill scale. Clearly there is no mill scale on any of our specimens since we used cold rolled panels and the samples were polished prior to use.

The 50 mA/m^2 case is probably the most interesting current density. The steel is still corroding at a rate of between 0.03 and 0.038 mm/y compared with an open circuit rate of 0.09 mm/y, only a 46% reduction, not an insignificant corrosion rate. Plate 4.7(a) clearly shows two different deposits, one containing calcium, the other containing magnesium. Interestingly, the EDX elemental distribution mapping for magnesium shown in Plate 4.7(b) now corresponds clearly with that of the iron, given in Plate 4.7(d), which may be explained by the coprecipitation process we have already investigated in this Chapter. Conversely, the distribution of the calcium rich precipitates illustrated in Plate 4.7(c) correspond to the regions in the iron and magnesium maps where these elements are absent. Such features are also observed in the cross-section images given in Plate 4.13, which present the SEM images and associated EDX element distribution maps of the deposit obtained at an applied current density of 100 mA/m^2, and which show codeposition of magnesium on top of iron corrosion deposits together with calcium deposits that have formed directly onto the uncorroded steel surface.

We have clearly shown that magnesium deposition occurs only in the presence of soluble iron in solution. This soluble iron can only have been generated as an anodic specie at anodic sites on the iron surface. Therefore our suggestion is that the co-precipitated iron/magnesium regions on the surface at least at the early stages (seven days or less) and at low current densities, correspond to anodic areas on the steel surface. It follows therefore that the calcium containing precipitates must have occurred at cathodic sites. We can then gain some idea of the spacial distribution of the anodic and cathodic areas

by observing the calcium and magnesium distribution (SEM/EDX maps of cross-section of deposit at 7 days, see Plate 4.13), cathodic areas being around 50 μm in diameter and 100 μm apart. Whether this distribution is a carry over of the situation at open circuit or whether this distribution is specific to the polarised state, remains to be determined. Looking at the Uhlig model of cathodic protection as described in Section 4.1.2.1 of this Chapter, it does seem that this model may be valid and our data provides some indication of the relative sizes and distribution of the anodic and cathodic areas, at least in conditions of underprotection.

4.3.8. Electrochemical Impedance Spectroscopy (EIS) study on films.

The technique of Electrochemical Impedance Spectroscopy (EIS) was used on the mild steel samples at different levels of galvanostatic cathodic polarization with applied current densities varying between 0 (the open circuit potential condition) and 400 mA/m^2. During galvanostatic polarisation the variation in potential of each specimen was monitored and the impedance was measured at the potential that the specimen had reached at the moment of time prior to commencing impedance measurement. In other words, the potential was not allowed to decay back to a natural potential as this would have removed the specimen from the specific test conditions that we were attempting to study. The measurements were conducted, starting from 6 hours immersion, then at 24 hour intervals thereafter for 7 days duration, using an ACM Gill potentiostat, with an inbuilt frequency response analyser over a frequency range 10000 Hz to 0.1 Hz. The maximum number of data readings per test was 100. All sets recorded were analysed using Zview software.

The model selected to simulate the behaviour of mild steel under conditions of cathodic protection with ongoing electrochemical anodic and cathodic processes, together with calcareous film formation was described by an equivalent circuit that was not arbitrarily chosen as is frequently the case and will be discussed in detail later in the next Section. The Nyquist and Bode impedance diagrams of the data with associated fitting curves were generated, and are presented in Figures 4.36 to Figures 4.63.

4.3.8.1. Equivalent circuits.

The equivalent circuit that was used for modelling our system and generating the interpretation of our impedance data was based on our SEM experimental observations of calcareous deposition and models that were proposed previously. Our model was based partly on the models proposed by Deslouis [19], [20] and Chung [21]. The Deslouis model had already been used for interpretation of the corrosion resistance of the mild steel under cathodic protection in the presence of calcareous deposition that partially covered the surface (Figure 4.31(a)). In this model the properties of the continuous film were represented by a parallel combination of film capacitance and resistance, C_f and R_f respectively, together with a charge transfer resistance R_{ct}, and a double layer capacitor C_{dl}, and collectively these represent the corrosion processes proceeding at the metal interface. The aforementioned workers also introduced an additional parallel combination

of R_d and C_d to mimic the uncovered areas (pores) of the surface. However this model does not take into consideration the formation of corrosion products within the film.

The model introduced by Chung [21] has been used for the description of the corrosion resistance of an anodic porous coating formed during spark anodising on zinc in a NaCl solution. According to this model the coating film consists of outer and inner layers where the pores of the inner layer are filled with corrosion products formed during metal dissolution at the interface (Figure 4.31(b)). This model or a modification of it was considered as a possibility to explain our data.

The original Deslouis [19, 20] model does not consider the occurrence of cathodic electrochemical processes, which clearly should have a significant contribution to the impedance of the cathodically protected steel. A second and subsequent model from Deslouis and co-workers [22] showed that the corrosion of a filmed mild steel under natural immersion conditions in NaCl solutions can be modelled by equivalent circuits with anodic and cathodic branches being in parallel with the double layer capacitor C_{dl}. The anodic branch is represented by the anodic charge transfer resistance R_{ct}, and the cathodic branch is under mixed control and comprises the resistance of the charge transfer reaction R_c, together with a diffusion limited Warburg impedance W_c (Figure 4.31(c)).

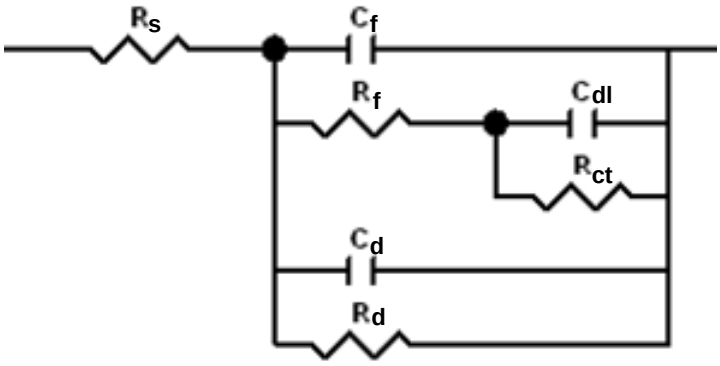

(a) The original Deslouis equivalent circuit model.

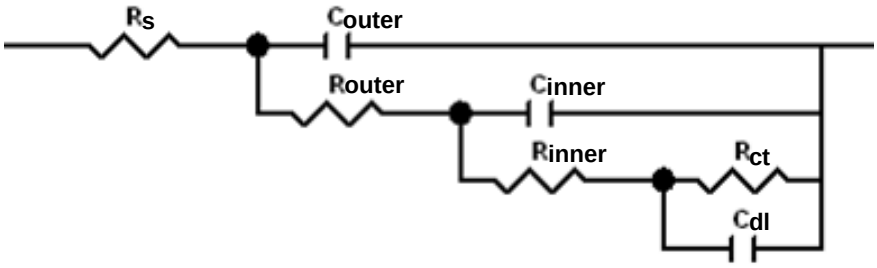

(b) The Chung equivalent circuit model.

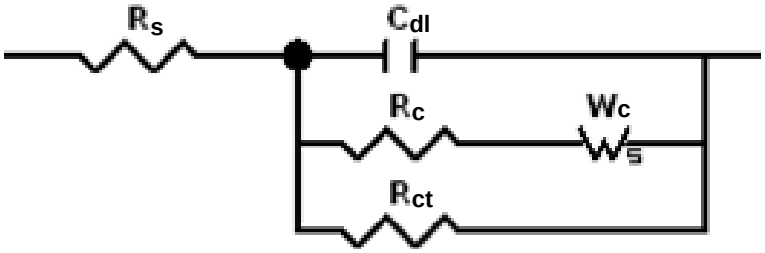

(c) The Bonnel and Deslouis equivalent circuit model.

Figure 4.31. Equivalent circuits of the models used previously.

(1). Choice of model based on SEM data and Nyquist diagrams.

Analysis of our EIS data revealed that in most cases the impedance spectra consist of three semicircles with two semicircles of relatively small diameters probably associated with the properties of the calcareous film observed at higher frequencies and one semicircle of large diameter probably associated with dissolution (corrosion of steel) at lower frequencies. Figure 4.33 is a typical example and a schematic diagram is given in Figure 4.32.

The value of resistance of R (in Figure 4.36) could be calculated by the following equation:

$$\frac{1}{R} = \frac{1}{W_{C-R}} + \frac{1}{R_a} \quad \text{..... (4-13)}$$

Where $W_{C\text{-}R}$ is the resistive component of the Warburg Impedance (see Section 3.6.3).

R_a is the anodic charge transfer resistance.

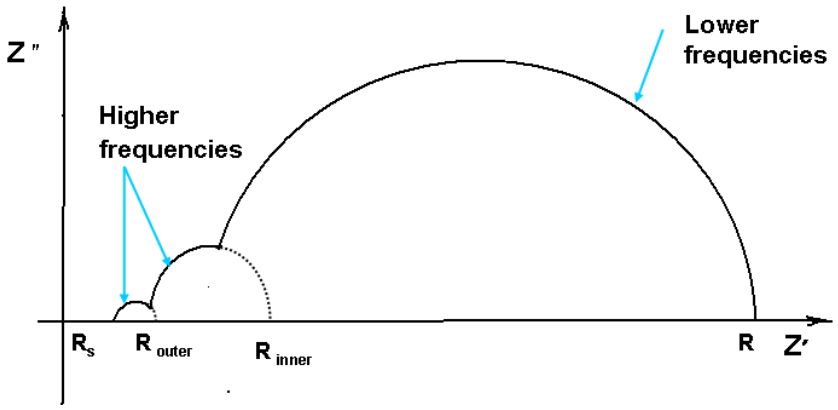

Figure 4.32. Schematic diagram of complex plane plot (Nyquist plot).

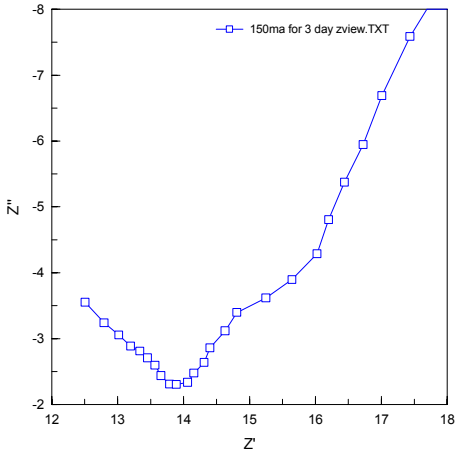

Figure 4.33. Real experimental data in higher frequency
(The Nyquist Graph for a mild steel sample with a current density of 150 mA/m^2 for 3 days immersion in artificial seawater).

(2). The proposed equivalent circuit

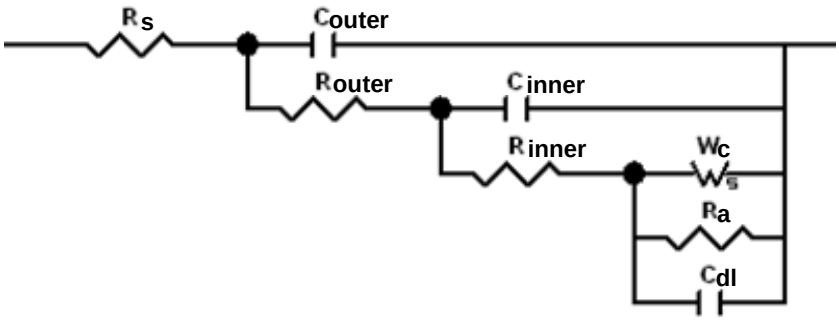

C_{dl} = interface reaction; R_a = anodic charge transfer resistance; W_c = cathodic Warburg

Figure 4.34. Equivalent circuit for mild steel in artificial seawater under cathodic protection.

Both from the SEM/EDX results reported earlier in this Chapter, and experimental impedance plots, we suggest that the plot given in Figure 4.32 represents calcareous film deposition on a mild steel surface. Our film in Figure 4.32, as well as the solution resistance R_s, consists of two layers: the outer layer L_{outer} is a calcium rich layer; and the inner layer L_{inner} is a magnesium rich layer. These are represented by the high frequency region in Figure 4.32. From the equivalent circuit given in Figure 4.34, the outer layer L_{outer} is considered to be porous and is characterized by a parallel combination of a capacitor C_{outer} that is directly associated with the thickness of the calcium containing deposits, and a pore resistance R_{outer} that is defined by the resistance of all of the pores. The inner compact layer L_{inner} and the corroding interface are introduced into the equivalent circuit which is in series with R_{outer}. The L_{inner} is also characterized by a parallel combination of a capacitor C_{inner} and a resistance R_{inner}. The corroding interface is characterised by a parallel combination of a double layer capacitor C_{dl}, charge transfer anodic resistance R_a, and a finite length diffusional impedance W_c, which represents the cathodic process. To simplify our already complex equivalent circuit the resistance of the cathodic charge transfer reaction R_c was small and therefore (see the Bonnel model given in Figure 4.31(c)) was not taken into consideration since the system was cathodically polarized. The quality of our data fit (Figures 4.36 - 4.63) clearly shows the validity of the model chosen.

(3). Schematics of cross-sections of calcareous film deposits on cathodically under-protected, fully-protected and over-protected steel.

An alternative and complimentary approach to analysis by equivalent circuits is to visualize the situation as a physical model, so schematic diagrams of sections of calcareous deposits formed on under-protected, fully protected and over protected steel samples are presented in Figure 4.35. These are largely based on previous experimental SEM observations (Plates 4.13 to 4.16 in Section 4.3.4.4).

In cathodically under-protected conditions the steel must undergo dissolution. During dissolution there will also be some cathodically generated alkali and the iron will be deposited as corrosion products in the form of oxides and hydroxides. As shown by other workers [18], we have found that magnesium compounds are able to co-precipitate together with iron compounds to form the inner layer of the film in Section 4.3.5 and deposits on the cross-sections in the Section 4.3.4.4. Precipitation of the protective outer

layer enriched with calcium carbonate commences after the pH of the solution near the steel surface reaches 7.58 by calculation. However some areas of the underprotected steel are still actively dissolving; these areas may be regarded as defects in the protective film and filled with a precipitated mixture of magnesium and iron.

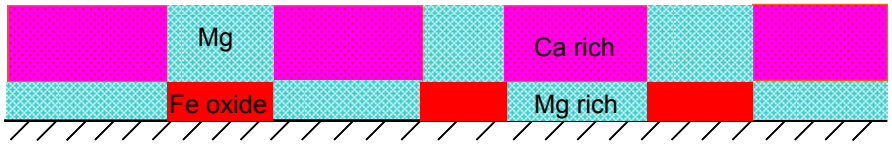

(a). Schematic of cross-section of deposit formed in cathodically under protected situation.

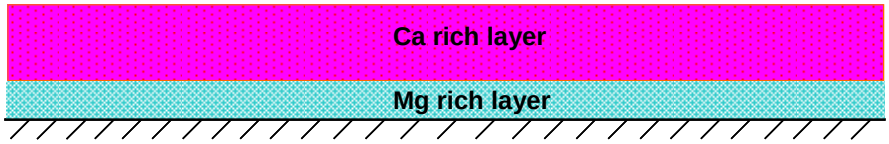

(b). Schematic of cross-section of deposit formed in full cathodic protection situation.

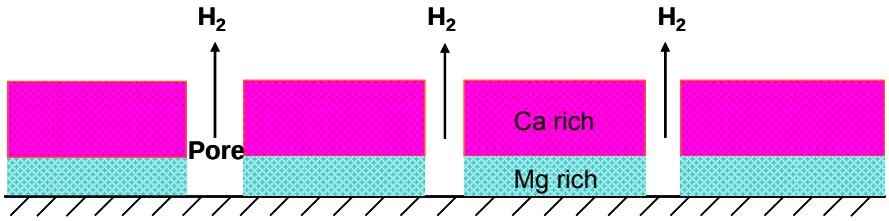

(c). Schematic of cross-section of deposit formed in over cathodic protection situation.

Figure 4.35. Schematic diagrams of interface impedance models of deposits formed on mild steel in artificial seawater under various conditions of cathodic protection: (a) under-protection, (b) full protection, (c) over protection.

Under conditions where steel is fully cathodically protected, as illustrated in Figure 4.35(b) above, and Plates 4.14 and 4.15 in Section 4.3.4.4, the deposit that forms on the surface consists of two clearly defined layers: the thin outer layer (L_1) is composed of a Ca rich layer, whilst the inner layer (L_2) is a Mg rich layer. The deposition follows the mechanism proposed for the underprotected system except that the defects are now no longer present under these new conditions of full cathodic protection.

For the situation of overprotection, as illustrated in Figure 4.35(c) above, and Plate 4.16 in Section 4.3.4.4, we propose an alternative cathodic process of water reduction giving hydrogen. We therefore have the interesting situation where evolution of hydrogen at the deposit/metal interface is thought to cause fracture of the brittle films on the iron surface. These pores are also represented in our model as R_{outer} and/or R_{inner}.

4.3.8.2. The Nyquist and Bode impedance diagrams at different applied current densities.

The Nyquist and Bode graphs generated for mild steel samples under different levels of cathodic protection in artificial seawater are presented in the set of graphs given in Figures 4.36 to Figure 4.63, and these show both the experimental curves and the fitting curves. Not all the impedance data is displayed as graphs in this Thesis but all the values that were calculated from the equivalent circuits are given in Tables 4.14 to 4.20.

From Figure 4.36 to Figure 4.63, the high frequency regions are thought to represent the porous calcareous film with the low frequencies being ascribed to the charge transfer resistance at the film metal interface. The graphs of whole frequency regions (Frequency from 10000Hz to 0.1Hz) together with an inset plot of a partial enlargement of the high frequency regions will be given in the same Nyquist graphs.

Explanations for the behaviour of this low frequency region as a function of time and current density have been put forward in terms of the specific electrochemical reaction taking place and the nature and integrity of the calcareous films produced.

(1) Open circuit.

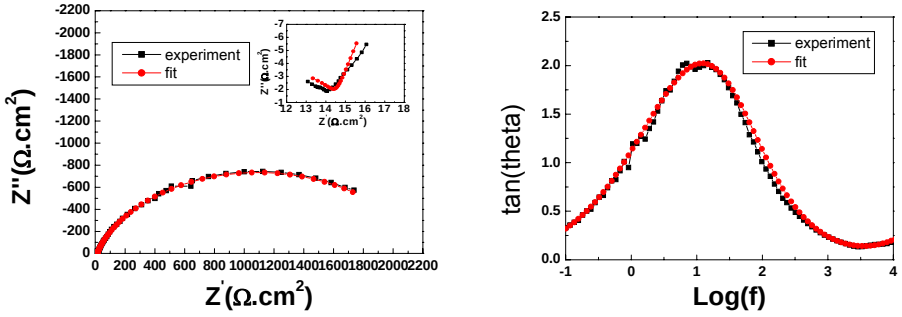

(a) Nyquist graph **(b) Bode graph**

Figure 4.36. Impedance spectra for open circuit conditions of mild steel sample immersed for 6 hours in artificial seawater.

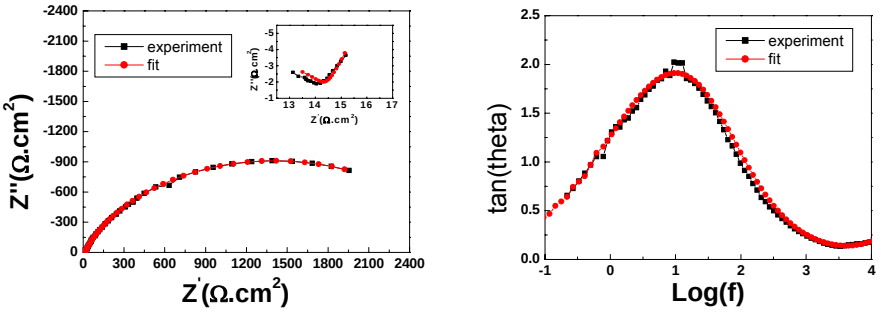

(a) Nyquist graph **(b) Bode graph**

Figure 4.37. Impedance spectra for open circuit conditions of mild steel sample immersed for 24 hours in artificial seawater.

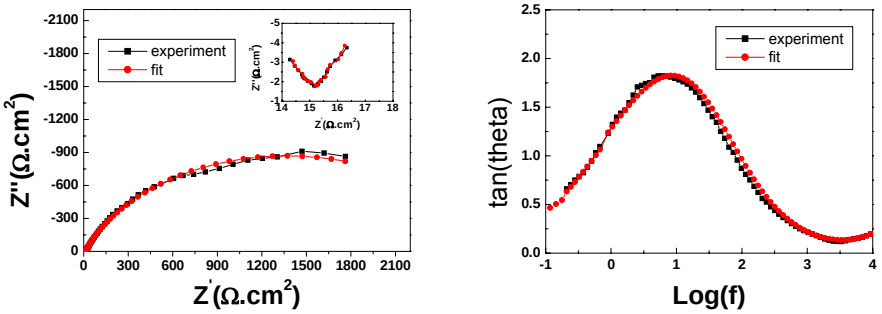

(a) Nyquist graph **(b) Bode graph**

Figure 4.38. Impedance spectra for sample under open circuit conditions immersed for 72 hours (3 days) in artificial seawater.

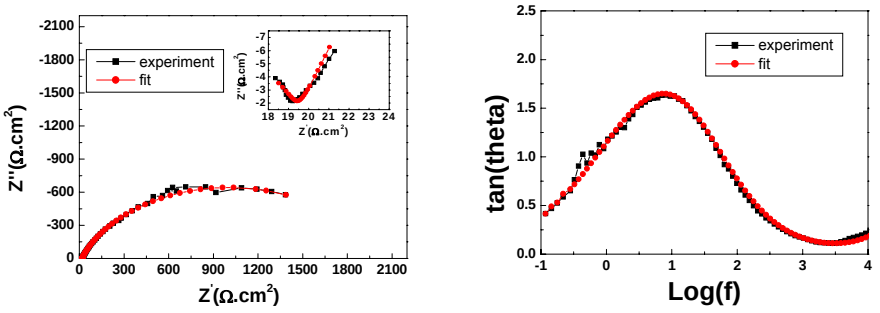

(a) Nyquist graph **(b) Bode graph**

Figure 4.39. Impedance spectra for sample under open circuit conditions immersed for 168 hours (7 days) in artificial seawater.

Table 4.14. Best fit results for equivalent circuit elements for open circuit conditions.

Immersion time (h)	6h	24h	48h	72h	96h	120h	144h	168h
$R_s(\Omega.cm^2)$	9.8	10.9	12.7	10.8	11.5	11.5	9.6	11.7
C_{outer} (F/ cm^2)	$2.1*10^{-6}$	$3.3*10^{-6}$	$5.6*10^{-6}$	$2.1*10^{-6}$	$1.9*10^{-6}$	$1.4*10^{-6}$	$0.7*10^{-6}$	$0.9*10^{-6}$
$R_{outer}(\Omega.cm^2)$	5.5	4.4	5.0	5.5	5.6	7.5	10	8.4
C_{inner}(F/ cm^2)	$51*10^{-6}$	$39*10^{-6}$	$51*10^{-6}$	$47*10^{-6}$	$52*10^{-6}$	$54*10^{-6}$	$51*10^{-6}$	$60*10^{-6}$
$R_{inner}(\Omega.cm^2)$	19.7	24.3	30.5	30	31	40	26	36.7
$W_{C-R}(\Omega.cm^2)$	2200	2900	3000	3500	2200	3400	3100	3300
W_{C-T}	3.3	2.1	1.2	1.8	0.9	1.5	1.7	2.1
W_{C-P}	0.5	0.5	0.5	0.5	0.5	0.5	0.5	0.5
$R_a(\Omega.cm^2)$	2700	6000	5000	4200	4300	3100	4300	3100
C_{dl}(F/ cm^2)	$27*10^{-6}$	$27*10^{-6}$	$37*10^{-6}$	$33*10^{-6}$	$34*10^{-6}$	$35*10^{-6}$	$30*10^{-6}$	$39*10^{-6}$

(2) Applied current density of 50 mA/m^2.

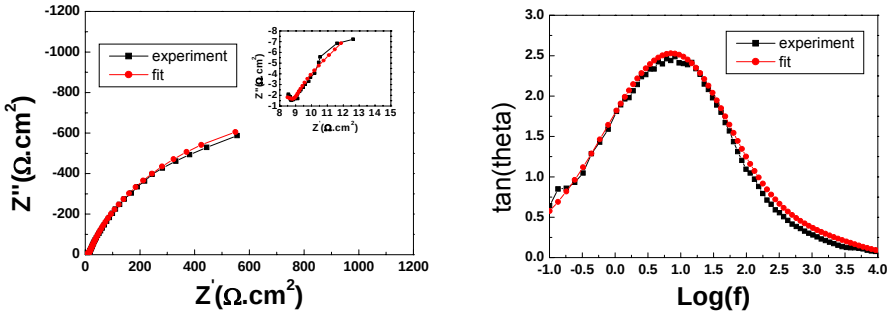

(a) Nyquist graph **(b) Bode graph**

Figure 4.40. Impedance spectra for mild steel samples with current density of 50 mA/m^2 for 6 hours immersion in artificial seawater.

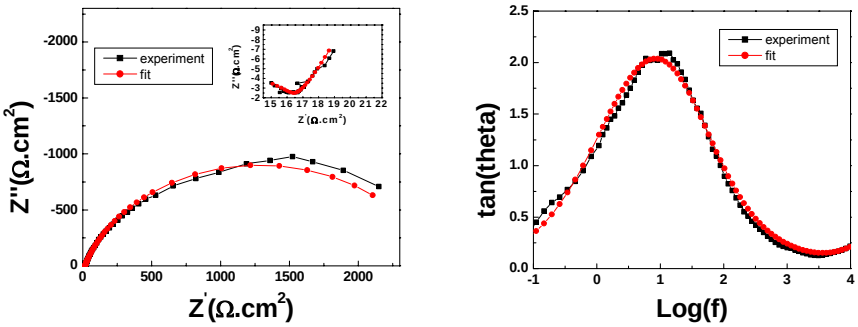

(a) Nyquist graph **(b) Bode graph**

Figure 4.41. Impedance spectra for mild steel samples with current density of 50 mA/m^2 for 24 hours immersion in artificial seawater.

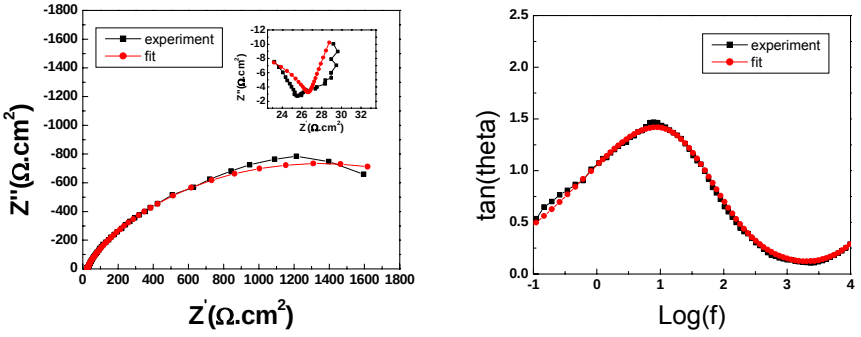

(a) Nyquist graph **(b) Bode graph**

Figure 4.42. Impedance spectra for mild steel samples with current density of 50 mA/m^2 for 72 hours (3 days) immersion in artificial seawater.

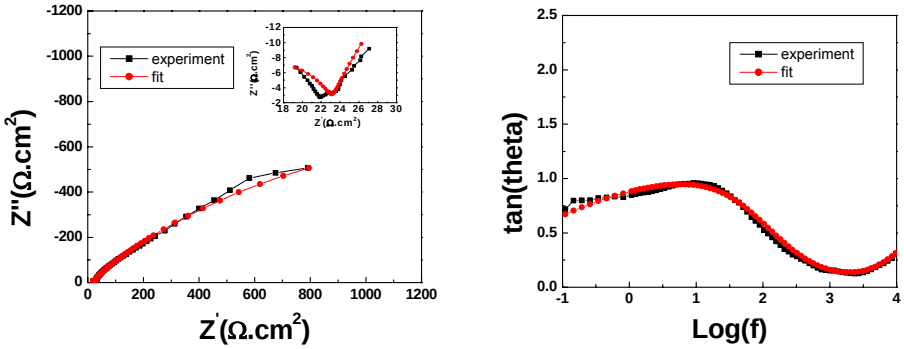

(a) Nyquist graph **(b) Bode graph**

Figure 4.43. Impedance spectra for mild steel samples with current density of 50 mA/m^2 for 168 hours (7 days) immersion in artificial seawater.

Table 4.15. Best fit results for equivalent circuit elements at applied current density of 50mA/m^2.

Immersion time (h)	6h	24h	48h	72h	96h	120h	144h	168h
$R_s(\Omega.cm^2)$	5.5	11.1	8.5	11.6	10.2	11.5	11.8	11.6
C_{outer} (F/ cm^2)	$2*10^{-6}$	$1.7*10^{-6}$	$3.7*10^{-6}$	$0.5*10^{-6}$	$1.0*10^{-6}$	$4.1*10^{-6}$	$1.3*10^{-6}$	$1*10^{-6}$
$R_{outer}(\Omega.cm^2)$	4.1	6	4.7	15.3	8.7	5.2	9.6	11
C_{inner}(F/ cm^2)	$34*10^{-6}$	$32*10^{-6}$	$45*10^{-6}$	$46*10^{-6}$	$38*10^{-6}$	$52*10^{-6}$	$52*10^{-6}$	$41*10^{-6}$
$R_{inner}(\Omega.cm^2)$	18.7	16.2	33	35	20	26.3	21	21
$W_{C-R}(\Omega.cm^2)$	3000	5800	4800	4300	4300	3700	2100	3300
W_{C-T}	1	3	3.3	3.2	3.6	3.3	4	3.2
W_{C-P}	0.5	0.5	0.5	0.5	0.5	0.5	0.5	0.5
$R_a(\Omega.cm^2)$	3100	4000	3500	3100	5700	3100	2400	2600
C_{dl}(F/ cm^2)	$54*10^{-6}$	$34*10^{-6}$	$23*10^{-6}$	$28*10^{-6}$	$19*10^{-6}$	$25*10^{-6}$	$19*10^{-6}$	$27*10^{-6}$

(3) Applied current density of 100 mA/m^2.

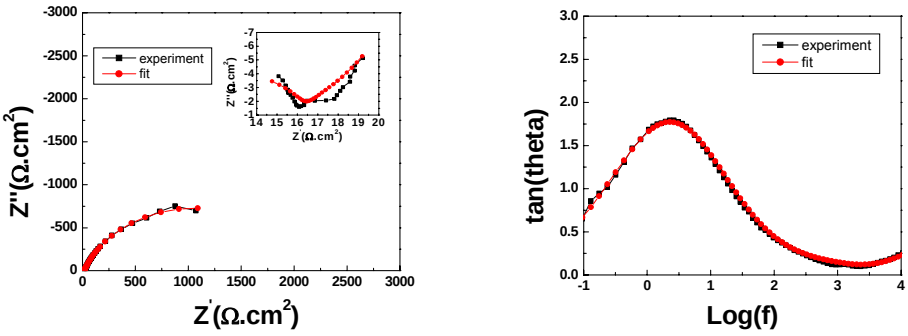

(a) Nyquist graph **(b) Bode graph**

Figure 4.44. Impedance spectra for mild steel samples with current density of 100 mA/m^2 for 6 hours immersion in artificial seawater.

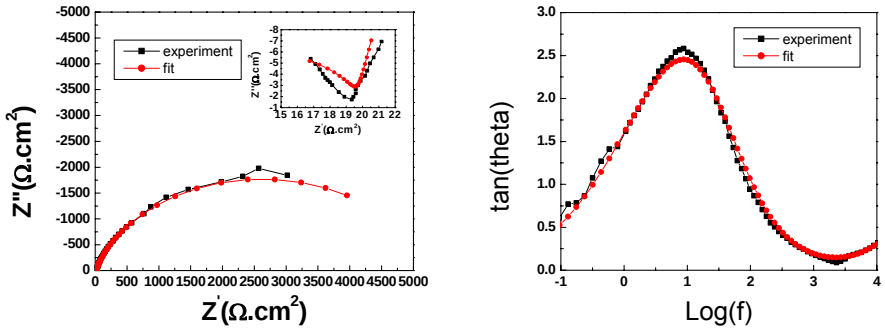

(a) Nyquist graph **(b) Bode graph**

Figure 4.45. Impedance spectra for mild steel samples with current density of 100 mA/m^2 for 24 hours immersion in artificial seawater.

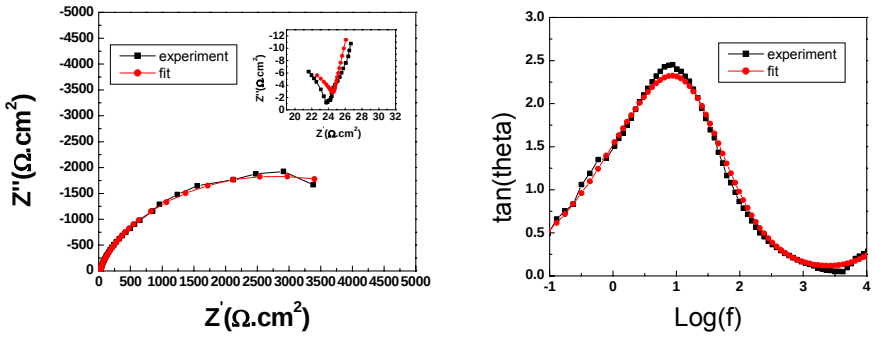

(a) Nyquist graph **(b) Bode graph**

Figure 4.46. Impedance spectra for mild steel samples with current density of 100 mA/m^2 for 72 hours (3 days) immersion in artificial seawater.

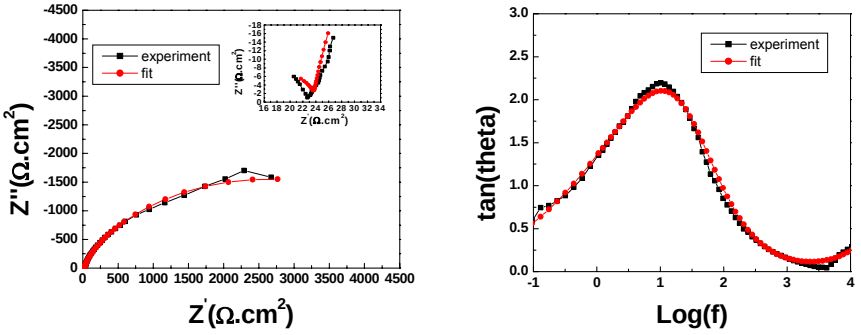

(a) Nyquist graph **(b) Bode graph**

Figure 4.47. Impedance spectra for mild steel samples with current density of 100 mA/m^2 for 168 hours (7 days) immersion in artificial seawater.

Table 4.16. Best fit results for equivalent circuit elements at applied current density of 100mA/m^2.

Immersion time (h)	6h	24h	48h	72h	96h	120h	144h	168h
$R_s(\Omega.cm^2)$	10.2	7.7	12.9	12.9	8.1	11.8	11	12.4
C_{outer} (F/ cm^2)	$1.9*10^{-6}$	$0.6*10^{-6}$	$0.7*10^{-6}$	$0.7*10^{-6}$	$1*10^{-6}$	$1*10^{-6}$	$3.2*10^{-6}$	$3.7*10^{-6}$
$R_{outer}(\Omega.cm^2)$	6.8	11.7	10.9	11.9	8.3	9.1	5	4.5
C_{inner}(F/ cm^2)	$79*10^{-6}$	$31*10^{-6}$	$40*10^{-6}$	$41*10^{-6}$	$33.2*10^{-6}$	$36*10^{-6}$	$33*10^{-6}$	$33*10^{-6}$
$R_{inner}(\Omega.cm^2)$	20.3	10.1	24.4	38.5	23.8	30	40.7	22.8
$W_{C-R}(\Omega.cm^2)$	3100	5200	6900	8100	6800	7300	7500	7900
W_{C-T}	3.3	1.7	3.3	2.8	2.3	3	3.7	2.2
W_{C-P}	0.5	0.5	0.5	0.5	0.5	0.5	0.5	0.5
$R_a(\Omega.cm^2)$	58700	20000	8000	9600	6600	8800	10000	20000
C_{dl}(F/ cm^2)	$94*10^{-6}$	$2.6*10^{-6}$	$15*10^{-6}$	$15*10^{-6}$	$19*10^{-6}$	$17*10^{-6}$	$32*10^{-6}$	$11*10^{-6}$

(4) Applied current density of 150 mA/m^2.

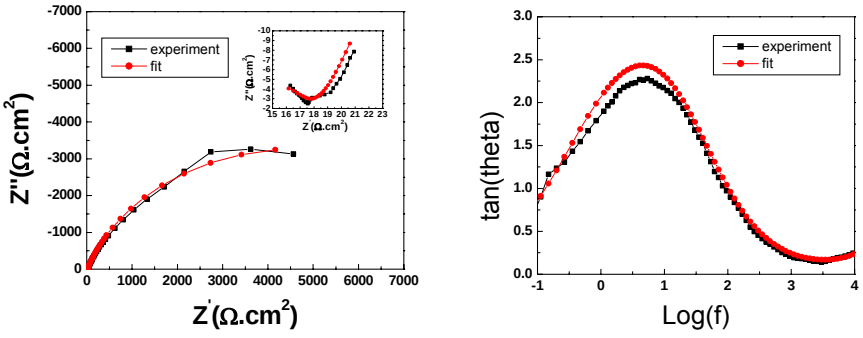

(a) Nyquist graph **(b) Bode graph**

Figure 4.48. Impedance spectra for mild steel samples with current density of 150 mA/m^2 for 6 hours immersion in artificial seawater.

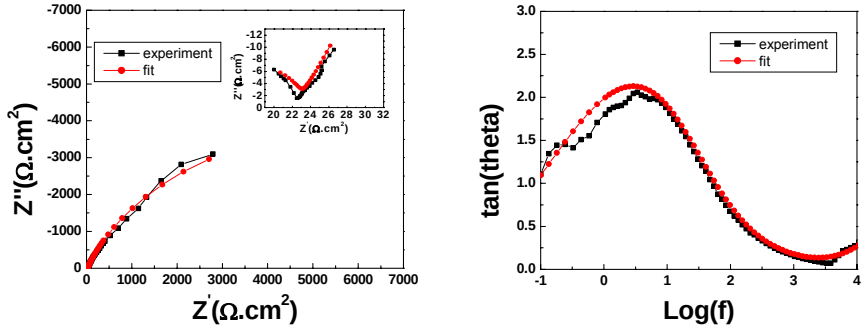

(a) Nyquist graph **(b) Bode graph**

Figure 4.49. Impedance spectra for mild steel samples with current density of 150 mA/m^2 for 24 hours immersion in artificial seawater.

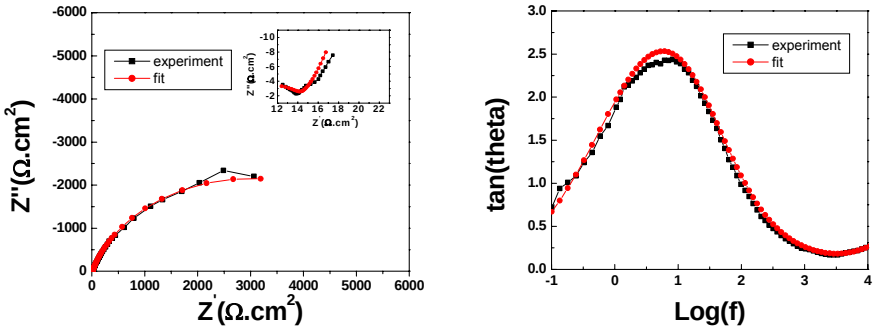

(a) Nyquist graph **(b) Bode graph**

Figure 4.50. Impedance spectra for mild steel samples with current density of 150 mA/m^2 for 72 hours (3 days) immersion in artificial seawater.

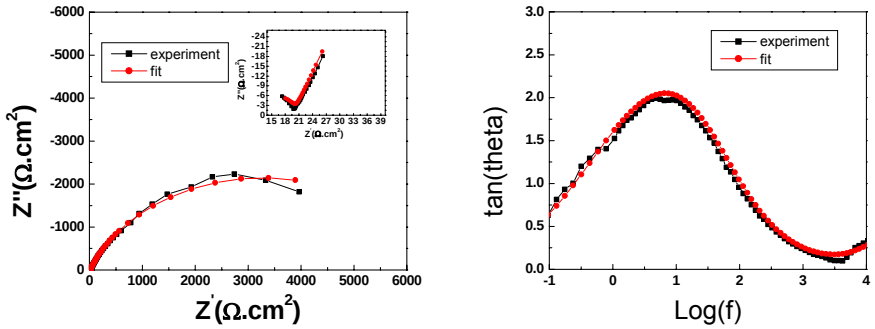

(a) Nyquist graph **(b) Bode graph**

Figure 4.51. Impedance spectra for mild steel samples with current density of 150 mA/m^2 for 168 hours (7 days) immersion in artificial seawater.

Table 4.17. Best fit results for equivalent circuit elements at applied current density of 150mA/m^2.

Immersion time (h)	6h	24h	48h	72h	96h	120h	144h	168h
$R_s(\Omega.cm^2)$	12.3	13.6	12.1	9	10.5	9.8	10.8	11.8
C_{outer} (F/ cm^2)	2.1*10^{-6}	1.1*10^{-6}	0.6*10^{-6}	2.4*10^{-6}	3.4*10^{-6}	2.6*10^{-6}	3.2*10^{-6}	1.3*10^{-6}
$R_{outer}(\Omega.cm^2)$	7.4	10.7	14.6	6	5.4	6.8	6.3	9.8
C_{inner}(F/ cm^2)	43*10^{-6}	52*10^{-6}	45*10^{-6}	43*10^{-6}	35*10^{-6}	37*10^{-6}	34*10^{-6}	36*10^{-6}
$R_{inner}(\Omega.cm^2)$	58	55	67	28	34	48	41	61
$W_{C-R}(\Omega.cm^2)$	7400	7400	8900	7900	9000	10000	8800	7800
W_{C-T}	2.8	4.4	4.6	3.6	4.3	5	5	3.5
W_{C-P}	0.5	0.5	0.5	0.5	0.5	0.5	0.5	0.5
$R_a(\Omega.cm^2)$	100400	130000	15400	14900	13800	14600	22200	14300
C_{dl}(F/ cm^2)	26*10^{-6}	36.7*10^{-6}	28*10^{-6}	32*10^{-6}	24*10^{-6}	25*10^{-6}	25*10^{-6}	23*10^{-6}

(5) Applied current density of 200 mA/m^2.

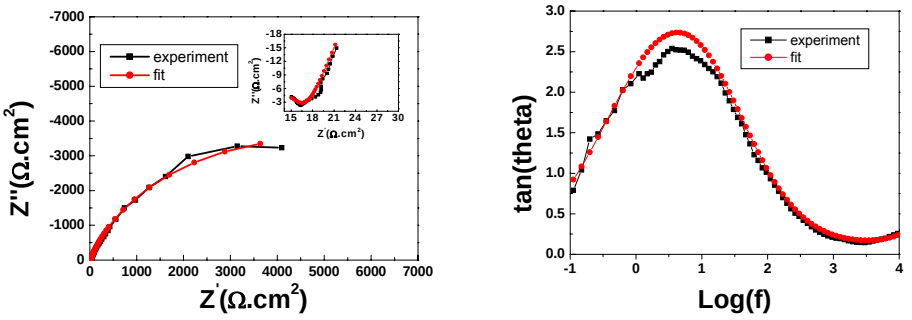

(a) Nyquist graph **(b) Bode graph**

Figure 4.52. Impedance spectra for mild steel samples with current density of 200 mA/m^2 for 6 hours immersion in artificial seawater.

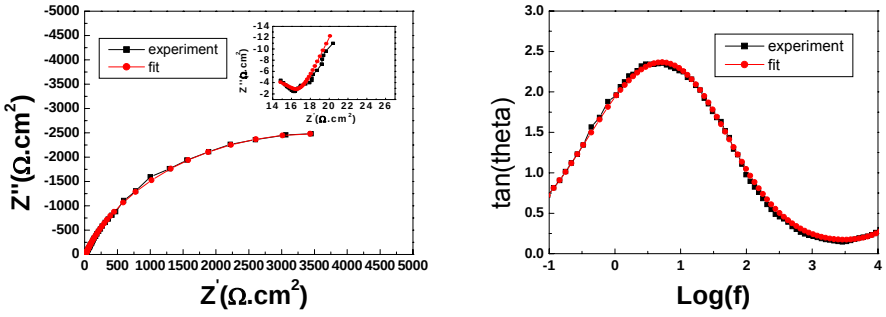

(a) Nyquist graph **(b) Bode graph**

Figure 4.53. Impedance spectra for mild steel samples with current density of 200 mA/m^2 for 24 hours immersion in artificial seawater.

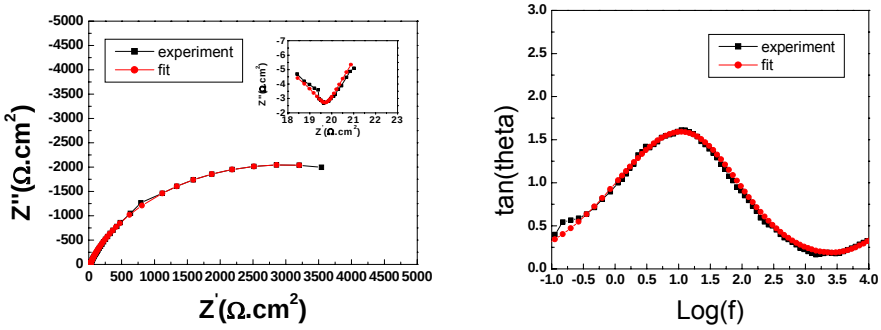

(a) Nyquist graph **(b) Bode graph**

Figure 4.54. Impedance spectra for mild steel samples with current density of 200 mA/m^2 for 72hours (3days) immersion in artificial seawater.

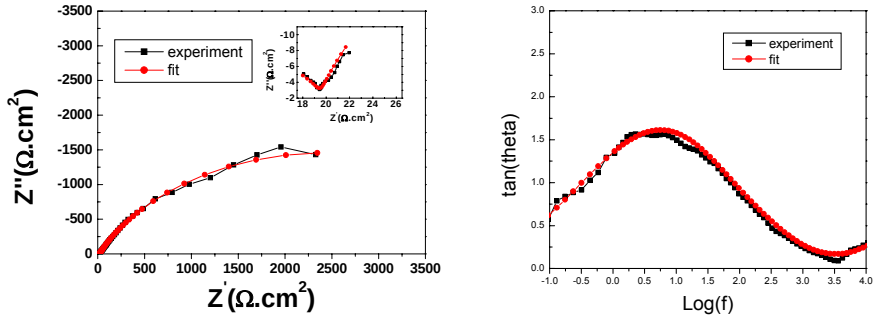

(a) Nyquist graph **(b) Bode graph**

Figure 4.55. Impedance spectra for mild steel samples with current density of 200 mA/m^2 for 168 hours (7 days) immersion in artificial seawater.

Table 4.18. Best fit results for equivalent circuit elements at applied current density of 200mA/m^2.

Immersion time (h)	6h	24h	48h	72h	96h	120h	144h	168h
$R_s(\Omega.cm^2)$	11	10.7	13.3	13.4	13.3	11.6	13	13.6
C_{outer} (F/ cm^2)	$2*10^{-6}$	$2*10^{-6}$	$1.1*10^{-6}$	$1.7*10^{-6}$	$1.5*10^{-6}$	$3.1*10^{-6}$	$2*10^{-6}$	$2.1*10^{-6}$
$R_{outer}(\Omega.cm^2)$	7.2	7.4	10.1	7.6	8.5	6.8	8.3	8.1
C_{inner}(F/ cm^2)	$48*10^{-6}$	$48*10^{-6}$	$49*10^{-6}$	$44*10^{-6}$	$42*10^{-6}$	$37*10^{-6}$	$39*10^{-6}$	$35*10^{-6}$
$R_{inner}(\Omega.cm^2)$	55	65.6	73	52.9	66.1	61.7	73.8	70
$W_{C-R}(\Omega.cm^2)$	6900	10600	8800	7300	8700	11100	10000	9000
W_{C-T}	2.1	6.96	4.3	3.7	3.6	5.8	7.3	8.6
W_{C-P}	0.5	0.5	0.5	0.5	0.5	0.5	0.5	0.5
$R_a(\Omega.cm^2)$	$1.15*10^{15}$	$2.8*10^{10}$	34600	10300	23800	12000	25000	30000
C_{dl}(F/ cm^2)	$26*10^{-6}$	$27*10^{-6}$	$28*10^{-6}$	$28*10^{-6}$	$26*10^{-6}$	$32*10^{-6}$	$30*10^{-6}$	$37*10^{-6}$

(6) Applied current density of 300 mA/m^2.

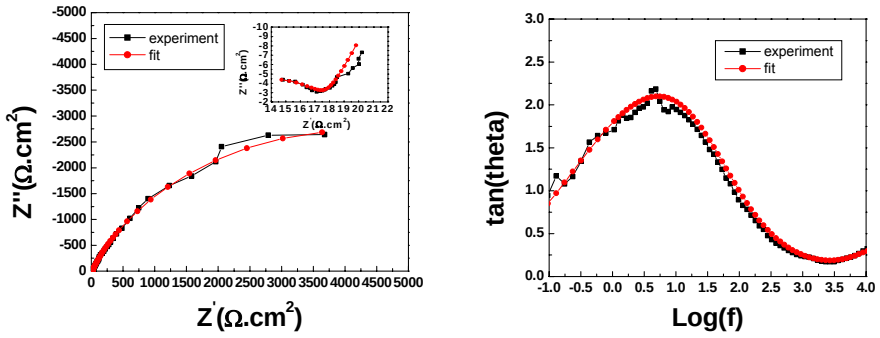

(a) Nyquist graph **(b) Bode graph**

Figure 4.56. Impedance spectra for mild steel samples with current density of 300 mA/m^2 for 6 hours immersion in artificial seawater.

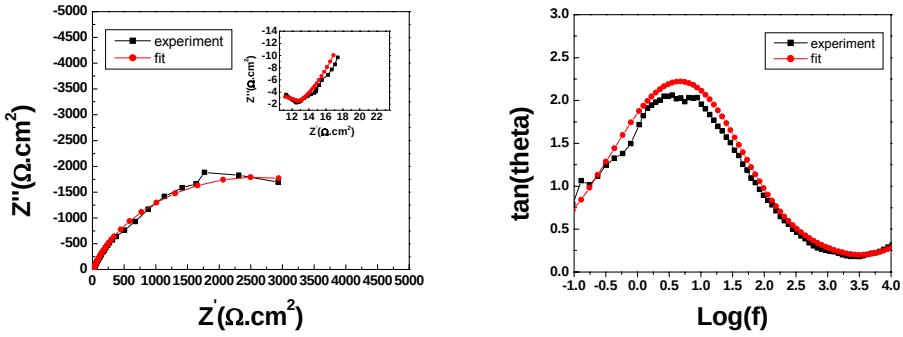

(a) Nyquist graph **(b) Bode graph**

Figure 4.57. Impedance spectra for mild steel samples with current density of 300 mA/m^2 for 24 hours immersion in artificial seawater.

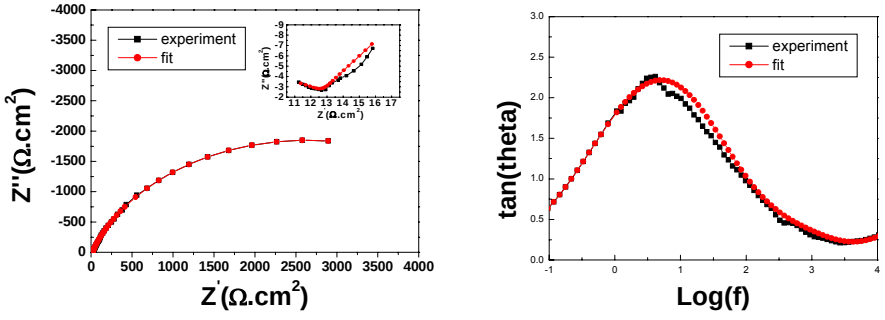

(a) Nyquist graph **(b) Bode graph**

Figure 4.58. Impedance spectra for mild steel samples with current density of 300 mA/m^2 for 72 hours (3 days) immersion in artificial seawater.

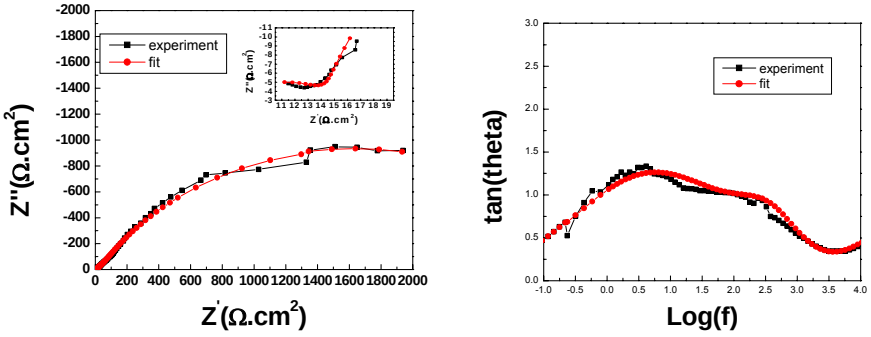

(a) Nyquist graph **(b) Bode graph**

Figure 4.59. Impedance spectra for mild steel samples with current density of 300 mA/m^2 for 168 hours (7 days) immersion in artificial seawater.

Table 4.19. Best fit results for equivalent circuit elements at applied current density of 300mA/m^2.

Immersion time (h)	6h	24h	48h	72h	96h	120h	144h	168h
$R_s(\Omega.cm^2)$	7.7	8.	8	8.7	8.7	9.6	8.8	8.1
C_{outer} (F/ cm^2)	2.3*10^{-6}	2.5*10^{-6}	2.1*10^{-6}	3.1*10^{-6}	3.2*10^{-6}	4.3*10^{-6}	3*10^{-6}	2.3*10^{-6}
$R_{outer}(\Omega.cm^2)$	5.8	6.1	6.4	6	6.4	6.8	8.3	8.9
C_{inner}(F/ cm^2)	41*10^{-6}	46*10^{-6}	37*10^{-6}	33*10^{-6}	34*10^{-6}	26*10^{-6}	20*10^{-6}	16*10^{-6}
$R_{inner}(\Omega.cm^2)$	26.8	24	21	27	35	54	58	52
$W_{C-R}(\Omega.cm^2)$	4100	4000	3300	2400	2600	2200	2000	1800
W_{C-T}	1.4	2.2	1.4	0.6	1.1	0.7	0.8	0.8
W_{C-P}	0.5	0.5	0.5	0.5	0.5	0.5	0.5	0.5
$R_a(\Omega.cm^2)$	1*10^{20}	1*10^{20}	1*10^{20}	1*10^{20}	1*10^{20}	1*10^{20}	1*10^{20}	1*10^{20}
C_{dl}(F/ cm^2)	27*10^{-6}	41*10^{-6}	39*10^{-6}	38*10^{-6}	38*10^{-6}	36*10^{-6}	28*10^{-6}	19*10^{-6}

(7) Applied current density of 400 mA/m^2.

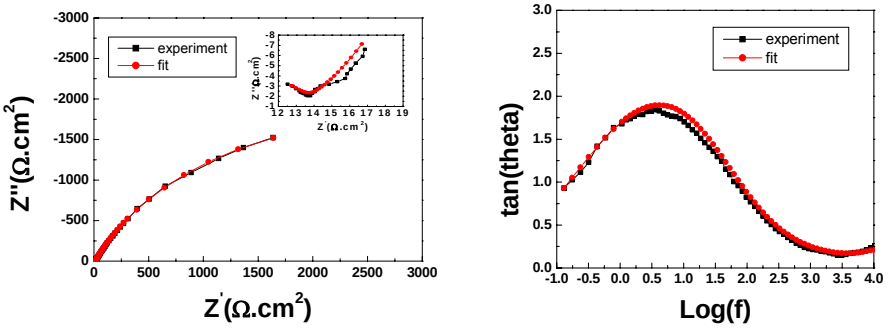

(a) Nyquist graph **(b) Bode graph**

Figure 4.60. Impedance spectra for mild steel samples with current density of 400 mA/m^2 for 6 hours immersion in artificial seawater.

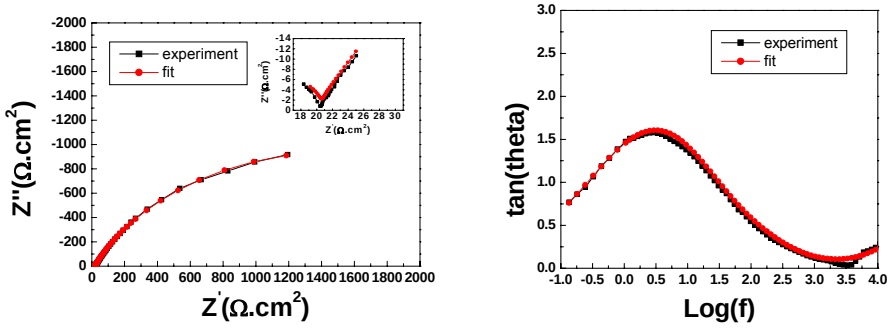

(a) Nyquist graph **(b) Bode graph**

Figure 4.61. Impedance spectra for mild steel samples with current density of 400 mA/m^2 for 24 hours immersion in artificial seawater.

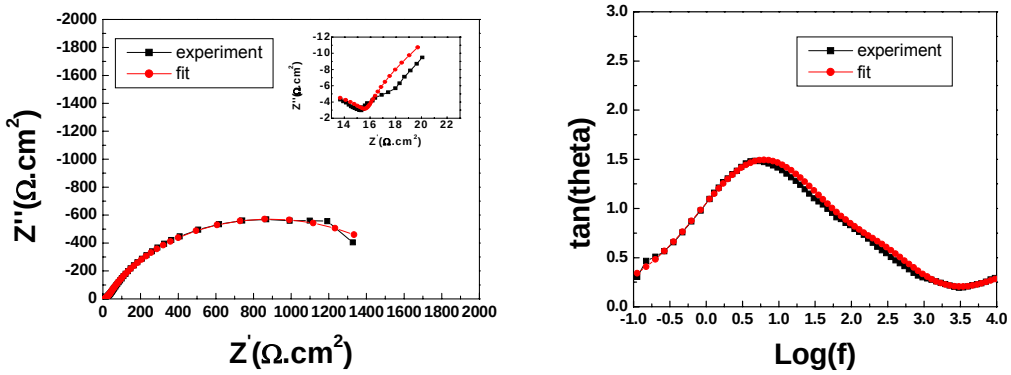

(a) Nyquist graph **(b) Bode graph**

Figure 4.62. Impedance spectra for mild steel samples with current density of 400 mA/m^2 for 72 hours (3 days) immersion in artificial seawater.

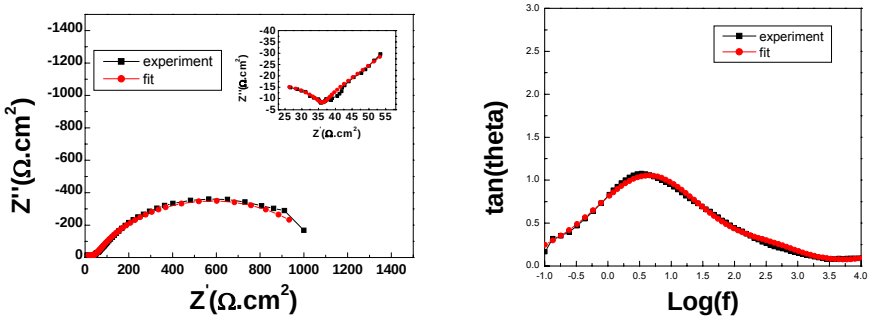

(a) Nyquist graph **(b) Bode graph**

Figure 4.63. Impedance spectra for mild steel samples with current density of 400 mA/m^2 for 168 hours (7 days) immersion in artificial seawater.

Table 4.20. Best fit results for equivalent circuit elements at applied current density of 400mA/m^2.

Immersion time (h)	6h	24h	48h	72h	96h	120h	144h	168h
$R_s(\Omega.cm^2)$	10.2	12.1	10.1	9.1	12.8	15.4	17.81	15
C_{outer} (F/ cm^2)	$3.6*10^{-6}$	$1*10^{-6}$	$2.6*10^{-6}$	$1.6*10^{-6}$	$0.7*10^{-6}$	$0.6*10^{-6}$	$0.5*10^{-6}$	$0.5*10^{-6}$
$R_{outer}(\Omega.cm^2)$	5.3	9.2	5.8	7.8	14.9	17.3	17	22.2
C_{inner}(F/ cm^2)	$52*10^{-6}$	$68*10^{-6}$	$38*10^{-6}$	$29*10^{-6}$	$26*10^{-6}$	$24*10^{-6}$	$24*10^{-6}$	$28*10^{-6}$
$R_{inner}(\Omega.cm^2)$	32.2	29	28	29	38	43	38	43.8
$W_{C-R}(\Omega.cm^2)$	3100	2000	2500	1400	1100	1400	1000	1000
W_{C-T}	2.2	1.7	1.4	0.64	0.62	0.81	0.62	0.63
W_{C-P}	0.5	0.5	0.5	0.5	0.5	0.5	0.5	0.5
$R_a(\Omega.cm^2)$	$1*10^{20}$	$1*10^{20}$	$1*10^{20}$	$1*10^{20}$	$1*10^{20}$	$1*10^{20}$	$1*10^{20}$	$1*10^{20}$
C_{dl}(F/ cm^2)	$43*10^{-6}$	$50*10^{-6}$	$41*10^{-6}$	$33*10^{-6}$	$38*10^{-6}$	$51*10^{-6}$	$47*10^{-6}$	$28*10^{-6}$

4.3.8.3. Comparison and Discussion.

The cathodic processes on the steel surface are described by the diffusion Warburg impedance since diffusion of the electrochemically active species is thought to be a limiting stage of the cathodic process. The data which has been extracted from our model shows an excellent fit with the Warburg impedance $W_{C\text{-}R}$ which is thought to equate to the limiting current density of the process.

Another parameter contained within the Warburg impedance and which is a feature of Zview, is W-T which equals δ^2/D, where D is the diffusion coefficient of the diffusing electroactive species and δ is its diffusion layer thickness.

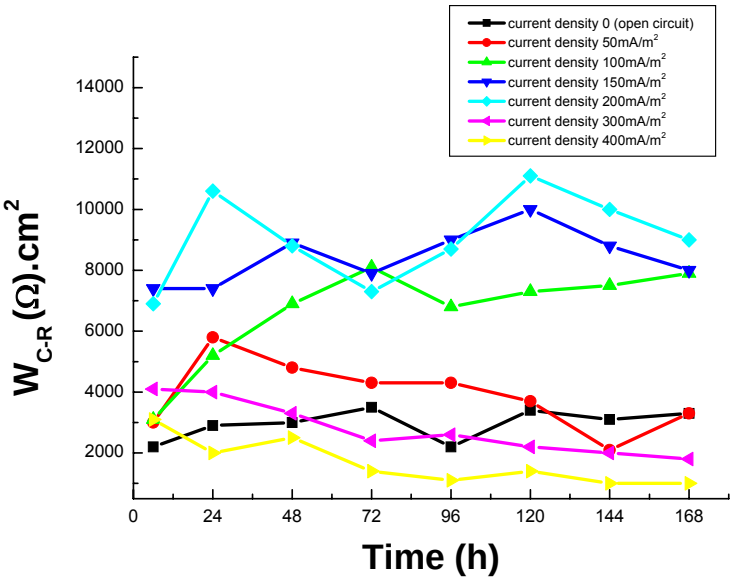

Figure 4.64. Plots of values for the cathodic charge transfer resistance $W_{C\text{-}R}$ with increasing time at different applied current densities.

The parameters for the cathodic charge transfer resistance $W_{C\text{-}R}$ are given in Figure 4.64, and Tables 4.21, and the values of anodic charge transfer resistance R_a are also presented in Table 4.22. The anodic charge transfer process is clearly iron corrosion, and as the resistance increases so corrosion rate decreases. Referring to the data given in Table 4.22 the regions of full protection can be seen. Arbitrarily we have highlighted those regions where anodic charge transfer resistances (R_a) are over 100,000 $\Omega.cm^2$ (highlighted in the blue area) this indicates that the anodic reaction has become infinitely small and that the cathodic protection is working.

Table 4.21. Values of cathodic charge transfer resistance W_{C-R} ($\Omega.cm^2$) with increasing immersion time at the different applied current densities.

Applied current densities (mA/m^2)	6 h	24h	48h	72h	96h	120h	144h	168h
0 (open circuit)	2200	2900	3000	3500	2200	3400	3100	3300
$50mA/m^2$	3000	5800	4800	4300	4300	3700	2100	3300
$100mA/m^2$	3100	5200	6900	8100	6800	7300	7500	7900
$150mA/m^2$	7400	7400	8900	7900	9000	10000	8800	7800
$200mA/m^2$	6900	10600	8800	7300	8700	11100	10000	9000
$300mA/m^2$	4100	4000	3300	2400	2600	2200	2000	1800
$400mA/m^2$	3100	2000	2500	1400	1100	1400	1000	1000

Table 4.22. Values of anodic charge transfer resistance R_a ($\Omega.cm^2$) with increasing immersion time at the different applied current densities.

Applied current densities(mA/m^2)	6 h	24h	48h	72h	96h	120h	144h	168h
0 (open circuit)	2700	6000	5000	4200	4300	3100	4300	**3100**
$50mA/m^2$	3100	4000	3500	3100	5700	3100	2400	**2600**
$100mA/m^2$	58700	20000	8000	9600	6600	8800	10000	**20000**
$150mA/m^2$	100400	130000	15400	14900	13800	14600	22200	**14300**
$200mA/m^2$	$1.15*10^{15}$	$2.8*10^{10}$	34600	10300	23800	12000	25000	**30000**
$300mA/m^2$	$1*10^{20}$	$1*10^{20}$	$1*10^{20}$	$1*10^{20}$	$1*10^{20}$	$1*10^{20}$	$1*10^{20}$	$\mathbf{1*10^{20}}$
$400mA/m^2$	$1*10^{20}$	$1*10^{20}$	$1*10^{20}$	$1*10^{20}$	$1*10^{20}$	$1*10^{20}$	$1*10^{20}$	$\mathbf{1*10^{20}}$

In the open circuit and 50 mA/m^2 cases (Figure 4.64 and Table 4.21), we are obviously looking at an unprotected and underprotected surface where the charge transfer processes are both the oxygen reduction reaction and the iron corrosion reaction. In these cases, the values of cathodic resistance with increasing time at various current densities are given in Table 4.21, and these range between 2000 - 6000 $\Omega.cm^2$. In addition, the values obtained for the anodic resistance R_a were also fairly low, being between 2000 - 6000 $\Omega.cm^2$, as shown in Table 4.22. Overall, these findings indicate that the oxygen reduction reaction and the iron corrosion reaction are both happening at the same time. Both these reactions are taking place on an iron surface which is not too well covered by the calcareous film and is clearly corroding; as can be seen in the optical images obtained (Plates 4.2(a) and (b)).

Considering next the values of cathodic resistance W_{C-R} obtained in the case of using applied current densities of 100 mA/m^2, 150 mA/m^2 and 200 mA/m^2. It is evident from Table 4.21, that the values of cathodic resistance W_{C-R} obtained at these three applied current densities increased concurrently with increasing applied current density. With the

sole exception of the values obtained at 72 hours, all the values of cathodic resistance W_3-R obtained at a current density of 200 mA/m^2 were substantially higher than the corresponding values obtained at a current density of 100 mA/m^2. This indicates that the surfaces were covered by a fairly good calcareous deposit.

The values obtained for W_{C-R} at 100 mA/m^2 can be discussed further. There is a slow steady increase in W_{C-R} between 3100 to 8100 Ω.cm^2 during the first 72 hours of the immersion period, then W_{C-R} declines steadily to 6800 Ω.cm^2 after a further 24 hours of immersion (total 96 h), before increasing again to almost 8000 Ω.cm^2 at 168 hours of immersion. This pattern of increasing resistance followed by decrease then subsequent increase is most likely explained by detachment of regions of the calcareous film after 72 hours. At this level of current density the visual evidence is that there is still some corrosion of the steel (Plate 4.2(d)). Also, the potential data (Figure 4.10) indicates that it has reached the nominal accepted protection criterion (-774 mV (SCE)), but our weight loss data (Figure 4.4) indicates some corrosion has occurred after 30 days immersion, and a similar result can be seen with the Humble data (Figure 4.5) after an experimental period of 1 year. The SEM micrographs presented in Plate 4.8 and Plate 4.13 together with the EDX spectra given in Figure 4.16 show coherent deposits of magnesium rich precipitates underlying iron corrosion products with calcium containing growths occurring at adjacent areas. The steady increase is probably a consequence of a decline in the oxygen reduction reaction due to the growth and compactness of these mixed iron, magnesium and calcium films inhibiting oxygen transport. One would expect from other longer term data that at this current density the film would eventually fully protect the steel substrate and the potential would then decline to significantly below the protection potential. There is some evidence for this from data obtained for real marine structures [14].

The two intermediate current densities of 150 and 200 mA/m^2 may be considered together. Our weight loss data clearly shows corrosion to have ceased at these values. Photographic evidence shows slight browning of the surface at 150 mA/m^2 (Plate 4.2(e)). An analysis of a cross section of the sample and film deposit using SEM clearly shows evidence of the film beginning to fracture especially at 200 mA/m^2 (Plate 4.2(f)). A tentative explanation of the behaviour of W_{C-R} with time at these two current densities can now be proposed. Initially, after one day of immersion, the value of W_{C-R} rises dramatically to around 10000 Ω.cm^2. Again it is suggested that a film grows on the steel

surface which is an oxygen barrier and we are seeing a reduction in the oxygen charge transfer resistance. However, at these current densities, over time, the film eventually begins to crack, and subsequently becomes less compact and as a consequence, W_{C-R} begins to fall erratically. With further time, the film repairs and W_{C-R} begins to climb again. This is our explanation of the longer term behaviour of the films at these two current densities. A slight indication of film fracture and repair was observed in the case of a current density of 100 mA/m^2, but with the next two higher current densities of 150 and 200 mA/m^2, the phenomenon was much more pronounced and obvious. In addition, comparing with the open circuit and 50 mA/m^2 cases, the values obtained in these conditions for the anodic resistance R_a were generally increased significantly at the higher applied current densities, which are shown in Table 4.22. Overall, for these 150 mA/m^2 and 200 mA/m^2 cases, the data indicates that there were mainly oxygen reduction reactions and decreased iron corrosion reactions taking place on the steel surface.

For the 300 mA/m^2 and 400 mA/m^2 cases, according to the plots presented in Figure 4.64 and values given in Table 4.21, the values of cathodic resistance W_{C-R} were generally very low because of the start of hydrogen evolution which is thought to be responsible for the detachment of the calcareous film. This was especially evident in the case of an applied current density of 400 mA/m^2 where the steel potential was around -1100 mV (SCE) in Figure 4.10. The 300 mA/m^2 curve looks very similar and the same explanation as given for the 400 mA/m^2 case is thought to hold, except that the values obtained for the 300 mA/m^2 situation were noted to be slightly higher than the values obtained with a current density of 400 mA/m^2, as is evident from the data given in Table 4.21. This means that the films present on the surface of the steel provide some resistance to the cathodic reaction. The SEM image shown in Plate 4.12(b) clearly gives the appearance of a break-away process occurring at -1050 mV SCE. At this potential, we would expect hydrogen evolution, which would cause intermittent dislodging of the calcareous film and a metal surface which would be partially film free. The anodic resistances R_a shown in Table 4.22, which were over 100,000 Ω.cm^2, indicated that in these cases, the anodic reaction had stopped, so there was only the cathodic reaction (the oxygen reduction reaction and hydrogen evolution) occurring on the steel surface.

So, overall, the values of W_{C-R} would appear to represent the restricted or unrestricted diffusion of active species that support the cathodic reaction on a steel surface that is

mainly the oxygen reduction reaction plus a contribution from the water reduction process.

According to the data given in Table 4.22, the values of anodic resistance R_a generally become higher with the increasing current densities. As can be seen from Table 4.22, the anodic reactions slowed down when the structure had been cathodically polarized with the higher applied current densities. This also indicates that the anodic reactions ceased at the full protected situation (300 mA/m^2: -1050 mV(SCE); and 400 mA/m^2: -1100 mV (SCE)). The surface has been polarized to below the oxidation/reduction potential of the reaction

$$Fe + 2OH^- = Fe(OH)_2$$

which may be calculated [18] as -877 mV SHE (-1119 mV (SCE)).

Table 4.23. Values of W_{C-T} with increasing time at different applied current densities.

Applied current densities(mA/m^2)	6 h	24h	48h	72h	96h	120h	144h	168h
0 (open circuit)	3.3	2.1	1.2	1.8	0.9	1.5	1.7	2.1
50mA/m^2	1	3	3.3	3.2	3.6	3.3	4	3.2
100mA/m^2	3.3	1.7	3.3	2.8	2.3	3	3.7	2.2
150mA/m^2	2.8	4.4	4.6	3.6	4.3	5	5	3.5
200mA/m^2	2.1	7	4.3	3.7	3.6	5.8	7.3	8.6
300mA/m^2	1.4	2.2	1.4	0.6	1.1	0.7	0.8	0.8
400mA/m^2	2.2	1.7	1.4	0.6	0.6	0.8	0.6	0.6

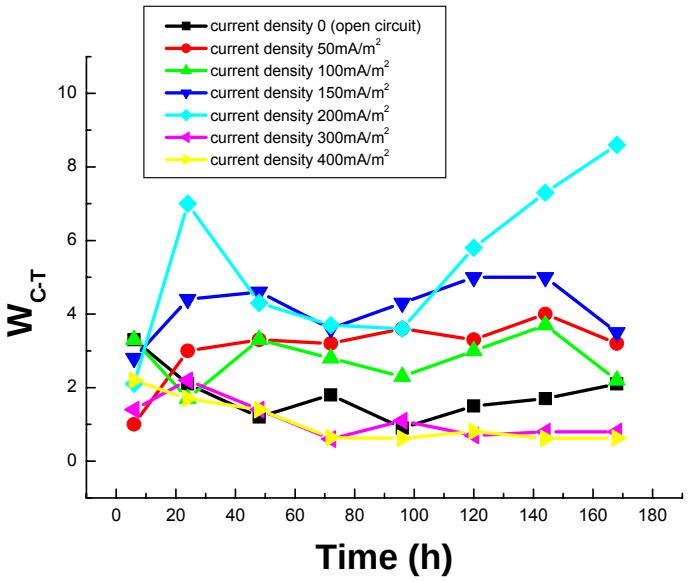

Figure 4.65. Plots of values for W_{C-T} with increasing time at different applied current densities.

At the open circuit potential condition, the average value of $W_{C\text{-}T}$ is 1.8. The average diffusion path of the active specie (oxygen) can be calculated from $\delta = \sqrt{W_{C-T} * D}$, where $D=225*10^{-5} cm/s$ [23] the diffusion coefficient of oxygen. This value is assumed to be constant during our measurements and can be used to calculate various values of δ at our chosen current densities. Therefore the average diffusion path of oxygen at the open circuit condition is $64*10^{-3}$ mm which is 64 μm.

In the cases of applied current densities of 50 mA/m^2 and 100 mA/m^2 (Figure 4.65 and Table 4.23), the values of $W_{C\text{-}T}$ were fairly similar over the total immersion time with average values of 3.1 and 2.8 respectively. The average diffusion path for O_2 increased to 83 μm and 79 μm.

In the 150 mA/m^2 and 200 mA/m^2 cases, the values of $W_{C\text{-}T}$ were higher, lying between 2.8 - 8.6, which indicates that protective deposits were forming under conditions of full cathodic protection, especially at 200 mA/m^2, where the values of $W_{C\text{-}T}$ increased with time after 96 hours immersion, from 3.6 at 96 hours to 8.6 at 168 hours. The average values of $W_{C\text{-}T}$ in these two cases were 4.2 and 5.3 respectively over the total immersion time, and the diffusion path for oxygen increased to 97.2 μm and 109 μm.

It is interesting to note, that at the cathodic polarisation conditions of 300 mA/m^2 and 400 mA/m^2, the values of $W_{C\text{-}T}$ reduced to 1.14 and 1.06, which was probably due to hydrogen evolution that lead to film detachment and easy access of active species to the steel surface, and the diffusion path for oxygen decreased to 50.3 μm and 48.9 μm.

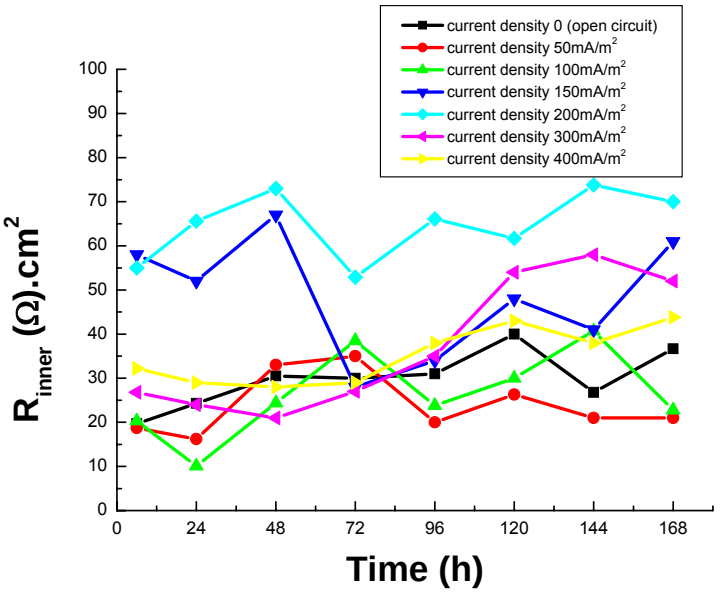

Figure 4.66. Plots of values for the inner layer resistor R_{inner} with increasing time at different applied current densities.

Table 4.24. The inner layer (L_2) resistance R_{inner} ($\Omega.cm^2$) with increasing immersion time. at the different applied current densities.

Applied current densities(mA/m^2)	6h	24h	48h	72h	96h	120h	144h	168h
0(open circuit)	19.7	24.3	30.5	30	31	40	26	36.7
50mA/m^2	18.7	16.2	33	35	20	26.3	21	21
100mA/m^2	20.3	10.1	24.4	38.5	23.8	30	40.7	22.8
150mA/m^2	58	55	67	28	34	48	41	61
200mA/m^2	55	65.6	73	52.9	66.1	61.7	73.8	70
300mA/m^2	26.8	24	21	27	35	54	58	52
400mA/m^2	32.2	29	28	29	38	43	38	43.8

The contribution of the inner and outer layers of the film to the impedance is insignificant. However the variation of R_{inner} and C_{inner} can be deduced from the results.

Considering the results given in Figure 4.66 and Table 4.24, the resistance R_{inner} of the inner layer increases with increasing time in artificial sea water at different levels of cathodic protection. For the cathodic protection cases of 150 mA/m^2 and 200 mA/m^2, the inner layer (L_2) was assumed to be primarily composed of the compact magnesium and iron compounds and has a slightly increased R_{inner}. But in the cases of the applied current densities of 50 mA/m^2 and 100 mA/m^2, the inner layer (L_2) was assumed to be primarily composed of a mixture of the iron corrosion product and a co-deposited Mg compound. Generally the values of R_{inner} are similar for all applied current densities.

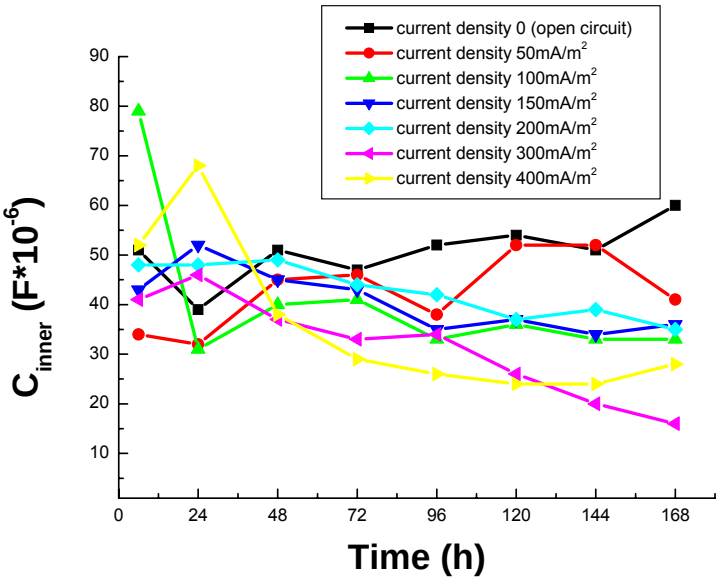

Figure 4.67. Plots of values for the capacitor C_{inner} with increasing time at different applied current densities.

Table 4.25. Values of the inner layer (L_2) capacitor C_{inner} (F) with increasing immersion time at the different applied current densities.

Applied current densities(mA/m^2)	6h	24h	48h	72h	96h	120h	144h	168h
0(open circuit)	$51*10^{-6}$	$39*10^{-6}$	$51*10^{-6}$	$47*10^{-6}$	$52*10^{-6}$	$54*10^{-6}$	$51*10^{-6}$	$60*10^{-6}$
$50mA/m^2$	$34*10^{-6}$	$32*10^{-6}$	$45*10^{-6}$	$46*10^{-6}$	$38*10^{-6}$	$52*10^{-6}$	$52*10^{-6}$	$41*10^{-6}$
$100mA/m^2$	$79*10^{-6}$	$31*10^{-6}$	$40*10^{-6}$	$41*10^{-6}$	$33.2*10^{-6}$	$36*10^{-6}$	$33*10^{-6}$	$33*10^{-6}$
$150mA/m^2$	$43*10^{-6}$	$52*10^{-6}$	$45*10^{-6}$	$43*10^{-6}$	$35*10^{-6}$	$37*10^{-6}$	$34*10^{-6}$	$36*10^{-6}$
$200mA/m^2$	$48*10^{-6}$	$48*10^{-6}$	$49*10^{-6}$	$44*10^{-6}$	$42*10^{-6}$	$37*10^{-6}$	$39*10^{-6}$	$35*10^{-6}$
$300mA/m^2$	$41*10^{-6}$	$46*10^{-6}$	$37*10^{-6}$	$33*10^{-6}$	$34*10^{-6}$	$26*10^{-6}$	$20*10^{-6}$	$16*10^{-6}$
$400mA/m^2$	$52*10^{-6}$	$68*10^{-6}$	$38*10^{-6}$	$29*10^{-6}$	$26*10^{-6}$	$24*10^{-6}$	$24*10^{-6}$	$28*10^{-6}$

From the data presented in Figure 4.67 and Table 4.25, the values of the capacitance C_{inner} of the inner layer (L_2) did not change much with increasing immersion time and cathodic polarization and has an average value of $40*10^{-6}$ F/cm^2. This indicates that the thickness of the inner layer remains similar for all cases of cathodic protection. This finding confirms that the thickness of calcareous deposit is determined by growth of the outer layer.

The thickness of the inner film has been calculated by the following equation:

$$C = \frac{\varepsilon\varepsilon_0}{d} \quad \text{……} \quad (4\text{-}14)$$

Where ε_0: dielectric permeability $\varepsilon_0 = 8.854 * 10^{-12}\ F/m^{-1}$;

ε: the dielectric constant, $\varepsilon = \theta\varepsilon_{H_2O} + (1-\theta)\varepsilon_{MgCO_3}$;

$\varepsilon_{H_2O} = 80$; $\varepsilon_{MgCO_3} = 8.1$ [23]

θ : the proportion of water in the layer.

By varying θ, the thicknesses of inner layer could be calculated from the previous equations and were in the order of nanometers, which indicates that the high frequency tail of the impedance spectra with low values of impedance were impossible to resolve.

The contribution of the outer layer to the total impedance is negligible as well. According to the data presented in Tables 4.14 to 4.20, the variation of R_{outer} is in the range 4 - 22 $\Omega.cm^2$, similar to solution resistance that varies from 5 - 18 $\Omega.cm^2$. The outer layer capacitance C_{outer} was in the range of 0.5 - $5*10^{-6}$ F/cm^2. There was also no significant change in capacitance with varying applied current density.

4.3.8.4. Impedance work conclusions.

1. We have proposed an equivalent circuit to correspond with our impedance data based on the evidence obtained from SEM/EDX analysis.

2. This equivalent circuit is valid for all levels of current density used in this work from zero (open circuit) to 400 mA/m^2.

3. The basic concept of our equivalent circuit is a limited layer Warburg diffusion model in combination with a porous layer with defects.

4. The effect of increasing the current density is clearly seen in the anodic charge transfer process of iron dissolution with the charge transfer resistance becoming infinitely large at higher current densities (Applied current densities at 300 mA/m^2 and 400 mA/m^2 cases).

5. The Warburg diffusion model is applied to the cathodic process, mainly the oxygen reduction reaction. The cathodic Warburg diffusion W_C, consisted of three parameters, W_{C-R}, W_{C-T}, and W_{C-P}, and it evaluated the cathodic reaction level.

6. We have assumed literature values of the oxygen diffusion coefficients from which we have calculated oxygen diffusion path distances.

7. The values of the oxygen diffusion path distances correspond well with the SEM values obtained for the calcareous film thicknesses.

8. The effects of over protection and hydrogen evolution are to cause film rupture. Film rupture events can be clearly seen from the oxygen diffusion path distances.

4.4. Variable current density experiments.

Earlier in the introduction to this Chapter (Section 4.3) we have already given the justification for carrying out this next set of experiments. For this part of the study, a higher current density (either 200 mA/m^2 or 300 mA/m^2) was initially used for the first three days, during which time some deposits were formed, and then a reduced current density of 100 mA/m^2 was employed for the remainder (9 days) of the test period (total immersion time 12 days).

A further experimental study was performed using samples which were subjected to constant current densities of 200 mA/m^2 and 300 mA/m^2 during an initial immersion period of six days, and then the current density was subsequently decreased to 50 mA/m^2 for a further 6 days (total immersion time 12 days).

An additional set of control samples was tested by being immersed for the entire 12 day period at a constant current density of 200 mA/m^2 and 300 mA/m^2 respectively.

In all cases, the potential of the samples which had the same initial applied current densities were compared. For all samples, at the termination of the 12 day period of immersion, the appearance and composition of the deposited films were then investigated and analysed using SEM, EDX and XRD techniques, as described in previous experiments.

4.4.1. Potential Measurements.

For this set of immersion tests designed to study and compare the effects of both constant and variable current densities, the six different experimental regimes employed can be summarized as follows:

(i). A constant current density of 200 mA/m^2 was used for the entire 12 day immersion period.

(ii). A current density of 200 mA/m^2 was employed for an initial three days, then the current density was reduced to 100 mA/m^2 for the remainder of the 12 day test period.

(iii). A current density of 200 mA/m^2 was employed for an initial six days, then a reduced current density of 50 mA/m^2 was employed for a further six days.

(iv). A constant current density of 300 mA/m^2 was used for the entire 12 day immersion period.

(v). A current density of 300 mA/m^2 was employed for an initial three days, then the current density was reduced to 100 mA/m^2 for the remainder of the 12 day test period.

(vi). A current density of 300 mA/m^2 was employed for an initial six days, then a reduced current density of 50 mA/m^2 was employed for a further six days.

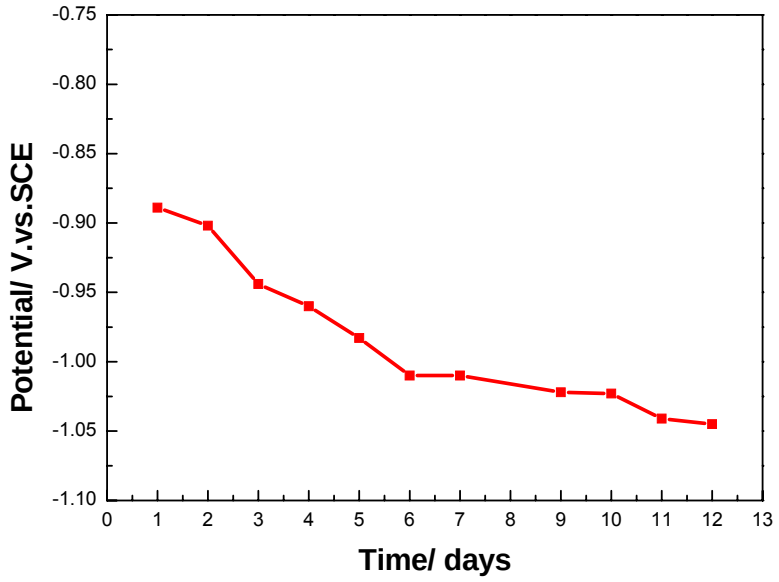

Figure 4.68. Graph showing plot of daily potential measurements obtained over a 12-day immersion period in artificial seawater (Applied constant current density of 200 mA/m^2).

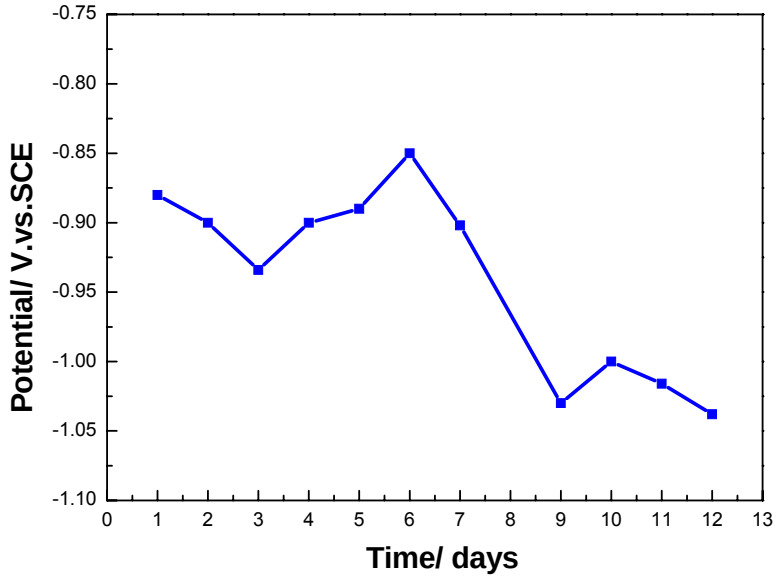

Figure 4.69. Graph showing plot of daily potential measurements obtained over a 12-day immersion period in artificial seawater (Applied current density of 200 mA/m^2 for the first 3 days then decreased to 100 mA/m^2).

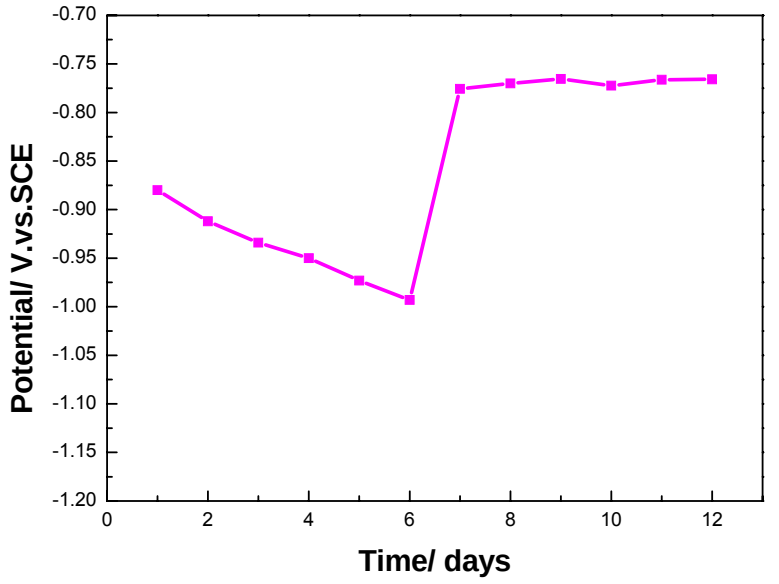

Figure 4.70. Graph showing plot of daily potential measurements obtained over a 12-day immersion period in artificial seawater (Applied current density of 200 mA/m^2 for the initial 6 days then decreased to 50 mA/m^2).

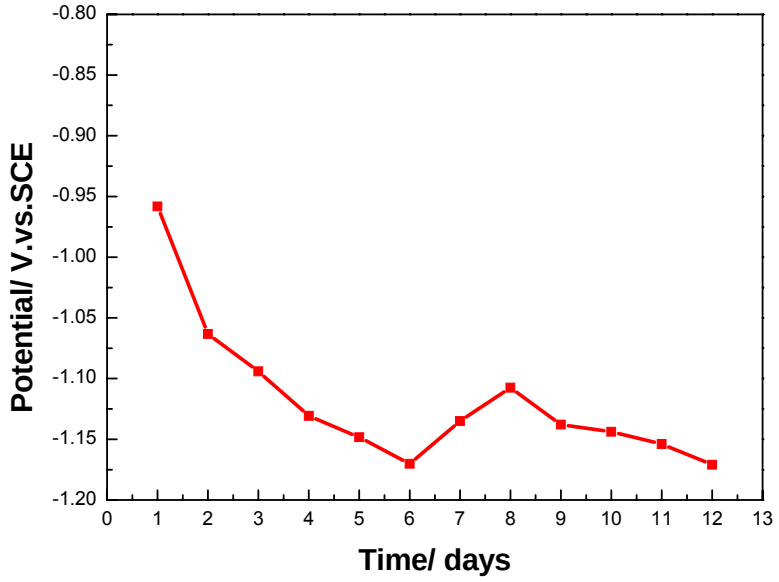

Figure 4.71. Graph showing plot of daily potential measurements obtained over a 12-day immersion in artificial seawater (Applied constant current density of 300 mA/m^2).

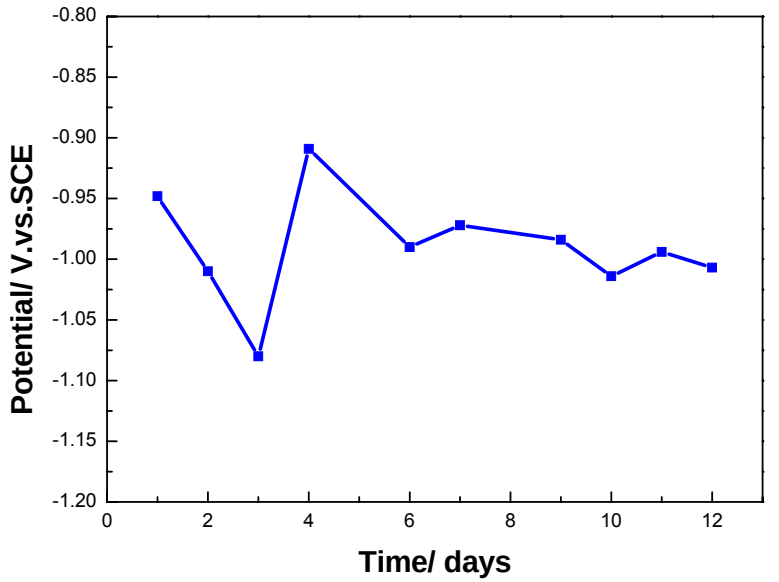

Figure 4.72. Graph showing plot of daily potential measurements obtained over a 12-day immersion in artificial seawater (Applied current density of 300 mA/m^2 for the initial period of 3 days then decreased to 100 mA/m^2).

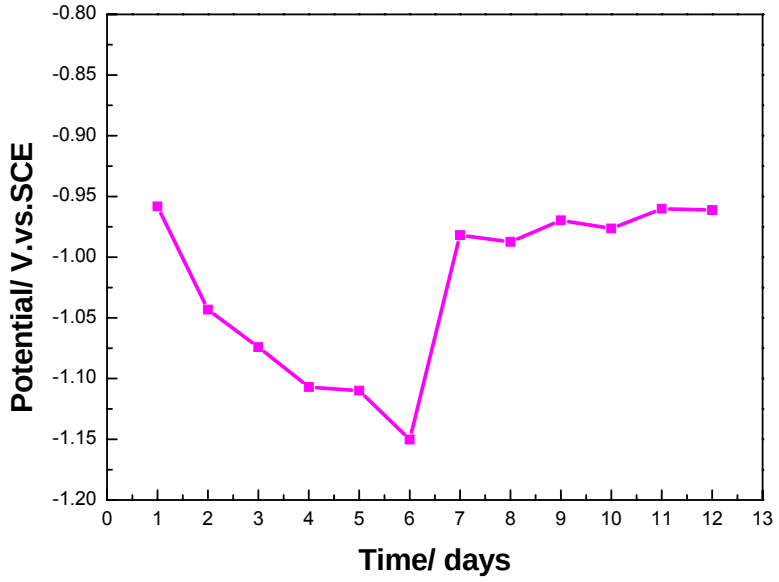

Figure 4.73. Graph showing plot of daily potential measurements obtained over a 12-day immersion in artificial seawater (Applied current density of 300 mA/m^2 for the first 6 days then decreased to 50 mA/m^2).

Figures 4.68 to 4.70 illustrate the graphs plotted for the potential/time measurements recorded daily for the three different experimental situations (i) to (iii) respectively over the 12 day testing period. From Figure 4.68, it was evident that the potential was decreasing with time over the entire 12 days, which indicated that the calcareous film was growing with time. According to the potential plots illustrated in Figure 4.69, the potential became slightly positive between day 3 to 6 after the current density was reduced to 100 mA/m^2, but then become more negative again after day 9. Also, since the values of potential recorded were mainly about or over -0.9V (see Figure 4.69), this indicated that this sample would still be cathodically protected (earlier we have shown that the minimum potential required to achieve complete protection was -0.895V (SCE) from Section 4.2.1). In the case of the sample that was subjected to an initial current density of 200 mA/m^2 for 6 days, then followed by a reduced current density of 50 mA/m^2 for the remaining 6 days (Figure 4.70), the values of the sample potentials became much more positive after the current density was reduced to 50 mA/m^2, and it was around -0.77V at 7 days. In addition, it was noted that significant corrosion occurred on the sample surface, which means that the sample was under protected.

Figures 4.71 to 4.73 illustrate the graphs plotted for the potential/time measurements recorded daily for the three different experimental situations (iv) to (vi), over the 12 day testing period. From Figures 4.71 to 4.73, all of the potentials obtained for the three samples were over -900mV, which suggests that they would still be totally protected (Chapter 4, Section 4.2.1). Also, from the visual inspection of the samples, there was no corrosion occurring on the surfaces of the samples, and also no corrosion was observed on the sample surfaces that were covered by a porous calcareous film. These observations and results indicate that the initial applied current density is playing a major important role in the cathodic protection of the samples. These results are in agreement with those available in the literature [14], which also suggest that the initial applied current density is very important for the formation of a protective calcareous film.

4.4.2. SEM and EDX results.

To investigate the differences in percentage content of calcium and magnesium in the deposits on the steel surfaces, both SEM examination and EDX analyses were performed (see Section 4.3.4). The relative percentages of the various elements determined using EDX quantification is presented in Tables 4.26 to 4.29. The working area of the samples was 10cm^2, the areas selected for the EDX analysis were chosen as three different areas along the length direction of the sample. It was decided to analyse three replicate areas, in order to improve the accuracy of the results and to demonstrate consistency in the composition of the deposit film. The secondary electron SEM micrographs of the surface topographies of the deposits are given in Plates 4.17 to 4.20.

(1). Current density of 200 mA/m^2 for initial 3 days then decreased to 100 mA/m^2.

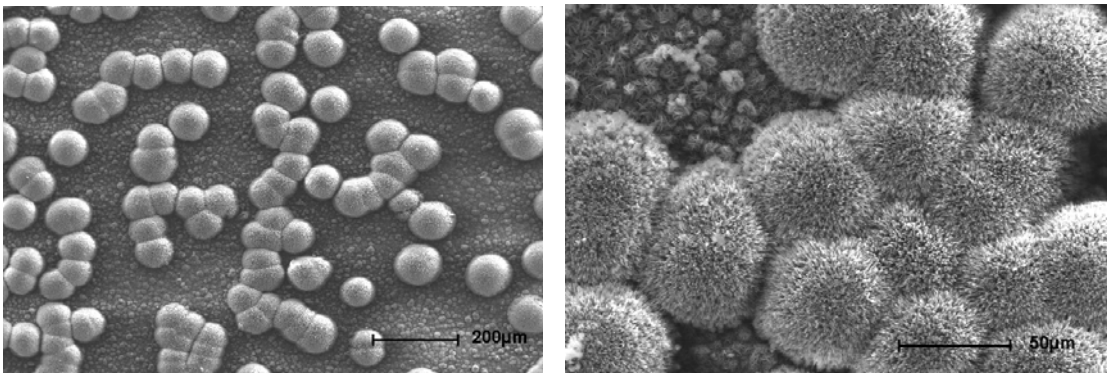

(a). Secondary electron image taken at 100x. **(b). Secondary electron image taken at 500x.**

Plate 4.17. SEM micrographs of surface of sample after immersion in artificial seawater for 12 days (applied current density of 200 mA/m^2 for the initial 3 days then decreased to 100 mA/m^2).

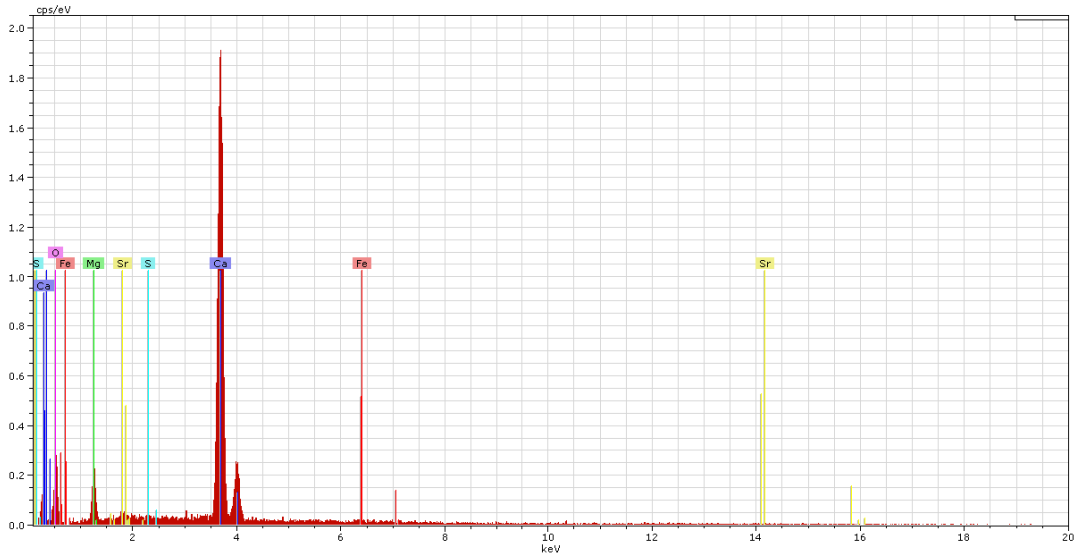

Figure 4.74. EDX spectra of surface of sample after immersion in artificial seawater for 12 days (Applied current density of 200 mA/m^2 for the initial 3 days then decreased to 100 mA/m^2).

Table 4.26. The relative percentages of various elements determined using EDX quantification, of calcareous film on steel samples after immersion in artificial seawater for 12 days (applied current density of 200 mA/m^2 for the initial 3 days then decreased to 100 mA/m^2 at magnification of 100x).

Percentage of element	Calcium	Magnesium	Sulfur	Iron	Strontium	Oxygen
Area 1	10.09832	18.59714	0.312721	0.442209	0.301968	70.24764
Area 2	6.851045	21.77534	0.321962	0.595348	0.235271	70.22104
Area 3	9.011396	19.31851	0.227421	0.598357	0.185457	70.65886
Average	8.653587	19.89399				

(2). Constant current density of 200 mA/m^2 for 12 days.

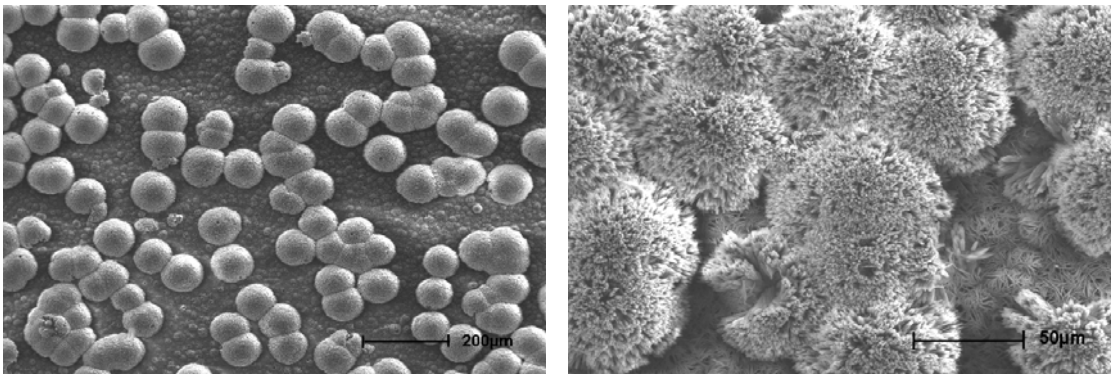

(a). Secondary electron image taken at 100x. **(b). Secondary electron image taken at 500x.**

Plate 4.18. SEM micrographs of surface of sample after immersion in artificial seawater for 12 days (Applied constant current density of 200 mA/m^2).

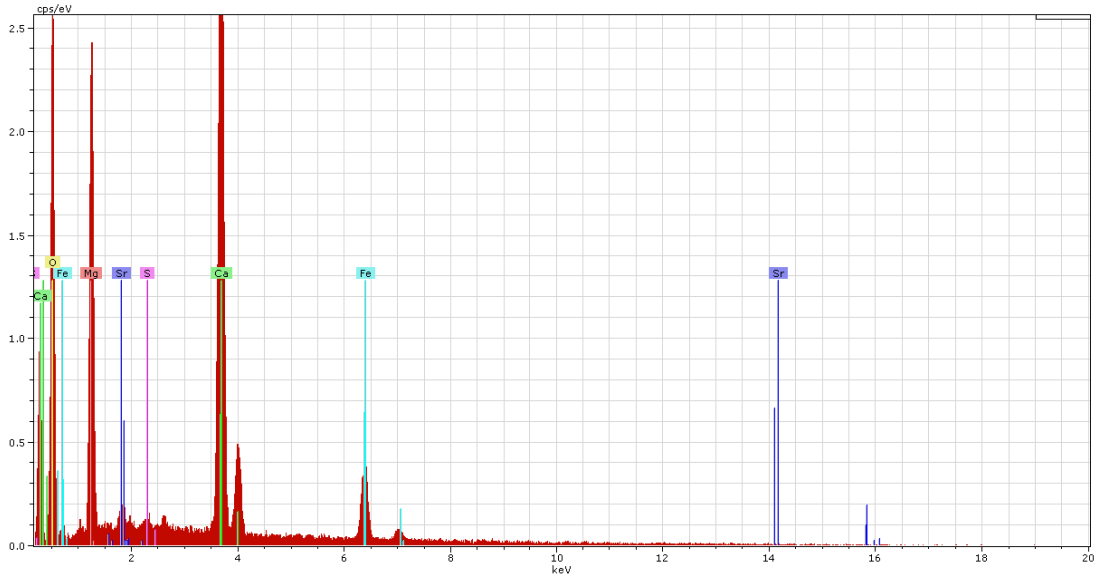

Figure 4.75. EDX spectra of surface of sample after immersion in artificial seawater for 12 days (Applied constant current density of 200 mA/m^2).

Table 4.27. The relative percentages of various elements determined using EDX quantification, of calcareous film on steel samples after immersion in artificial seawater for 12 days (applied constant current density of 200 mA/m^2 at magnification of 100x).

Percentage of element	Calcium	Magnesium	Sulfur	Iron	Strontium	Oxygen
Area 1	10.07133	17.61306	0.324186	0.291138	0.368447	71.33184
Area 2	14.88112	13.48883	0.31009	3.050116	0.379151	67.89069
Area 3	12.00294	19.16085	0.419077	0.289159	0.502628	67.62534
Average	12.31846	16.754246				

(3). Current density of 300 mA/m^2 for 3 days then decreased to 100 mA/m^2.

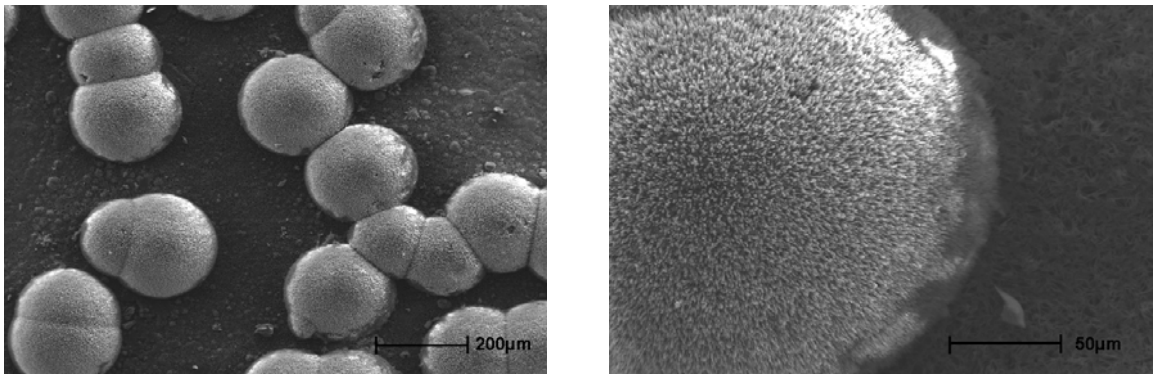

(a). Secondary electron image taken at 100x **(b). Secondary electron image taken at 500x**

Plate 4.19. SEM micrographs of surface of sample after immersion in artificial seawater for 12 days (Applied current density of 300 mA/m^2 for the initial 3 days then decreased to 100 mA/m^2).

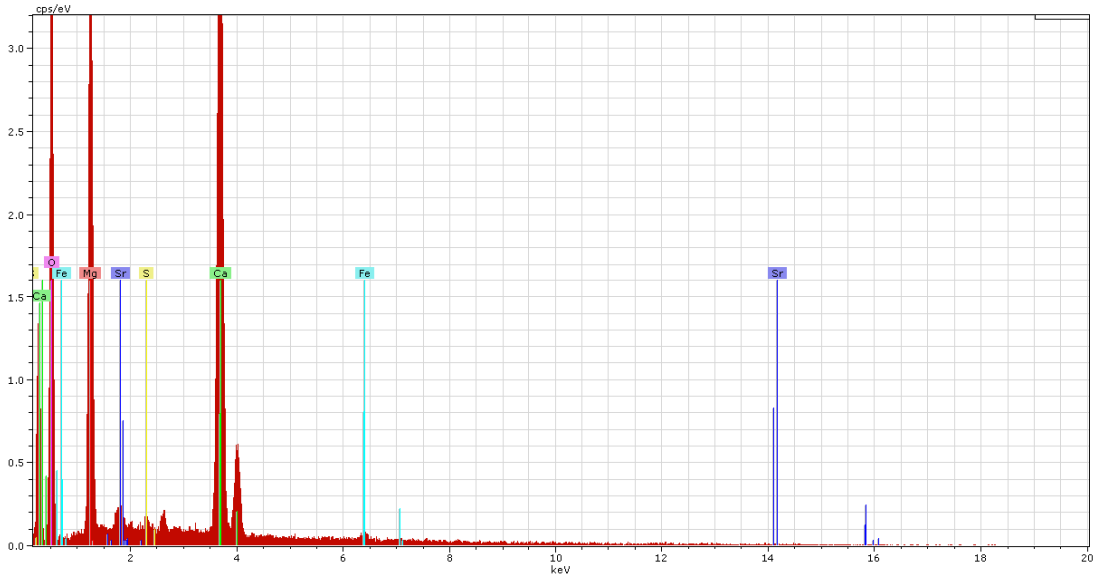

Figure 4.76. EDX spectra of surface of sample after immersion in artificial seawater for 12 days (applied current density of 300 mA/m^2 for the initial 3 days then decreased to 100 mA/m^2).

Table 4.28. The relative percentages of various elements determined using EDX quantification, of calcareous film on steel samples after immersion in artificial seawater for 12 days (applied current density of 300 mA/m^2 for the initial 3 days then decreased to 100 mA/m^2), [Magnification = 100 X].

Percentage of element	Calcium	Magnesium	Sulfur	Iron	Strontium	Oxygen
Area 1	13.63397	18.42115	0.403137	0.326338	0.436851	66.77855
Area 2	17.83058	12.89118	0.415029	0.283295	0.680228	67.89968
Area 3	13.8412	16.67639	0.345437	0.323419	0.451832	68.36173
Average	15.101916	15.99624				

(4) Current density of 300 mA/m^2 for 6 days then decreased to 50 mA/m^2.

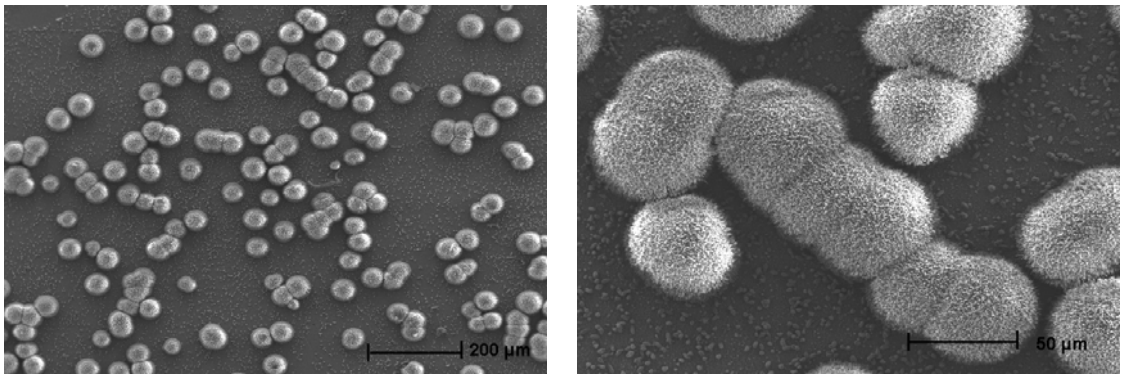

(a). Secondary electron image taken at 100x **(b). Secondary electron image taken at 500x**

Plate 4.20. SEM micrographs of surfaces of sample after immersion in artificial seawater for 12 days (applied current density of 300 mA/m^2 for the initial 6 days then decreased to 50 mA/m^2).

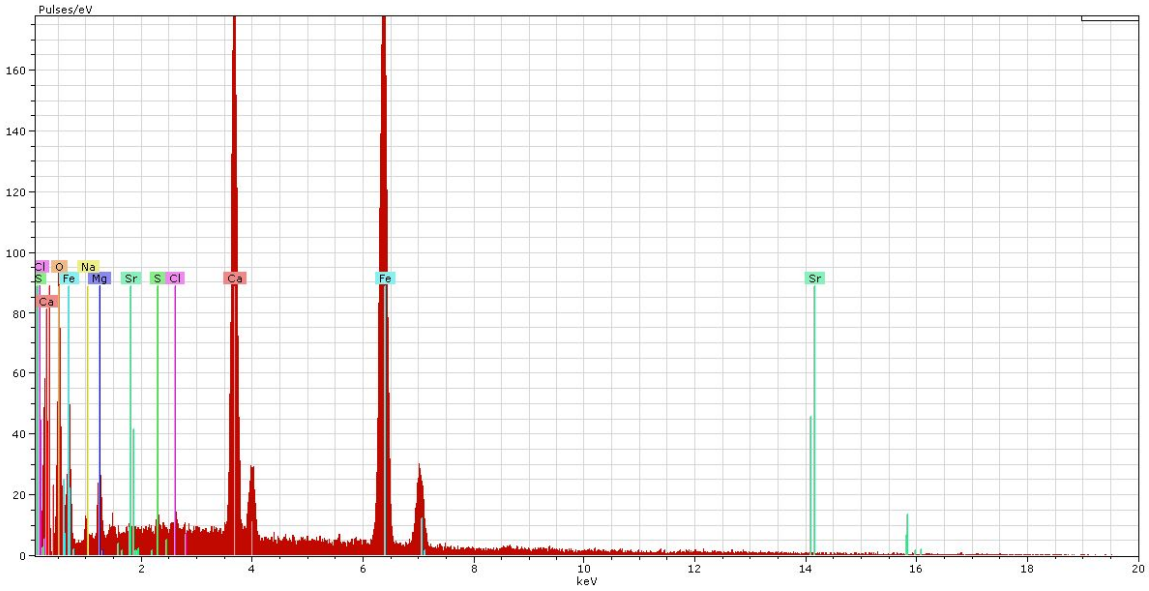

Figure 4.77. EDX spectra of surface of sample after immersion in artificial seawater for 12 days (applied current density of 300 mA/m^2 for the initial 6 days then decreased to 50 mA/m^2).

Table 4.29. The relative percentages of various elements determined using EDX quantification, of calcareous film on steel samples after immersion in artificial seawater for 12 days (applied current density of 300 mA/m^2 for the initial 6 days then decreased to 50 mA/m^2 (magnification = 100x).

Percentage of element	Calcium	Magnesium	Sulfur	Iron	Strontium	Oxygen	Chlorine	Sodium
Area 1	18.79	4.67	0.49	37.96	0.54	33.56	0.75	3.22
Area 2	18.83	3.77	0.1	40.22	0.16	34.37	0.28	2.26
Area 3	13.45	6.52	0.39	48.04	0.2	27.64	0.47	3.28
Average	17.02	4.99						

The aragonite ($CaCO_3$) clusters that form at the higher applied current density of 300 mA/m^2 (Plates 4.19(a), (b)) appear to be larger than those that form under the lower current density of 200 mA/m^2 (compare with Plates 4.17(a), (b)) . The average content of magnesium (Table 4.27) determined in the deposit obtained with the applied constant current density of 200 mA/m^2 was slightly lower than that obtained under the conditions where an applied current density of 200 mA/m^2 was applied for an initial 3 days, then subsequently decreased to 100 mA/m^2 (Table 4.26). However, the situation regarding the calcium contents of these two deposits was found to be the opposite. The average content of calcium (Table 4.27) that formed in the deposit obtained using a constant applied current density of 200 mA/m^2 was slightly higher than that measured in the deposit obtained under conditions where an applied current density of 200 mA/m^2 was used for an initial 3 days then subsequently decreased to 100 mA/m^2 for the remainder of the immersion period (Table 4.26).

Also, the average content of calcium was found to be greater at the higher applied current density of 300 mA/m^2 (see Table 4.28 and Table 4.29), compared to when a lower applied current density of 200 mA/m^2 was employed (see Tables 4.26 and 4.27). However, in the case of magnesium, the reverse situation was found to occur, with magnesium content being greater in the deposits formed at the lower current density of 200 mA/m^2.

Also, the magnesium content determined in the sample at an applied current density of 300 mA/m^2 for an initial 6 days then decreased to 50 mA/m^2 (Table 4.29), is lower than the magnesium content of the sample at an applied current density of 300 mA/m^2 for the initial 3 days then decreased to 100 mA/m^2 (see data in Table 4.28). However, in case of the calcium content, the reverse situation was found to occur, with the calcium content determined in the sample at an applied current density of 300 mA/m^2 for an initial 6 days then decreased to 50 mA/m^2, being higher than the calcium content of the sample at an applied current density of 300 mA/m^2 for the initial 3 days then decreased to 100 mA/m^2.

4.4.3. X-Ray Diffraction (XRD) results.

Figure 4.78 and Table 4.30 show the results of the XRD analysis for the sample at an initial current density of 200 mA/m^2 for the first 3 days, and then reduced to 100 mA/m^2 for the remainder of the 12 day immersion period. The main compounds present are predominantly calcium carbonate as aragonite, and magnesium hydroxide as brucite. A similar result was obtained for the XRD analysis of the sample at a constant current density of 200 mA/m^2 for the entire 12 day immersion period. (Figure 4.79 and Table 4.31).

When cathodic protection was applied with the initial applied current density of 200mA/m^2, the XRD pattern for the metal substrate from the iron peaks showed another two crystalline phases, these were for aragonite ($CaCO_3$) and brucite ($Mg(OH)_2$). (Figure 4.78 and Figure 4.79).

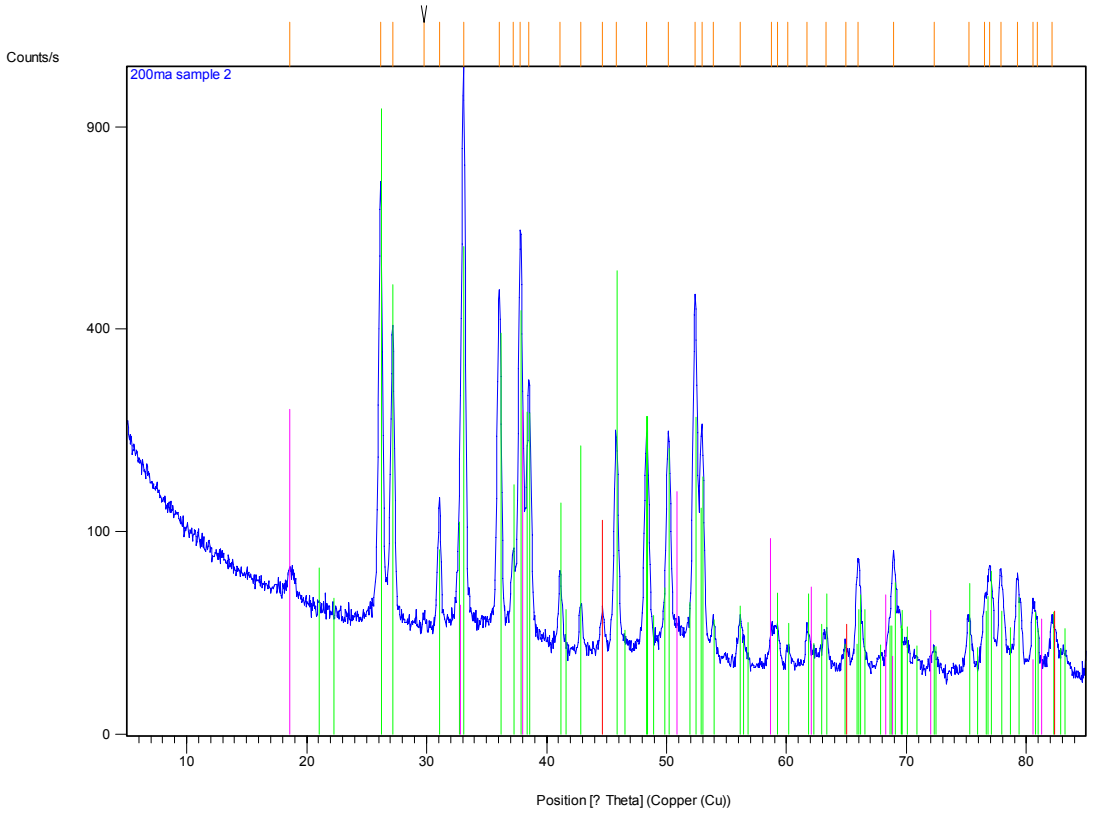

Figure 4.78. XRD pattern for sample surface after immersion in artificial seawater for 12 days (Applied current density of 200mA/m^2 for the initial 3 days then decreased to 100mA/m^2).

Table 4.30. The Compound Name and Chemical Formula using XRD quantification, of calcareous films on steel samples after immersion in artificial seawater for 12 days (Applied current densities of 200 mA/m^2 for the initial 3 days then decreased to 100 mA/m^2).

Visible	Ref. Code	Score	Compound Name	Scale Factor	Chemical Formula
*	00-041-1475	89	Aragonite	0.721	$CaCO_3$
*	00-007-0239	44	Brucite, syn	0.168	$Mg(OH)_2$
*	00-006-0696	23	ferrite, ledkunite, bainite	0.012	Fe

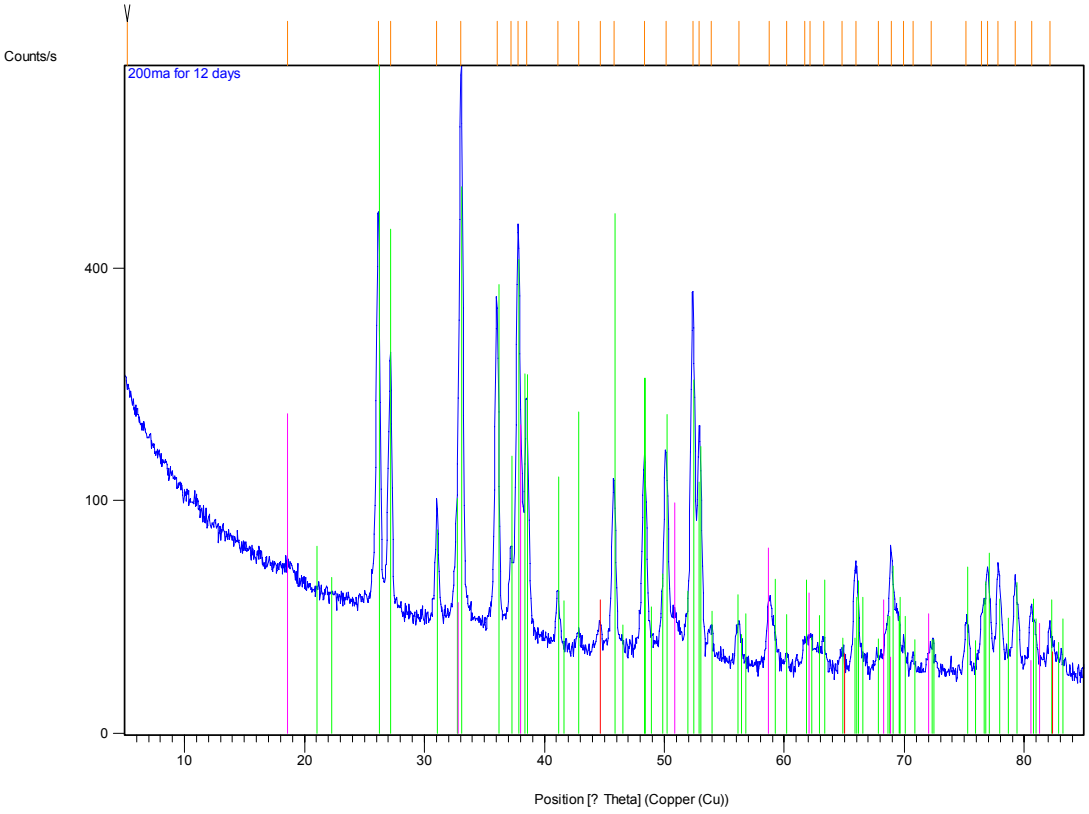

Figure 4.79. XRD pattern obtained for deposit on mild steel sample surface after immersion in artificial seawater for 12 days (Applied constant current density 200 mA/m^2).

Table 4.31. The Compound Name and Chemical Formula using XRD quantification, of calcareous film on steel samples after immersion in artificial seawater for 12 days (Applied constant current density of 200 mA/m^2).

Visible	Ref. Code	Score	Compound Name	Scale Factor	Chemical Formula
*	00-041-1475	93	Aragonite	0.812	$CaCO_3$
*	00-007-0239	46	Brucite, syn	0.125	$Mg(OH)_2$
*	00-006-0696	46	ferrite, ledkunite, bainite	0.023	Fe

To summarise, from the data given in the Tables 4.30 and 4.31, it is evident that the compounds present are the same, namely aragonite and brucite; the amount of Ca is slightly higher at constant current density than the varied one, but for Mg, it is the opposite, slightly higher at the varied current density, and lower at the constant current density.

4.4.4. Discussion.

The rationale for these series of experiments has already been provided in Section 4.1.2 early in this Chapter. Briefly, field experience has shown that in real offshore situations a higher initial current density is capable of growing a more effective protective calcareous film and this may be followed by a significant reduction in subsequent current density [14]. We decided to carry out this preliminary investigation to explore the possibilities of this interesting concept. The first problem was to select the initial current densities and initial polarisation times. We chose 200 and 300 mA/m^2 from our previous data and from practical experience.

From the data given in Figure 4.68, the 200 mA/m^2 system shows a steady fall in potential over the 12 day period but even at 12 days the system has not yet reached steady state. Figure 4.71 is the corresponding 300 mA/m^2 data. A much faster decline in potential is observed but an obvious "event" has occurred at 6 days causing ennoblement of potential followed by recovery. We have suggested earlier in this Thesis that this event is probably due to hydrogen generation from the steel surface damaging the growing calcareous film. So our choice of initial potential and time needs to try and avoid this risk of hydrogen damage. The final current densities of 50 and 100 mA/m^2 were also chosen based on our previous work described in this Chapter and also from field experience [14]. The 50 mA/m^2 potential time decay shown in Figure 4.10 shows after 1 week of immersion a potential of around -770 mV (SCE), and the sample clearly showed corrosion. For the 100 mA/m^2 situation, a similar behaviour was observed with a final 7 day potential of around -830 mV(SCE) and still some corrosion, albeit somewhat less. In the limited time available, we chose to test the higher final current density at the 3 day pre-exposure conditions and the lower current density at the 6 day pre-exposure.

Restricted instrument access limited our use of SEM/EDX and X-ray Diffraction analysis to less specimens than would have been desirable. Our criteria of success were two fold, the final potential at 12 days and the visual appearance of the specimen.

The results may be summarized as following:
(1) Apart from the single case of the sample at a current density of 200 mA/m^2 for 6 days then decreased to 50 mA/m^2 for a further 6 days, which ended up at -776 mV SCE and obviously corroded, the other three samples subjected to variable current densities were successful both in terms of final potential and visual appearance.

(2) X-ray Diffraction analysis on the 200 mA/m^2 for 12 days sample and the 200 mA/m^2 for 3 days then decreased to 100 mA/m^2 samples, showed as expected both aragonite and brucite.

(3) The SEM studies showed how the aragonite crystals were assembled and arranged on the surface and their distribution, size and coverage. The EDX analysis gave one interesting and curious observation, the 300 mA/m^2 for 6 days then decreased to 50 mA/m^2 sample, showed high and significant levels of iron in the film. It is thought that this is due to incomplete coverage of the steel surface by the aragonite film allowing sampling of the substrate.

We have only carried out a preliminary investigation of this interesting and important field. Further work is clearly necessary to clarify the issues raised in our work.

4.5. Conclusions.

- Weight loss measurements of cold-rolled mild steel have been made in artificial sea water over a 30 day period. Values obtained for corrosion rates at open circuit of 0.09 mm/y compare favourably with the accepted value of 0.13 mm/y.

- Corrosion product analysis of the steel after 3 days and 7 days immersion periods at open circuit by EDX gives clear indication of the presence of magnesium as well as iron. No calcium was observed, and no calcium and magnesium were detected by X-Ray Diffraction.

- The distribution of magnesium in the calcareous deposits formed at open circuit by EDX was non uniform, although the iron distribution was uniform.

- Constant current cathodic polarisation has been carried out at varying values of current density from 0 to 400 mA/m^2 together with 30 day weight loss measurements.

- At a potential of -783 mV (SCE), [9 mV more negative than the accepted protection potential of -774 mV (SCE)] the steel is not fully protected and is still corroding at 25% of its open circuit value.

- To fully protect the steel a further 112 mV shift in potential to -895 mV (SCE) is necessary.

- Ashworth's [8] conclusion that the relationship between protection level and potential is logarithmic is unfounded. The real relationship has been shown to be approximately linear.

- Digital scanned images of the steel surfaces after immersion for one week at various levels of applied current density gave clear indication of the progress and effectiveness of cathodic protection. On a purely macroscopic visual level, there is no indication of any non uniformity across the steel surface.

- SEM/EDX in plan indicates the uneven distribution of magnesium, iron and calcium across the steel surface as a function of time and current density. The first precipitating specie at open circuit and at low applied current densities is shown to be magnesium and not calcium as was previously assumed.

- Potentiometric titration experiments were performed to study this magnesium precipitation and showed that mixed oxide precipitation between the magnesium from the solution and the ferrous iron from the steel dissolution process was highly possible during the underprotection process.

- GDOES analysis also confirms this clear presence of magnesium at a lower current density (50 mA/m^2) even at 6 hours immersion.

- SEM examination and EDX analysis of cross-sections of deposits, combined with EDX mapping of the distribution of selected single elements has been successfully accomplished and to our knowledge, this is the first time such images have been produced.

- Clear evidence has been obtained of the distribution of calcium, magnesium and iron across the underprotected surface. Two distinct areas exist; firstly calcium precipitation directly onto the steel surface and secondly an iron containing inner layer with an over layer of magnesium.

- A hypothesis has been floated based on the above, suggesting that since the magnesium can only precipitate in association with soluble ferrous iron, then these regions must be anodic sites on the surface. It therefore follows that the calcium regions are cathodic.

- Some indication of the dimensions of the anodic and cathodic areas can therefore be made; cathodic regions being 50 μm in diameter and 100 μm apart. The remaining surface is anodic.

- At higher current densities closer to protection, significant dissolution of ferrous ions are suppressed, magnesium precipitation is severely limited and a simple three layer uniform system is found, the inner layer being iron containing, the middle layer contains the magnesium and the outer layer the calcium.

- At current densities well beyond protection, evidence of film cracking is seen in the SEM/EDX cross-section images and complete film detachment can be observed from the optical photographs and the SEM photomicrographs.

- Hydrogen evolution is thought to be responsible for this film detachment.

- Initial investigations have shown the possibility of reducing the current density for cathodic protection by laying down the calcareous film at an initial high current density for a limited time and subsequently applying a much reduced current density, below that which would normally be required to achieve full protection.

- Based on the results of the SEM imaging and EDX results, impedance analysis was carried out using not a generalised equivalent circuit but an appropriately chosen equivalent circuit. The basic concept of our equivalent circuit is a limited layer Warburg diffusion model in combination with a porous layer with defects.

- The high frequency regions are thought to represent the porous calcareous film with the low frequencies being ascribed to the charge transfer resistance at the film metal interface.

- The effect of increasing the current density is clearly seen in the anodic charge transfer process of iron dissolution with the charge transfer resistance becoming infinitely large at higher current density. (Applied current densities at 300 mA/m^2 and 400 mA/m^2 cases).

- Explanations for the behaviour of this low frequency region as a function of time and current density have been proposed in terms of the specific electrochemical

reactions taking place and the nature and integrity of the calcareous films produced.

- The Warburg diffusion model is applied to the cathodic process, mainly the oxygen reduction reaction. The cathodic Warburg diffusion W_C, which consisted of three parameters, $W_{C\text{-}R}$, $W_{C\text{-}T}$, and $W_{C\text{-}P}$, was used to evaluate the cathodic reaction level.

- We have assumed literature values of the oxygen diffusion coefficients from which we have calculated oxygen diffusion path distances.

- The values of the oxygen diffusion path distances correspond well with the SEM values obtained for the calcareous film thicknesses.

4.6. References.

1. H. Davy. "On the corrosion of copper sheeting by sea water; and on methods of preventing this effect; and on their application to ships of war and other ships". Phil. Trans. Royal Soc., **114**, p151. 1824.

2. H. Davy. "Additional experiments and observations on the application of electrical combinations to the preservation of the copper sheathing of ships", Phil. Trans. Royal Soc. **114**, p242. 1824.

3. H. Davy. "Further researches on the preservation of metals by electrochemical means", Phil. Trans. Royal Soc. **115**, p328. 1825.

4. T. P. Hoar. "A graphical representation of the main parameters associated with cathodic protection" J. Electrodep. Tech. Soc., **14.** p33. 1938.

5. R. B. Mears and R. H. Brown, "Cathodic protection and the use of polarization diagrams", Trans. Electrochem., Soc. **74**. p519. 1938.

6. U. R. Evans. "The Corrosion and Oxidation of Metals". Edward Arnold & Co., London. p275. 1960.

7. H. H. Uhlig. "Corrosion and Corrosion Control". 2nd Ed., John Wiley & Sons Inc., New York. p97. 1971.

8. V. Ashworth. In: "Cathodic protection, Theory and Practice". (eds), V. Ashworth and C. J. L Booker. Ellis Horwood. Chichester. 1986.

9. R. J. Kuhn. Proc API, **14**. p157. Nov 1933.

10. R. A. Gummow. Cathodic Protection criteria, a review of NACE standard RP-01-69. Mat. Performance. p9-16. 1986.

11. D. A. Jones. Corrosion, 2nd Edition. Prentice-Hall. London. 1996.

12. D. Fairhurst. "Cathodic Protection; What have we learnt?" J. Corrosion Science and Engineering. **4,** (6). www.JCSE.org.

13. W. H. Hartt, C. H. Culberson and S. W. Smith. "Calcareous deposit on metal surfaces in seawater-a critical review". Corrosion, **40.** p11. November 1984.

14. J. D. Scantlebury, T. Tsukada, Y. F. Yang and M. Du. "Long–Term Cathodic Protection Performance Data of Two Off-Shore Structures". NACE Corrosion Conference. Atlanta. USA, March 2009.

15. R. A. Humble. "Cathodic Protection of Steel in Sea Water with Magnesium Anodes". Corrosion. 74. pp358-370, 1948.

16. J. C. Hudson. The Corrosion of Iron and Steel. Chapman and Hall. London. 1940.

17. Yu.lurie.″Handbook of analyzed chemistry″ .Chimia. 1979.

18. A. Packter and A. Derby. "Co-precipitation of magnesium iron III, hydroxide powders from aqueous solutions". Cryst. Res. Technol., **21**. pp1391-1400. 1986.

19. C. Deslouis, D. Festy and O. Gil. "Characterization of calcareous deposits in artificial seawater by impedance techniques-I. Deposit of $CaCO_3$ in the absence of $Mg(OH)_2$" . Electrochimica Acta. **43**, (12-13). pp1891-1901. 1998.

20. Ch. Barchiche, C. Deslouis, D. Festy, O. Gil , Ph. Refait , S. Touzain and B. Tribollet. "Characterization of calcareous deposits in artificial seawater by impedance techniques - II. Deposit of $CaCO_3$ in the presence of Mg(II)". Electrochimica Acta. **48**, pp1645- 1654. 2003.

21. S. C. Chung, J. R. Cheng, S. D. Chiou and H. C. Shih. "EIS behavior of anodized zinc in chloride environments". Corrosion Science. **42**. pp1249-1268. 2000.

22. A. Bonnel , F. Dabosi, C. Deslouis, M. Duprat, M. Keddam and B. Tribollet. ″Corrosion study of a carbon steel in neurtal chloride solutions by impedance Techniques″. J.Electrochem. Soc.: Electrochemical science and technology. April, 1983.

23. D. Dobos. ″Electrochemical Data". Akademia Kiado, Budapest. 1980.

Chapter 5. Studies Using a Calcium/Magnesium Containing Anti-Corrosion Pigment.

5.1. Introduction.

In the work described in the previous Chapter, the calcium and magnesium containing deposits that formed on the surfaces of the steel samples originated from ions present in the artificial seawater solution. However, in the work reported in this Chapter, an anti-corrosion pigment containing calcium and magnesium was deliberately added into the immersion solutions. The other major difference between the two deposits discussed in this and Chapter 6, is that in the studies reported in Chapter 4, the calcium and magnesium containing deposits were precipitated onto the surfaces of the mild steel samples under conditions of cathodic protection during immersion in artificial seawater; whereas in the studies described in the following Sections, the precipitates were formed under open circuit conditions. Each individual immersion experiment was carried out at least twice. The results obtained from duplicated experiments were extremely close and the data presented was not averaged but is merely given as one set.

5.2. Corrosion Studies.

Recently, a novel anti-corrosion pigment (D5-B) containing calcium and magnesium has become available, produced by a Japanese paint company (Dai Nippon Toryo Co., Ltd). The relevant literature associated with this part of the work is given in Section 2.11 of Chapter 2. To evaluate the mechanism of action and effectiveness of the new pigment D5-B, comparative experiments between D5-B and four other different pigments were performed using four different solutions. The methodology will be discussed in Section 5.2.1.

Subsequently, several analytical techniques and instruments were utilized to measure and assess the results of these comparative studies, including: potential measurements, optical photography (digital scanner), electrochemical tests (Linear Polarization Resistance (LPR), Electrochemical Impedance Spectroscopy (EIS), Potentiodynamic polarisation, Scanning Electron Microscopy (SEM) in conjunction with Energy Dispersive X-Ray Analysis (EDX), and Glow-Discharge Optical Emission Spectroscopy (GDOES).

5.2.1. Immersion tests.

A small hole was drilled in the top of each mild steel sample and an electrical connection was made using a self tapping screw. They were partly immersed in the appropriate test solutions at a depth of 2.0 cm, with the hole and screw connection remaining above the water line.

Four pigments were examined, these were Ca 650 (aluminium tripolyphosphate, calcium neutralized), KW105 (aluminium tripolyphosphate, zinc neutralized), zinc phosphate, and the new pigment D5-B (calcium polyphosphate, magnesium neutralised). Blank solutions (without a pigment) were also examined as a control comparison in each group being tested. Potential measurements and optical photography were also carried out. In addition, visual assessment and examination of the samples was carried out on a daily basis. Later, due to time constraints, we concentrated solely on experiments utilising the novel pigment.

Four test solutions were selected; these were deionised water as used by Mayne [1], 3.5% NaCl to mimic marine conditions, 0.025M sodium chlorate (following the recommendation of the Japanese Company) and a simulated acid rain solution to mimic industrial conditions as described in Section 3.2.2 of Chapter 3. Experiments were carried out with the pigment dispersed in a half litre of solution at a 1:100 weight ratio. The experiments were performed at a laboratory temperature of between 20^{o}C and 25^{o}C.

5.2.1.1. Potential Measurements.

Because deionised water has a low conductivity it was only used for immersion experiments. Potential/time measurements were carried out in the other three test solutions and were recorded daily over a 7 day period. A similar reference electrode system was used to that described previously in Chapter 3 and Chapter 4.

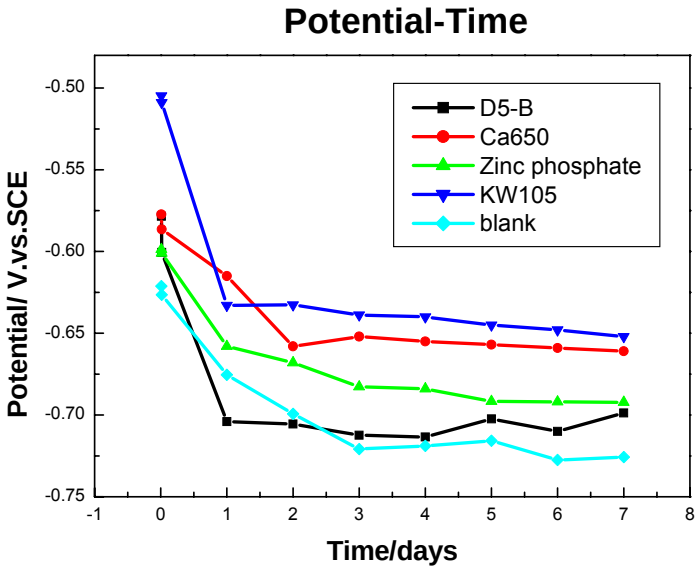

Figure 5.1. Graph showing plots of daily potential/time measurements for the 4 pigment inhibitors, and control; obtained over a 7-day test period in 3.5% NaCl solution.

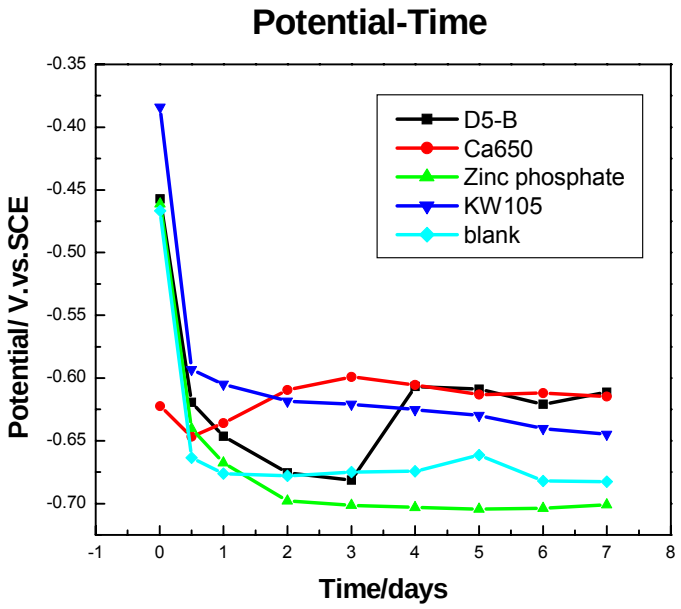

Figure 5.2. Graph showing plots of daily potential/time measurements for the 4 pigment inhibitors, and control; obtained over a 7-day test period in 0.025M $NaClO_4$ solution.

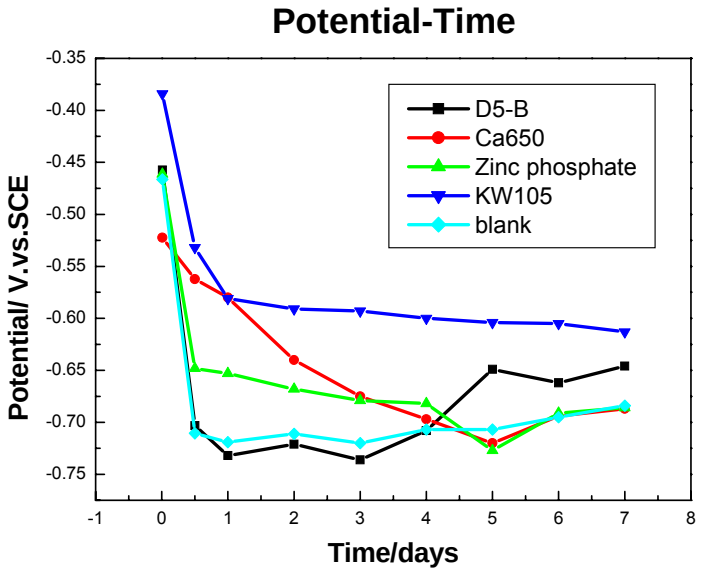

Figure 5.3. Graph showing plots of daily potential/time measurements for the 4 pigment inhibitors, and control; obtained over a 7-day test period in acid rain solution.

Figures 5.1 to 5.3 are the graphs plotted for the potential/time measurements recorded daily for the three test solutions (3.5% NaCl, 0.025M $NaClO_4$ and simulated acid rain) over a period of 7 days.

In the case of samples immersed in 3.5% NaCl (Figure 5.1), the potentials of samples inhibited with D5-B were more negative than those of the samples inhibited using the other three inhibitor pigments (Ca 650, KW105 and zinc phosphate). Also, in comparison with the blank sample, the potentials of samples inhibited with D5-B were slightly more negative than that of the blank sample for the first two days of immersion, and then became more positive.

Figure 5.2 shows that for an initial period of 2 days, the potentials of samples inhibited with D5-B were slightly more negative compared with potentials obtained for samples inhibited with both Ca 650 and KW105, in the $NaClO_4$ solution. However, after the first two days of immersion, the potentials also then became positive. In addition, the potentials for samples inhibited with zinc phosphate were more negative than those for the other samples evaluated using the other inhibitor pigments.

In the case of samples immersed in acid rain (Figure 5.3), for the first four days of immersion, the potentials obtained for samples inhibited with D5-B were more negative than those obtained for the samples inhibited using the other three inhibitor pigments and the blank sample. After this period, it became noble for the rest of the immersion time.

Overall, the above observations suggest that the mechanism of inhibition of the new pigment D5-B is not purely cathodic; but is likely to be mixed. However, to investigate this further will require additional experimental work and analysis which will be described later in this Chapter.

5.2.1.2. Exposure behaviour.

All samples were scanned using a flat bed scanner at the end of the 7 day immersion period. They were positioned vertically and in this Chapter the specimen top corresponds to the top of the photograph. These photographic images are presented in Plates 5.1 to 5.4.

(1)Deionized water.

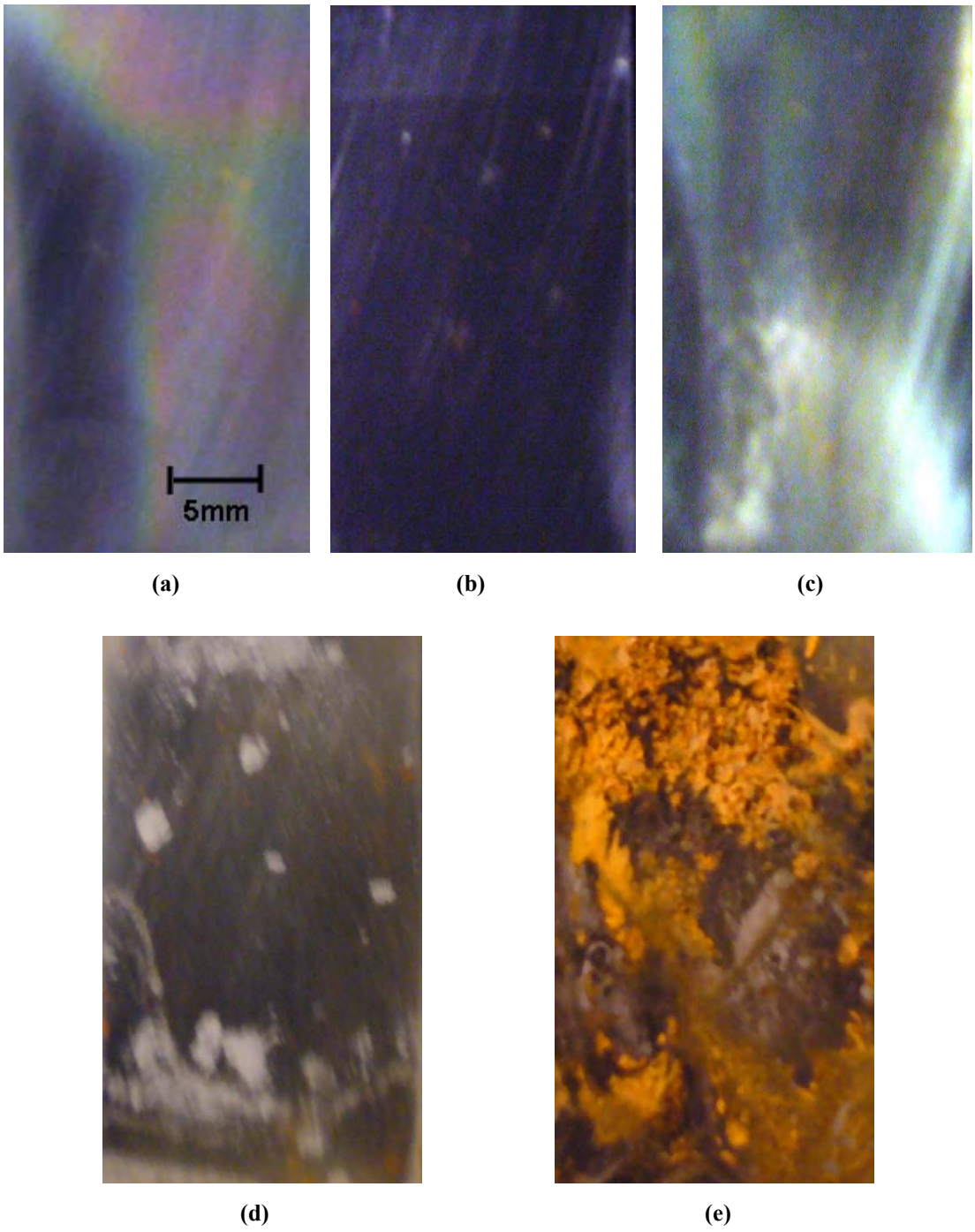

Plate 5.1. Photographs of surfaces of mild steel samples after immersion for 7 days in deionised water, in the presence of four different inhibitor pigments, and a control blank: (a) D5-B (b) Ca 650 (c) KW105 (d) Zinc phosphate (e) Blank.

(2) 3.5% NaCl.

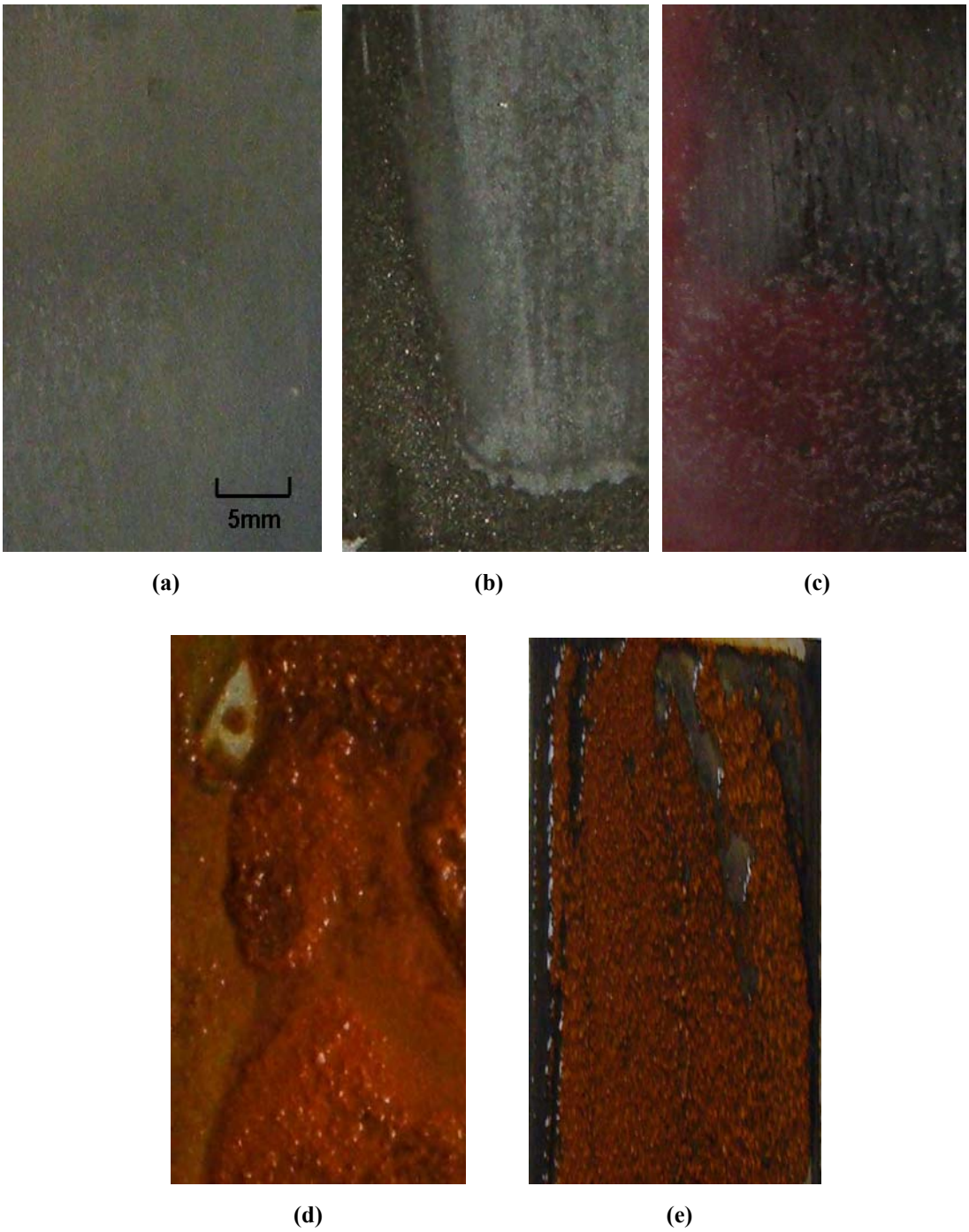

Plate 5.2. Photographs of surfaces of mild steel samples after immersion for 7 days in 3.5% NaCl solutions, in the presence of four different inhibitor pigments, and a control blank: (a) D5-B, (b) Ca 650 (c) KW105 (d) Zinc phosphate (e) Blank.

(3) Acid rain solution.

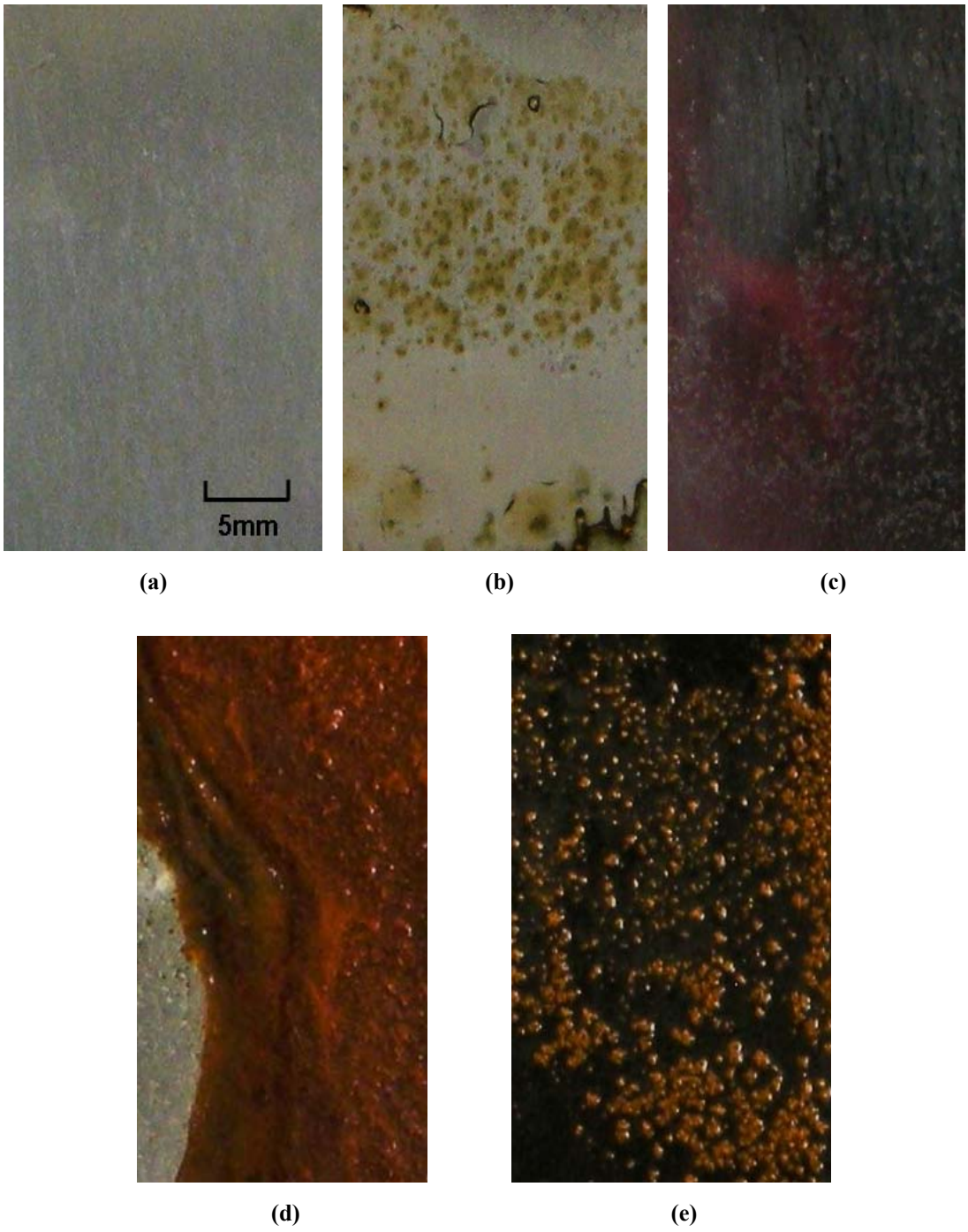

Plate 5.3. Photographs of surfaces of mild steel samples after immersion for 7 days in acid rain solution, in the presence of four different inhibitor pigments, and a control blank: (a) D5-B, (b) Ca 650 (c) KW105 (d) Zinc phosphate (e) Blank.

(4) 0.025% $NaClO_4$.

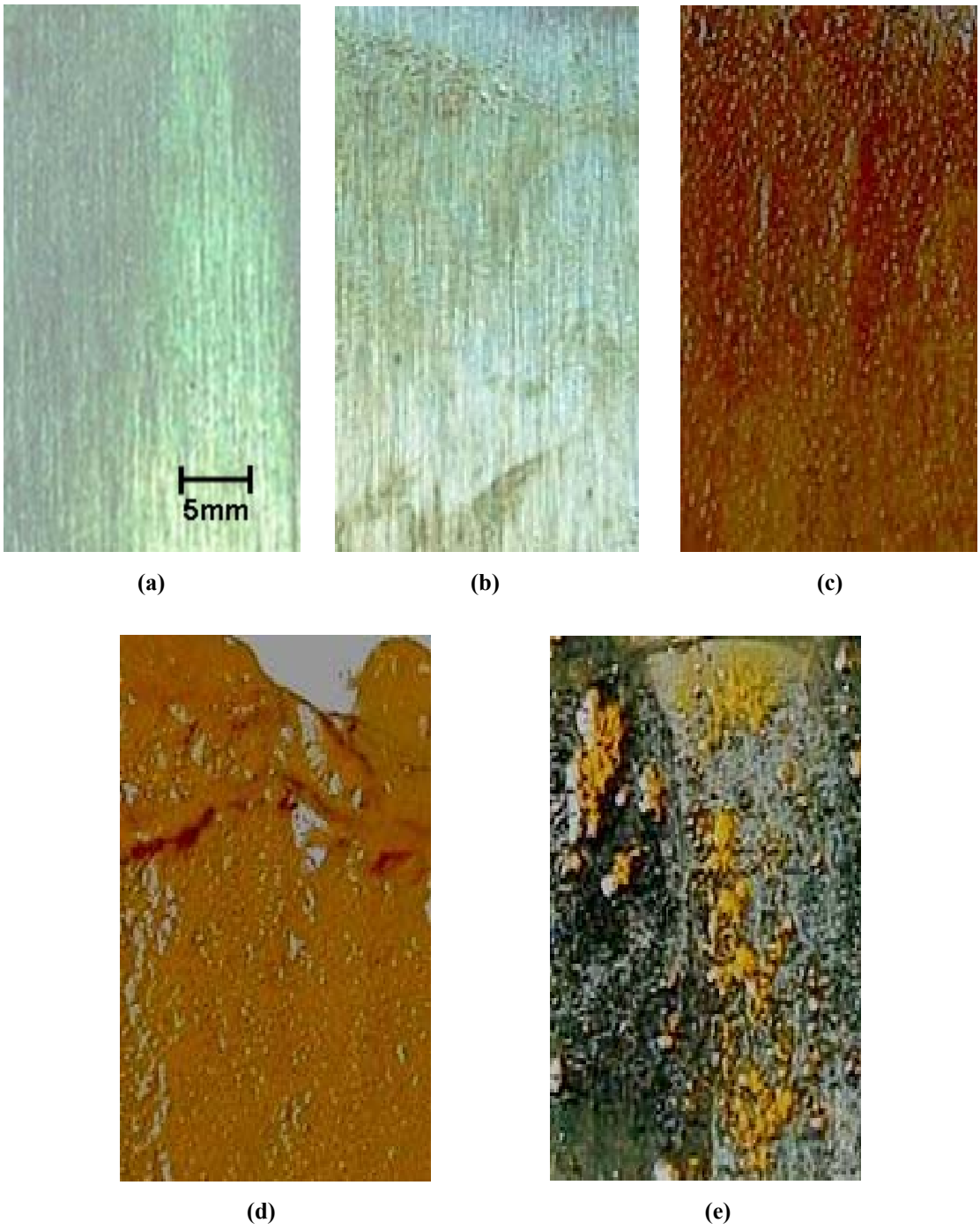

Plate 5.4. Photographs of surfaces of mild steel samples after immersion for 7 days in 0.025% $NaClO_4$ solution, in the presence of four different inhibitor pigments, and a control blank: (a) D5-B (b) Ca 650 (c) KW105 (d) Zinc phosphate (e) Blank.

From the visual observations made of the corroded mild steel samples and illustrated in the photographs in Plates 5.1 to 5.4, we suggest:

From Plate 5.1 (7 days in deionised water), corrosion only occurred on the blank and the sample with zinc phosphate inhibitor. All the other remaining samples showed no visible evidence of significant corrosion.

From Plate 5.2, 3.5% NaCl solution is clearly very corrosive. After 7 days immersion, corrosion was observed with all samples, although the sample protected using the new D5-B pigment was only slightly corroded, whereas the sample protected using zinc phosphate and also the blank sample were both very severely corroded.

Plate 5.3 shows the extent of corrosion occurring after immersion of samples for 7 days in the simulated acid rain solution. It was observed that samples protected using the inhibitors Ca 650, KW105 and zinc phosphate all commenced corrosion after 2 days immersion. The samples protected using Ca650 showed only slight corrosion. In the case of samples protected using the new D5-B pigment, almost no corrosion was observed after 7 days immersion.

From Plate 5.4, it was evident the samples immersed in 0.025% $NaClO_4$ solution with D5-B and Ca 650 showed almost no evidence of corrosion after the 7 day test period. However the sample immersed in 0.025% $NaClO_4$ with zinc phosphate corroded almost immediately, whilst the sample tested in the presence of KW105 inhibitor started to corrode after three days.

In summary; from the photographs obtained (presented in Plates 5.1 to 5.4), and daily visual examination of the mild steel samples, it was possible to conclude that the new pigment D5-B clearly gave the best overall performance as a corrosion inhibitor, and also the other pigments Ca650, KW105 and Zinc phosphate had fairly acceptable performance.

5.2.2. Introduction and justification for the galvanic zinc experiments.

A further series of experiments were carried out in aqueous solutions to mimic the hypothetical situation where the novel pigment was incorporated into a primer together with zinc metal particles, see Figure 5.4. The coating therefore would be an interesting combination of a conventional anti-corrosion primer and a conventional zinc metal containing primer. The rationale behind this suggestion was that:

- Maybe the pigment would work more effectively if the steel surface were made a cathode with enhanced deposition of cathodic inhibitor.
- And/or the inhibitive reaction on the steel surface due to the novel pigment would be enhanced by the presence of zinc ions in solution.

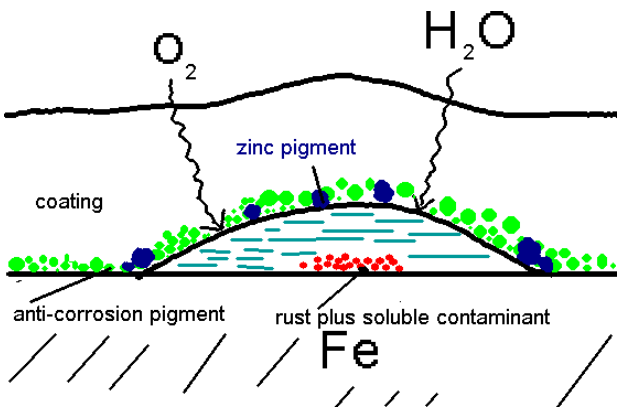

Figure 5.4. The combination of zinc metallic primers and conventional anti-corrosion pigments.

The successful use of the addition of zinc ions together with conventional corrosion inhibitors is very common in the field of corrosion inhibition and also the field of anti-corrosion pigments. Polyphosphates are used in combination with calcium or zinc ions in solution on iron, steel and zinc substrates [2]. The role that zinc and calcium ions play in corrosion inhibition has been investigated by means of impedance studies, cyclic voltammetry and SEM/EDX techniques [3]. In the field of anti-corrosion pigments the classic example from Mayne's work is the use of zinc with chromate as a pigment [4].

The actual experiment that was undertaken as part of the present Study was to utilise the same set of corrosive aqueous environments as investigated previously (3.5% NaCl, 0.025M sodium chlorate and simulated acid rain solution) and in conjunction with the use of D5-B pigment, but then instead of simply immersing the mild steel sample in each of the solutions, the mild steel samples were coupled to pure zinc sheet. This experimental

set-up is illustrated in Figure 5.5. The resulting surface film was then compared with the "normal" film deposited in the presence of D5-B alone, using electrochemical and non electrochemical methods.

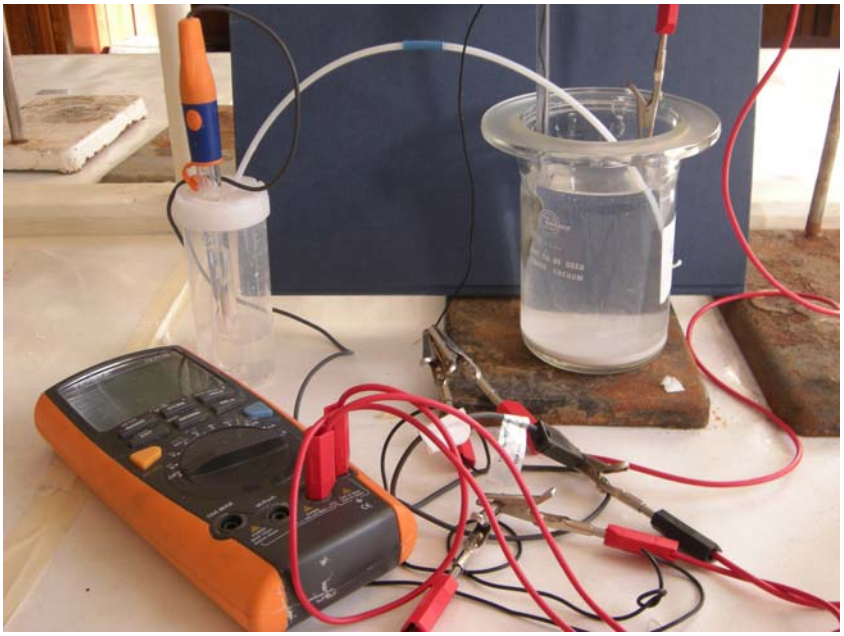

Figure 5.5. Experimental set-up.

5.3. Electrochemical tests.

5.3.1 Linear polarization resistance (LPR).

We have already described this method in Section 2.4.1.3. We used a sweep from -10 mV to +10 mV at 0.2 mV/sec around the rest potential.

To avoid drift during R_p measurements for the samples connected to the zinc, the steel was disconnected from the zinc and the potential allowed to stabilize (usually around five minutes) before making the R_p measurement at this stable potential.

5.3.1.1. 3.5% NaCl solution.

Three mild steel samples were immersed separately in 3.5% NaCl solution, the first sample was immersed without any inhibitor being present, the second sample was immersed with D5-B inhibitor, and third sample was immersed in the presence of D5-B pigment, and also connected to a zinc metal anode for the duration of the 7 day test period.

Measurements of potential (Figure 5-6(a)) and linear polarization resistance (Table 5-1) were carried out at daily intervals. As we have seen in Section 2.4.1.3, the corrosion current is proportional to $1/R_p$. We therefore plotted the reciprocal $1/R_p$ against time, (Figures 5-6(b), (c) and (d)). The photographs of samples taken after 7 days immersion are shown in Plate 5.5.

Values of polarization resistance R_p are given in Table 5.1, the value of R_p obtained for samples in 3.5% NaCl solution with D5-B as inhibitor (Figure 5.6(c)) is about 1.5 - 2.5 times greater than the R_p obtained for samples in 3.5% NaCl solution (Figure 5.6(b)) with no inhibitor. Also, values of R_p obtained for samples both in the presence of D5-B only and also D5-B connected with zinc were from 3.5 to 20 times greater than the R_p values obtained for samples in 3.5% NaCl solution with no inhibitor present. It was noted, that values of R_p obtained for samples tested with the addition of both D5-B and zinc were also significantly larger (Figure 5.6(d)) (around 2.5 to 10 times greater) than the R_p readings obtained for samples immersed solely in the presence of D5-B inhibitor (Figure 5.6(c)) alone.

Table 5.1. The comparison of values of polarization resistance R_p obtained for samples both with and without the addition of D5-B inhibitor, or connected with a Zn anode after immersion in 3.5% NaCl solution for 7 days.

Unit: Ohm.cm²

Time	3.5% NaCl	3.5% NaCl with D5-B	3.5% NaCl with D5-B and Zn Anode
Day 1	2200	3000	7400
Day 2	2600	3500	17000
Day 3	2400	3800	31000
Day 4	2000	4700	34900
Day 5	2000	5000	40700
Day 6	2200	4800	49100
Day 7	2200	5100	49500

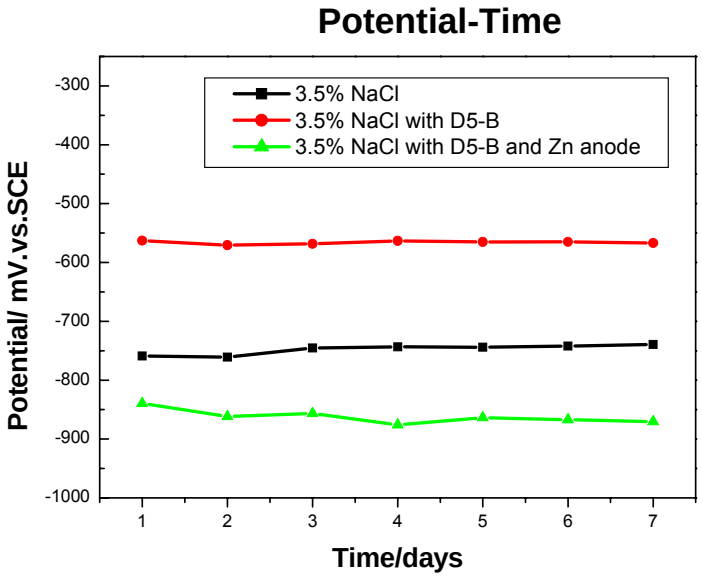

Figure 5.6(a). Graph showing plots of daily potential/time measurements for samples both with and without the addition of D5-B inhibitor, or connected with a Zn anode; obtained over a 7-day test period in 3.5% NaCl solution.

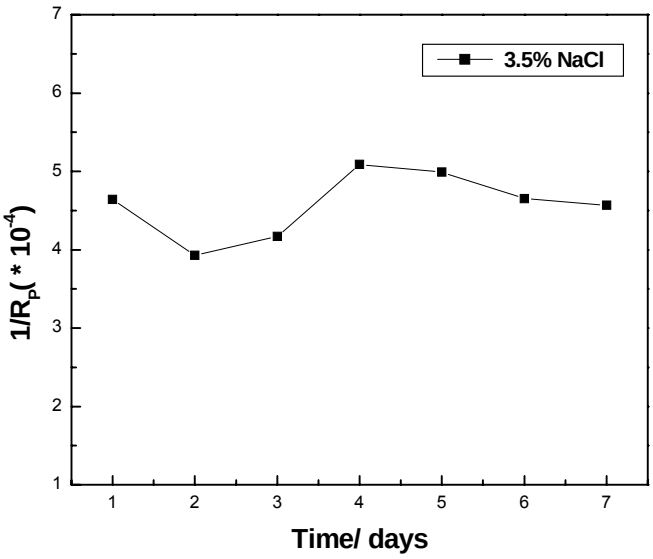

Figure 5.6(b). Graph showing plots of daily $1/R_p$-time measurements: obtained over a 7-day test period in 3.5% NaCl solution with no inhibitor.

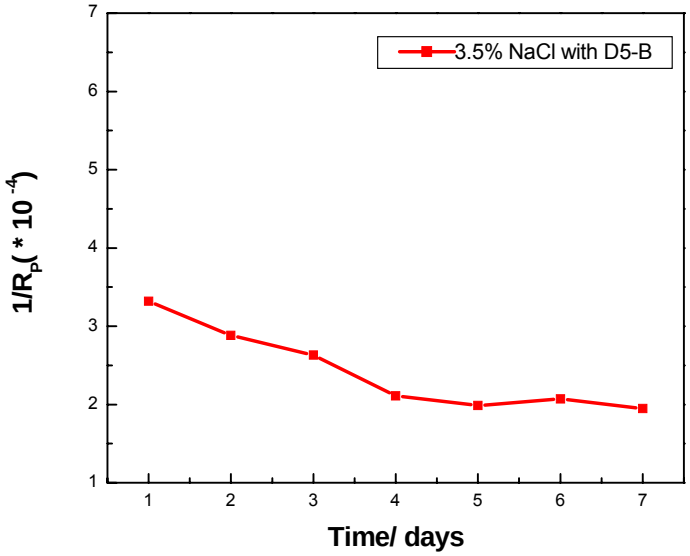

Figure 5.6(c). Graph showing plots of daily $1/R_p$ measurements over a 7-day test period for mild steel samples with D5-B inhibitor in 3.5% NaCl solution.

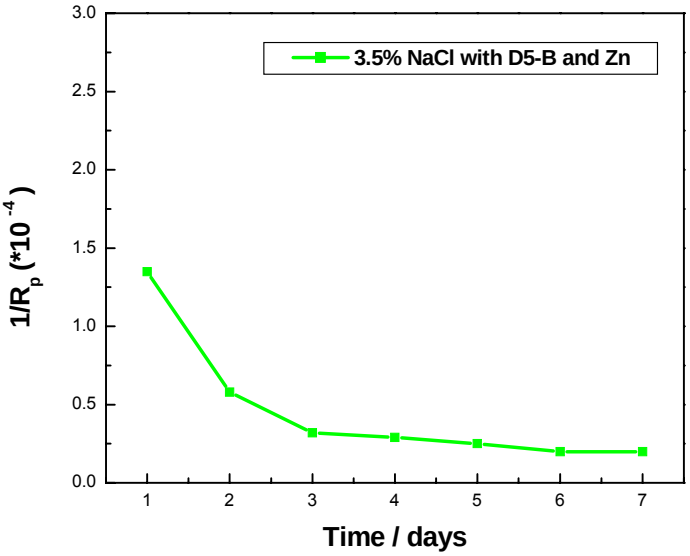

Figure 5.6(d). Graph showing plots of daily $1/R_p$ measurements over a 7-day test period in 3.5% NaCl solution, for mild steel samples with D5-B inhibitor and connected to a Zn anode.

Figure 5.6. Graphs showing plots of daily potential/time and $1/R_p$ measurements over a 7-day test period for mild steel samples in 3.5% NaCl solution, both with and without the addition of D5-B inhibitor, or connected with a Zn anode.

From Figure 5.6(a), which gives the values of potential for samples immersed in 3.5% NaCl solution both with and without the addition of D5-B inhibitor, or connected with a Zn metal anode, the potential for the sample immersed in the presence of D5-B was around 200 mV more positive in comparison with the one without inhibitor. The potential for the sample immersed in the presence of both D5-B and zinc is more negative than the other two because of the presence of zinc. Since $1/R_p$ is related to the corrosion rate in Figures 5.6(b), (c) and (d), the value of $1/R_p$ appears to be significantly decreased by the presence of D5-B, especially D5-B in combination with a zinc anode. In the case of the sample tested with D5-B and zinc, the value of $1/R_p$ was reduced by nearly 20 times compared with the sample with no inhibitor present. These results indicate that either the Zn cation or negative potential or both may have played a significant role in film deposition and also enhancing the performance of the inhibitor. To clarify this situation it was necessary to do further experiments which will be described in Section 5.3.1.3.

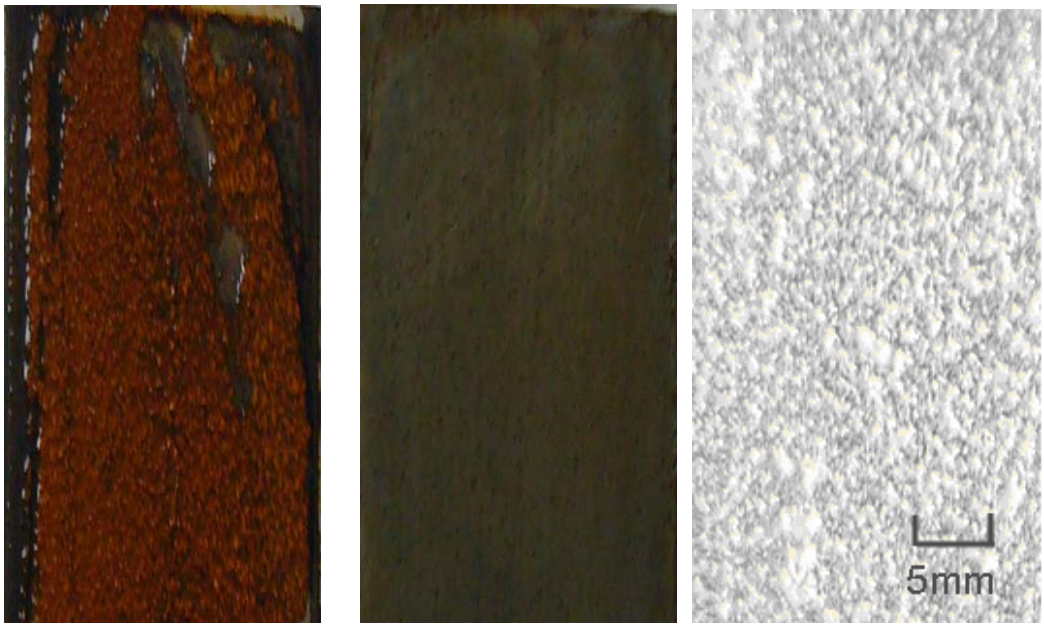

(a) **(b)** **(c)**

Plate 5.5. Photographs of surfaces of mild steel samples after immersion for 7 days in 3.5% NaCl solution, (a) no inhibitor, (b) with D5-B, (c) with D5-B and Zn anode

From the series of photographs of the samples after 7 days immersion illustrated in Plate 5.5, it was evident that severe corrosion occurred on the sample immersed in 3.5% NaCl with no inhibitor present. In the case of the sample immersed in the presence only of D5-B, only slight corrosion was evident. However, the sample immersed in 3.5% NaCl

solution with the addition of D5-B pigment and also coupled to a zinc anode was covered by a white deposit and no corrosion was evident.

5.3.1.2. Acid rain solution.

The composition of the acid rain solution used has been given previously in Section 3.2.2. In order to assess the corrosion behaviour of mild steel, specimens were exposed to simulated acid rain conditions over a period of seven days to determine the performance of the D5-B pigment as an inhibitor under a variety of test regimes. Each experimental procedure was designed to assess the impact that the presence of D5-B inhibitor had on the progression of corrosion under various test conditions on uncorroded and also pre-corroded steel surfaces.

Four situations were examined:
(i) The blank solution.
(ii) Without D5-B for the first three days only (precorroded).
(iii) The solution with D5-B only.
(iv) With D5-B and connected to a zinc metal anode.

For the specimen connected to the zinc, the steel potential reached around -850mV (SCE). Before LPR measurements were made the specimen was disconnected until the potential became stable (usually around five minutes), after which LPR was carried out at this stable potential. This was done daily, and measurements of potential (Figure 5.7(a), and 1/Rp (Figures 5.7(b), (c), (d) and (e)) were also undertaken daily. From Figure 5.7(a), values of potential were obtained for samples immersed in different acid rain solutions. Photographs (digital scans) were also taken of each sample at the end of the immersion period (Plate 5.6).

Table 5.2. The comparison of values of polarization resistance R_p obtained for samples immersed in acid rain solution, both with and without (first 3 days only) the addition of D5-B inhibitor, or connected with a Zn anode.

Unit: Ohm.cm².

Time	Acid rain	Without D5-B for first three days	Acid rain with D5-B	Acid rain with D5-B and Zn Anode
Day 1	4400	3400	13800	50600
Day 2	2900	3600	34800	58700
Day 3	3100	3800	31100	58900
Day 4	3300	3700	49800	69600
Day 5	3400	4500	61100	59400
Day 6	2500	4100	62100	88200
Day 7	3200	6000	73500	144400

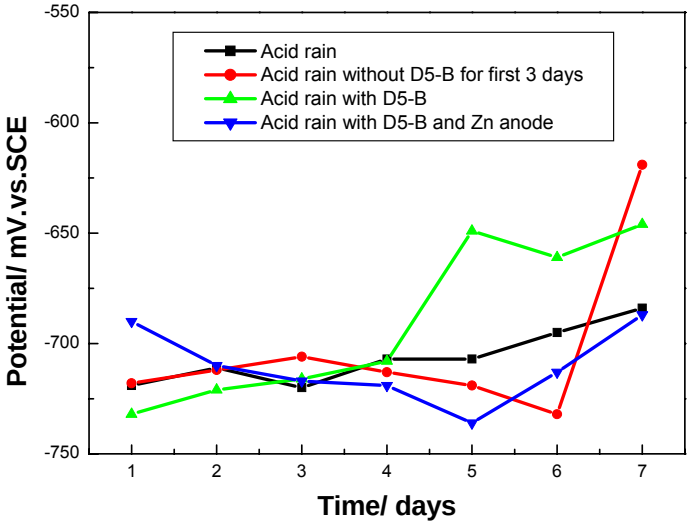

Figure 5.7(a). The potential-time plots obtained in acid rain solution; obtained over a 7-day test period, both with and without (first 3 days only) the addition of D5-B inhibitor, or connected with a Zn anode.

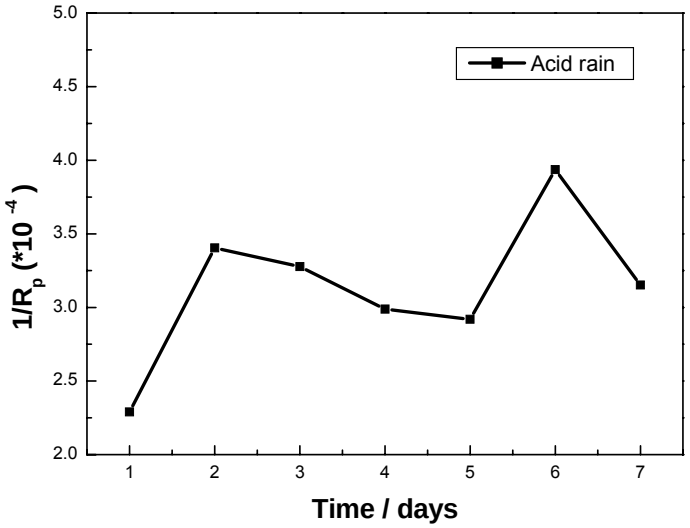

Figure 5.7(b). Graph showing plots of daily $1/R_p$ measurements; obtained over a 7-day test period in acid rain solution.

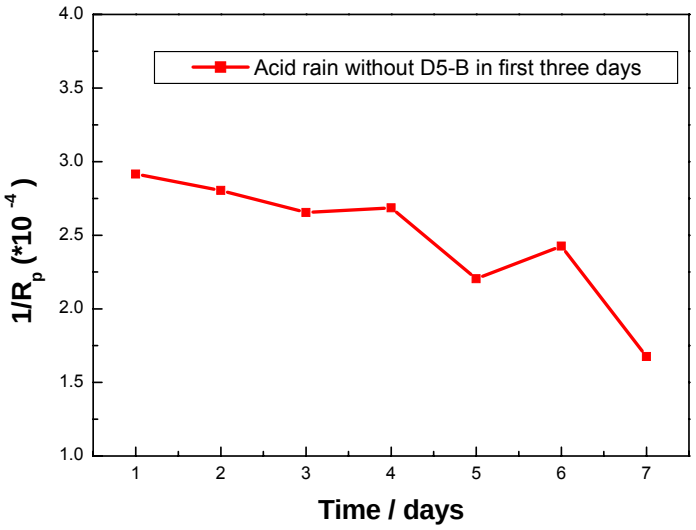

Figure 5.7(c). Graph showing plots of daily $1/R_p$ measurements; obtained over a 7-day test period in acid rain solution without D5-B during first three days only.

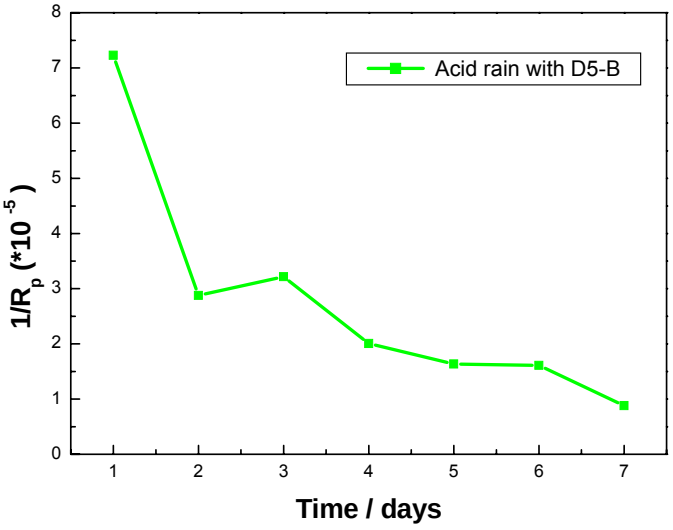

Figure 5.7(d). Graph showing plots of daily $1/R_p$ measurements; obtained over a 7-day test period in acid rain solution with D5-B.

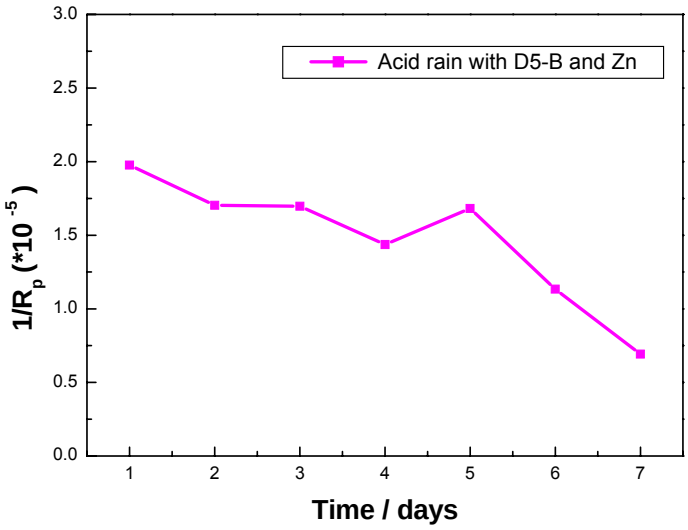

Figure 5.7(e). Graph showing plots of daily $1/R_p$ measurements; obtained over a 7-day test period in acid rain solution with D5-B and Zn Anode.

Figure 5.7. Graphs showing plots of daily potential/time and $1/R_p$ measurements over a 7-day test period for mild steel samples in acid rain solutions, both with and without (first 3 days only) the addition of D5-B inhibitor, or connected with a Zn anode.

From Figure 5.7(d) which shows plots of daily $1/R_p$ measurements obtained in the acid rain solution in the presence of D5-B, it can be seen that the $1/R_p$ value became substantially smaller after immersion for one day. Furthermore, it then remained fairly stable, so this indicates that D5-B is a fairly rapidly-acting and effective inhibitor. For the precorroded situation where D5-B was added after three days of immersion (Figure 5.7(c)), the values of $1/R_p$ decreased slowly after the D5-B was added and had dropped significantly by day 7. This interesting observation seems to suggest that D5-B might well be worth studying as an anti-corrosion pigment for application onto rusty steel. However we did not pursue this avenue further in this Study, but will leave for others to investigate in future research work.

Figure 5.7(e) indicates that the R_p value of the sample immersed with D5-B and connected to a metallic zinc sheet is stable, and reduces by 80% when compared with the sample immersed continuously for 7 days with D5-B inhibitor alone (Figure 5.7(d)).

Photographs of the samples immersed in acid rain solution with the addition of D5-B (Plate 5.6(c), and also with D5-B in combination with a zinc metal anode (Plate 5.6(d)) at the end of the 7 day test period show no corrosion.

From Tables 5.1 and 5.2, and Figures 5.6 and 5.7, in the case of the immersion experiment conducted in the solution containing D5-B in combination with a zinc metal anode, the significant changes in values of $1/R_p$ observed over the duration of the 7 day test period indicated an excellent degree of inhibition which was confirmed from visual observations (Plates 5.5 and 5.6).

From a comparison of the change of samples' potential in both 3.5% NaCl and acid rain solutions (Figure 5.6(a) and Figure 5.7(a)), it was noted that the potential of the inhibited samples were more noble than the uninhibited samples. The inhibitor D5-B may therefore be classed as an anodic inhibitor. Furthermore, the R_p data obtained suggests that D5-B is reasonably successful as a corrosion inhibitor in both 3.5% NaCl solution and acid rain solution, both on bare steel and in the 3 day precorroded situation.

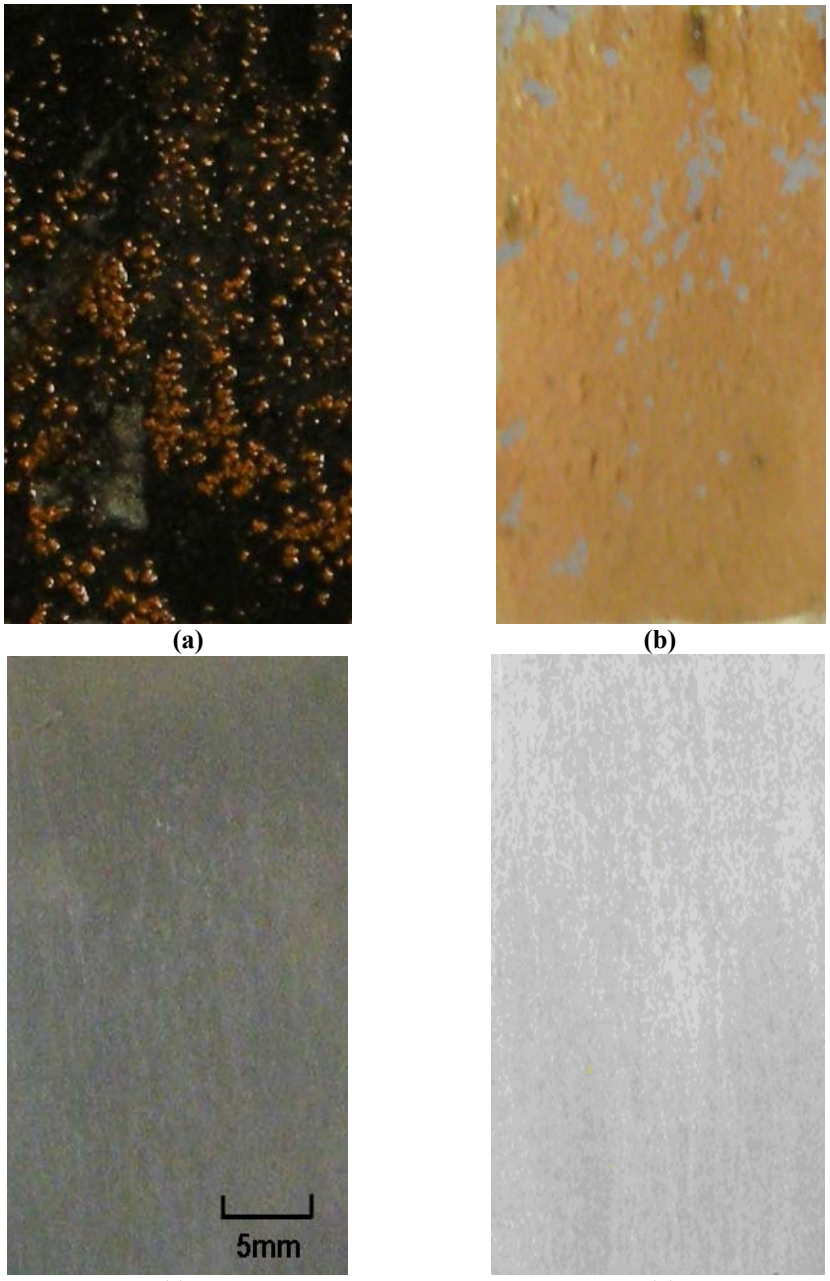

(a) **(b)**

(c) **(d)**

Plate 5.6. Photographs of surfaces of mild steel samples after immersion for 7 days in different acid rain solution: (a) no inhibitor, (b) acid rain solution without D5-B in first three days (c) with D5-B, (d) with D5-B and Zn anode.

5.3.1.3. The research on the Zn cation and constant potential.

Clearly the effectiveness of D5-B as an inhibitor in the two aqueous solutions (NaCl and acid rain) studied has been significantly enhanced when the steel specimen has been simultaneously connected to a zinc anode. The potential in both situations moves negatively, much more so in the NaCl solutions (-1050mV vs. SCE) compared with the acid rain solution (-850mV vs. SCE), probably because of the lower conductivity of the acid rain which in turn will lead to a much reduced current output from the anode. There

are two possible explanations of the role of the zinc. The first is that the negative potential attained on connecting the steel to the zinc enhances the cathodic reactions on the steel and increases the interfacial pH at the steel and further enhances cathodic inhibition. The second is that the action of the zinc anode provides a source of soluble zinc ions in the solution which in turn can act to supplement the calcium and magnesium already present from the inhibitor. Of course, there is always the possibility of both mechanisms acting concurrently. To attempt to distinguish and choose between these two mechanisms, we carried out a series of additional experiments. They both involved the same two solutions, the same steel specimens, and also the same D5-B inhibitor additions. In one situation we added the zinc ions directly to the solution at a concentration of 1g $ZnSO_4$ in 200ml of solution rather than have them generated from dissolution of the zinc anode. We chose this value of 1g $ZnSO_4$ since a simple Faraday calculation on the zinc dissolution gives approximately this value after seven days. In the second situation, we used a potentiostat (ACM), to maintain the potential of the steel at the potential that the steel had attained when it was connected to the zinc, namely -1050mV in the NaCl solution and -850mV in the acid rain solution.

The results may be seen in Table 5.3 for NaCl and Table 5.4 for the acid rain solution in the above conditions. The relevant curves of potential and $1/R_p$ over the 7 day period are given in the accompanying Figures 5.8 and 5.9. Consequently with the potentiostat experiments we also disconnected the power for five minutes before taking a reading, so that in Figure 5.8(a), the potential is not at -1050 mV SCE and in Figure 5.9(a) the potential is not at -850 mV SCE.

(1). 3.5% NaCl solutions.

The first sample was immersed in 3.5% NaCl with D5-B and $ZnSO_4$, and the second sample was immersed in 3.5% NaCl with D5-B at constant potential -1050mV (SCE) using an ACM potentiostat.

Measurements of potential (Figure 5.8(a)) and linear polarization resistance (Table 5.3) were carried out at regular daily intervals, and plotted as the reciprocal $1/R_p$ (Figures 5.8(b) and (c)). The photographs of samples taken after 7 days immersion are shown in Plate 5.6.

Table 5.3. The comparison of values of polarization resistance R_p obtained for samples immersed in 3.5% NaCl solution, with addition of D5-B inhibitor alone at constant potential -1050mV, or with D5-B and $ZnSO_4$.

Unit: Ohm.cm²

Time	3.5% NaCl with D5-B and $ZnSO_4$	3.5% NaCl with D5-B at -1050mV (SCE)
Day 1	13400	14700
Day 2	16900	19200
Day 3	21400	17500
Day 4	22000	17100
Day 5	23100	15000
Day 6	26200	17100
Day 7	27200	18600

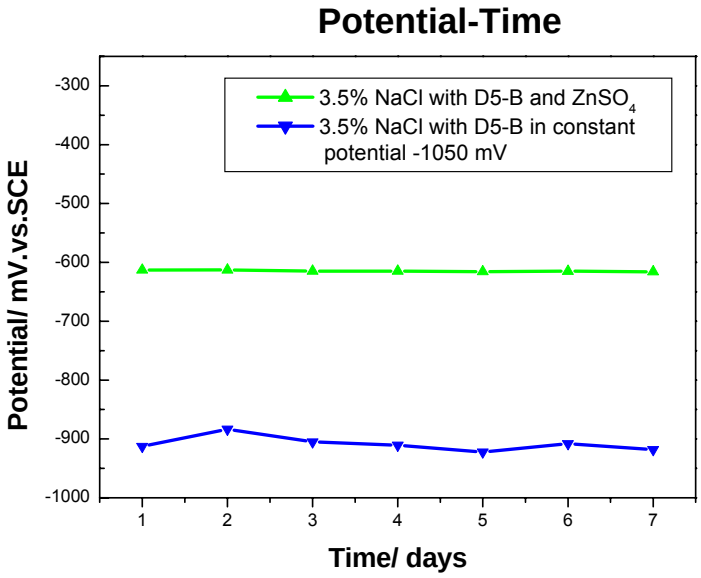

Figure 5.8(a). Graph showing plots of daily potential/time measurements for mild steel samples with addition of D5-B inhibitor alone at constant potential -1050mV, or with D5-B and $ZnSO_4$ over a 7-day test period in 3.5% NaCl solution.

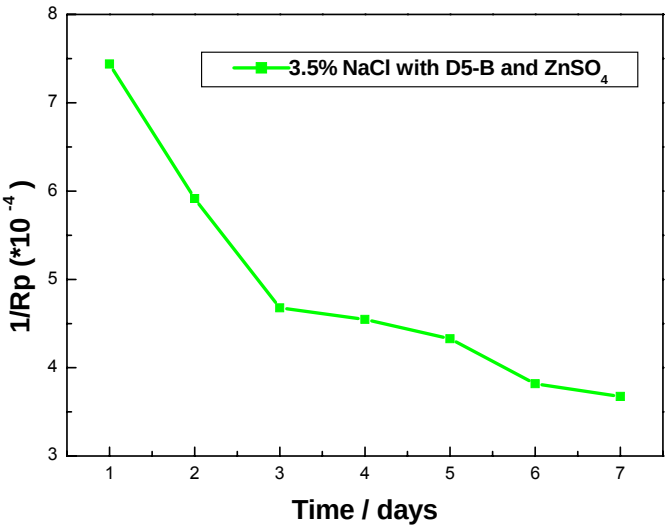

Figure 5.8(b). Graph showing plots of daily 1/Rp measurements for mild steel samples over a 7-day test period in 3.5% NaCl solution with D5-B and $ZnSO_4$.

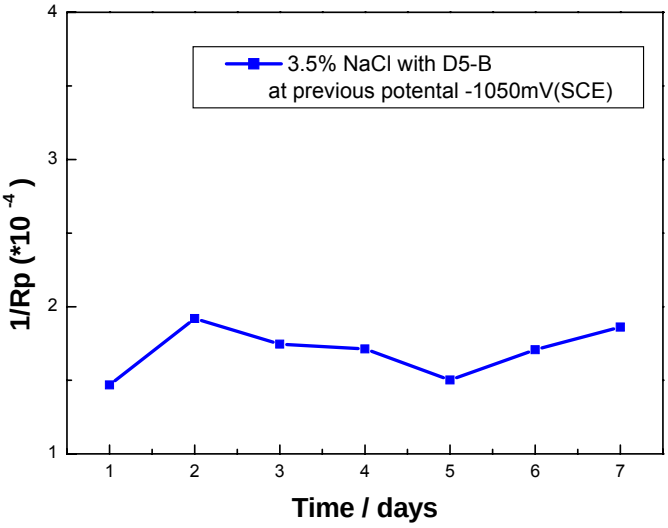

Figure 5.8(c). Graph showing plots of daily 1/Rp measurements over a 7-day test period with D5-B inhibitor at previous potential of -1050mV in 3.5% NaCl solution.

Figure 5.8. Graphs showing plots of daily potential/time measurements over a 7-day test period for mild steel samples in 3.5% NaCl solution, with addition of D5-B inhibitor at constant potential -1050mV, or with D5-B and $ZnSO_4$.

(a) **(b)**

Plate 5.7. Photographs of surfaces of mild steel samples after immersion for 7 days 3.5% NaCl solution, (a) with D5-B and $ZnSO_4$ (b) with D5-B at potential -1050 mV SCE.

(2). Acid rain solution

A similar set of experiments were carried out as described above, but using simulated acid rain solution either with addition of D5-B inhibitor alone, at the constant potential -850 mV (SCE) or with D5-B and $ZnSO_4$. As with the previous experiment, measurements of potential (Figure 5.9(a), and $1/R_p$ (Figures 5.9(b) and (c)) were undertaken daily. Table 5.4 gives values of polarization resistance R_p obtained for the samples immersed in acid rain solution with addition of D5-B inhibitor alone at potential -850 mV, or with addition of D5-B and $ZnSO_4$.

Figure 5.9(a), gives the values of potential obtained for the samples immersed in acid rain solution with addition of D5-B inhibitor alone at potential -850 mV (SCE), or with D5-B and $ZnSO_4$. Photographs were also taken of each sample at the end of the immersion period (Plate 5.8).

Table 5.4. The comparison of values of polarization resistance R_p obtained for samples immersed in acid rain solution, with addition of D5-B inhibitor alone at constant potential -850 mV(SCE), or with D5-B and $ZnSO_4$.

Unit: Ohm.cm²

Time	Acid rain with D5-B and $ZnSO_4$	Acid rain with D5-B at -850mV(SCE)
Day 1	42900	30000
Day 2	57500	48000
Day 3	69200	78200
Day 4	71100	72300
Day 5	73900	65200
Day 6	74800	70700
Day 7	95000	78600

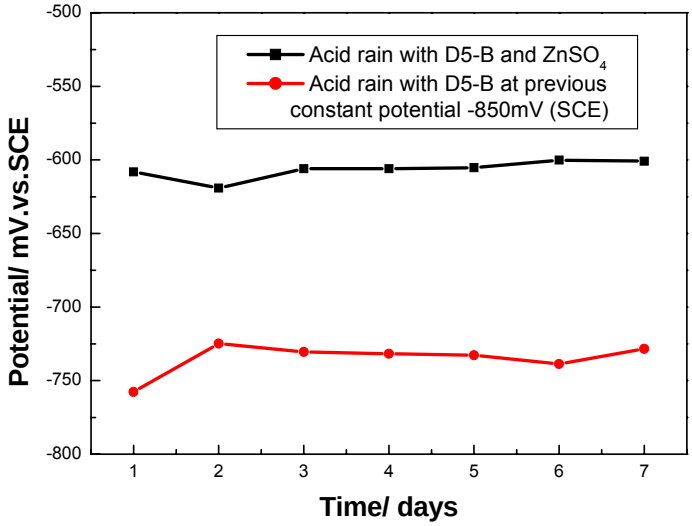

Figure 5.9(a). The potential-time plots obtained for mild steel samples obtained over a 7-day test period in acid rain solution, with addition of D5-B inhibitor alone at potential -850 mV(SCE), or with D5-B and $ZnSO_4$.

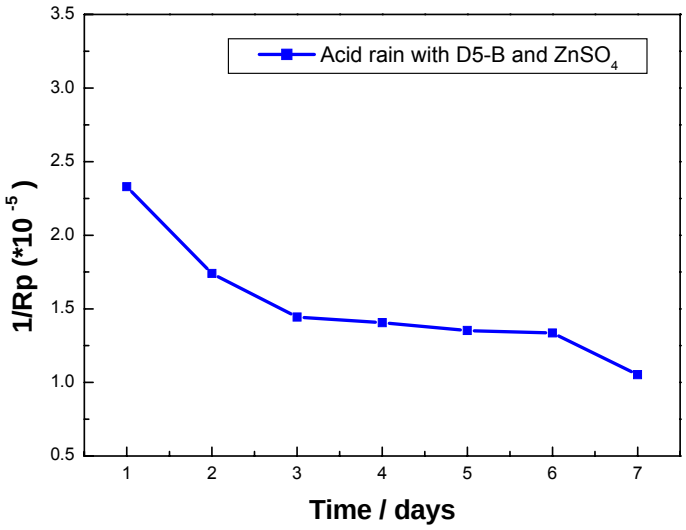

Figure 5.9(b). Graph showing plots of daily $1/R_p$ measurements; obtained over a 7-day test period in acid rain solution with D5-B and $ZnSO_4$.

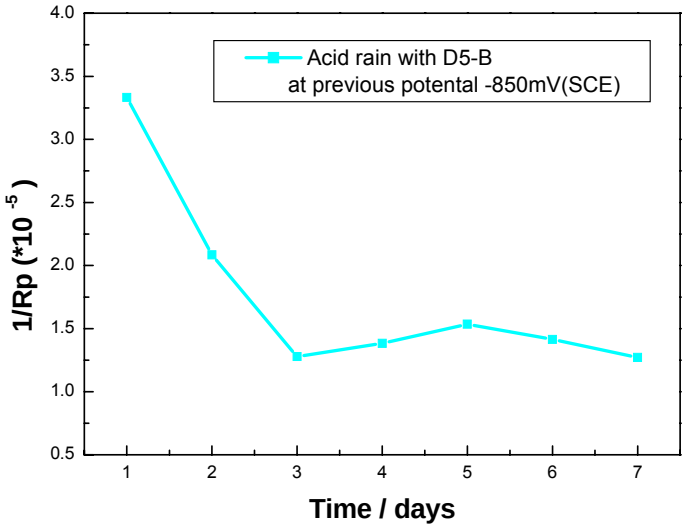

Figure 5.9(c). Graph showing plots of daily $1/R_p$ measurements; obtained over a 7-day test period in acid rain solution with D5-B at previous constant potential -850mV(SCE).

Figure 5.9. Graphs showing plots of daily potential/time and $1/R_p$ measurements for mild steel samples over a 7-day test period in acid rain solution, with addition of D5-B inhibitor alone at potential -850 mV(SCE), or with D5-B and $ZnSO_4$.

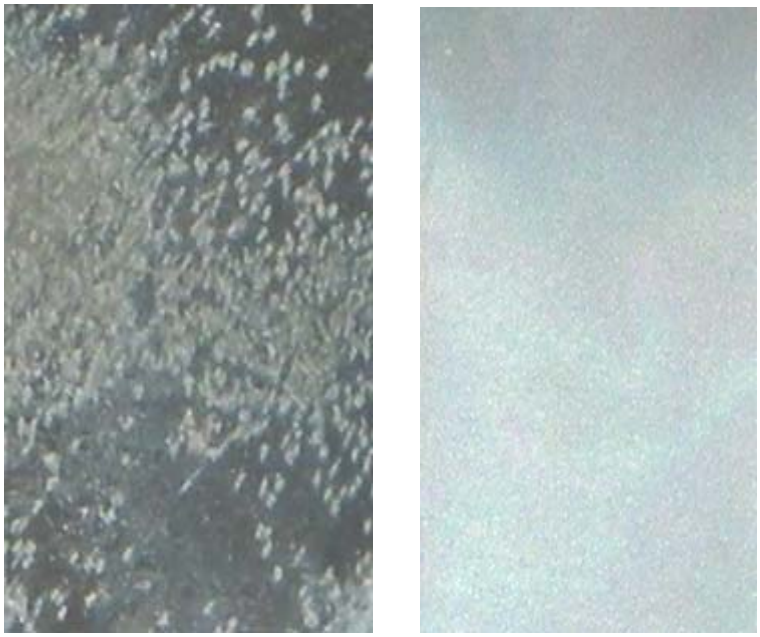

(a) **(b)**

Plate 5.8. Photographs of surfaces of mild steel samples after immersion for 7 days in different acid rain solution: (a) with D5-B and $ZnSO_4$ (b) with D5-B at potential -850mV(SCE).

It was noted from the photographs of the samples immersed in acid rain solution with the addition of D5-B alone (Plate 5.6(c)), and also the samples in acid rain with D5-B and $ZnSO_4$ (Plate 5.8(a)), and in acid rain with D5-B at a constant potential of -850mV (SCE) (Plate 5.8(b)); that at the end of the 7 day test period, none of the samples showed any evidence of corrosion.

From Tables 5.3 and 5.4, and Figures 5.8 and 5.9, in the case of the immersion experiments conducted in the solution containing D5-B in combination with $ZnSO_4$, the significant change in $1/R_p$ observed indicated an excellent degree of inhibition which was confirmed from visual observations (Plates 5.7 and 5.8).

The results of the values of polarisation resistance R_p obtained over 7 days, may be seen in Table 5.3 for NaCl and Table 5.4 for the acid rain solution. The relevant curves of potential and $1/R_p$ over the 7 day period are given in the accompanying Figures 5.8 and 5.9. From the data given in Table 5.3 and Table 5.4 and the relevant graphs given in Figures 5.8 and 5.9, it is clear that additions of zinc ions as zinc sulphate, and the maintenance of a potential of -1050 mV (SCE), has a significantly greater effect on the corrosion rate of the steel as measured by R_p compared with D5-B on its own. The reductions in corrosion rates obtained are between 4 and 5 times. However, the truly

significant reduction in corrosion rate occurs where the steel is coupled to a zinc anode, a 10 times reduction in corrosion rate was observed. The acid rain data presented in Table 5.2 and Table 5.4, is equally clear although it does seem that at 7 days, the system has still not completely reached steady state. There was a substantial improvement in reduction in corrosion rate with the addition of zinc ions and when operating at a constant potential of -850 mV SCE. But again as in the sodium chloride situation, the lowest corrosion rate was obtained when a zinc anode is used. It does appear from these data that the optimum performance is achieved where our two suggested mechanisms of inhibition are operating concurrently, namely the presence of zinc ions and a steel potential where cathodic inhibition is favoured.

5.3.2. Potentiodynamic polarisation.

To get further mechanistic information from the D5-B inhibited systems, a set of Potentiodynamic Polarization scans were carried out, which provides information on electrode processes.

A platinum electrode was used as a counter electrode and a saturated calomel electrode (SCE) was used as a reference electrode together with the usual salt bridge, Section 3.3.1. Samples were embedded in an epoxy resin, and prepared to provide an exposed working surface area of 10.0 cm^2. Prior to each run the sample was polished by using 4000 grade silicon carbide paper and then degreased in pure alcohol followed by pure acetone.

The corrosion measurements were conducted in 3.5% sodium chloride, 0.025M sodium chlorate and acid rain solutions both with and without the addition of the D5-B pigment.

For the D5-B systems, it took around 4 hours for each specimen to be tested. The samples were immersed for 2 hours and the potential was determined and recorded using a computer which links to the 1286 Electrochemical Interface and then the samples were subjected to potentiodynamic polarization for around 2 hours. Each potentiodynamic polarization scan was carried out from -1.5 V to +2.5 V at a scan rate of 1 mV/s.

5.3.2.1. Potential Measurements.

An open circuit potential (OCP) measurement was determined for all samples in all different solutions, immediately after immersion. The sample's potential was recorded using a 1286 Electrochemical Interface controlled by a desk-top computer over an initial 2 hours immersion. Comparison with the manual potential/time plots Figures 5.1, 5.2 and 5.3 over a seven day period shows the two sets of data were not widely dissimilar.

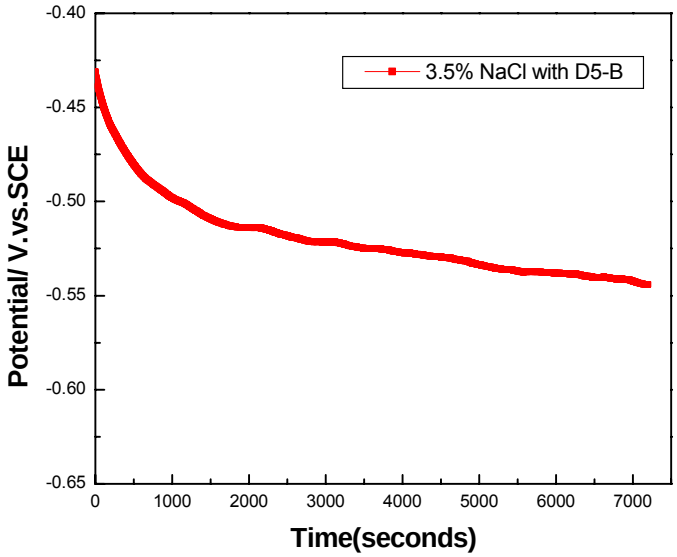

(a)

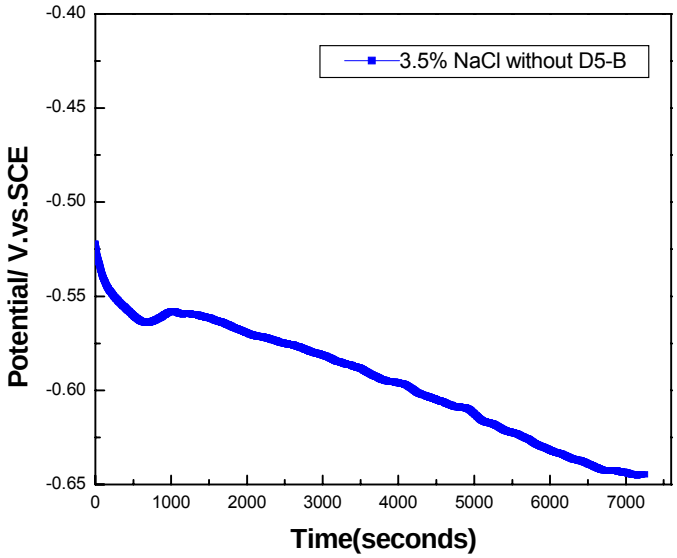

(b)

Figure 5.10. Graphs of open circuit potentials plotted against time for: (a) 3.5% NaCl solution with D5-B, (b) 3.5% NaCl solution without D5-B.

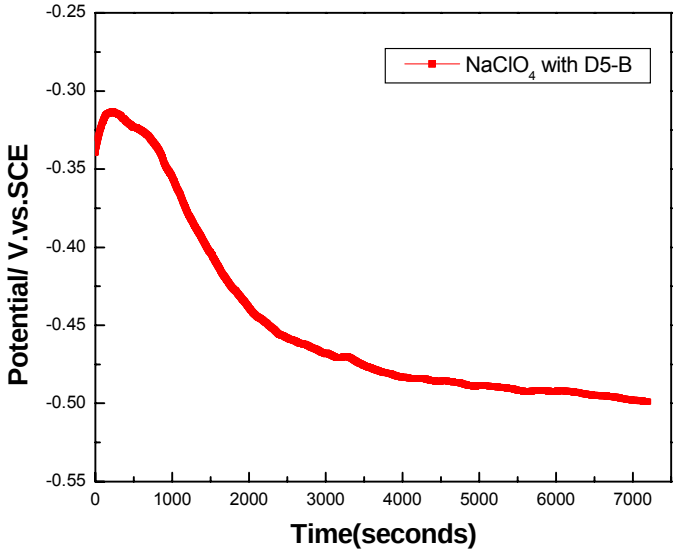

(a)

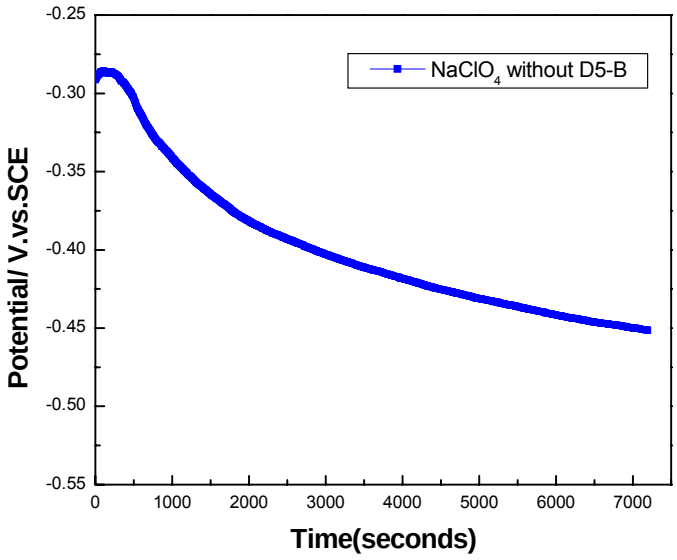

(b)

Figure 5.11. Graphs of open circuit potentials plotted against time for:
(a) 0.025M $NaClO_4$ solution with D5-B, (b) 0.025M $NaClO_4$ solution without D5-B.

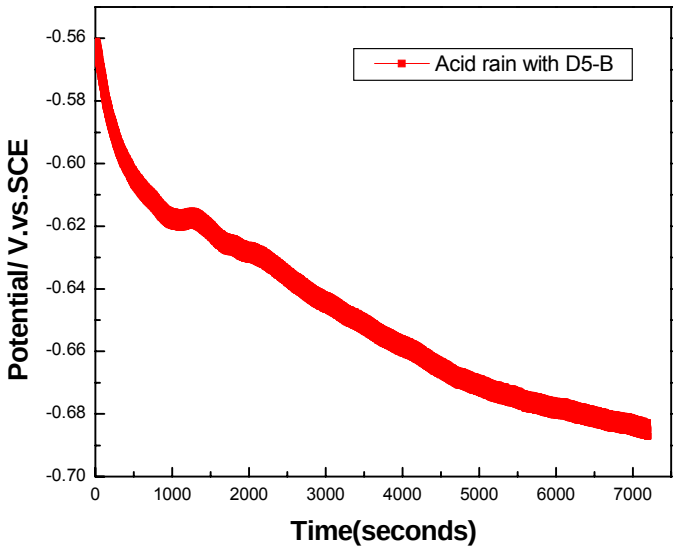

(a)

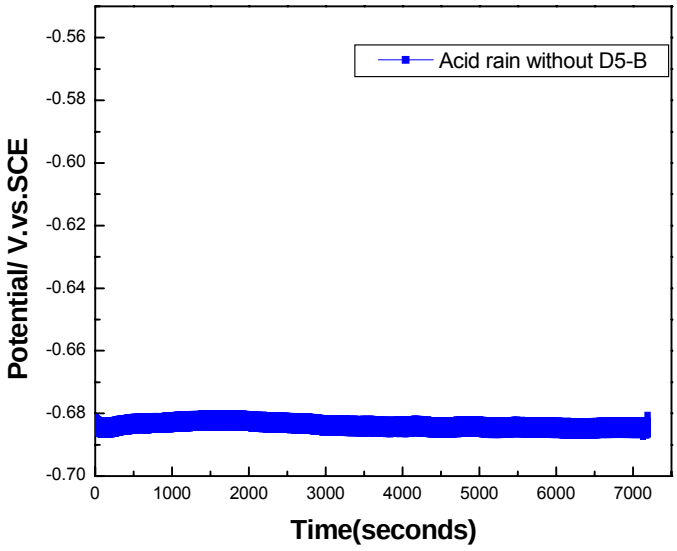

(b)

Figure 5.12. Graphs of open circuit potentials plotted against time for: (a) acid rain solution with D5-B, (b) acid rain solution without D5-B.

Figure 5.10 shows the plots of open circuit potentials for mild steel samples measured against time for samples immersed in 3.5% NaCl solution both with and without the addition of D5-B inhibitor. In both cases, the potential started to drift slowly in the

negative direction presumably as electrochemical reactions start and deposits appear at the metal-electrolyte interface. The potential of the sample immersed with D5-B present is more positive than the sample tested without inhibitor, and the difference was observed to be around 10 mV; this value is probably not significant. For steel in 3.5% NaCl solution, the cathodic reaction at open circuit is oxygen reduction ($O_2 + 2\ H_2O + 4e^- \rightarrow 4\ OH^-$).

From Figure 5.11, the potential of the sample immersed in the 0.025M sodium chlorate solutions with D5-B, is slightly more negative (5mv) than the potential of the sample immersed in 0.025M sodium chlorate without D5-B. For steel in 0.025M sodium chlorate solution, the cathodic reaction is probably also the oxygen reduction reaction.

From Figure 5.12, it can be seen that the potential of the sample immersed in simulated acid rainwater solution with D5-B took a longer time to attain a stable state, than the potential of the sample immersed without the presence of D5-B. This is probably because at the start of the immersion period the acid rain solution is quite resistive. It is possible that as dissolution of the pigment took place, this increases the conductivity of the solution. The potential of the samples were not significantly different in acid rain solutions either with or without the addition of inhibitor.

5.3.2.2. Potentiodynamic polarization

After the samples were immersed for two hours, and the potentials were almost stable then the samples were subjected to potentiodynamic polarization.

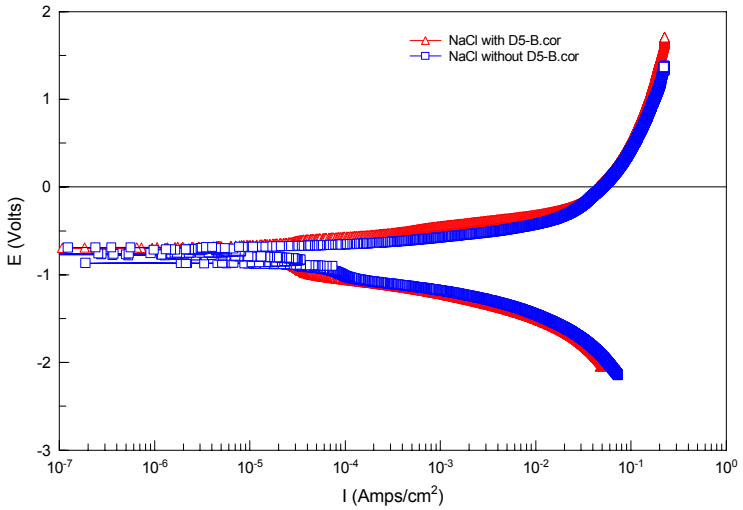

(a)

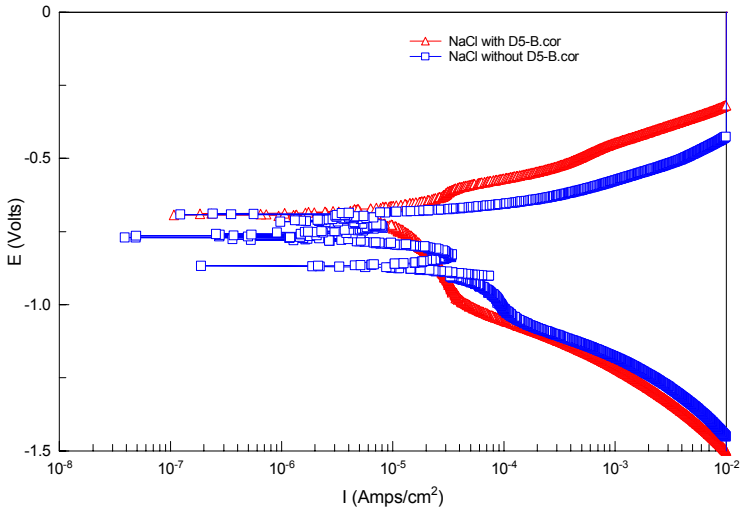

(b)

Figure 5.13(a). Graph showing plots illustrating relationship between Potential .vs. Current for mild steel samples immersed in 3.5% NaCl solution both with and without addition of D5-B inhibitor, (b) Graph showing a direct zoom into lower left-hand region of Graph (a), giving more detailed view of plots.

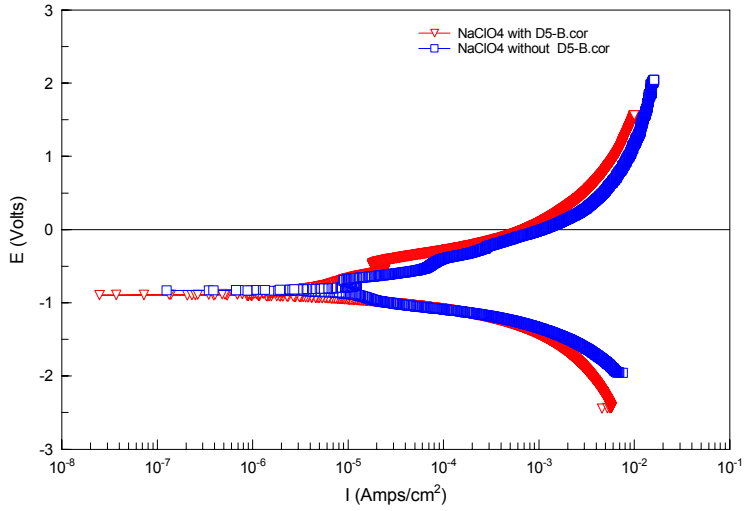

(a)

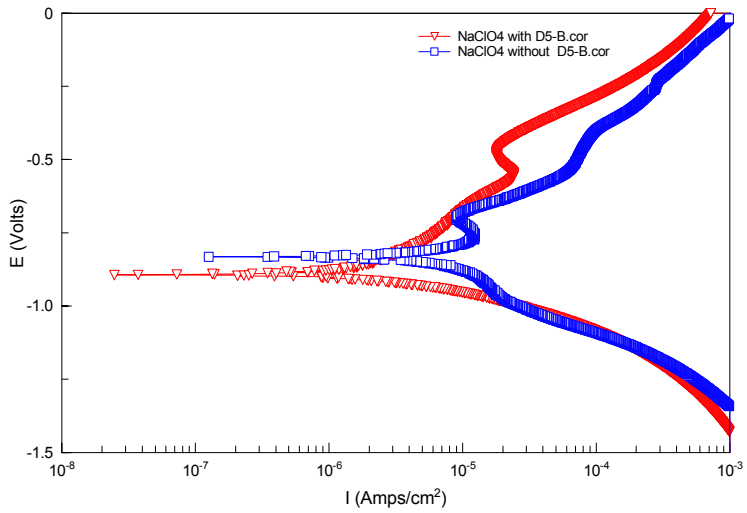

(b)

Figure 5.14(a). Graph showing plots illustrating relationship between Potential vs. Current for mild steel samples immersed in 0.025M $NaClO_4$ solution both with and without addition of D5B inhibitor, (b) Graph showing a direct zoom into lower left-hand region of Graph (a), giving more detailed view of plots.

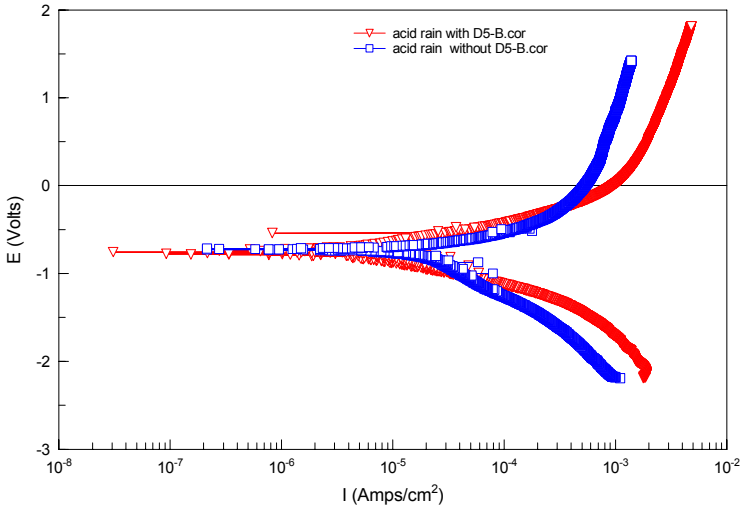

(a)

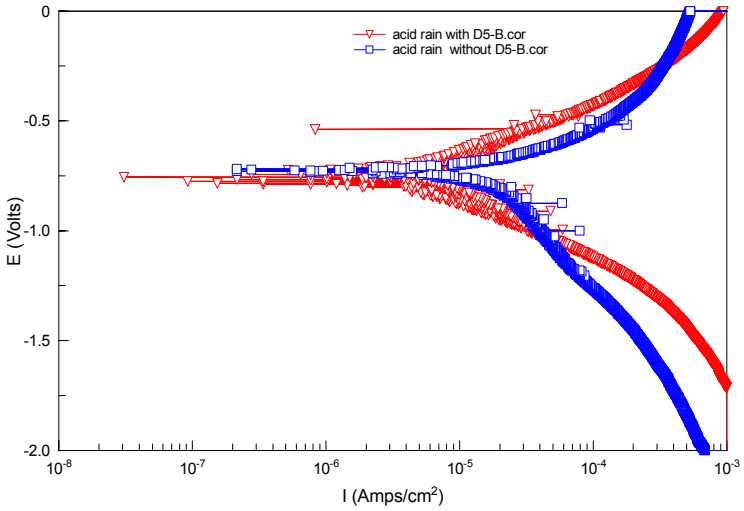

(b)

Figure 5.15(a). Graph showing plots illustrating relationship between Potential vs. Current for mild steel samples immersed in acid rain solution both with and without addition of D5B inhibitor, (b) Graph showing a direct zoom into lower left-hand region of Graph (a), giving more detailed view of plots.

According to the plots shown in Figure 5.13, the potential at zero current obtained for the sample immersed in 3.5% NaCl solution with D5-B became slightly more positive [-0.69 V (SCE)] than the potential [-0.63 V (SCE)] of the sample immersed without it. This is a similar result to those obtained from Figure 5.1 and Figure 5.10, so D5-B appears to be an anodic inhibitor in the presence of 3.5% NaCl solution.

From Figure 5.14, it can be observed that the potential of the sample immersed in $NaClO_4$ solution with D5-B became more negative than the potential obtained for the corresponding sample without D5-B by only around 10 mV, and I_{corr} was observed to drop significantly (Table 5.5), so D5-B may function as a mixed inhibitor in 0.025M $NaClO_4$ solution.

From Figure 5.15, it was evident that the potential of the sample immersed in simulated acid rain solution with the addition of D5-B was not significantly different from the potential observed for the sample immersed in acid rain without D5-B, but I_{corr} was observed to decrease greatly (see Table 5.5 in next Section), so D5-B may act as a mixed inhibitor in the acid rain solution.

5.3.2.3. Summary of Results and Overall Discussion.

Figures 5.13, 5.14 and 5.15 show the polarization curves recorded for mild steel samples immersed in the different corrosive solutions (3.5% NaCl, 0.025M $NaClO_4$ and acid rainwater) both with and without D5-B.

The corrosion current densities I_{corr} and the anodic and cathodic Tafel constants (β_a and β_c, respectively), were determined from the experimental curves on the basis of the Butler-Volmer equation, and this was also discussed in Chapter 2, the equation 2-28 was given as following:

$$i = i_0 \left\{ \exp\left[\frac{2.303}{\beta_a}(E - E_{eq}) \right] - \exp\left[-\frac{2.303}{\beta_c}(E - E_{eq}) \right] \right\} \quad \text{…….. ……..} \quad (5\text{-}1)$$

Where E_{eq} is the corrosion potential, i_0 is the current density; β_a and β_c are the anodic and cathodic Tafel constants respectively. The corrosion current densities obtained from the fitting procedure, as well as the anodic dissolution current densities derived from

potentiodynamic data, are summarized in Table 5.5. The polarization resistance (R_P) data had also been presented in Chapter 2 (the equation 2-33).

$$R_P = \frac{\beta_a \beta_c}{2.303 I_{corr}(\beta_a + \beta_c)} \quad \text{(5-2)}$$

The corrosion rates (*CR*) could be calculated from the corrosion current densities, using Faraday's law (values are presented in Table 5.5), which has also been presented in Chapter 3 (equation 3-1), and are given as:

$$CR = \frac{Ks}{\rho A} = \frac{MIs}{nF\rho A} = \frac{Mis}{nF\rho} \quad \text{(5-3)}$$

Where:

CR = corrosion rate (cm/y)

K = rate of corrosion (g/s)

A = area (cm^2)

ρ = density of metal (g/cm^3)

s = seconds in a year ($31.5*10^6$)

The values of β_a, β_c, and I_{corr} depend on the particular section of the polarization curve contained between the anodic and cathodic potential limits, which were fitted. Thus, the values of β_a, β_c, and I_{corr} indicated correspond to given anodic and cathodic potential limits which are also indicated in Table 5.5.

In the 3.5% NaCl solution with inhibitor (Figure 5.13), the ferrous ions were oxidised ($Fe^{2+} \rightarrow Fe^{3+}$), and the corrosion current density was about $3*10^{-6}$ A/cm^2 (0.03 A/m^2) at -0.69 V/SCE. Conversely, in the 3.5% NaCl solution without inhibitor, the corrosion current density was about $3*10^{-5}$ A/cm^2 (0.3 A/m^2) at -0.868 V/SCE. For 3.5% NaCl solution in the presence of the inhibitor, the cathodic Tafel constant was 76 mV/dec, whilst the anodic Tafel constant was 145 mV/dec. For 3.5% NaCl solutions in the absence of inhibitor, the cathodic Tafel constant was 92 mV/dec, whilst the anodic Tafel constant was 147 mV/dec. In comparison with the samples immersed with no inhibitor, the value of I_{corr} for the sample in 3.5% NaCl solution with the addition of inhibitor was significantly decreased by a factor of around ten times.

From Figure 5.14, which gives the values of E_{corr} for samples in the $NaClO_4$ solution with D5-B, the potential at zero current became more negative than the potential recorded for samples without D5-B, and from Table 5.5, I_{corr} was observed to drop significantly by a factor of around 3 - 4 times. In the 0.025M $NaClO_4$ solution with D5-B inhibitor, the mild steel was oxidised ($Fe^{2+} \rightarrow Fe^{3+}$) at the corrosion current density of about $2*10^{-6}$ A/cm^2 (0.02 A/m^2) at -0.9 V/SCE. Accordingly, in the case of samples immersed in 0.025M $NaClO_4$ solution without D5-B inhibitor, the corrosion current density was around $1*10^{-5}$ A/cm^2 (0.1 A/m^2) at -0.832 V/SCE. For samples in 0.025M $NaClO_4$ solution with the inhibitor, the cathodic Tafel constant was 100 mV/dec, and the anodic Tafel constant was 335 mV/dec. For samples in 0.025M $NaClO_4$ without inhibitor, the cathodic Tafel constant was 272 mV/dec, and the anodic Tafel constant is 234 mV/dec.

Table 5.5. Summary Table of all major parameters determined for mild steel samples immersed in the three corrosive test solutions, both with and without the addition of D5-B inhibitor.

Treament	Fitting	E_{corr}(V)	I_{corr} (Amp/cm^2)	β_a (mV)	β_c (mV)	Corrosion rate (mm/y)	R_P (Ω/cm^2)
3.5% NaCl without D5-B	Tafel fit	-0.868	3.0E-05	147	92	0.40	810
	R_P fit	-0.868	3.6E-05			0.42	720
3.5% NaCl with D5-B	Tafel fit	-0.690	2.7E-06	76	145	0.03	7950
	R_P fit	-0.692	7.9E-06			0.09	3280
0.025M $NaClO_4$ without D5-B	Tafel fit	-0.832	1.3E-05	234	272	0.10	4090
	R_P fit	-0.832	6.0E-06			0.05	4260
0.025M $NaClO_4$ with D5-B	Tafel fit	-0.893	2.3E-06	335	100	0.018	14680
	R_P fit	-0.846	4.3E-06			0.033	6120
Acid rainwater without D5-B	Tafel fit	-0.727	3.3E-06	101	140	0.026	7660
	R_P fit	-0.750	8.8E-06			0.064	3170
Acid rainwater with D5-B	Tafel fit	-0.785	9.0E-08	135	136	0.0011	32550
	R_P fit	-0.730	2.1E-06			0.025	12270

From Figure 5-15, it can be seen that the potential of samples immersed in simulated acid rainwater with the addition of D5-B was not significantly different from the potential recorded for samples immersed in acid rain without D5-B inhibitor. However, the value of I_{corr} of the sample immersed with D5-B inhibitor decreased around four times. In the case of acid rainwater with the addition of D5-B inhibitor, the cathodic Tafel constant was 136 mV/dec, whilst for samples in acid rainwater in the absence of the inhibitor; the cathodic Tafel constant was 140 mV/dec.

As part of the computer software, the facility existed to calculate R_p from Linear Polarisation Resistance obtained from the same sweep. The data given in Table 5.5 presents R_p values calculated from High field (Tafel extrapolation) and Low field (LPR). A comparison of the calculated values may be made using column eight. On examination of the data, a good correlation between the two techniques exists for the uninhibited samples. In the inhibited situations, a significant difference between the two may be seen. Since we have not polarized the specimen excessively, it is tempting to assume that LPR values are more accurate than Tafel extrapolation values which seem to give lower corrosion rates. Also there is the possibility of an inaccurate estimation of the Tafel constants for the inhibited surface

5.3.3. Electrochemical Impedance Spectroscopy (EIS) study on the deposit.

In order to investigate how a deposit changes with time on the surface of a sample, Electrochemical Impedance Spectroscopy (EIS) testing could be employed over regular time intervals. In contrast to the previous 7 day testing periods, this experiment was carried out over 30 days of immersion testing. Electrochemical Impedance Spectroscopy (EIS) measurements using the Solartron system previously described in Section 3.6. Experiments were carried out while the specimens were immersed in various test solutions for periods of 2 hours, 4 hours, 8 hours, 1 day, 2 days, 3 days, 4 days, 5 days, 1 week, 2 weeks and 1 month in order to obtain the polarization resistance R_p, and also other additional useful data, including the Constant Phase Element CPE, Section 3.6.3. The experimental testing solutions were similar to that described in Section 5.3.2; and consisted of: 3.5% NaCl solution, 0.025M $NaClO_4$ and artificial acid rain water. Mild steel specimens with an exposed area of 10.0 cm^2 were used as the test specimens. The samples were immersed in these solutions both with and without the addition of D5-B. The use of EIS testing also provided further mechanistic information regarding D5-B, and also further information was gained concerning the interactions occurring on steel samples immersed in corrosive solutions with the addition solely of D5-B, and also the effect of D5-B in the presence of zinc metal.

For each experiment, the data obtained from the Electrochemical Impedance Spectroscopy (EIS) were displayed by means of a Nyquist plot (Z' *vs* Z'') and a Bode plot ($\log |Z|$ *vs* $\log\omega$ and θ *vs* $\log\omega$), where $|Z|$ is the absolute value of the impedance, θ is the

phase angle and ω is the angular frequency (rad/s). The testing frequency at the start was 10000 Hz, whilst the final test frequency was 0.1 Hz.

In order to simulate the behaviour of the electrochemical reaction occurring at the corrosion interface, the simple equivalent circuit given in Figure 5.16 can be used. For this work, this simpler circuit was selected in preference to the more complex circuit used in Chapter 4. In this system, the thin uniform film was much simpler to model, and indeed the impedance data obtained looks much less complex.

During the free corrosion process, charge transfer controlled reactions occur. The model circuit is shown in Figure 5.16, where the resistance R_s represents the solution and corrosion product films. The parallel combination of R_{ct} and CPE (constant phase element) represents the charge transfer of the corroding surface, where R_{ct} is the charge transfer resistance arising from the anodic and cathodic electrochemical reactions and is related both to the rate of flow of electrons and also to the rate of electron transfer from the interfacial double layer. The value of the constant phase element (CPE) represents the capacitive component of the equivalent circuit. The fitting results, the resistance of the solution (R_s), the charge transfer resistance (R_{ct}) and some additional useful data (CPE_{-T} and CET_{-P}), are given in Tables 5.6, 5.7 and 5.8.

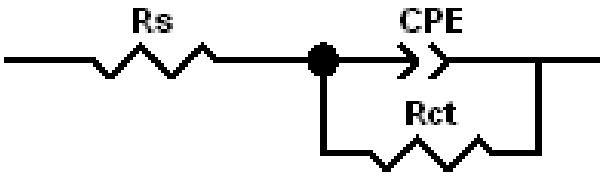

Figure 5.16. The equivalent circuit.

5.3.3.1. Commencing immersion testing (2h).

To evaluate the influence of the various inhibitor pigments at the very beginning of the immersion period, a set of mild steel samples (as discussed previously in Section 3.2.1) was immersed in the three different test solutions (same set of corrosive test solutions as described in Section 5.3.2). Values of R_s, CPE_{-T}, CPE_{-P} and R_{ct} were determined and recorded for each sample, and in each of the three test solutions, both with and without the addition of the inhibitor D5-B, after an initial two hours of immersion.

Table 5.6. The comparison of values of R_s, CPE_{-T}, CPE_{-P} and R_{ct} obtained for mild steel samples immersed in 3.5% NaCl solution for 2 hours, both with and without presence of D5-B inhibitor.

	Rs ($\Omega.cm^2$)	CPE_{-T} (F/cm^2)	CPE_{-P}	R_{ct} ($\Omega.cm^2$)
With D5-B	4	0.00041	0.80	5600
Without D5-B	6	0.00026	0.81	1400

Table 5.7. The comparison of values of R_s, CPE_{-T}, CPE_{-P} and R_{ct} obtained for mild steel samples immersed in 0.025M $NaClO_4$ solution for 2 hours, both with and without presence of D5-B inhibitor.

	Rs ($\Omega.cm^2$)	CPE_{-T} (F/cm^2)	CPE_{-P}	R_{ct} ($\Omega.cm^2$)
With D5-B	150	0.0024	0.61	6300
Without D5-B	160	0.0026	0.68	3300

Table 5.8. The comparison of values of R_s, CPE_{-T}, CPE_{-P} and R_{ct} obtained for mild steel samples immersed in acid rain solution for 2 hours, both with and without presence of D5-B inhibitor.

	Rs ($\Omega.cm^2$)	CPE_{-T} (F/cm^2)	CPE_{-P}	R_{ct} ($\Omega.cm^2$)
With D5-B	460	0.00042	0.57	2400
Without D5-B	590	0.00033	0.66	760

(1). 3.5% NaCl solution with D5-B.

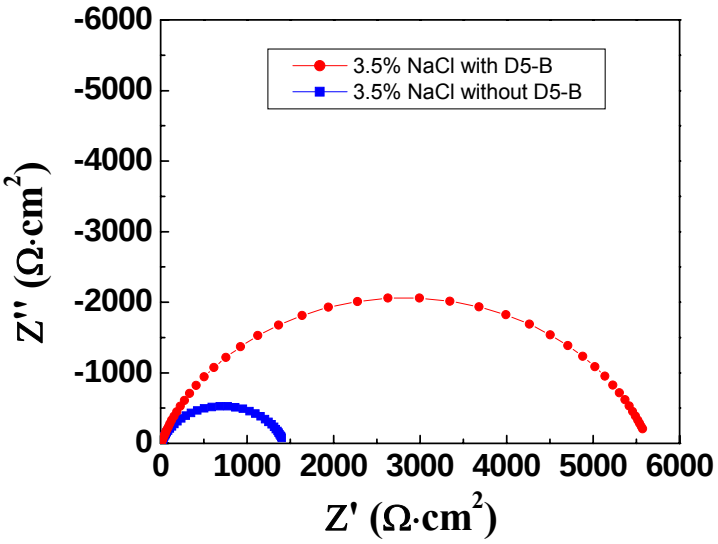

(a) Nyquist

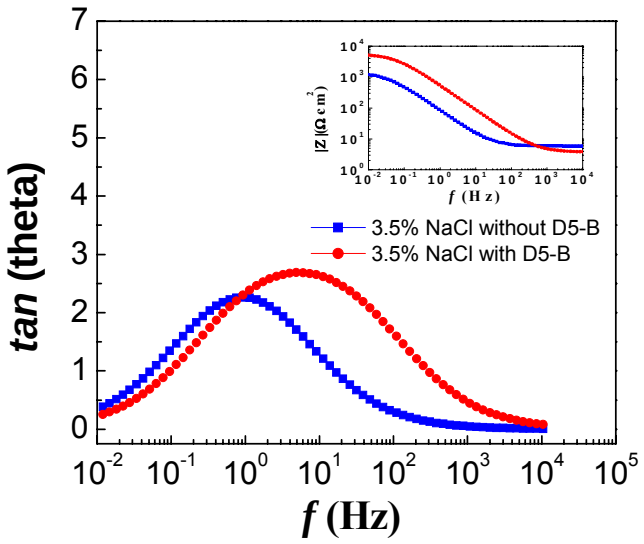

(b) Bode

Figure 5.17. Graphs showing the comparison of impedance spectra obtained during the initial 2 hour period of immersion, for mild steel samples immersed in 3.5% NaCl solution both with and without the addition of D5-B inhibitor: (a) Nyquist, (b) Bode.

(2). 0.025M $NaClO_4$ with D5-B.

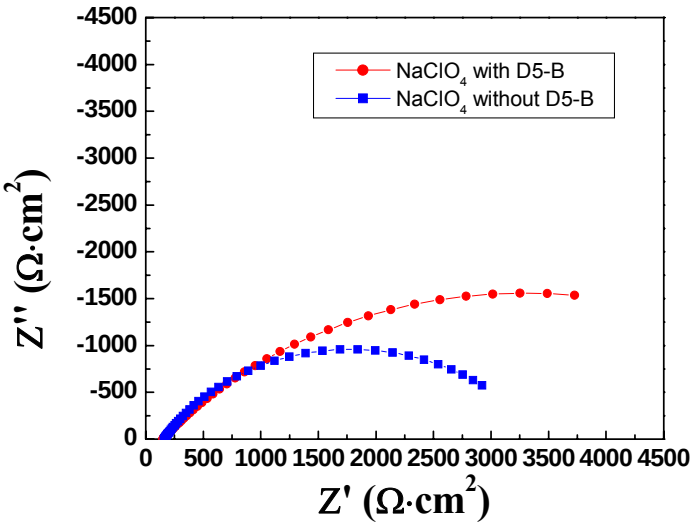

(a) Nyquist

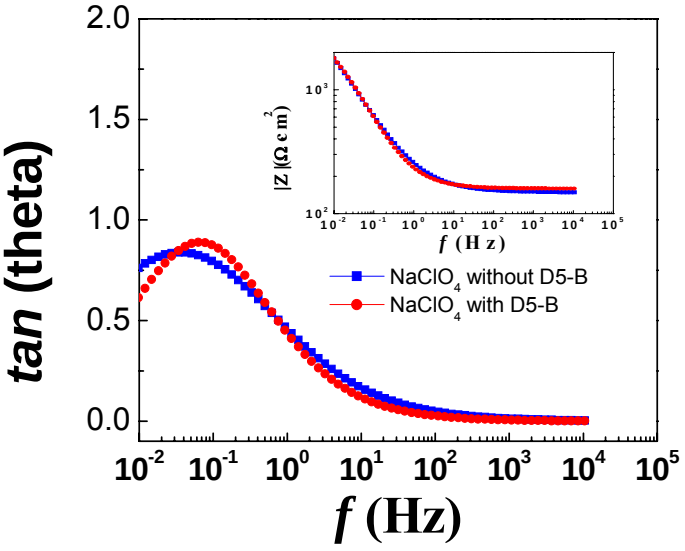

(b) Bode

Figure 5.18. Graphs showing the comparison of impedance spectra obtained during the initial 2 hour period of immersion, for mild steel samples immersed in 0.025M $NaClO_4$ solution both with and without the addition of D5-B inhibitor: (a) Nyquist, (b) Bode.

(3). Acid rainwater with D5-B.

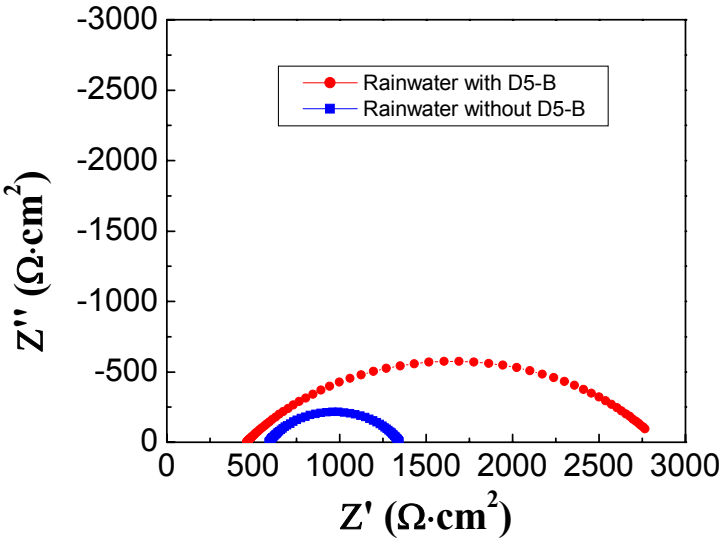

(a) Nyquist

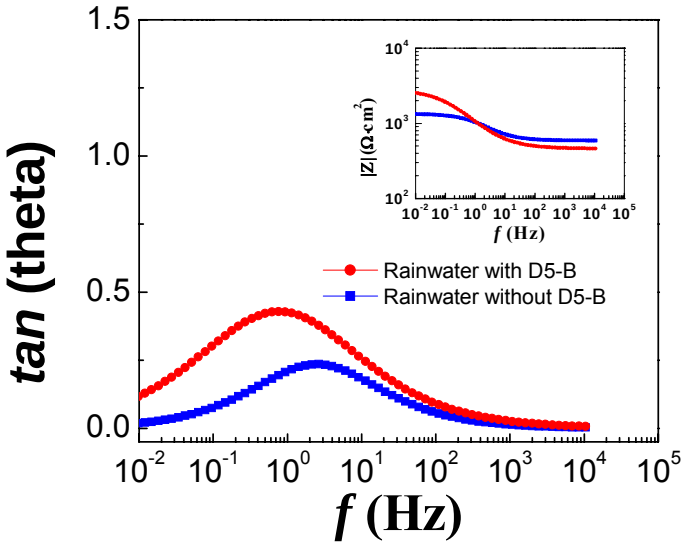

(b) Bode

Figure 5.19. Graphs showing the comparison of impedance spectra obtained during the initial 2 hour period of immersion, for mild steel samples immersed in acid rainwater solution both with and without the addition of D5-B inhibitor: (a) Nyquist, (b) Bode.

The parameters obtained for the electrochemical impedances measured and recorded for the mild steel samples in the three different testing solutions both with and without the addition of D5-B inhibitor are presented in Figures 5.17, 5.18 and 5.19, and Tables 5.6, 5.7 and 5.8. For all three testing solutions, the values obtained for R_{ct} (the charge transfer resistance) were found to be significantly increased by between 2 ~ 4 times, when D5-B inhibitor was present, compared to the values of R_{ct} obtained when D5-B was absent. These results are comparable with those obtained by potentiodynamic polarization testing (given in Table 5.5). The value of i_{corr} obtained with the addition of D5-B was lower than the value of i_{corr} obtained with no D5-B inhibitor present (see the values of i_{corr} given in Table 5.5). These i_{corr} values were calculated by applying equation 5-1 (Section 5.3.2.3), so the value of R_{ct} with D5-B was higher than the value of R_{ct} without D5-B. Later we shall show the presence of calcium/magnesium and polyphosphate on the steel surface. It may be assumed that this layer increased the charge transfer resistance. When values of R_{ct} obtained for samples in the 3 different test solutions (given in Tables 5.6, 5.7 and 5.8) are compared, the value of R_{ct} determined in acid rain solution was noticeably reduced. It may be that since the pH of the solution was 3.5, the deposit was not so easily formed and also, the acid rain solution had fairly low conductivity and it was therefore slightly more difficult to form the deposit film in acid rain solution than in the other two solutions.

5.3.3.2. Extended time immersion.

When the immersion experiments were continued for an extended continuous test period of 720 hours (30 days), in the set of three different test solutions with the addition of the inhibitor D5-B [same test solutions as stated previously (Section 5.3.3.1)], full sets of measurements were continuously noted and recorded at the intervals stated in the previous Section.

(1). 3.5% NaCl with D5-B.

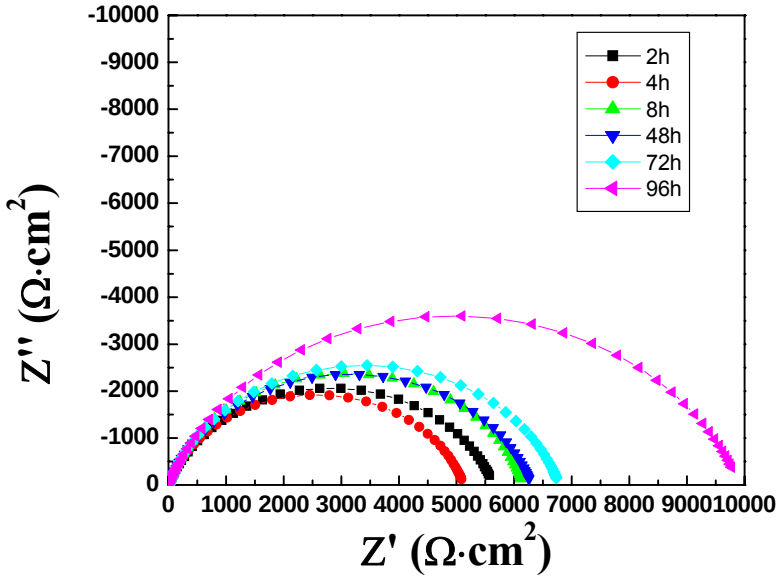

Figure 5.20(a). Nyquist graph for initial 96 hours test period in 3.5% NaCl solution with D5-B.

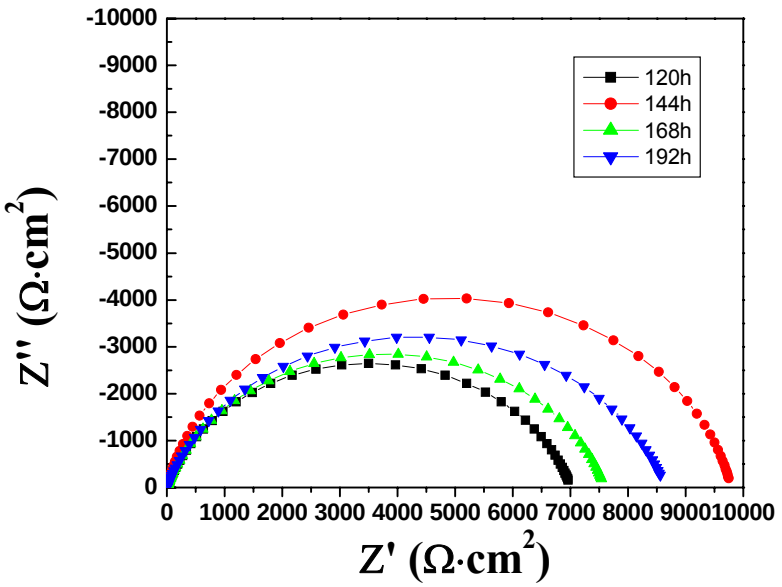

Figure 5.20(b). Nyquist graph for period between 120~192 hours of testing period in 3.5% NaCl solution with D5-B.

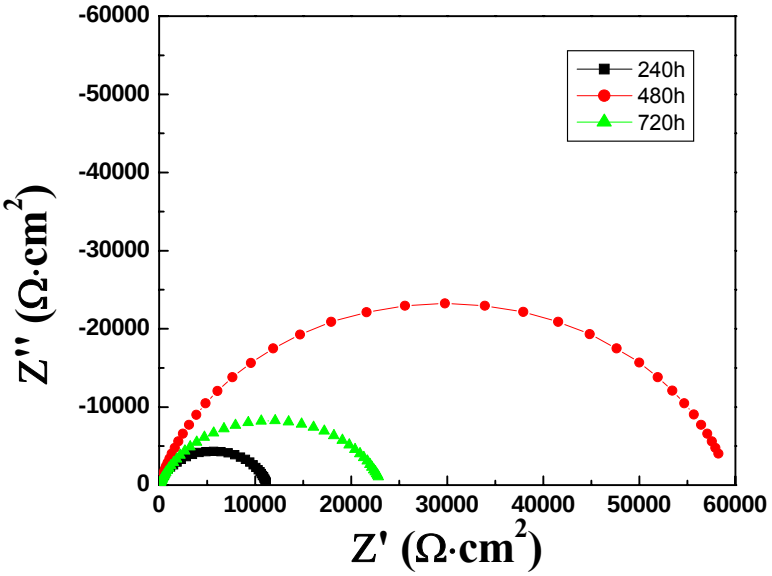

Figure 5.20(c). Nyquist graph for period between 240~720 hours of testing period in 3.5% NaCl solution with D5-B.

Figure 5.20. Nyquist graphs plotted over different test periods in 3.5% NaCl solution with D5-B.

Table 5.9. Table showing the change of various parameter values recorded for the equivalent circuit with increasing immersion time in 3.5% NaCl solution with D5-B.

Immersed time	Rs ($\Omega.cm^2$)	CPE_{-T} (F/cm^2)	CPE_{-P}	R_{ct} ($\Omega.cm^2$)
2h	4	0.00041	0.80	5600
4h	5	0.00031	0.82	5100
8h	4	0.00025	0.84	6200
48h	6	0.00023	0.82	6300
72h	5	0.00022	0.82	6800
96h	5	0.00024	0.80	9900
120h	3	0.00022	0.82	7000
144h	3	0.00018	0.88	9800
168h	4	0.00022	0.82	7600
192h	2	0.00023	0.81	8600
240h	5	0.00019	0.84	11300
480h	24	8.8e-5	0.84	59500
720h	29	0.00012	0.79	23200

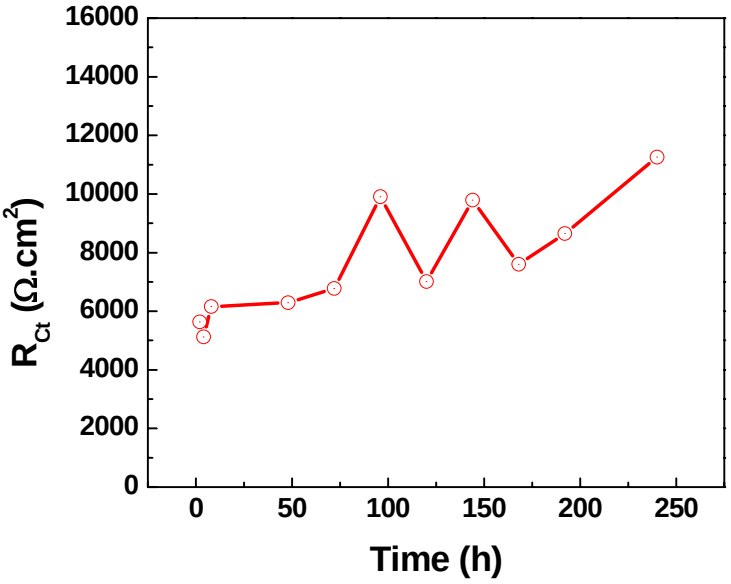

Figure 5.21. Graph showing plot of change in transfer resistance (R_{ct}) with increasing immersion time for mild steel samples in 3.5% NaCl solution with D5-B (up to 240 hours).

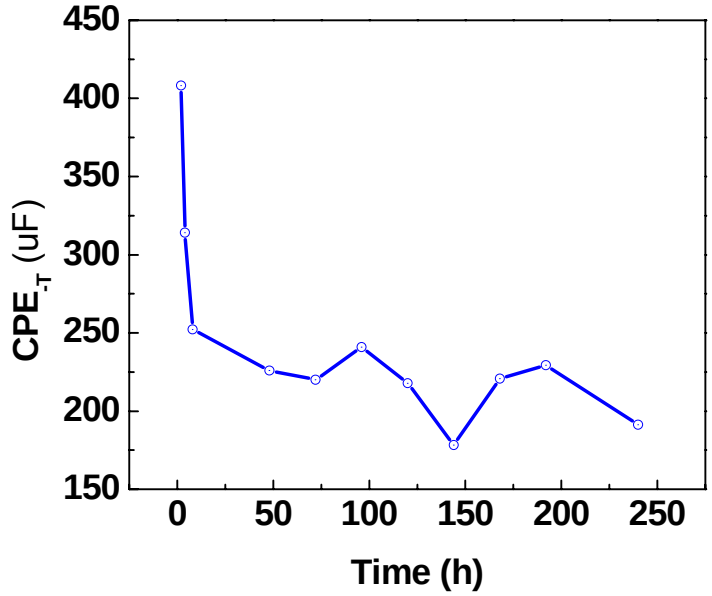

Figure 5.22. Graph showing change in CPE_{-T} (µF) values recorded over time for mild steel samples in 3.5% NaCl solution with D5-B (up to 240 hours).

(2). 0.025M $NaClO_4$ with D5-B.

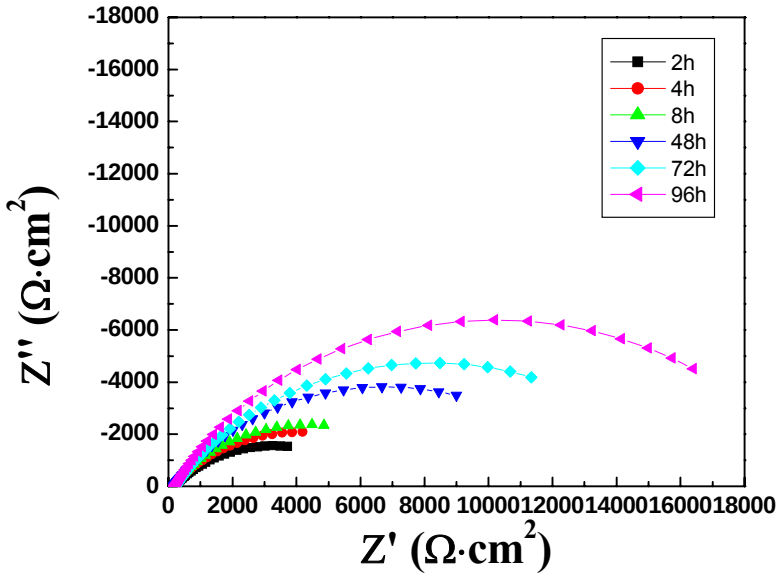

Figure 5.23 (a). Nyquist graph for the initial 0 - 96 hours of testing period in 0.025M $NaClO_4$ with D5-B.

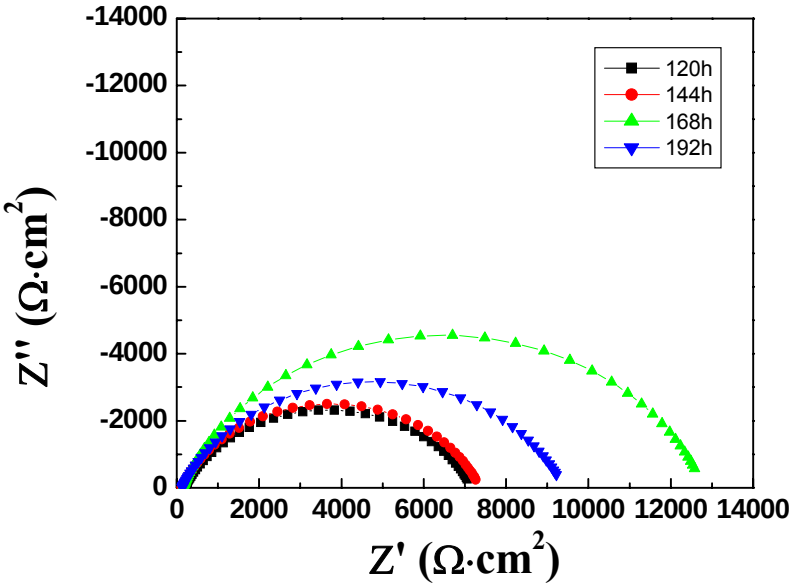

Figure 5.23(b). Nyquist graph for the period 120 - 192 hours of testing in 0.025M $NaClO_4$ with D5-B.

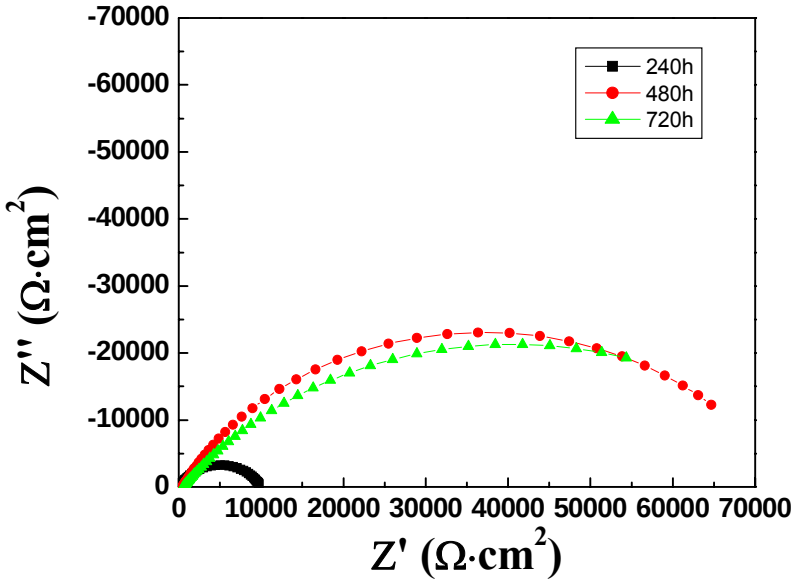

Figure 5.23(c). Nyquist graph for the period 240 -720 hours of testing in 0.025M $NaClO_4$ with D5-B.

Figure 5.23. Nyquist graphs plotted over various times in 0.025M $NaClO_4$ solution with D5-B.

Table 5.10. The change of parameter values recorded for the equivalent circuit with increasing immersion time in 0.025M $NaClO_4$ solution with D5-B.

Immersed time	Rs ($\Omega.cm^2$)	CPE_{-T} (F/cm^2)	CPE_{-P}	R_{ct} ($\Omega.cm^2$)
2h	150	0.0024	0.61	6300
4h	120	0.0027	0.61	8000
8h	130	0.0026	0.64	8500
48h	164	0.0013	0.67	13200
72h	220	0.0011	0.68	16000
96h	190	0.00068	0.73	20100
120h	170	0.00027	0.74	7000
144h	120	0.00025	0.77	7200
168h	150	0.00022	0.79	12700
192h	140	0.00024	0.76	9300
240h	170	0.00024	0.75	9800
312h	220	0.00026	0.69	23700
480h	430	0.00012	0.72	73300
720 h	560	0.00017	0.62	80000

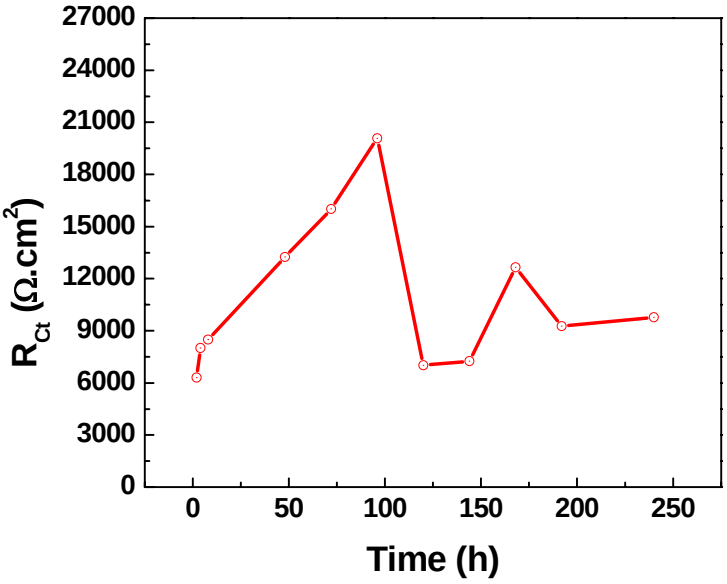

Figure 5.24. Graph showing plot of charge transfer resistance R_{ct} against Time for mild steel samples in 0.025M $NaClO_4$ solution with D5-B (from 2 to 240 hours).

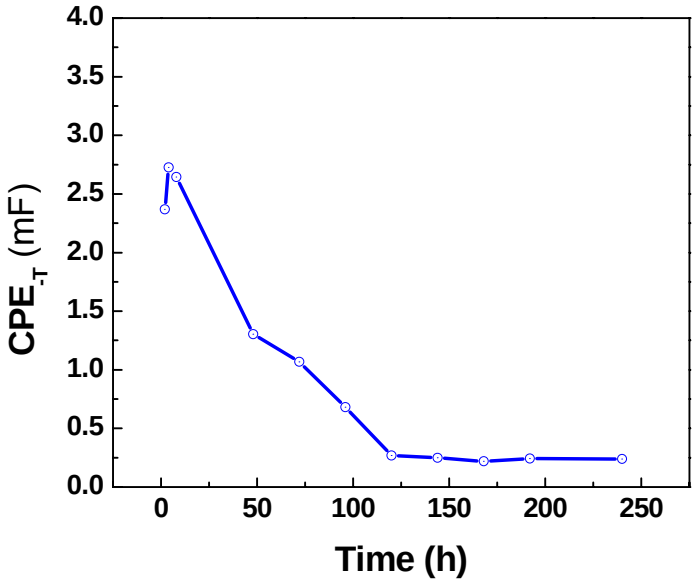

Figure 5.25. Graph of CPE_{-T} vs. Time for mild steel samples in 0.025M $NaClO_4$ solution with D5-B (from 2 to 240 hours).

(3). Acid rainwater with D5-B.

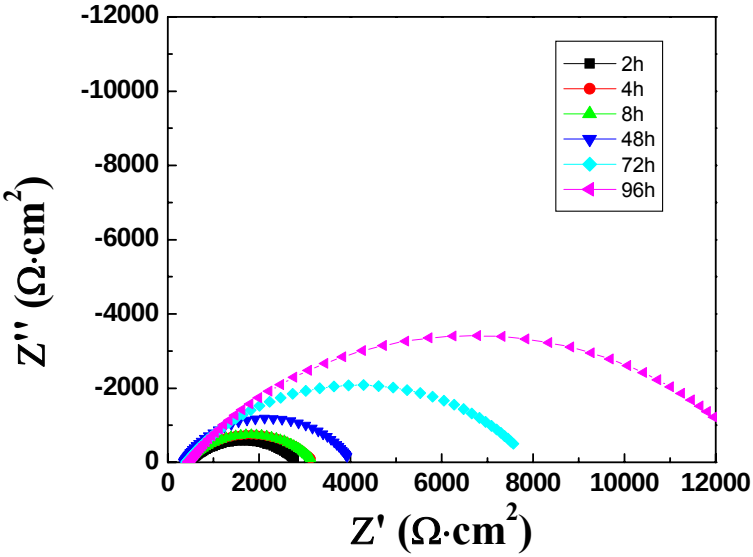

Figure 5.26 (a). Nyquist graph for the initial 0~96 hours of testing period in acid rainwater with D5-B.

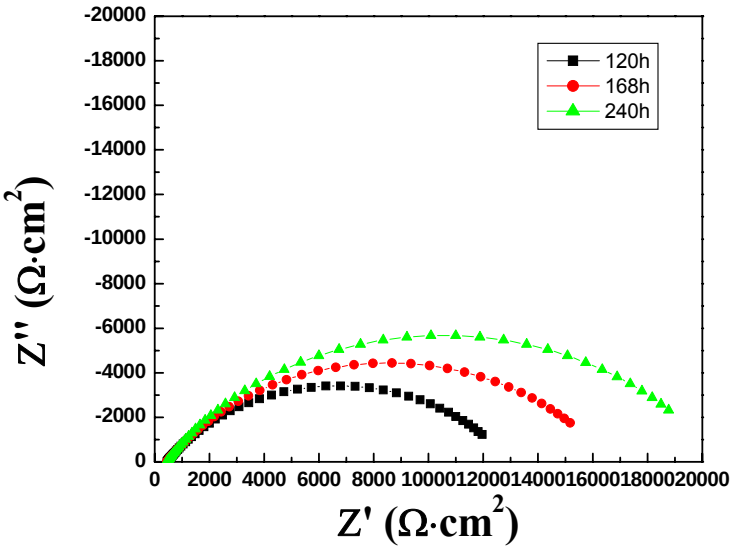

Figure 5.26 (b). Nyquist graph for the period 120 -240 hours of testing in acid rainwater with D5-B.

Figure 5.26. Nyquist graphs plotted over various time periods in acid rain solution.

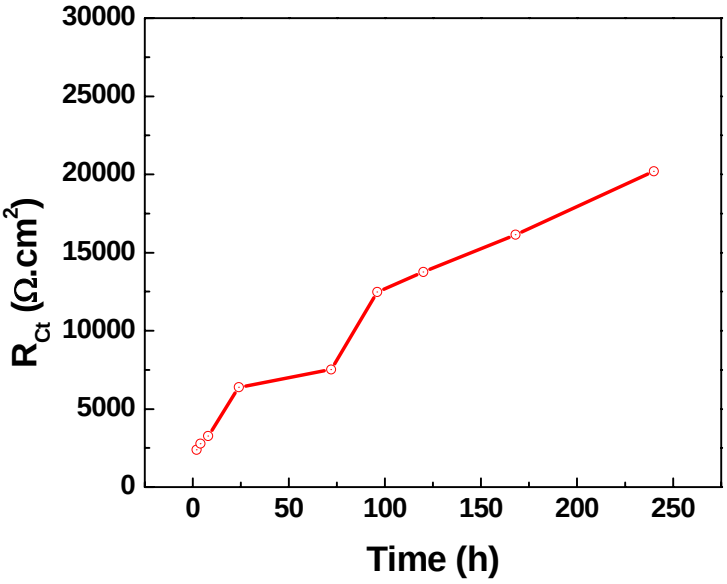

Figure 5.27. Graph showing plot of charge transfer resistance R_{ct} with Time obtained for mild steel samples in acid rain solution with D5-B.

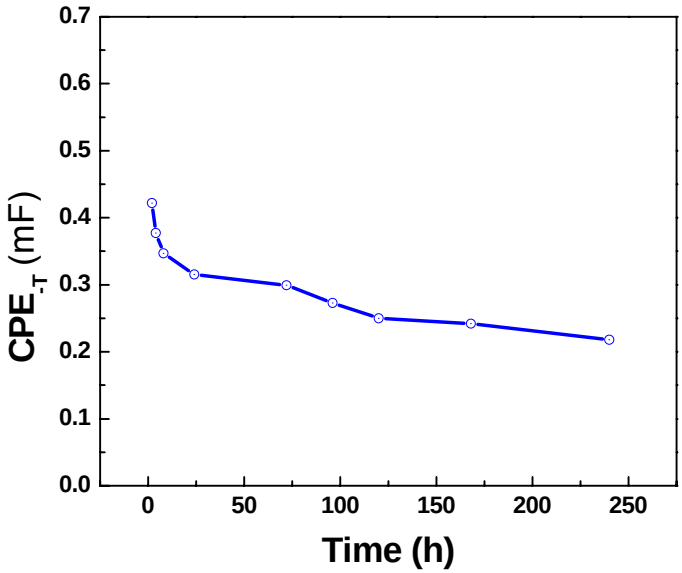

Figure 5.28. Graph of CPE_{-T} vs. Time in acid rain solution with D5-B.

Table 5.11. The change of various parameters of the equivalent circuit with increasing immersion time in acid rain solution with D5-B.

Immersed time	R_S ($\Omega.cm^2$)	CPE_{-T} (F/cm^2)	CPE_{-P}	R_{ct} ($\Omega.cm^2$)
2h	460	0.00042	0.57	2400
4h	430	0.00037	0.63	2800
8h	390	0.00035	0.67	3300
24h	470	0.00032	0.63	6400
72h	410	0.00030	0.64	7500
96h	450	0.00027	0.64	12500
120h	480	0.00025	0.64	13800
168h	450	0.00024	0.64	16100
240h	440	0.00022	0.65	20200
720h	2500	0.00016	0.58	47800

Figures 5.20, 5.23 and 5.26 and Tables 5.9, 5.10 and 5.11 show readings of R_{ct} obtained with time for samples immersed in the three solutions with addition of D5-B inhibitor for the initial 240 hours of the 720 hours experimental duration. Over the first 96 hours of immersion, the value of the charge transfer resistance (R_{ct}**)** was observed to increase. This is almost certainly due to film growth on the sample surface. Then, during the next 120~240 hours of immersion, R_{ct} became more variable, but overall, it increased. This instability is thought to be due to the protective film becoming detached from the steel surface and subsequently re-growing. After 240 hours, the data became fairly stable, and interestingly the resistance of the solutions (R_s) increased. For the chlorate and acid rain solutions it could be argued that because after such a long immersion time, there was substantial deposition of corrosion film on the surface of the steel sample and the concentration of ions in the solution therefore decreased with time, so the resistance of the solution was also concurrently increased. It is difficult however to use the same argument in the highly conductive sodium chloride solution and this feature remains unresolved. In all cases the plot of CPE_{-T} with time curve generally decreases while the R_{ct} value increased.

5.4. Scanning Electron Microscopy (SEM) and Energy Dispersive X-Ray Analysis (EDX).

An SEM examination and subsequent analysis using EDX was performed on the sodium chloride and acid rain solutions at the end of the immersion experiments. The sodium chlorate solutions were not examined due to lack of time. Either whole samples (to examine surfaces) or resin-embedded sample cross-sections (see Section 3.8.4) were mounted onto aluminium SEM specimen stubs using either adhesive carbon tabs or double-sided adhesive copper mounting tape, then samples were carbon coated using an Edwards Carbon coater. Samples were coated once, then turned 180 degrees and coated again to avoid shadowing and charging effects. A coating thickness reference chart was used to estimate that samples were coated with carbon to a thickness of approximately 5.0 to 8.0 nm. Prepared samples were examined in a FEI XL-30 FEGSEM, with attached RONTEC EDX system running Quantax Esprit 1.8 analytical software, which has also been discussed previously in Section 3.8.2.

5.4.1. SEM/EDX examination of the sample surface deposits.

Plate 5.9 shows the SEM images and corresponding EDX maps of the corrosion film deposits formed after 7 days immersion in 3.5% NaCl solution with addition of D5-B. Plate 5.9(a) shows an SEM photomicrograph of the sample surface taken at a magnification of 500 X, and Plates 5.9(b), (c), (d), (e), (f) and (g) present the set of EDX single element distribution maps that correspond with the image shown in Plate 5.9(a), whilst Figure 5.29 gives the EDX full spectra results of all the elements present, and Table 5.12 gives the quantitative percentages of all the selected elements in the deposit, over the area that was imaged at 500 X magnification.

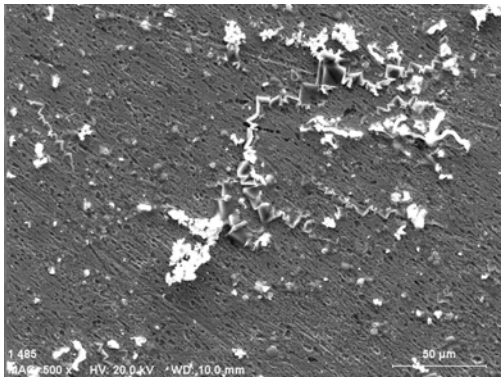

(a). Secondary electron image taken at 500x

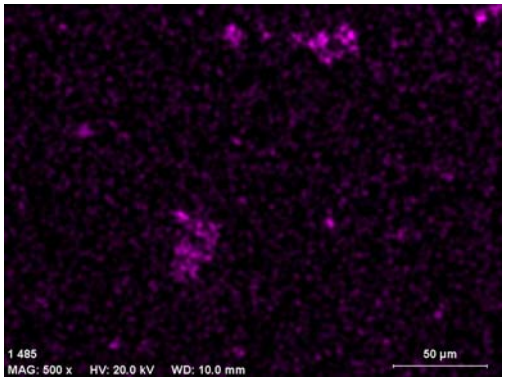

(b) Single EDX element map of distribution of Ca

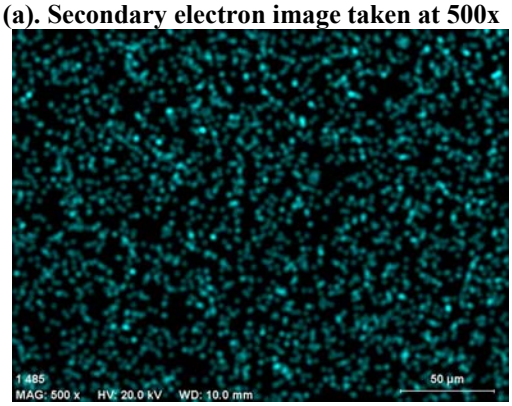

(c) Single EDX element map of distribution of Mg

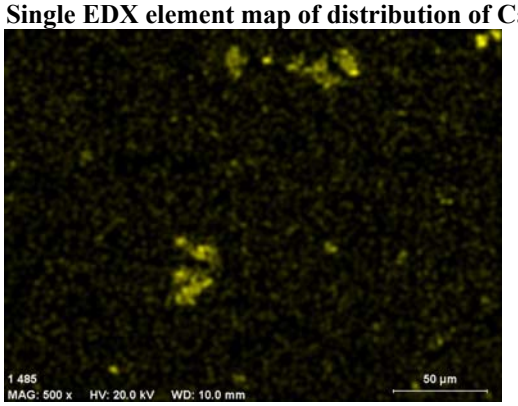

(d) Single EDX element map of distribution of P

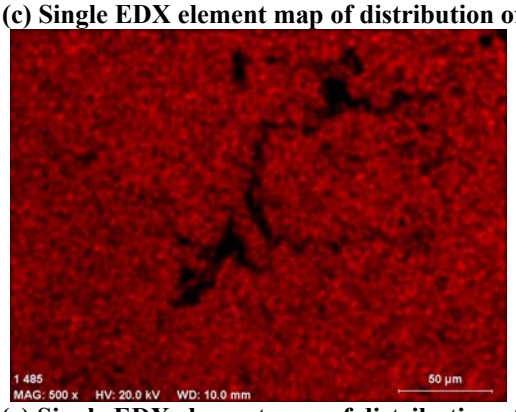

(e) Single EDX element map of distribution of Fe

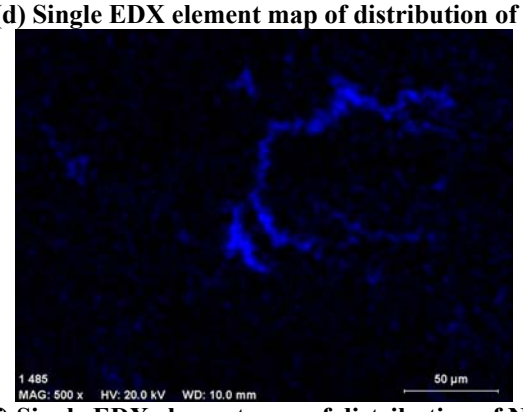

(f) Single EDX element map of distribution of Na

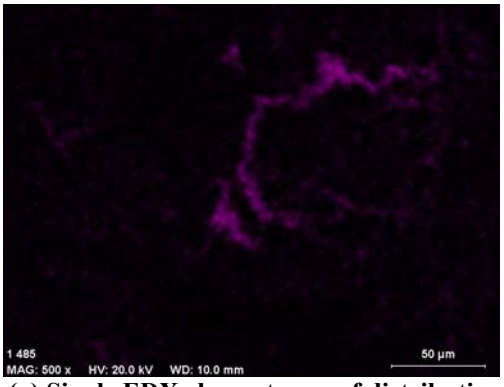

(g) Single EDX element map of distribution of Cl

Plate 5.9. SEM micrographs and associated EDX element distribution maps of surfaces of samples after immersion for 7 days in 3.5% NaCl solution with addition of D5-B inhibitor.

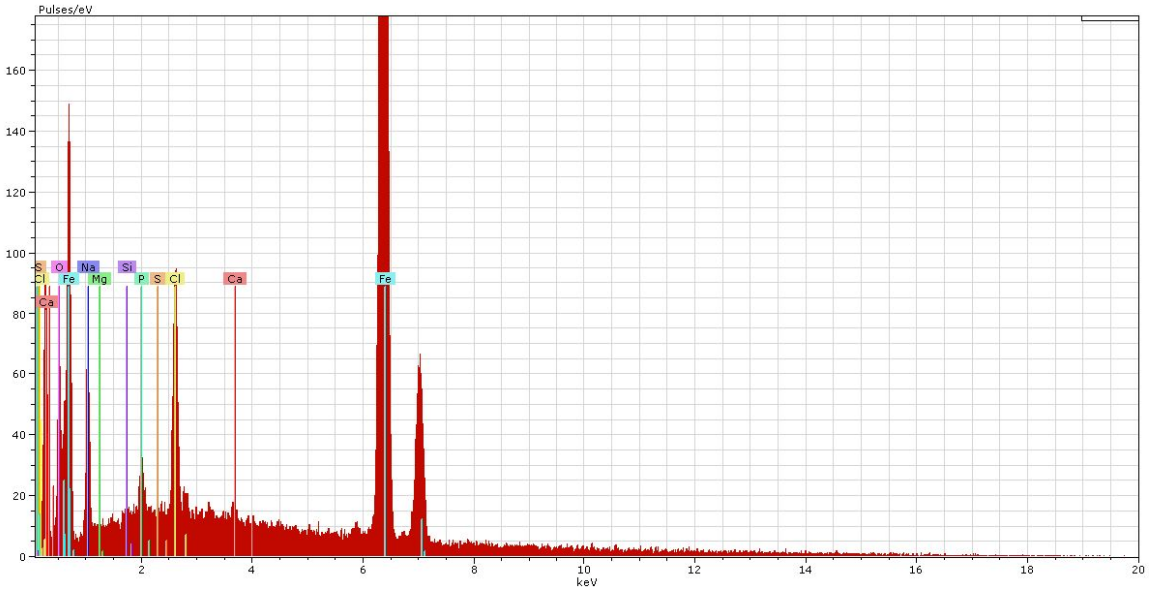

Figure 5.29. EDX spectra of surface of sample after immersion for 7 days in 3.5% NaCl solution with addition of D5-B inhibitor.

Table 5.12. The relative percentages of various elements determined using EDX quantification, of surface film deposits on steel samples after immersion in 3.5% NaCl solution for 7 days, with addition of D5-B inhibitor.

Element	Iron	Calcium	Magnesium	Phosphorus	Silicon	Oxygen	sulfur	Sodium	Chlorine
Percentage of Element	69.5	0.51	0.23	1.139	0.14	9.6	0.06	14.29	4.5

The results of the SEM imaging, EDX spectra analysis (Plate 5.9 and Figure 5.29) and EDX mapping clearly show two kinds of area on the steel surface; firstly a uniform coating on the steel which contains magnesium and phosphorous (probably a precipitated magnesium phosphate) which also might contain iron as well. This is not certain as the iron map might also have come from the underlying base metal. If the iron is part of the film, a co-precipitation mechanism (see Section 4.3.5) seems one possible explanation. The second area seems to stand proud of the surface, typically 20 μm in diameter and contains largely calcium and phosphorous, probably calcium phosphate. The rest of the deposit is clearly sodium chloride originating from the solution. The growth with time (up to 120 hours) of this film has already been tracked using impedance (Figure 5.21) and it is tempting to suggest that the unevenness in this plot is associated with the growth and fracture of these films.

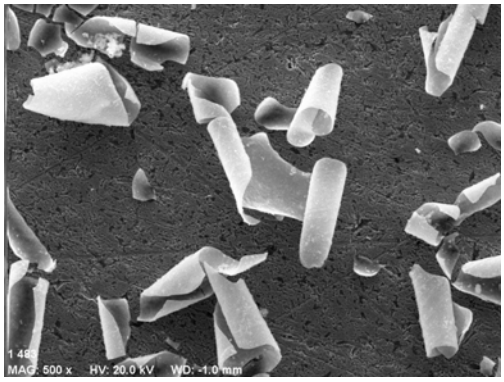

(a). Secondary electron image taken at 500x

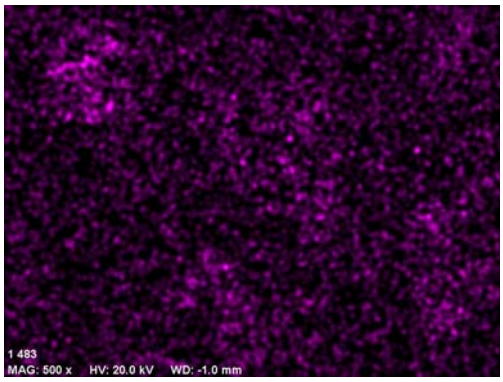

(b) Single EDX element map of distribution of Ca

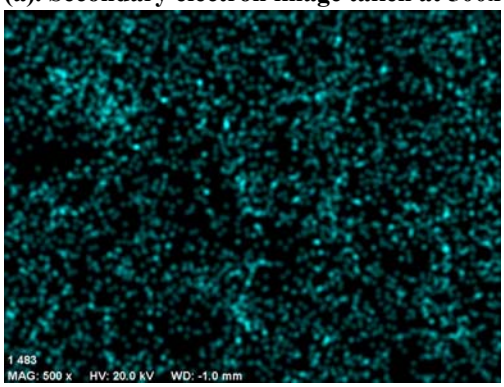

(c) Single EDX element map of distribution of Mg

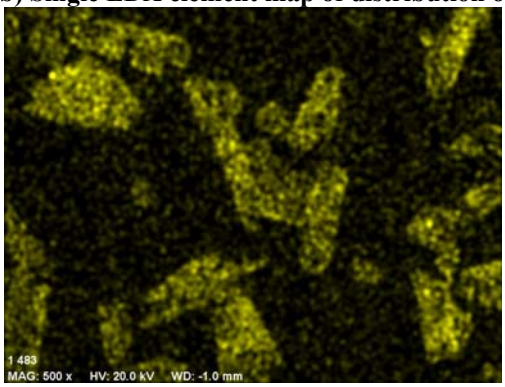

(d) Single EDX element map of distribution of P

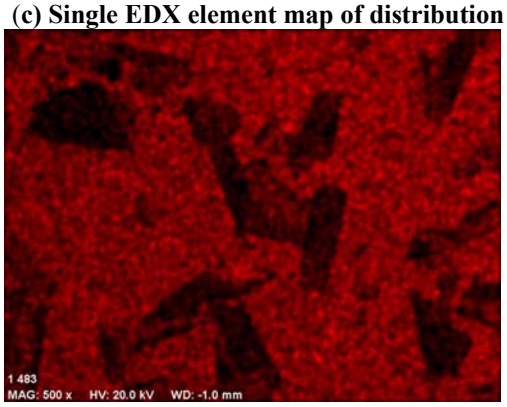

(e) Single EDX element map of distribution of Fe

Plate 5.10. SEM micrographs and associated EDX element distribution maps of surface of mild steel sample after immersion for 7 days in acid rainwater solution with addition of D5-B inhibitor

Plate 5.10 shows the corrosion film deposits formed on mild steel samples immersed in acid rainwater solution with addition of D5-B after 7 days. Plate 5.10(a) shows a SEM photomicrograph of the sample surface taken at a magnification of 500 X, and Plates 5.10(b), (c), (d) and (e) present the single EDX element distribution maps that correspond with the image shown in Plate 5.10(a), whilst Figure 5.30 gives the EDX full spectra results of all the elements present, and Table 5.13 gives the quantitative percentages of all the selected elements in the deposit.

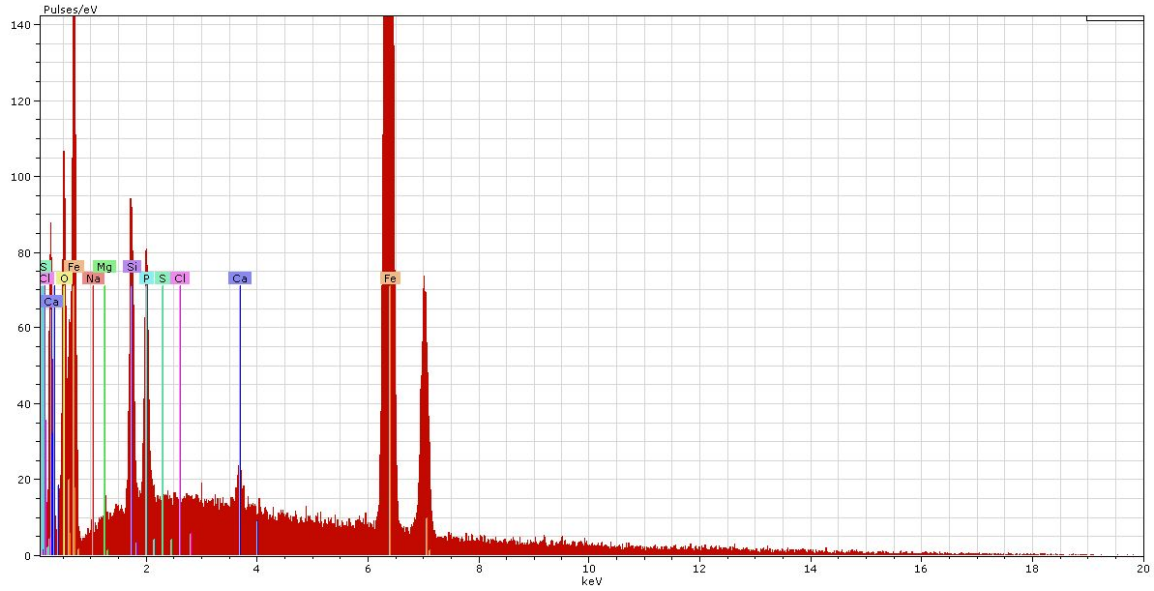

Figure 5.30. EDX full spectra of surface of sample after immersion for 7 days in acid rainwater solution with addition of D5-B inhibitor.

Table 5.13. The relative percentages of various elements determined using EDX quantification, of surface film deposits on steel samples after immersion in acid rainwater solution for 7 days, with addition of D5-B inhibitor.

Element	Iron	Calcium	Magnesium	Phosphorus	Silicon	Oxygen	Sulfur	Sodium	Chlorine
Percentage of Element	61.75	0.88	0.33	4.9	6.9	24.5	0.14	0.35	0.19

The results of the SEM imaging and EDX mapping (Plate 5.10), EDX analysis (Figure 5.30 and Table 5.13) show that; as with the NaCl situation, the film formed by the inhibitor on the steel surface is clearly composed of two layers. There is an inner compact layer containing magnesium, phosphorous and maybe iron, similar to the NaCl situation, with a film thickness of around 120 nm (Section 5.4.2). There is also a very obvious outer layer which curls up when it detaches, probably due to a residual tensile stress. This detachment is thought to be caused by drying out either on removal from the solution or in the low pressure atmosphere in the carbon coater. This spontaneous detachment due to residual stress has been observed before with organic coatings and has been discussed by Croll [5]. This detached outer layer differs from that observed in the NaCl case in that it contains not only calcium and phosphorous but also magnesium. It may be that the more acid conditions in the acid rain solution favours magnesium precipitation. Again, impedance analysis over 240 hours suggests a steady film growth with time (Figure 5.27). It is tempting to suggest that this growth is due to growth in the outer layer.

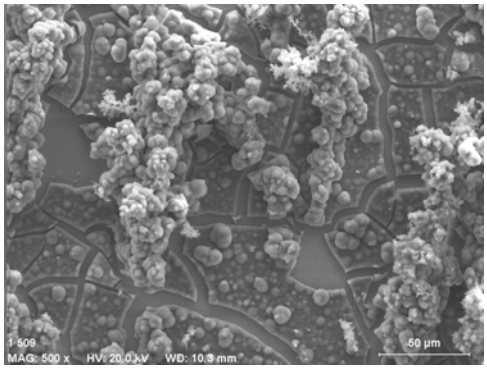

(a). Secondary electron image taken at 500x

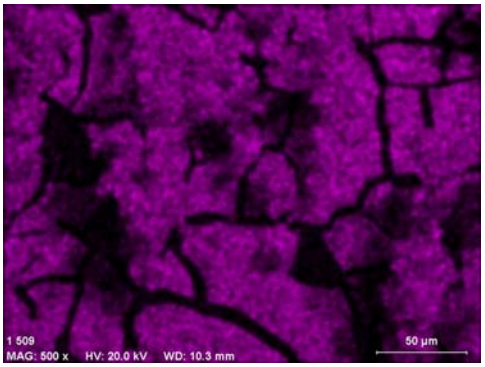

(b) Single EDX element map of distribution of Ca

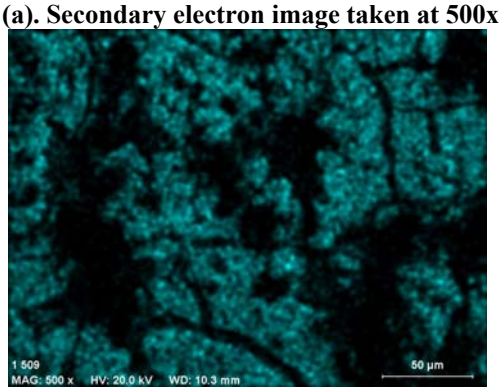

(c) Single EDX element map of distribution of Mg

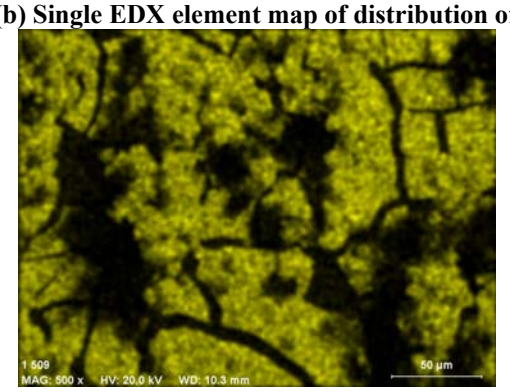

(d) Single EDX element map of distribution of P

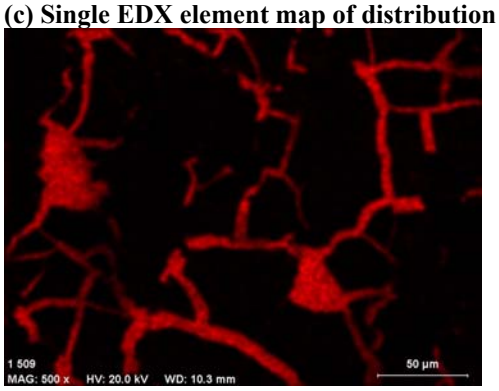

(e) Single EDX element map of distribution of Fe

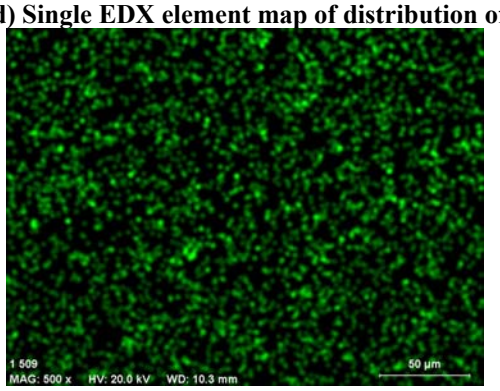

(f) Single EDX element map of distribution of Zn

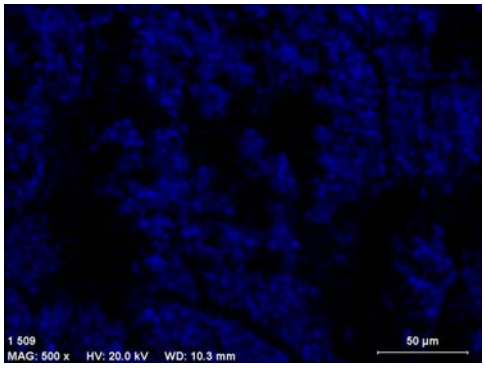

(g) Single EDX element map of distribution of Na

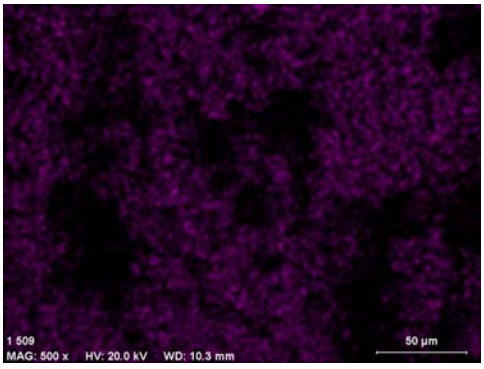

(h) Single EDX element map of distribution of Cl

Plate 5.11. SEM micrographs and associated EDX element distribution maps of surface of mild steel sample after immersion for 7 days in 3.5% NaCl solution with addition of D5-B inhibitor and connected to zinc metal anode.

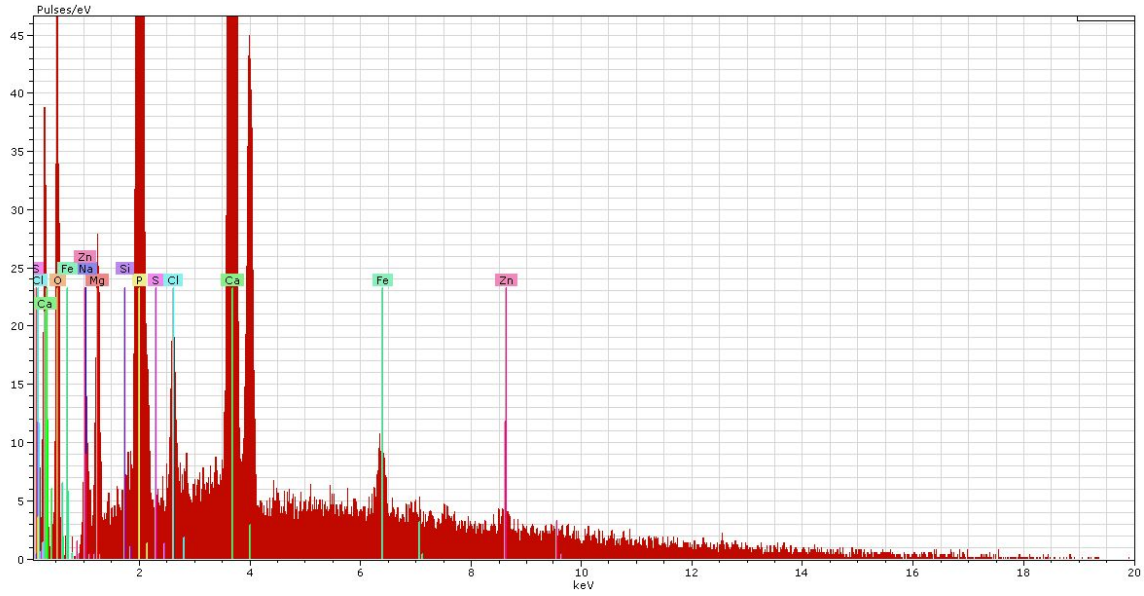

Figure 5.31. EDX full spectra of surfaces of samples after immersion for 7 days in 3.5% NaCl solution with addition of D5-B inhibitor and connected to zinc metal anode.

Table 5.14. The relative percentages of various elements determined using EDX quantification, of surface film deposits on steel samples after immersion in 3.5% NaCl solution with addition of D5-B inhibitor and connected to zinc metal anode.

Element	Iron	Calcium	Magnesium	Phosphorus	Silicon	Chlorine	Sodium	Oxygen	Zinc	Sulfur
Percentage of Element	7.24	16.48	4.46	15.37	0.15	0.77	2.64	51.84	0.97	0.07

Plate 5.11 shows the corrosion film deposits formed on mild steel samples after immersion for 7 days in 3.5% NaCl solution with the addition of D5-B and connected to a zinc metal anode. Plate 5.11(a) shows a SEM photomicrograph of the sample surface taken at a magnification of 500 times, and Plates 5.11(b), (c), (d), (e), (f), (g) and (h) present the associated single EDX element distribution maps that correspond to the sample area imaged in Plate 5.11(a), whilst Figure 5.31 gives the EDX spectra results of all the elements present, and Table 5.14 gives the quantitative percentages of all the selected elements in the deposit. The results of the SEM imaging and EDX analysis (Plate 5.11 and Figure 5.31) show that calcium, magnesium, phosphorus and zinc were all present within the film deposit, the porous deposits that were formed on the sample surface are illustrated in the SEM micrographs shown in Plate 5.11(a).

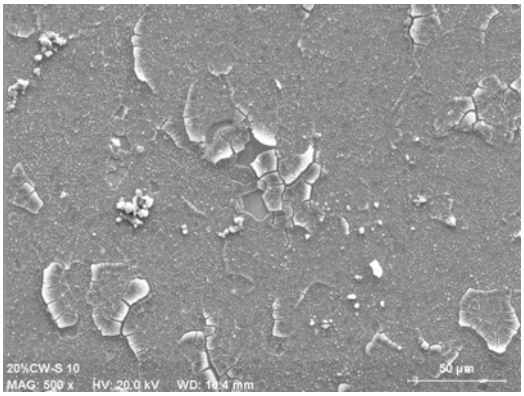

(a). Secondary electron image taken at 500x

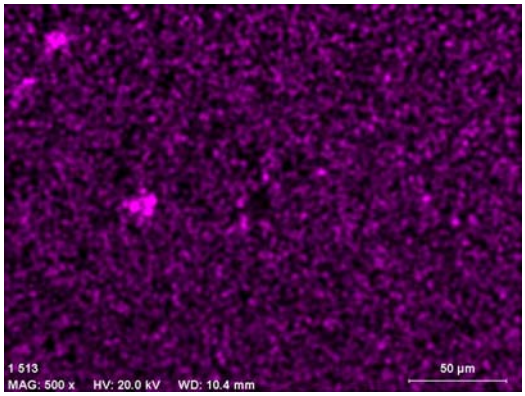

(b) Single EDX element map of distribution of Ca

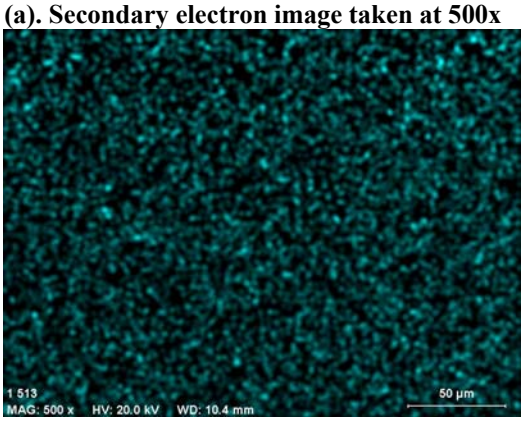

(c) Single EDX element map of distribution of Mg

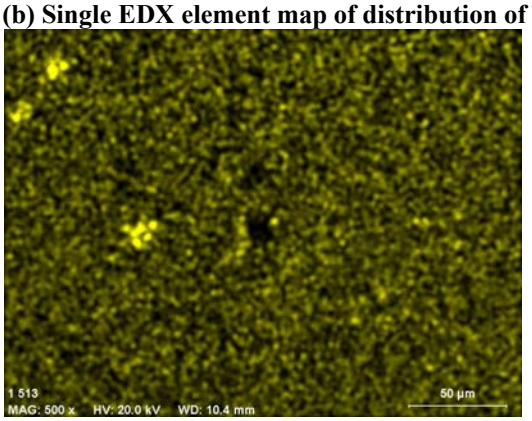

(d) Single EDX element map of distribution of P

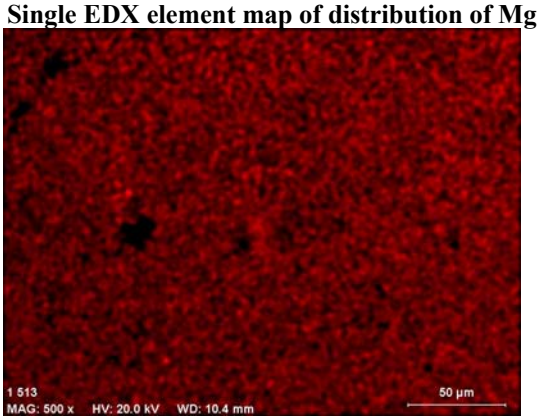

(e) Single EDX element map of distribution of Fe

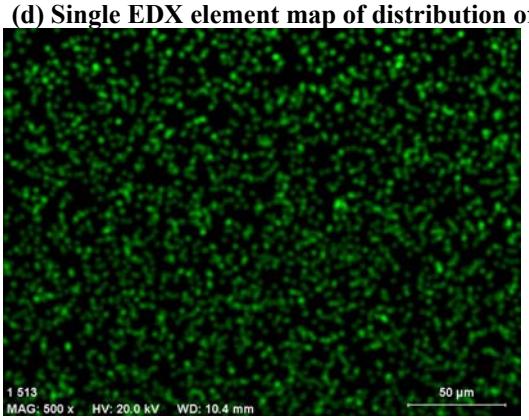

(f) Single EDX element map of distribution of Zn

Plate 5.12. SEM micrographs and associated EDX element distribution maps of surface of mild steel sample after immersion for 7 days in acid rain solution with addition of D5-B inhibitor and connected to zinc metal anode.

Table 5.15. The relative percentages of various elements determined using EDX quantification, of surface film deposits on steel sample after immersion in acid rainwater solution for 7 days, with addition of D5-B inhibitor and connected to zinc metal anode.

Element	Iron	Calcium	Magnesium	Phosphorus	Silicon	Chlorine	Sodium	Oxygen	Zinc	sulfur
Percentage of Element	68.5	3.03	2.17	5.61	0.12	0.1	0.33	19.26	0.76	0.08

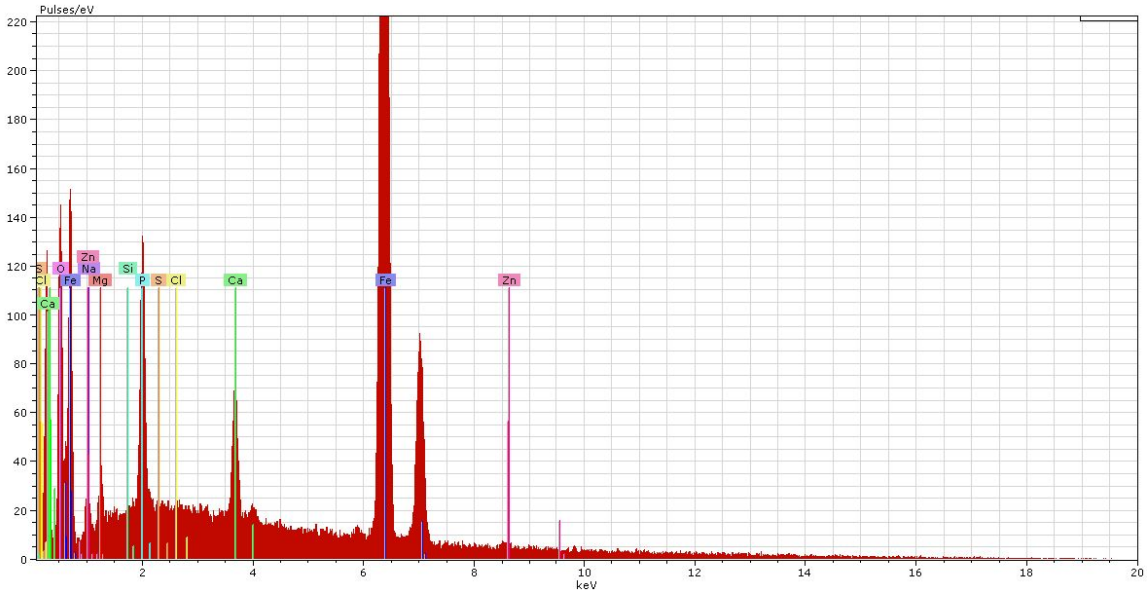

Figure 5.32. EDX spectra of surface of sample after immersion for 7 days in acid rain solution with addition of D5-B inhibitor and connected to zinc metal anode.

Plate 5.12 shows the corrosion film deposits formed in acid rainwater with the addition of D5-B and connected to a zinc metal anode after 7 days immersion. Plate 5.12(a) shows a SEM photomicrograph of a sample surface taken at an instrument magnification of 500 times, and Plates 5.12(b), (c), (d), (e) and (f) present the single EDX element distribution maps that correspond to are area imaged in Plate 5.12(a), whilst Figure 5.32 gives the EDX full spectra results of the elements present. The results of the SEM imaging and EDX analysis (Plate 5.12 and Figure 5.32) show that calcium, magnesium, phosphorus and zinc were all present within the film deposit, the porous deposits that were formed on the sample surface are illustrated in Plate 5.12(a) and (b). Table 5.15 gives the quantitative percentages of all the selected elements in the deposit.

5.4.2. SEM/EDX examination of deposit cross sections.

To investigate the thicknesses of the deposits formed on the surfaces of mild steel samples as a result of immersion in 3.5% NaCl solution and acid rain solution with the addition of D5-B inhibitor, some cross-section analyses were carried out. The method of preparation of samples and the procedures involved in this technique have already been described previously in Section 3.8.4 and Section 4.3.4.4.

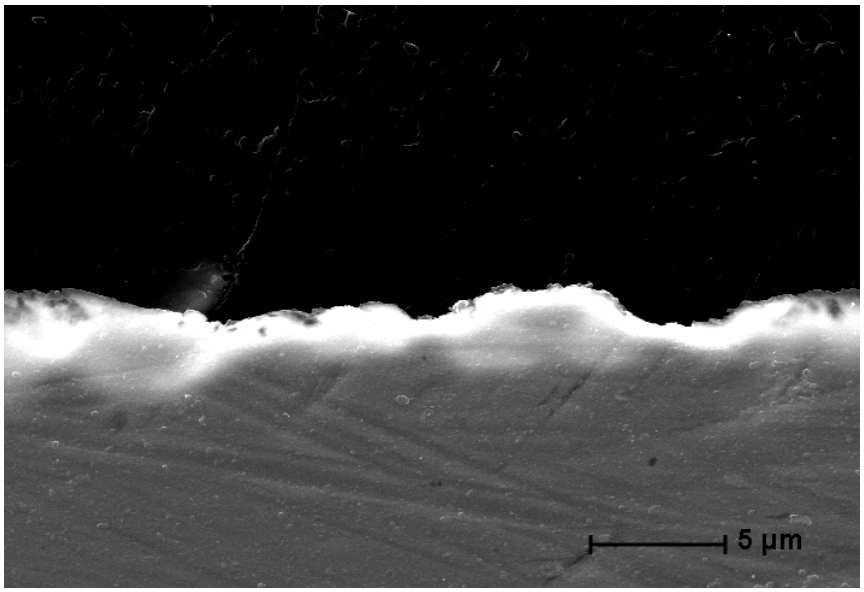

(a). Secondary electron image taken at 4000x.

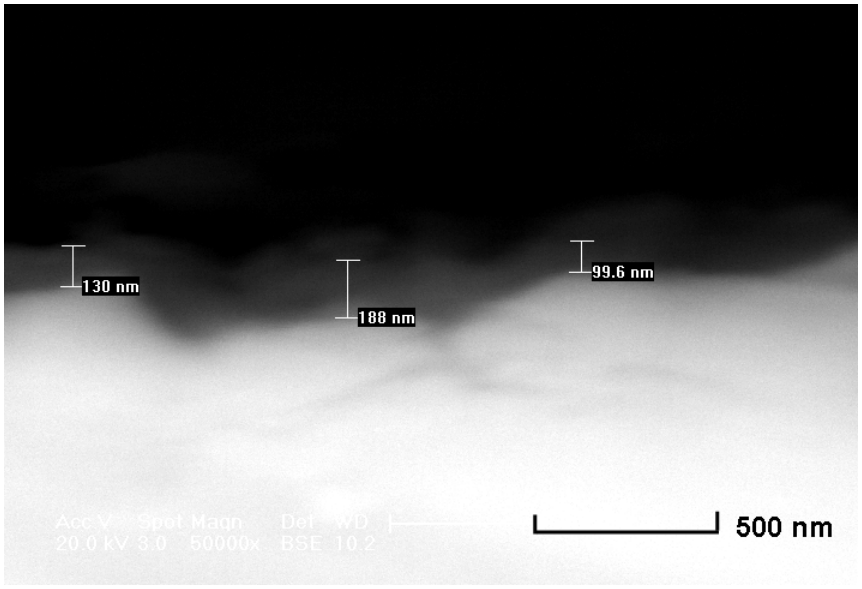

(b). Back scattered electron (BSE) image taken at 50000 X.

Plate 5.13. SEM and BSE micrographs of cross section of samples after immersion for 7 days in 3.5% NaCl solution with addition of D5-B inhibitor.

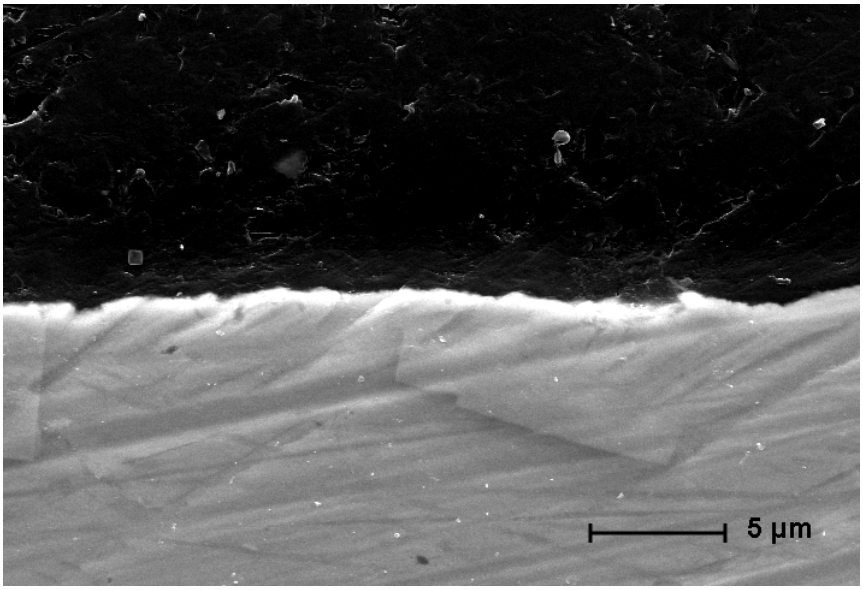

(a). Secondary electron image taken at 4000x

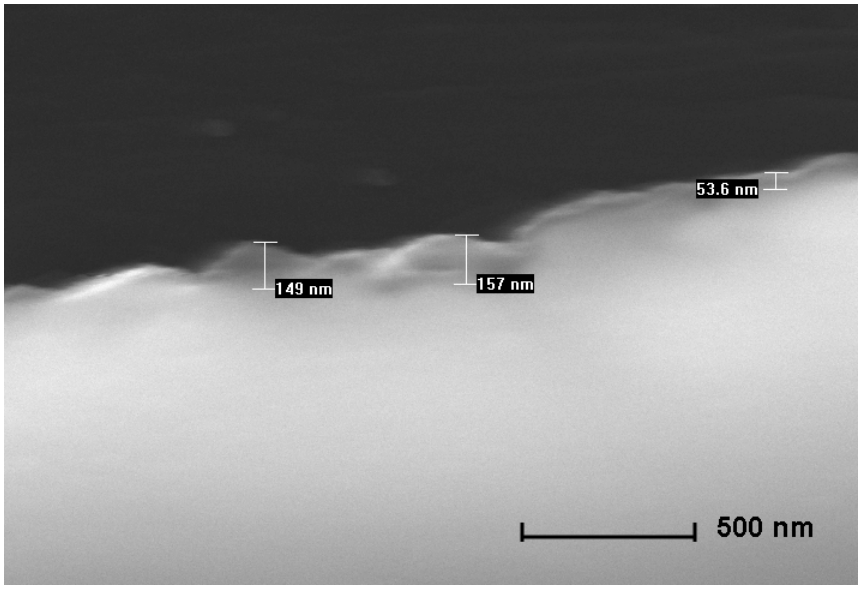

(b). Back scattered electron (BSE) image taken at 50000x

Plate 5.14. SEM micrographs of cross section of samples after immersion for 7 days in acid rain solution with addition of D5-B inhibitor.

Plates 5.13(a) and (b) and Plates 5.14(a) and (b) show SEM photomicrographs of sample cross sections taken at different instrument magnifications: (a) 4000 times (b) 50000 times. These thin sections are much thinner than the EDX beam diameter and so point analysis was not possible. Therefore the purpose of this specific study is merely to use the SEM/section techniques to determine the film thickness.

We already know the elements present on the film surface from our previous work. In Section 5.4.1, Figure 5.29 and Figure 5.30 give the EDX spectra for all the elements

present. Table 5.12 and Table 5.13 also present the quantitative percentages of all the selected elements in the deposit.

Plate 5.13 shows a SEM micrograph of a sample/film cross-section after immersion for 7 days in 3.5% NaCl solution with D5-B inhibitor. Film thickness measurements were carried out in three different locations and the thickness of the films were 130 nm, 188 nm and 99.6 nm. The SEM micrographs of a sample/film cross-section, after immersion for 7 days in acid rain solution with D5-B inhibitor are presented in Plate 5.14. Similar measurements were carried out in three different locations; the thicknesses obtained were 149 nm, 157 nm and 53.6 nm. Tempting though it is to carry out a statistical comparison between the thicknesses obtained in these two solutions such an exercise would be meaningless. All that can be said is that the films in both solutions have a range of thicknesses which vary between 60 and 200nm. A more convincing thickness comparison using GDOES will be shown in the next Section.

5.5. GDOES.

The technique of GDOES has already been explained and used earlier in this Thesis in Sections 3.11 and 4.33. The data below was generated after 4 days immersion in the inhibited solution and correspond to the visual images shown in Figure 5.33 and Figure 5.34. In each graph, two figures (a) and (b) were presented together which were chosen at two different locations of the same sample.

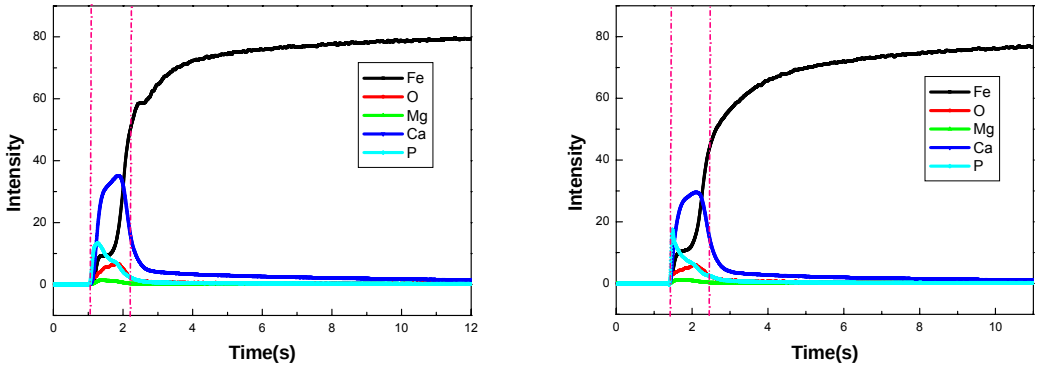

(a) area1 **(b) area2**

Figure 5.33. GDOES graphs of samples after immersion for 7 days in 3.5% NaCl solution with addition of D5-B inhibitor.

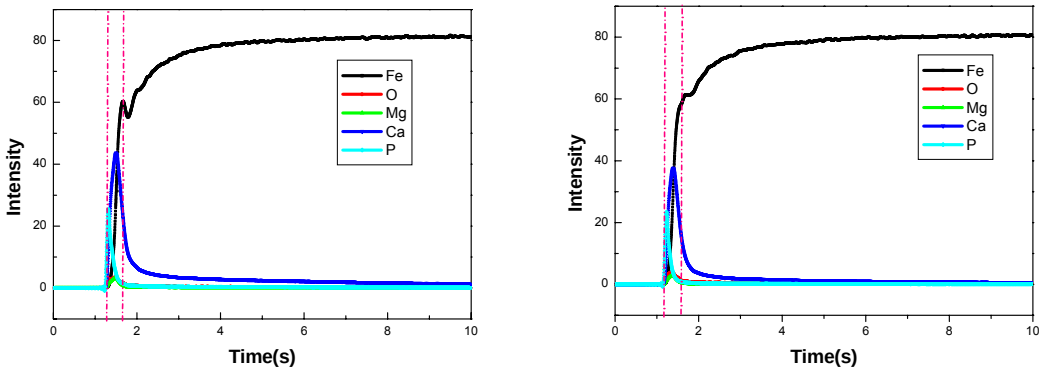

(a) area1 **(b) area2**

Figure 5.34. GDOES graphs of samples after immersion for 7 days in acid rain solution with addition of D5-B inhibitor.

Proceeding Left to Right across the graph indicates loss of the sputtered film and illustrates how the film composition varies with time, and the left-hand side represents the film surface (the vertical pink dotted line) and the second pink line represents the film-steel interface, so the thickness of films may be compared one with the other by

looking at the distance between the two pink lines within the same graph. In Figures 5.33(a) and (b), the film thicknesses are quite similar, and represented by 1s, while the film thickness is represented by 0.4s in Figures 5.34(a) and (b). Thus the GDOES data clearly shows a thinner film on the steel surface in acid rain compared to that formed in the 3.5% NaCl solution. It also clearly shows that the films contain calcium, magnesium, phosphorus and oxygen.

5.6 General Discussion.

5.6.1. Does D5-B work as a corrosion inhibitor?

From the simple exposure tests in the four chosen aqueous test solutions, it is clear that the D5-B pigment possesses substantial anti-corrosion properties which appear somewhat superior to zinc phosphate and two other commercially available pigments. These observations are backed up by electrochemical corrosion rate determinations, using Linear Polarisation Resistance, and Impedance analysis. Furthermore, the visual appearance of the film formed with the D5-B pigment in the four solutions gives a marked opalescence similar to an interference film which suggests a film thickness around the 100-200 nm range. These film thicknesses have been confirmed using analysis of cross sections in the SEM, for the inhibited systems containing D5-B in NaCl and acid rain solution (Section 5.4.2).

5.6.2. How efficient is D5-B as an inhibitor?

Using the three independent techniques of linear polarization resistance, EIS analysis and Tafel extrapolation we can calculate using equation 5-4, how efficient the inhibitor is as a function of solution composition and time; see Table 5.16 and Table 5.17. It can be seen that this inhibitor works well in the acid rain solution (Table 5.17) and moderately well in the 3.5% NaCl solution (Table 5.16). Further, it is interesting to note that in these two solutions, the level of inhibitor efficiency increases with time, suggesting that the growth of the film providing the inhibition is an ongoing process.

The inhibitor efficiency is based on the calculation of corrosion rate, and the value of Tafel constants. If the Stern-Geary constant is indeed constant, then efficiency can be calculated from the values of polarization resistance R_P and may be given by the following equation:

$$Efficency = \frac{1/R_{P1} - 1/R_{P2}}{1/R_{P1}} \times 100\% = \frac{R_{P2} - R_{P1}}{R_{P2}} \times 100\% \quad \text{……..……..……} \quad (5\text{-}4)$$

Where:

R_{p1} = polarization resistance without inhibitor, (Ω.cm²).

R_{p2} = polarization resistance with inhibitor, (Ω.cm²).

Table 5.16. The efficiency of the inhibitor D5-B in 3.5% NaCl solution.

Day	LPR(%)	EIS analysis(%)	Tafel extrapolation(%)
1	28.4	72	91.0 (after 2 hours immersion)
2	36.4	75	
3	36.9	73.6	
4	58.5	82	
5	60.1	75	
6	55.5	80	
7	57.3	82	

Table 5.17. The efficiency of the inhibitor D5-B in acid rain solution

Day	LPR(%)	EIS analysis(%)	Tafel extrapolation(%)
1	68.7	81	99.0 (after 2 hours immersion)
2	91.4	82	
3	90.1	80	
4	93.3	87	
5	94.4	92	
6	95.9	95	
7	97.2	96	

5.6.3. What is the mechanism of inhibition?

As we have seen in Chapter 3, the simplest and most common method of categorizing inhibitors is to define them as anodic, cathodic or mixed. These criteria are assigned after determining the movement of the open circuit potential after addition of the inhibitor. Our potential time data does seem to suggest that the D5-B inhibition is mixed. That is, both cathodic and anodic processes are inhibited.

SEM/EDX microscopy and analysis reveals in the NaCl case a two layer structure with an inner layer containing Mg and P, probably a magnesium phosphate precipitate with an outer discontinuous layer containing calcium and phosphorous, probably calcium phosphate.

In the acid rain solution, a two layer structure is also evident, the inner layer also contains magnesium and phosphorous, but the outer layer shows signs of fracture and detachment and contains not only Ca and P but also Mg.

When connected to zinc, in both the acid rain and NaCl solutions, there is no evidence of a two layer structure, there is a porous single film which contains Ca, Mg, P and Zn.

GDOES analyses was not used when the steel was connected to the zinc. With the NaCl and acid rain solutions, GDOES clearly shows the presence of calcium, magnesium and phosphorous in the film. Examination of sample/film sections in the SEM reveals a film thickness of 60-200 nm

SEM section imaging suggests that the thickness varies with location on the surface. GDOES indicates that the NaCl film is thicker than the acid rain film. We feel that this data may be explained by the concept of local anodes and cathodes. In neutral solutions at open circuit, local anodes and cathodes would develop on immersion and would be expected to be quite far apart and therefore any inhibitor film formed would be somewhat unevenly distributed. We are suggesting a mixed inhibition mechanism and one might expect the initial film produced on the steel surface would be an anodic inhibitor; namely the inner calcium and phosphorous containing films which we have observed on the steel surface. Later, pH changes would generate cathodic deposits as a second layer which in the NaCl case contains calcium and phosphorous, maybe a mixed calcium carbonate/ calcium phosphate precipitate. In the acid rain solutions the outer cathodic precipitate also contains magnesium, maybe a magnesium coprecipitate! Chemically a further difference with the acid rain solutions would be the predominant cathode reaction of hydrogen evolution. One would expect this to give a much finer distribution of anodic and cathodic areas thereby leading to a much thinner inhibitor deposit. This we have observed.

Much of what we have just said is speculative. In order to test the mechanisms proposed, thin-section TEM with EDX might provide the answer.

5.6.4. The effect of direct connection of the steel to zinc.

The justification for connecting the steel working electrode to a piece of pure zinc and then assessing the new role of D5-B has already been made in Section 5.2.3 of this Chapter. Clearly, the effectiveness of D5-B as an inhibitor in the two aqueous solutions studied has been significantly enhanced when the steel specimens have been simultaneously connected to a zinc anode. The potential in both situations moves

negatively, much more so in the NaCl solutions (-1050mV SCE) compared with the acid rain solution (-850mV SCE), probably because of the lower conductivity of the acid rain which in turn will lead to a much reduced current output from the anode. The visual appearance of samples indicates complete absence of corrosion and SEM/EDX analysis suggests a thin film of inhibitor containing calcium, magnesium, phosphorus and zinc. Also visually, the deposits formed with D5-B and a Zn anode together (Plate 5.11 and Plate 5.12) were thicker than those where only the inhibitor D5-B was used alone (Plate 5.9 and Plate 5.10).

5.6.5. The Role of Zinc.

There are two possible explanations for the role of the zinc.

The first is that the negative potential attained on connecting the steel to the zinc enhances the cathodic reactions on the steel and increases the interfacial pH at the steel and further enhances cathodic inhibition.

The second is that the action of the zinc anode provides a source of soluble zinc ions in the solution which in turn can act to supplement the calcium and magnesium already present from the inhibitor. Of course, there is always the possibility of both mechanisms acting concurrently.

To attempt to distinguish and choose between these two mechanisms, we carried out a series of additional experiments. They both involved the same two solutions, the same steel specimens, the same D5-B inhibitor additions. In one situation we added the zinc ions directly to the solution at a concentration of 1g $ZnSO_4$ in 200ml of solution rather than have them generated from dissolution of the zinc anode. From the results of our study it does appear that the optimum performance is where our two suggested mechanisms are operating concurrently, namely the presence of zinc ions and a steel potential where cathodic inhibition is favoured.

5.7. Conclusions.

- The novel pigment D5-B works as a corrosion inhibitor for mild steel in deionised water, 3.5% NaCl , 0.025M $NaClO_4$ and acid rain solutions and its performance in these solutions is comparable with and maybe exceeds three commercially available pigments.

- Potential time measurements and potentiodynamic polarization studies have been carried out and from the data produced, inhibition by the pigment is thought to be mixed; i.e. both anodic and cathodic.

- Electrochemical studies have been used to look at its inhibitor efficiency as a function of time in the NaCl, sodium chlorate, and acid rain solutions.

- A simple electrical analogue circuit has been used to model the electrochemical behaviour of the steel electrode in the D5-B conditions. We have used this model with electrochemical impedance techniques to successfully study the growth of the inhibitor film on the steel surface as a function of time. Even after 240 hours the film has not reached steady state and continued to grow.

- SEM/EDX and GDOES were used to provide information on the inhibitor films produced on the steel surface namely film thickness and film composition. Films were seen to have a two layer structure. The film composition depended on the solution. Film thicknesses were within the range 80 to 200 nm.

- The inner layer in both the NaCl solutions and acid rain consisted of magnesium and phosphorus; the outer layer in NaCl contained calcium and phosphorus, in acid rain the outer layer also contained magnesium.

- We suggest that the inner layer is an anodic deposit and the outer layer is a cathodic deposit; i.e. anodic insoluble phosphates plugging anodic sites with cathodic calcium and magnesium containing alkali generated precipitates.

- Based on the GDOES data, films produced in the acid rain solution are significantly thinner than that from the sodium chloride solution.

- The novel pigment performance is enhanced when the steel sample is coupled to a zinc anode. A single layer inhibitive film is produced which contains calcium, magnesium, phosphorus and zinc.

- The mechanism of enhancement seems not just due to the negative potential attained, nor just due to the presence of zinc ions in solution but seems to be due to a combination of both effects.

5.8. References.

1. J. E. O. Mayne and and E. H. Ramshaw, "Autoxidation of lead soaps of the linseed oil fatty acids", J. Applied Chemistry, **13,** pp553-560, 1963.

2. A. D. Mercer. In: Corrosion. (ed). L. L. Shreir. "Corrosion Inhibition: Principles and Practice" Newnes-Butterworth. London. 1976.

3. C. M. Rangel, J. De Damborenea. A. I. De Sa and M. H. Simplicio. "Impedance analysis of zinc and calcium cations as corrosion inhibitors" Brit. Corros. J. **27,**(3), p207. (1992).

4. J. E. O. Mayne and J. Golden. "Inhibition by zinc potassium chromate" Brit. Corr. J. **13**. p45. 1978.

5. S. G. Croll, "Residual Stress and the adhesion of organic coatings on mild steel", J.O.C.C.A., **63**, pp 220-226. 1980.

Chapter 6. General Discussion on the Action of the Films Studied and Future Work.

6.1. General discussion.

In this Thesis we have looked at two kinds of calcium and magnesium containing films on mild steel; firstly ones produced by growing a film using cathodic protection in an electrolyte containing calcium and magnesium, namely artificial sea water and secondly ones produced by immersion in a corrosion inhibitive solution where the calcium and magnesium ions are generated by dissolution of the slightly soluble pigment. We have looked at both films and at first sight the two areas seem totally separate. However in this final Chapter it is considered worthwhile and instructive to compare and contrast the two forms of films produced.

Both films are inorganic, and in many situations on the same surface there are different regions, one calcium containing and the other magnesium containing. Both films have been shown to influence the corrosion of mild steel by reducing the corrosion rate. The calcareous film is thought to work in a way very similar to classic cathodic inhibitors which we have already described in our literature review in Section 2.6 in Chapter 2. Briefly, pH driven precipitation reactions take place at cathodic regions on the steel surface and the final produced film works as a barrier to movement of oxygen from the bulk solution through to the steel surface. Further, being a non electron conductor, the cathodic reduction reactions are no longer capable of taking place at the film electrolyte interface. The D5-B inhibition mechanism has been shown to be mixed, namely the D5-B acts both as an anodic and a cathodic inhibitor. Those cathodic functions of the D5-B inhibitor are also thought to act in the same way as described above.

We have shown earlier in this Thesis (Section 4.3.4.3. and 4.3.4.4 in Chapter 4) that the magnesium deposition in the calcareous film, especially during underprotection, is strongly influenced by the steel substrate by a process of co-precipitation. Early stages of the magnesium part of the calcareous film growth may well be influenced uniquely by the presence of ferrous ions in solution. We have also shown using elemental mapping, the possibility of a combination of the magnesium in D5-B and the underlying iron in the substrate as well. The D5-B pigment is clearly an excellent inhibitor for the corrosion of

mild steel in the four solutions investigated, namely deionised water, 3.5% NaCl, a dilute perchlorate solution (0.025M) and an acid rain solution. We have not looked at its inhibitive functions in a seawater environment since it would never be used in this situation. Early theories concerning corrosion inhibition usually centred around Uhlig and his co-workers[1] concentrate on adsorption as the main mechanism of inhibition. In the three solutions chosen there is no evidence of a simple adsorption process taking place.

In both the D5-B and the calcareous situations, we have shown there to be the presence of a three dimensional film on the steel surface. The calcareous film has an obvious microscopic multilayer structure. The D5-B layer in 3.5% NaCl and the acid rain solution has a more compact structure with a visually slight optical interference sheen. The optical properties of the interference film formed by the interaction between the D5-B pigment and the acid rain and sodium chloride solutions suggest a film thickness around the 100-300 nm range. This value is confirmed by SEM cross-section analysis of around 60-200 nm.

SEM pictures of the change in the calcareous film with time seems to suggest a growth mechanism involving the calcium containing calcite crystals acting as nuclei for adjacent crystals. We have not looked at changes in D5-B growth with time using SEM due to time constraints. However we have used impedance to look at growth of these films over a thirty day testing period. It seems that a film appears very early on during exposure, which continues to grow in an approximately linear manner over a 240h exposure period.

In spite of their similarities, there are fundamental and basic differences between the two systems. The main difference is simply the way the two systems perform. The calcareous film, although it does significantly reduce the cathodic protection current density, there is a permanent and probably continuous requirement of the presence of cathodic protection current to maintain the film and keep it intact. Although it is not entirely clear how low a steady state current density needs to be to achieve this, in this Thesis we have shown values of 200 mA/m^2 and 300 mA/m^2 are possible and in a recent publication [2], we have suggested a value of 15-19 mA/m^2. Conversely, the D5-B film clearly forms spontaneously and merely needs a solution presence to operate as an anti-corrosion film. Indeed it does seem that the D5-B film improves with time of exposure.

The main chemical difference is that the source of inhibitor is a solid pigment also containing phosphorous whereas the calcareous film merely needs the presence of calcium and magnesium in solution in seawater.

There is a considerable difference in the structure and morphology of the films produced in the two systems. The calcareous film as we have seen has a variable composition depending on the applied current density. Typically an inner layer is composed of a magnesium containing compound with an outer layer of calcium containing compound which clearly colonises the surface and grows in characteristic shapes with thicknesses of typically 40 - 50μm.

The D5-B film in both solutions provides clear evidence of two types of deposit, both containing phosphorous, probably as phosphate, an inner layer composed of magnesium and phosphorous, and an outer region containing calcium and phosphorous in the NaCl solution with additional Mg in the acid rain. In the acid rain solution this outer region has a layered structure, whereas in sodium chloride solutions, the outer region is in the form of individual precipitates. Potential/time curves for the D5-B pigment in NaCl and the acid rain solution suggest that its mechanism is one of a mixed inhibitor, namely the inhibition is operating both on the anodic and cathodic half reactions.

We suggest that the inner layer is an anodic deposit and the outer layer is a cathodic deposit; i.e. anodic insoluble phosphates plugging anodic sites with cathodic calcium and magnesium containing alkali generated precipitates.

6.2. Future work.

- The work described in Chapter 4 on weight loss and cathodic protection used a stagnant artificial seawater solution, a thirty day exposure period and a relatively small area of exposure. This work needs to be repeated in real seawater, under well defined conditions of temperature, oxygen content and flow for a much longer exposure condition; at least one year and maybe a much larger exposed area. In particular, attention needs to be given to the nature of the corrosion process in terms of its visual appearance. Our claim concerning the validity of the so-called protection potential also needs further testing under real seawater conditions.

- Further to the above, our work was carried out under sterile conditions. Clearly with natural seawater, a whole range of living organisms may have an influence on corrosion and the calcareous film and this will need to be considered during any future testing.

- We have looked briefly at the situation of starting with a high protection current density for a given time and then reducing its value and assessing whether the cathodic protection is successful or not. This concept could be extended by varying the initial current density, initial time, final current density to cover an extensive study. A further study might include switching on and off the CP system for a period of time and looking at whether the calcareous film is capable of maintaining protection during the off period.

- Under conditions of more negative potential, we have clearly seen the film becoming detached. We have suggested that evolution of hydrogen is the most likely cause of this detachment. However this suggestion is still only a hypothesis which needs testing. Hydrogen could be collected using a gas burette; different metal substrates could be studied of similar electrochemical potentials to iron but with differing exchange current densities for hydrogen.

- Our work on co-precipitation has highlighted the contribution of dissolved iron on the initial stages of the development of the calcareous film. Clearly the film should grow differently in the absence of this dissolved iron. The growth of calcareous films on stainless steels would be an obvious and worthwhile extension to this work.

- With our work on the corrosion inhibitive pigment, the obvious extension of our work is to incorporate the pigment into typical binders and to carry out conventional accelerated corrosion testing on the new paint systems. Binders which might be considered would include epoxys, alkyds, and maybe a water based acrylic with both clean and corroded steel, zinc and aluminium as possible substrates.

- The combination of the novel pigment and metallic zinc looks like an exciting concept. A conventional, fully-formulated zinc metal containing paint system (epoxy or silicate) should be created where a portion of the pigment were replaced with our pigment and again put through an accelerated test programme to see whether our results are reflected in a real system.

- The combination of ionic mixtures calcium, magnesium, phosphate and zinc as conventional corrosion inhibitors seems like a fruitful area of study. Changes in their relative proportions could be made, solutions could be varied, metals other than mild steel could be studied, indeed such a study could be made into a life's work!

6.3. References.

1. H. H. Uhlig. "Corrosion and Corrosion Control". 2nd Ed., John Wiley & Sons Inc., New York. p97. 1971.

2. J. D. Scantlebury, T. Tsukada, Y. F. Yang and M. Du. "Long–Term Cathodic Protection Performance Data of Two Off-Shore Structures". NACE Corrosion Conference. Atlanta. USA, March 2009.